Angular momentum generation mechanisms in mass-100 region

by

Niyaz Ahmad Rather

Enrolment No.: PHYS05201004009

Saha Institute of Nuclear Physics
Kolkata

A thesis submitted to the
Board of Studies in Physical Science Discipline
In partial fulfillment of requirements
For the Degree of

DOCTOR OF PHILOSOPHY

of

HOMI BHABHA NATIONAL INSTITUTE

August, 2015

STATEMENT BY AUTHOR

This dissertation has been submitted in partial fulfillment of requirements for an advanced degree at Homi Bhabha National Institute (HBNI) and is deposited in the Library to be made available to borrowers under rules of the HBNI.

Brief quotations from this dissertation are allowable without special permission, provided that accurate acknowledgement of source is made. Requests for permission for extended quotation from or reproduction of this manuscript in whole or in part may be granted by the Competent Authority of HBNI when in his or her judgment the proposed use of the material is in the interests of scholarship. In all other instances, however, permission must be obtained from the author.

NIYAZ AHMAD RATHER

DECLARATION

I, hereby declare that the investigation presented in the thesis has been carried out by me. The work is original and has not been submitted earlier as a whole or in part for a degree / diploma at this or any other Institution / University.

NIYAZ AHMAD RATHER

Publications from the present work

Journal

1. **"Emergence of principal axis rotation in ^{110}Ag."**
   Santosh Roy, **N. Rather**, Pradip Datta, S. Chattopadhyay, R.A. Bark, S. Pal, S. Bhattacharya, R.K. Bhowmik, A. Goswami, H.C. Jain, R. Kumar, E. Lawrie, S. Muralithar, D. Negi, R. Palit and R.P. Singh. "Emergence of principal axis rotation in ^{110}Ag"
   PHYSICS LETTERS **B**, 710 (2012) 587-593.

2. **"Exploring the Origin of Nearly Degenerate Doublet Bands in ^{106}Ag."**
   N. Rather, P. Datta, S. Chattopadhyay, S. Rajbanshi, A. Goswami, G. H. Bhat, J. A. Sheikh, S. Roy, R. Palit, S. Pal, S. Saha, J. Sethi, S. Biswas, P. Singh, and H. C. Jain.
   PHYSICAL REVIEW LETTERS **112**, 202503 (2014).

3. **"Antimagnetic rotation in ^{104}Pd."**
   N. Rather, S. Roy, P. Datta, S. Chattopadhyay, A. Goswami, S. Nag, R. Palit, S. Pal, S. Saha, J. Sethi, T. Trivedi, and H. C. Jain.
   PHYSICAL REVIEW C **89**, 061303(R) (2014).

Conference Proceedings

1. **"High Spin Spectroscopy Of ^{105}Pd."**
   N. Rather, P. Datta, Santosh Roy, S. Chattopadhyay, A. Goswami, S. Nag, R. Palit, S. Saha and T. Trevadi. "Emergence of principal axis rotation in ^{110}Ag"
   Proceedings of the DAE Symp. on Nucl. Phys. 57 (2012) pg. 310-311.

2. **"Staircase bands in odd-odd Ag isotopes: ^{107}Ag a case study."**
   P. Datta, **Niyaz Rather**, Santosh Roy, S. Chattopadhyay, A. Goswami, S. Nag, R. Palit, S. Saha and T. Trevadi.
   Proceedings of the DAE Symp. on Nucl. Phys. 57 (2012) pg. 312-313..

3. **"Search for Anti-magnetic rotations in ^{104}Pd."**
Niyaz Rather, P. Datta, Santosh Roy, S. Chattopadhyay, A. Goswami, S. Nag, R. Palit, S. Saha, and T. Trevad.
Proceedings of the DAE Symp. on Nucl. Phys. 58 (2013) pg. 124-125.

4. **"High Spin Spectroscopy of ^{105}Pd."**
N. Rather, P. Datta, S. Roy, S. Chattopadhyay, A. Goswami, S. Nag, R. Palit, S. Saha, J. Sethi, T. Trivedi.
Proceedings of the DAE Symp. on Nucl. Phys. 58 (2013) pg. 122-123.

5. **"Co-existance of AMR and collective rotation in ^{105}Pd."**
Niyaz Rather, P. Datta, Santosh Roy, S. Chattopadhyay, A. Goswami, S. Nag, R. Palit, S. Saha, and T. Trevad.
Proceedings of the DAE Symp. on Nucl. Phys. 59 (2014) pg. 108-109.

6. **"Staircase bands in ^{105,107,109}Ag: Fingerprint of interplay between Shears Mechanism and Collective Rotation"**
B. Das, **Niyaz Rather**, P. Datta, S. Chattopadhyay, A. Goswami, S. Rajbanshi, G. H. Bhat, J. A. Sheikh, S. Roy, R. Palit, S.Pal, S. Saha, J. Sethi, S. Biswas, P. Singh, and H. C. Jain.
Proceedings of the DAE-BRNS Symp. on Nucl. Phys. 60 (2015).

NIYAZ AHMAD RATHER

DEDICATION

Dedicated to my parents, Gulam Qadir and Rahmat

ACKNOWLEDGMENTS

It is pleasure to express my deep gratitude to Prof. Sukalyan Chattopadhyay whose guidance and inspiration has made the successful completion of this thesis work possible. His advices, teaching and a lot of fruitful ideas during the course of this work have helped me a lot and provided a good basis for the present thesis. It was an excellent opportunity of learning the various aspects of nuclear structure physics and the relevant experimentation while working with him.

I am also greatly indebted to my senior and friend Dr. Pradeep Datta whose company was both fruitful and beautiful. I am particularly thankful to him for helping me understand the various analysis techniques and their usage during the course of this work. My knowledge on the data analysis owes much to his help. I am also thankful to Dr. Santosh Roy for his help, particularly during the early days when he was also working in this division.

I also extend my sincere thanks to the non-teaching staff of the High Energy Nuclear and Particle Physics Division (HENPP) who were always available whenever needed. I am particularly thankful to Mr. Sanjoy Sarkar and Mr. Rakesh Ram and Sudham da. I also appreciate the company of my colleagues in the HENPP division, namely Dr. Palash Khan and Mr. Biswarup Das.

The work presented in this thesis owes much to the smooth functioning of the Pelletron at TIFR. I am heartily thankful to the Pelletron staff for making the smooth operation of Pelletron possible. Mr. Balaji, Mr. Rajnesh and Mr. Sheetal were very helpful during my stay at TIFR for the experiments. Their friendly behavior and technical help during the beam time is immensely appreciated.

I was also lucky to have very cheerful and helpful friends at the SINP campus. The company of Bishwarup Paul, Abhijit Gosh, Rajni Raman, Aminul Islam, Uttam Kumar, Susmita Dhara, Mala Mukhapadhyay and Rajeshwari Roychowdhery will be remembered for a long time. I also acknowledge the help of my best friend Mr. Muzaffar Qadir Lone in my early days at SINP when I was new to this place.

I would also like to thank the motherly service of Mr. Shakti Bisoi, Mr. Suresh Das and all the other helpers at the hostel canteen. Their delicious preparations made me feel at home and I enjoyed them a lot. I am also very grateful to all the boarders of the MSA-1 hostel for their friendliness. In their company I hardly missed my home.

Above all, I am very indebted to my parents for their sacrifice and unconditional support. The patience of my beloved mother on my abscence at home was a great sacrifice. Their prayers and moral support is the source of my success. I am also thankful to my brother, Sajad Ahmad, particularly for bearing the family responsibilities in my absence. My thanks are also due to my sisters who constantly kept my morale up. At last but not least, I also owe to the love and affection of my wife, Shabnam Wali who shared my pain and was always encouraging.

Finally, I acknowledge the financial support from Universities Grants Commission (UGC) and Department of Atomic Energy (DAE) of India that made the research carried out during this course possible.

NIYAZ AHMAD RATHER

Contents

List of Figures

List of Tables

SYNOPSIS

The atomic nucleus consists of protons and neutrons which are bound together by the nuclear force. This force is strong enough to form a stable nucleus despite the coulomb repulsion among its constituent protons. Thus, the nucleus is a many body quantum mechanical system with finite number of particles. But this particle number is large enough to produce collective correlations such as the rotation and vibration. However, these correlations are at best marginally stable. The addition or removal of a single valence shell nucleon can completely alter the correlations. This distinctive feature of a nucleus makes its spectroscopy both rich and varied. To determine the energetics of a nucleus, one should calculate the Hamiltonian of the ground and excited states by taking into account all the 2-body, 3-body and any other effective interactions which are suitable. This method is referred to as the “ab-initio" method. This method has a very limited success as the number of computations as a function of the nucleon number increases very rapidly that it becomes insoluble very quickly. With such calculations being insoluble, various assumptions have to be made to make such a computation tractable and this is the basis of utilizing a model.

The spherical shell model was the first model which heralded considerable success in accounting for various regularities in nuclear properties. This model considers a nucleon as moving independently in an averaged potential. For a particular nucleon, this potential represents its interaction with all other nucleons in the nucleus. In particular, it has been possible by choosing an appropriate field, containing rather strong spin-orbit coupling, to obtain a succession of single particle states which reproduce the experimentally observed discontinuities associated with the so-called magic numbers. This spin-orbit interaction is analogous to the precursive concept of the spin-orbit interaction within electron orbits in atomic physics. The shell model

assumes that protons and neutrons occupy separate, degenerate orbits and that the energy, spin and parity of the nucleus depends entirely on the occupations of these orbits. Various models have since developed from this, notably the axially deformed shell model of Nilsson, where the nucleus is assumed to be non-spherical and the energy levels of the orbits become non degenerate, however, the occupation of these orbits still determines the energy, spin and parity of the nucleus. The assumption of a deformed nucleus was necessary due to the observation of large non-zero electric quadrupole moments in many nuclei throughout the periodic table which indicated non-spherical electric charge distributions in these nuclei. The angular momentum in these nuclei are predominantly generated by the collective rotation and several models have been developed to describe this mode of excitation.

In the particle-rotor model, the rotational angular momentum of the core (rotor) is coupled with the angular momentum of one or two of the valence nucleons to generate the total angular momentum. It is a phenomenological model, and gives an approximate description of low-lying bands in odd-A or odd-odd nuclei. In 1954, the cranking model was developed by Inglis to describe magnetic moments of rotating molecules. In the cranking model, the nucleons are assumed to move independently in a deformed mean-field generated by the nucleons themselves. This field along with a pairing field, is forced to rotate uniformly about an axis perpendicular to the symmetry axis. The model applies particularly well to regions of middle and high angular momentum, and has been the most widely used model for comparing with experimental high spin data.

In a nearly spherical nucleus with a substantial number (four or more) of valence nucleons, the total angular momentum is almost fully generated by the valence nucleons. A very special situation arises near certain shell closures where the neutrons (protons) just above a shell closure (particles) have their angular momentum along

the rotational axis (j_p) while for the protons (neutrons) just below the closure (holes) the angular momentum is along the symmetry axis (j_h). Thus, the resultant angular momentum is tilted with respect to both the symmetry and rotational axes. This description of shears model was first proposed by S. Frandrof. The situation can also be described classically by the geometric shears model by Clark and Macchiavelli, where the band head spin is generated by the perpendicular coupling of the angular momentum vectors of particle and holes, j_p and j_h, respectively. The high angular momentum states are generated by the gradual closure of the two angular momentum vectors and the highest angular momentum state that can be generated is $j_p + j_h$. Thus, the only important degree of freedom in this model is the angle between these two vectors (blades of the shear), namely, the Shears angle (θ). This shears structure of particle and holes leads to a large magnetic dipole moment (μ) which precesses around **I** and leads to a large M1 transition rates ($B(M1)$) for the shears band as it is proportional to ${\mu_\perp}^2$. However, as the shear closes (θ decreases), $\mu_\perp$ decreases and the B(M1) rates also decrease with increasing angular momentum. A large number of such bands with sequences of M1 transitions have been found in A$\sim$200, A$\sim$140 and A$\sim$100 mass regions. These bands are known as M1 or Shears band where the B(M1) rates exhibit the characteristic fall. In few cases band crossing in Shears band have been found and the observed features have also been well described by the Shears model.

An interesting consequence of the shear structure has been pointed out by S. Frauendorf. It is possible to have a symmetric double shears structure (See Fig. 1 for schematic illustration), where each hole in the time reversed orbit, combines with the particles whose angular momentum vector is along the rotational axis. Thus, the angle between the two hole vectors is 2θ . The higher angular momentum states in this scenario, will be generated by simultaneous closing of the two shears and is represented by $I = j_p + 2j_h cos\theta$. The symmetry of this shears structure implies

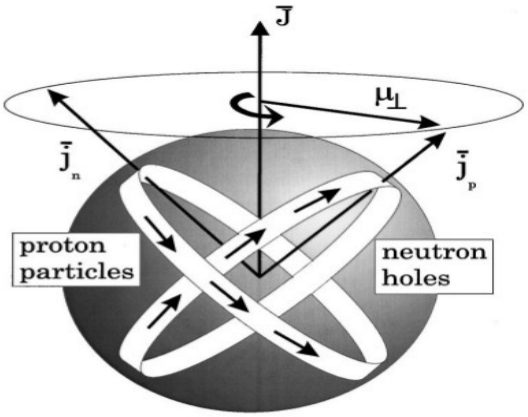

Figure 1: Schematic diagram of Anti-magnetic rotation.

that the perpendicular components of the magnetic moment cancel each other. For this reason the magnetic dipole transition rate vanishes. This cancellation of the magnetic moment has induced the name Anti-magnetic Rotation (AMR) due to its similarity with anti-ferromagnetism where the dipole moment of one sub-lattice is in opposite direction to the other half leading to the absence of the net magnetic moment. However, as the $R_z(\pi)$ symmetry is retained, the rotational structure decays by weak electric quadrupole (E2) transitions. This transition rate is given by

$$B(E2) = \frac{15}{32\pi}(eQ)^2_{eff} sin^4\theta \tag{1}$$

where Q_{eff} is the effective quadrupole moment of the core (rotor). Thus, the B(E2) rates are expected to drop with increasing angular momentum for AMR. Recently, the interplay of collective and anti-magnetic rotations has been identified by S. Roy *et al.* in the generation of angular momentum in ^{110}Cd.

In the last decade, a number of nearly degenerate pairs of rotational bands with same parity have been reported in nuclei of mass A$\sim$130 and A$\sim$100 regions. This observation of the doublet bands indicates a different mode for the generation of angular momentum. It has been proposed that a possible reason for the occurrence

of these doublet bands is spontaneous breaking of chiral symmetry in triaxial nuclei due to the presence of three orthogonal angular momenta of the valence protons, valence neutrons and the core. However, for the two bands to be chiral partners, the near degeneracy in level energy and spin is a necessary but not a sufficient condition. In addition, these bands should exhibit nearly similar moment of inertia (MOI), quasi-particle alignment, signature staggering behavior and, more importantly, the transition probabilities. This situation is best realized only in ^{128}Cs and ^{135}Nd and not in any other case. Thus, there may be alternate reasons for the occurrence of the doublet bands.

All these different angular momentum generation mechanisms manifest themselves in the high spin level structures of the deformed nuclei and also influence the electromagnetic transition rates. The high spin levels of a nucleus can be populated through the fusion evaporation reactions using the heavy ion beam from the Indian Pellletron accelerators. The properties of these levels can be studied *via* discrete gamma ray spectroscopy by employing large gamma detection arrays like Indian National Gamma Array (INGA).

The present thesis presents the results from the data collected at the Pelletron accelerator at TIFR with the INGA array which consisted of 20 Compton suppressed Clover detectors. These data collected with the backed targets, were also utilized to measure the sub-pico second life times of the high spin levels by the use of DSAM technique. These measurements made it possible to identify different angular momentum generation modes in ^{104,105}Pd and ^{106}Ag.

The thesis is composed of seven chapters and these are as follows:

Chapter 1. Introduction :

In this chapter the general framework of the nuclear structure studies will be presented. The motivation for the thesis work will also be discussed.

Chapter 2. Mechanisms for high angular momentum generation :

This will describe the different mechanisms to generate the high angular momentum in atomic nucleus and the prerequisites for a given mechanism in order to manifest itself in a given nucleus.

Chapter 3. Experimental Techniques :

This chapter will describe the different experimental techniques which have been used during the course of this thesis. Special emphasis will be given to the technique of DSAM which has been used extensively.

Chapter 4. Anti-magnetic rotations in ^{104}Pd :

The high-spin states of ^{104}Pd were populated using a 63-MeV ^{13}C beam delivered by the 14-UD Pelletron at the Tata Institute of Fundamental Research (TIFR). A 1 mg/cm^2 enriched ^{96}Zr target with ^{206}Pb backing of 9 mg/cm^2 thickness was used as target. The de-exciting γ rays were detected by using the Indian National Gamma Array (INGA), which consisted of 20 Compton-suppressed clover detectors. The spin and the parity of the various excited states were assigned by the DCO and the PDCO measurements. In order to study the mode of excitation mechanism which generated the high spin states, the level life times were measured using the DSAM technique. The B(E2) rates which followed from these measurements showed a falling trend as a function of spin, a characteristic feature of AMR. In this way, the AMR as an excitation mechanism was for the first time established in any nucleus other than the Cd isotopes by the present work.

Chapter 5. High spin level structure in ^{105}Pd :

The high spin states of ^{105}Pd were also populated by the above mentioned

reaction. It was the second dominant evaporation channel after ^{104}Pd. Previously only the low spin levels were known. In this work the level scheme was extended upto a spin of about $55/2\hbar$. Spin and parity was determined for all the levels. The DSAM was used to determine the level life times for the three high spin bands in ^{105}Pd. The estimated B(E2) rates have a falling trend with respect to spin for the two positive parity bands, while these rates remain constant for the third negative parity band. These results conclusively establish the co-existence of collective and anti-magnetic rotation in ^{105}Pd.

Chapter 6. Angular momentum generation mechanism in ^{106}Ag :

The 68 MeV ^{14}N beam from the 14-UD Pelletron at TIFR was used to populate the excited states of ^{106}Ag through ^{96}Zr(^{14}N, 4n) reaction. A detailed level scheme of ^{106}Ag was established from the data of this experiment. The origin of the different bands have been explored by comparing with theoretical calculations based on different collective models. The unique behaviour of the doublet bands of ^{106}Ag has been published in Physical Review Letters.

Chapter 7. Summary :

The summary of the thesis is presented in this chapter along with the prospects of high spin structure studies in the A$\sim$100 region.

Chapter 1

Introduction

The constituents of a nucleus, the protons and neutrons collectively called "nucleons", interact primarily through the strong interaction (the nuclear force) which holds them together to form a stable nucleus. The relatively weak Coulomb force between the constituent protons determines the relative number of protons and neutrons inside it. The Weak force is responsible for the β-decay. By the collective contribution of these forces, a distribution of the nucleons is determined, leading to the charge distribution which defines the shape of the nucleus. Thus, apart from the intrinsic motion of the individual nucleons, there is a possibility of collective degrees of freedom for a deformed nucleus i,e the coherent motion of all the nucleons which includes the shape vibration and the collective rotation.

The nuclear structure studies aim to quantitatively relate the nuclear force to the properties of the nuclei. The microscopic *ab initio* approach aims to determine the nuclear force from the properties of the two, three and four nucleon interactions with the fundamental assumption that these interactions are the consequence of the interchange of mesons (π, ρ, ω etc) among the nucleons. This approach is

mathematically complex and numerically intensive. This approach leads to an approximate description of a real nucleus.

The other approach is derived from the discovery that the various nuclear modes of motion can be identified with the breaking of different symmetries, quantum numbers and selection rules. In the nuclear structure physics, one common example of spontaneous symmetry breaking is the existence of the rotational bands due to the loss of the spherical symmetry. These rotational bands can have different structure due to discrete symmetries like the π-rotation symmetry. Recently, two novel types of bands have been observed experimentally, they are called magnetic and chiral bands. The magnetic bands are the result of spherical symmetry breaking by a large dipole moment, which, in turn, is produced by highly asymmetric current distributions. The chiral bands, on the other hand, have been attributed to the spin chiral symmetry breaking in a triaxial odd-odd nucleus. The macroscopic models based on such symmetries lead to the exact solution of an ideal nucleus. However, these models depend on a number of free parameters whose values are determined from the comparisons with the experimental results. If these parameters vary smoothly over a sizable number of nuclei across the periodic table, then the model is considered to be good. However, such a macroscopic description of finite fermion system seems to be improbable. The success of this approach is due to two facts.

1. It is possible to construct a mean field generated by all the nucleons and the motion of nucleons in this mean field is found to reproduce the observed nuclear properties. The success of the shell model to reproduce the "magic numbers" is the best example of the correctness of such an assumption.

2. The ground state spin of all the even-even nuclei is known to be zero. This shows that the pairing interaction between protons (neutrons) is strong.

Thus, a nucleus can be simply imagined to consist of an even-even core which is responsible for the generation of the mean-field and the valence nucleons which in general dictates the properties of the nucleus. If this core is deformed, it leads to additional collective degrees of freedom for the nucleus namely, rotation and vibration.

This macroscopic description and the associated models are best tested when the nuclei are subjected to extreme conditions such as the large excitation energy, high angular momentum, large values of isospin and considerable amount of deformation. The high resolution γ-spectroscopy is one of the most powerful tools used to investigate the nuclear structure under these conditions in particular to the situation of nuclei at high angular momentum. The study of the nuclear properties like quadrupole moments, excitation energy, angular momentum and transition probabilities of the excited discrete levels help in exploring the validity of the macroscopic models.

The fusion-evaporation reactions are the best way to produce a nucleus at high angular momentum. In this technique, two stable nuclei are brought together at an energy above the Coulomb barrier. The procedure normally involves the bombardment of a heavy projectile accelerated by an accelerator on a fixed target to form a compound nucleus with high excitation energy and angular momentum. The excitation energy of the compound nucleus gets dissipated through particle evaporation and the statistical γ-ray emission thus leaving the residual nuclei at high angular momentum. In order to return to the ground state, these nuclei shed their angular momentum through the emission of a cascade of discrete γ-rays which carry the information about the structure of the nuclei at high angular momentum. This process is schematically shown in figure 1.1. The detection and the study of the properties of these gamma rays constitutes the field of high spin nuclear structure studies which is the topic of the present thesis.

The early experiments in this field have established two distinct angular

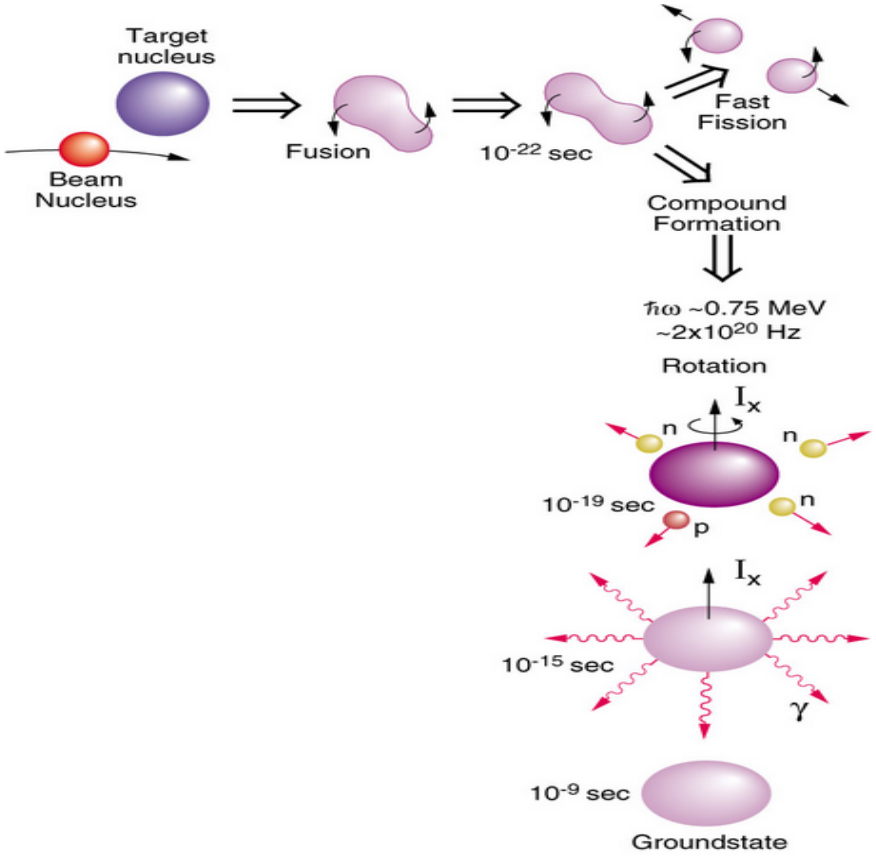

Figure 1.1: The schematic diagram of the fusion-evaporation reaction.

generation mechanisms in atomic nuclei, namely, single particle excitations in spherical nucleus and collective excitations in deformed nucleus. Subsequently the interplay between these two modes was established through the observation of *back bending* [1] which was found to happen when the Coriolis force due to the rotation becomes strong enough to break the pairing between two nucleons. This leads to the observation of sudden increase in the angular momentum as a function of excitation energy.

In last two decades, due to the sufficiently improved gamma detection techniques, a number of exotic angular momentum generation mechanisms have been established namely magnetic rotation [2], anti-magnetic rotation [3], rotation of a hexadecapole shape [4], nuclear wobbling [5], spin chirality [6] etc. Each of these

modes exhibit a characteristic variation of gamma transition rates as a function of angular momentum. Therefore, the level lifetime measurements are crucial to pin point the existence of one mechanism and not the other. These lifetimes are in the picoseconds domain and are measured by the Doppler-shift Attenuation Method (DSAM).

The present work aims to study the different conventional and exotic angular momentum generation mechanisms in the nuclei of mass-100 region and to explore the possibilities of the interplay or the co-existence of these modes.

The nuclei of mass-100 region have proton holes in $g_{9/2}$ orbital and are separated from the other single particle orbitals by the $A = 50$ shell gap. Thus, the configuration space available for the protons is small which is helpful for the different macroscopic models used during the course of this thesis. On the other hand, the neutron configuration space consists of $d_{5/2}$, $g_{7/2}$ and $h_{11/2}$ orbitals and out of these $h_{11/2}$ is the unique negative parity orbital. Thus, the observation of a negative parity state uniquely identifies the occupation of the odd number of neutrons in $h_{11/2}$ orbital and it is relatively simple to identify the different single particle configurations of a nucleus in mass-100 region.

Besides the regular rotational bands [7] found in this region, the phenomenon of shears mechanism [8] and spin chirality [9] which is a consequence of triaxiality, are also observed. An interplay between the shears mechanism and the collective rotation has also been established in this mass region. The possibility of band crossing in magnetic bands is also studied [10]. Thus, the nuclear structure studies around mass-100 offer a scope to study a rich variety of complex phenomenon at high angular momentum.

I have studied three nuclei of this mass region namely, ^{104,105}Pd and ^{106}Ag

and have identified the different angular momentum generation mechanisms through the measurement of magnetic dipole and electric quadrupole transition rates using the technique of Doppler-shift Attenuation Method. The experimental data have been compared with the numerical values from different macroscopic and geometrical models.

The high spin states of ^{104,105}Pd and ^{106}Ag were populated in two experiments. In order to populate the high-spin states of ^{104,105}Pd, the 63-MeV ^{13}C beam delivered by the 14-UD Pelletron at the Tata Institute of Fundamental Research (TIFR) was used to bombard a 1 mg/cm^2 enriched ^{96}Zr target with ^{206}Pb backing of 9 mg/cm^2 thickness. The high spin states of ^{106}Ag were populated with the same target and ^{14}N beam at 68 MeV. The de-exciting γ rays were detected by using the Indian National Gamma Array (INGA) [11], which consists of 20 Compton-suppressed clover detectors. The two-and higher fold coincidence data were recorded by a fast digital data acquisition system based on Pixie-16 modules [12]. The partial level schemes were built up to a spin of $\sim$25 $\hbar$. The detailed spectroscopic analysis were done to establish the spin and parity of each new excited state. The DSAM technique was used to estimate the level lifetimes of the high spin states in each case. The results from these measurements are discussed in subsequent chapters.

The different nuclear structure models that have been used to understand the results from the above mentioned experiments are discussed in the next chapter.

Bibliography

[1] A. Johnson, H. Reyde and J. Sztarkier, Phys. Lett. **B** 34 605 (1971).

[2] B. Fant *et al.,* J. Phys. G **17** 319 (1991).

[3] A. J. Simons *et al.,* Phys. Rev. Lett. **91** 162501 (2003).

[4] F. Flibotte *et al.,* Phys. Rev. Lett. **71** 4299-4302 (1993) .

[5] S. W. Ødegȧrd et al., Phys. Rev. Lett. **86**, 5866 (2001).

[6] E. Grodner *et al.,* Phys. Rev. Lett. **97** 172501 (2006).

[7] M. A. C. Hotchkis, *et. al.,*, Nuc. Phy. A **530** 111 (1991).

[8] P. datta, *et. al.,* Phy. Rev. C **71**, 041305(R) (2005).

[9] P. Joshi, *et. al.,* J. Phys. G: Nucl. Part. Phys. **31** S1895-S1898 (2005).

[10] Santosh Roy, *et al.,* Phys. Rev. C **81** 054311 (2010).

[11] S. Muralithar *et al.,* Nucl. Instrum. Methods A **622**, 281 (2010).

[12] R. Palit *et al.,* Nucl. Instrum. Methods A **680**, 90 (2012).

Chapter 2

Mechanisms for High Angular Momentum Generation

2.1 Introduction

The mechanisms of generating the high angular momentum in atomic nuclei has long been a topical question in nuclear-structure physics. A nucleus can generate the high angular momentum states either through single-particle excitations or as a result of collective phenomena and in most cases, due to an interplay of these two contributions. Classically, a deformed nucleus can rotate ever more faster to produce a collective spin. Microscopically, however, quantal effects of the large, yet finite, ensemble of strongly interacting fermions need to be considered. The nucleus is a unique many body quantum system in nature which can neither be treated from the first principle calculations as they become intractable [1] as the mass number, A, increases nor by the principles of statistical mechanics. The finite number of nucleons ($A \sim 200$) is small enough to make the statistical fluctuations prevail over the results

predicted by the statistical mechanics techniques. Thus, a unique approach is essential to understand the evolution of nuclear structure with angular momentum. Various assumptions have been made to make the computations tractable and this forms the basis of constructing the various phenomenological models that can reproduce not just the excited energy levels, but also their spins, multipolarities and transitions rates etc.

2.2 The Shell Model

From the microscopic perspective, the nucleons are strongly interacting and densely packed inside a nucleus, thus, it is expected that each nucleon must be suffering continuous collisions inside a nucleus. Therefore, dense-gas models of nuclei with multiple collisions between particles were built. However, these models did not fit the observed data, and remarkable patterns like the "magic numbers" in the stability of nuclei suggested the 'seemingly improbable' shell structure, similar to that of the electron shell model for atom which leads to extra stability of the noble gases. As a consequence, spherical shell model was developed [2, 3]. This model was considerably successful in accounting for various other nuclear properties. The main assumption of this model is that the nucleons are moving independently inside a nucleus under the influence of an effective potential well created by the forces of all the other nucleons. This leads to the energy quantization in a manner similar to the 'square well' and 'harmonic oscillator' potentials. Since the nature of this potential determines the single particle energies, much effort has gone into the construction of the potential wells for the modeling of the observed nuclear energy levels. A realistic shape of such

a nuclear potential is described by a Woods-Saxon function [4]

$$V_{WS}(r) = \frac{V_0}{\left(1 + e^{\left(\frac{r-r_0}{a}\right)}\right)} \tag{2.1}$$

with depth V_0 , radius r_0 and diffuseness a of the effective potential.

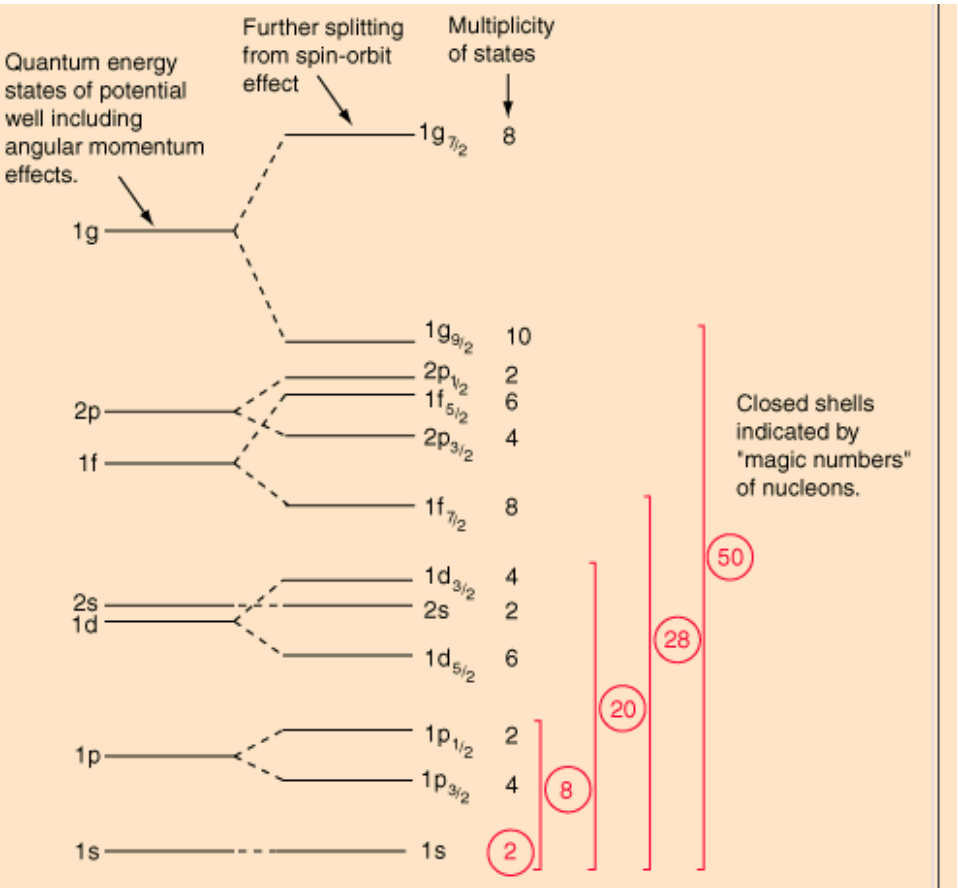

Figure 2.1: A figure highlighting the transition from the 'scattered' levels resulting from Woods-Saxon potential without spin-orbit coupling to the shell structure with both Woods-Saxon and spin-orbit coupling. The Fig. can be found in [5].

In addition to the dependence on the details of the potential well and the orbital quantum number, there is a sizable spin-orbit interaction which splits the levels by an amount which increases with orbital quantum number. This leads to the overlapping levels across the shells as shown in Fig. 2.1. The subscripts on the spectroscopic

symbols (s, p, d, ...) indicate the values of the total angular momentum j, given by $l\pm$s where l and s are the orbital and the spin angular momenta, respectively and the degeneracy of the state is (2j+1). The proton single particle energies are somewhat different from that of the neutrons because of the coulomb repulsion, but it makes little difference in the relative spacing of the energy levels. The parity of a level is given by $(-1)^l$.

With this set of identified single particle states, we can predict the net nuclear spin of a nucleus in its ground state and describe it's excited states based on the identification of the levels of the unpaired nucleons in the order of states shown above. The parity of the state can also be predicted. Thus, the single particle shell model has significant predictability in characterizing the ground and the excited levels of a nucleus.

A large number of nuclei across the periodic table have properties consistent with the predictions of the shell model which assumes a spherical shape of the charge distribution. However, it has been found that nuclei with proton and neutron numbers very different from those corresponding to the closed shells, exhibit nuclear deformation which is evident from the observation of large quadrupole moments. In addition, the rotational band structures were discovered in 1951 [6] which was another indicator of the nuclear deformation. This deformation of the nuclear field have a great influence on the properties of a nucleus.

It is generally believed that in the presence of many valence nucleons outside the closed shells, the residual proton-neutron interaction can drive the nucleus to an energetically favorable deformed state. In the alternative description of the Nilsson model [7] the nucleons move independently in a non-spherical potential, generating a deformed macroscopic shape. This model describes the single-particle states of deformed nuclei. It generalizes the shell model, which describes the spherical nuclei.

An important foundation for the theoretical framework of the Nilsson model is the definition and classification of nuclear deformation. Nilsson's original model dealt with only quadrupole deformations (prolate or oblate). It was cast in the form of a modified harmonic oscillator potential with a spin orbit coupling term. Later developments of the Nilsson model also allowed for generalization to higher-order nuclear deformations, which in turn depends on the single particle configuration.

The introduction of a non-spherical binding field by Nilsson implies that the nuclear shape and orientation must be considered as the dynamical variables. These variables are associated with the various types of nuclear motion which accompany variations in the binding field. The interplay between these collective modes of motion and the individual-particle motion forms the basis of many nuclear models. The nuclear properties that result from this interplay are found to depend essentially on the magnitude of deformation. Fig. 2.2 shows a symmetrically deformed nucleus as proposed by Nilsson, where z axis is the symmetry axis. The various quantum numbers are also shown. For a spherical nucleus, no preferential direction exists and all (2j+1) sub-states for a given j are degenerate in energy. In an axially deformed nucleus, one can define the symmetry axis and the m-components will be split according to the projection on the symmetry axis, Ω. Hence the degeneracy of the 2j+1 sub-levels is lifted. Only the time-reversed orbits $+\Omega$ and $-\Omega$ are degenerate. Intuitively this can be understood as follows: if the core's matter distribution is not uniform, the energy of a nucleon orbiting the deformed core will depend on the overlap or on the orientation of the single-particle orbit with respect to the core. The states with different Ω will thus have a different energy.

The Nilsson diagram describes the evolution of the single-particle energies as a function of the deformation parameter. They are calculated using a deformation

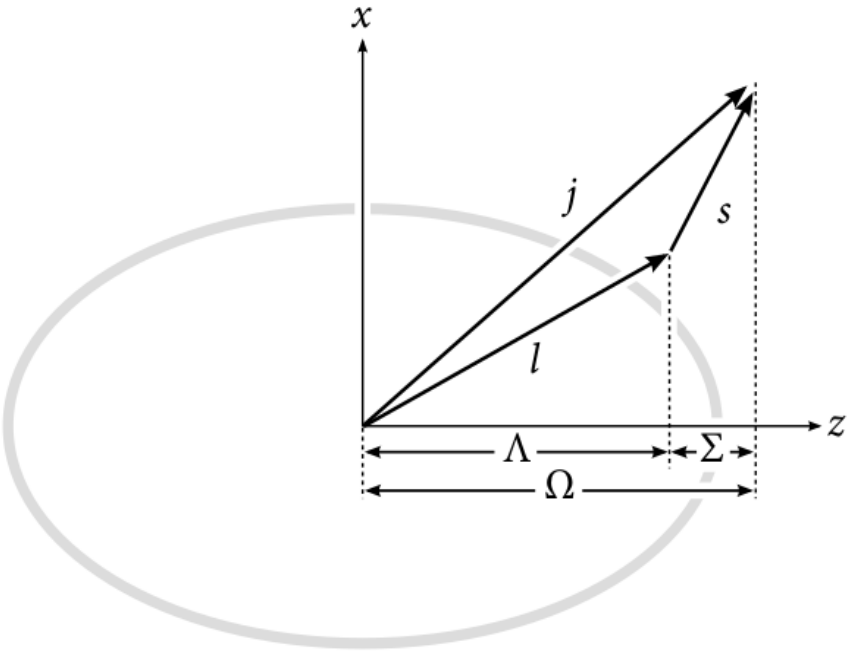

Figure 2.2: Pictorial representation of a symmetrically deformed nucleus proposed by Nilsson and the relevant quantum numbers.

dependent Hamiltonian of the form

$$V_{WS}(r,\theta,\phi) = \frac{-V_0}{\left[1+e^{\left(\frac{r-R(\theta,\phi)}{a(\theta,\phi)}\right)}\right]} \tag{2.2}$$

where $\mathrm{R}(\theta,\phi)$ represents a radius vector from the origin to the surface of a deformed nucleus and $a(\theta,\phi)$ is the diffuseness of nuclear surface corresponding to the co-ordinates (θ,ϕ). Fig. 2.3 show the example of energy diagram obtained for the Nilsson model.

The asymptotic quantum numbers are often used to describe the Nilsson orbitals with the following form:

$$\Omega^{\pi}[Nn_z\Lambda] \tag{2.3}$$

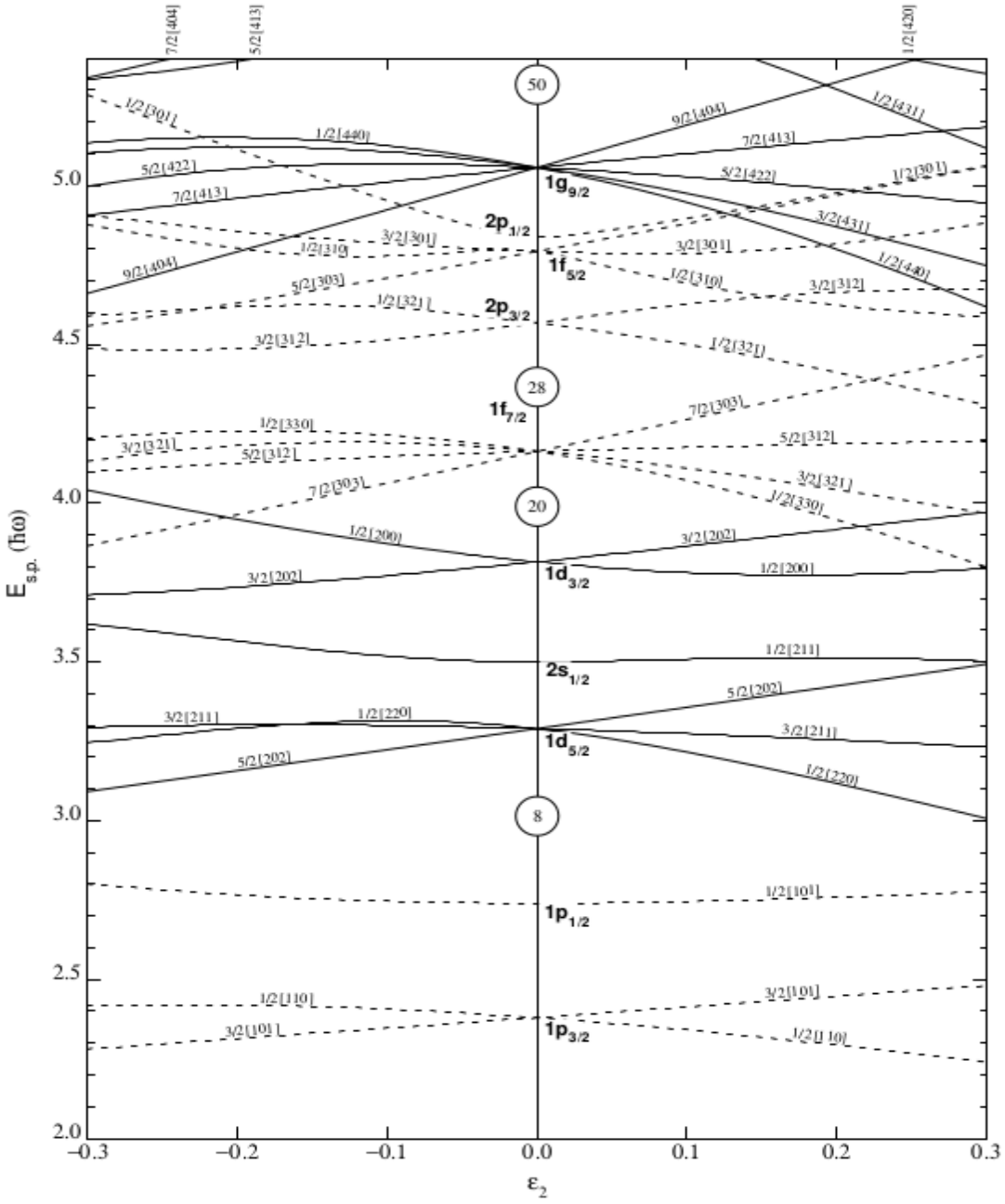

Figure 2.3: The example of a Nilsson diagram for N or Z $\leq$ 50. The parameter ϵ_2 is related to the deformation parameter β_2.

where Ω is the projection of the single particle total angular momentum along the axis of symmetry, N the principle quantum number, n_z the oscillator quanta projected along the z-axis, π the parity of the state and Λ the projection of the orbital angular

momentum along the z-axis. With Ω being the sum of Λ and Σ, where Σ is the intrinsic single particle spin along the z-axis, we can define Ω as

$$\Omega = \Lambda \pm \frac{1}{2} \tag{2.4}$$

as Σ can take values $\pm\frac{1}{2}$. We can determine the parity of a state, π, from the principle quantum number N using the relation

$$\pi = (-1)^N \tag{2.5}$$

The principal quantum number N also allows the constraint of Λ to discrete values. If N is odd (even) then $n_z + \Lambda$ must also be odd (even). From the plots for Nilsson orbitals shown in Fig. 2.3, it can be seen at $\epsilon = 0$ the orbitals are 2j+1 degenerate and the shell model states are recovered. This degeneracy is lifted with the onset of deformation. It is observed from this plot that for a nucleus with prolate deformation, the low Ω orbits will have lower energies and the high Ω orbits will have higher energies. The converse being true for oblate nuclei. With the projection of the total nuclear angular momentum along the axis of symmetry being K, which is equal to Ω for a nucleus with a single valence nucleon, we can denote the angle between the orbital plane and the axis of symmetry to be

$$\theta = sin^{-1}\left(\frac{K}{j}\right) \tag{2.6}$$

For high K values, θ changes greatly leading to rapid changes in energy as deformation increases. This can lead to two orbits with the same quantum numbers approaching each other. The Pauli exclusion principle ensures that no two Nilsson levels with the same value of Ω and π can cross. As orbits with the same values of Ω and π are driven closer together, due to the onset of deformation, the Pauli exclusion principle

cause the orbits to repel. At the inflection point wave functions interact and leads to a mixing of the Nilsson levels.

Based on the spherical shell model, a nucleus can generate the high angular momentum through single particle excitations only. The transition rates of such excitatons depend entirely on the single particle configuration of each level and don't generally follow any pattern. The deformed Nilsson model on the other hand has spherical symmetry broken and will generate a band with a regular level spacing characteristic of a quantum rotor which depends on the angular momentum (I) as: $E \sim I(I+1)$. Thus, a band is generated due to the rotation of a deformed nucleus with a specific single particle configuration. The corresponding de-exciting gammas are predominantly $E2$ in nature signifying a large quadrupole deformation. These two contrasting mechanisms of generating the high angular momentum in a nucleus are schematically shown in Fig. 2.4.

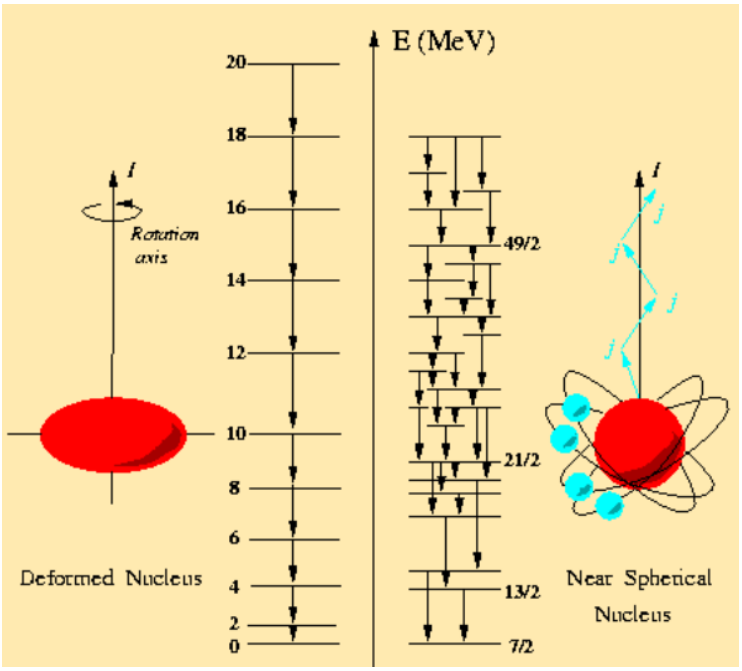

Figure 2.4: A schematic representation of high angular momentum generation from collective rotation (left) and single particle excitations (right).

In order to describe the rotation and vibration of a nucleus, the nuclear deformation is discussed in the next section where the Lund convention has been used.

2.3 Deformation

The general shape of a nucleus can be expressed in terms of spherical harmonics according to the equation

$$R(\theta,\phi) = c(\beta_\lambda)R_0\left[1+\sum_{\lambda=1}^{\lambda=\infty}\sum_{\mu=-\lambda}^{\mu=\lambda}\alpha_{\lambda\mu}Y_{\lambda\mu(\theta,\phi)}\right] \tag{2.7}$$

where $R(\theta,\phi)$ represents a radius vector from the origin to the surface, R_0 is the radius of a sphere which has equal volume of the deformed nucleus. The factor $c(\beta_\lambda)$ ensures the volume conservation, $\alpha_{\lambda\mu}$ is the deformation parameter and $Y_{\lambda\mu}(\theta,\phi)$ a spherical harmonic of order λ, with λ classifying the multipole order. λ= 1 corresponds to a dipole which represents the motion of the centre of mass of the nucleus. But as we are considering the motion in the centre of mass frame, therefore, this term vanishes. λ= 2 corresponds to a quadrupole and λ= 3 corresponds to an octupole. For quadrupole deformation Eqn. 2.7 becomes

$$R(\theta,\phi) = c(\beta_\lambda)R_0\left[1+\sum_{\mu=-2}^{\mu=2}\alpha_{2\mu}Y_{2\mu(\theta,\phi)}\right] \tag{2.8}$$

When the principle axes are made to coincide with the nuclear axes the five coefficients reduce to two as $a_{22} = a_{2-2}$ and $a_{21} = a_{2-1} = 0$. The standard parameters to describe quadrupole deformation are thus

$$a_{20} = \beta\ \cos\gamma \qquad \text{and} \qquad a_{22} = \tfrac{1}{\sqrt{2}}\beta\ \sin\gamma$$

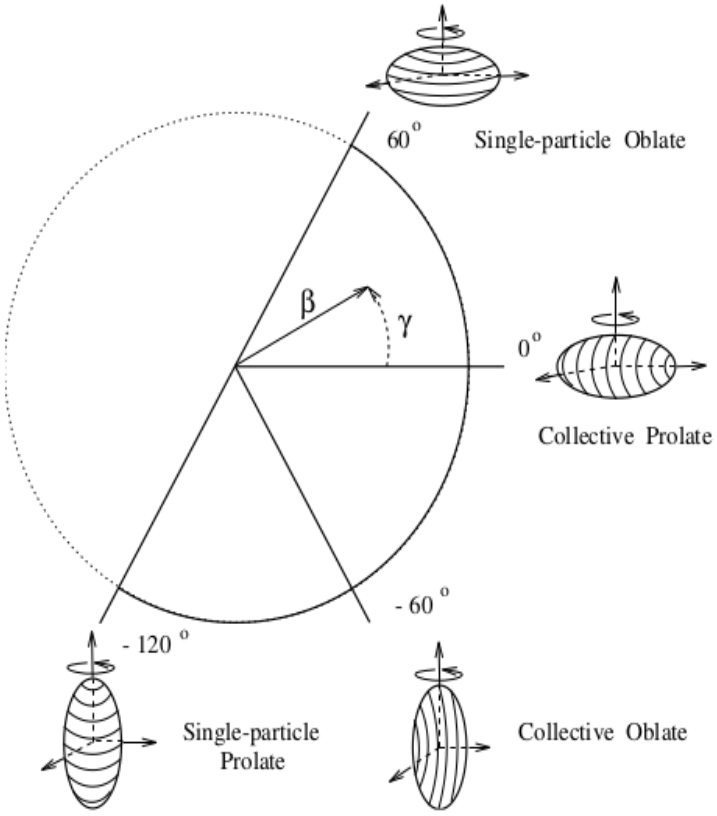

Figure 2.5: The Lund convention showing the deformation parameters β and γ for oblate and prolate deformations.

where β is a measure of the deviation from the surface of a sphere and γ is a measure of the deviation from axial symmetry. A common convention to describe the range of shapes for $\lambda = 2$ in terms of the β and γ variables is the Lund convention [8]. Fig.2.5 shows the various shapes that result from quadrupole deformation and places them in the $(\beta - \gamma)$ plane. From this convention it can be stated that if $\gamma = 0$, then $R_1 = R_2$. If R_3 is then less than R_0 the nucleus will be *oblate*. If R_3 is greater than R_0 the nucleus will be *prolate*. For $\gamma = 30°$, the nucleus has a triaxial shape i.e there is no preferred axis of symmetry and the rotation is allowed around any of the three axis.

2.3.1 Rotation

For a deformed nucleus, collective rotation is a possible degree of freedom. From quantum mechanical perspective, this is not possible with a spherical nucleus since it is not possible to observe the change in orientation of a spherical system. To a first approximation the energy associated with rotational excitation of a nucleus can be calculated classically. The classical formula for the energy of a rotating rigid body is

$$E = \frac{1}{2}\mathcal{J}\omega^2 \tag{2.9}$$

where $\mathcal{J}$ is the moment of inertia and ω the rotational frequency. With the rotational frequency being related to the moment of inertia by the formula

$$\omega = \frac{I}{\mathcal{J}} \tag{2.10}$$

where I is the total angular momentum, consisting of the rotational angular momentum, I_R of the nucleons about the axis of symmetry and the individual intrinsic angular momentum of valance nucleons, J such that

$$I = \vec{I_R} + \vec{J} \tag{2.11}$$

Then, Eqn. 2.9 becomes

$$E = \frac{I^2}{2\mathcal{J}} \tag{2.12}$$

Now, for a quantum mechanical rotor the moment of inertia is given by $I^2 = \hbar^2 I(I+1)$, where I= 1,2,3, etc. such that the Eqn. 2.12 becomes

$$E = \frac{\hbar^2}{2\mathcal{J}} I(I+1) \tag{2.13}$$

Due to the reflection symmetry of the prolate or oblate shape, the odd-I values are not allowed. This gives the characteristic pattern to the energy levels and a useful experimental signature for rotational bands being that the ratio of the $E_4/E_2 \approx 3.33$.

For a spherical rigid body the classical moment of inertia is defined as

$$\mathcal{J}_{rig} = \frac{2}{5} M R^2 \tag{2.14}$$

where R is the radius and M is the mass of the rigid sphere. For a nucleus, the radius is related to the atomic mass through $R = R_0 A^{\frac{1}{3}}$. The rigid moment of inertia for a spherical nucleus is therefore

$$\mathcal{J}_{rig} = \frac{2}{5} A^{\frac{5}{3}} m_n R_0^2 \tag{2.15}$$

where $R_0 \approx 1.2$ fm, A is the atomic number and m_n is the mass of the nucleon. For an ellipsoidal shape the moment of inertia can be expressed as

$$\mathcal{J}_{rig}(\epsilon) \approx \left(1 + \frac{3\epsilon}{4}\right) \mathcal{J}(sphere) \tag{2.16}$$

where ϵ is the eccentricity of the ellipsoid. The moment of inertia defined in the above equations is a static moment of inertia where the nucleus is assumed to be a rigid body. However, the true values for the moment of inertia are often considerably less than the rigid body value [9]. This is due to the pairing correlation between the multiple configurations arising due to the scattering of a pair of protons (neutrons) to different single particle levels near the Fermi level.

The nucleus is usually imagined as a rigid core surrounded by valence nucleons. In this description, two moments of inertia must be defined to fully describe the rotation of the nucleus. When one assumes maximum alignment on the x-axis so that

$I_x \approx I$, the *kinematic* moment of inertia can be defined as

$$\mathcal{J}^{(1)} = \left(\frac{dE}{dI_x}\right)^{-1} \hbar^2 = \hbar \frac{I_x}{\omega} \tag{2.17}$$

and the *dynamic* moment of inertia as

$$\mathcal{J}^{(2)} = \left(\frac{d^2E}{dI_x^2}\right)^{-1} \hbar^2 = \hbar \frac{dI_x}{d\omega} \tag{2.18}$$

with the kinematic moment of inertia being due to the motion of the system and the dynamic moment of inertia a response of the system to an external force. The transition energy in a rotational band can be related to the kinematic moment of inertia through Eqn. 2.13,

$$E_\gamma = \frac{\hbar^2}{2\mathcal{J}^{(2)}}(4I - 2) \tag{2.19}$$

and the dynamic moment of inertia related to the difference in consecutive γ rays through the equation

$$\Delta E_\gamma = \frac{4\hbar^2}{\mathcal{J}^{(2)}} \tag{2.20}$$

2.3.2 Vibration

A nucleus can oscillate in numerous modes, the basis of which are described by the deformation in Eqn. 2.7. The dipole vibrations (λ=1) are the displacement of the center of mass of the nucleus and cannot generate angular momentum. The quadrupole vibrations (λ=2) add two units of angular momentum and even parity. There are two possible modes of quadrupole vibration defined by the direction in which they are aligned. β vibrations are aligned along the symmetry axis and cause

fluctuations on the β deformation parameter, as described by the Lund convention. γ vibrations correspond to oscillations of the γ deformation parameter and cause the axial symmetry to be instantaneously broken. The octupole vibrations (λ=3) carry three units of angular momentum and negative parity.

These vibrations are quantized in units of phonons with the excitation energy for the n^{th} phonon of a vibration with frequency ω given by

$$E_n = \hbar\omega\left(n + \frac{N}{2}\right) \tag{2.21}$$

where N is the number of dimensions in the harmonic oscillator for the vibrational mode. For a quadrupole vibration there are three spatial dimensions and two possible vibrational modes (β and γ) thereby giving $N = 5$.

2.4 Principal Axis Cranking

An atomic nucleus is not an ideal quantum rotor as the valence nucleons have a significant role in generating the the high angular momentum states. The model which describes the effect of rotation of the deformed nucleus on the motion on these valence nucleons to generate the angular momentum is the principal axis cranking (PAC). This model assumes the motion of the symmetrically deformed nucleus about an axis perpendicular to the symmetry axis. The main aspects of this model are described below.

The cranking Hamiltonian in the intrinsic frame of reference [10], given by

$$h_{PAC} = h_0 - \omega I_x = \sum h_\omega + \Delta(P^+ + P) - \lambda N \tag{2.22}$$

where h_0 is the sum of all the single-particle static Hamiltonians, ω is the rotational frequency, I_x is the projection of the total angular momentum onto the rotation axis. $H_{pair} = \Delta(P^+ + P) - \lambda N$ in the Hamiltonian is the two body monopole pairing interaction. The single-particle Hamiltonians are given by

$$h_\omega = h_0 - \omega i_x \tag{2.23}$$

The -ωi_x term is analogous to the classical Coriolis and centrifugal forces.

The term H_{pair} corresponds to the pairing interactions can be broadly classified into two categories. One is the short range correlation among the identical nucleons the other component is long range in nature and generally known as pairing correlation. The short range pairing interaction operates on the nucleons that are in time reversed states. Due to this interaction, the zero angular momentum state for a pair of such nucleons are lower in energy than other angular momentum states. This effect is experimentally observed in the even-even nuclei where the lowest observed state is always coupled to zero angular momentum. The energy required to separate this pair is higher than nearest odd-mass nuclei. As a consequence the first excited state of a even-even nuclei is always higher than the nearest odd-mass nuclei.

In rapidly rotating nuclei, the Coriolis force (proportional to ω) may become stronger than the pairing energy of the two nucleons in time reversed orbits. As a result, the pair breaks and one of the constituent nucleon of that pair is lifted to next higher unoccupied orbital. This phenomenon results in the sudden gain in the angular momentum and is observed in the $i_x(\omega)$ plot and is known as back-bending, due to large gain in the angular momentum of the nuclei, with decreasing frequency. An example of this phenomena is demonstrated in Fig. 2.6.

The long range pairing interaction (Pairing correlation) is important for the

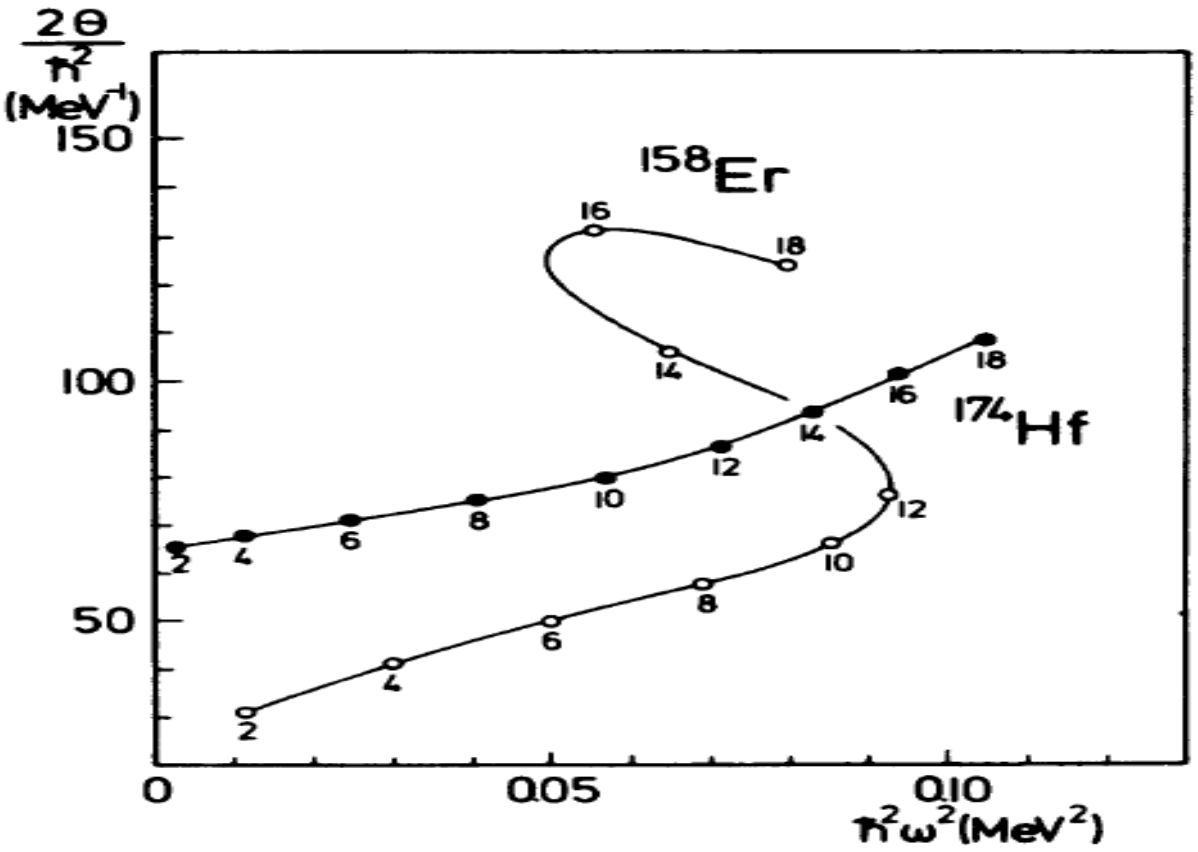

Figure 2.6: The standard backbending plot for ^{158}Er while it is blocked in odd-odd ^{174}Hf

nucleons near the Fermi surface. This correlation couples the pair of nucleons in a state i with the another state j.

At $I = 0$, each Nilsson orbital is doubly degenerate, with pairs of nucleons occupying symmetrical time-reversed orbits. Under rotation, time-reversal symmetry is broken and orbitals are split into partners with opposite values of the signature exponent quantum number α. This quantum number originates from the eigenvalue of the rotation operator $R_x(\pi)$, which represents a rotation of the particle wave function by 180° around the rotation axis, or

$$R_x(\pi)\psi = e^{-i\pi I_x}\psi = r\psi \tag{2.24}$$

where r is the signature quantum number and is related to α by

$$r = e^{-i\pi\alpha} \tag{2.25}$$

For single-particle orbitals, r has a phase factor of $\pm i$, and so $\alpha = \pm\frac{1}{2}$.

As the nucleus is rotated, the energies of opposite-signature orbitals are affected differently and a further rearranging of orbitals together with the appearance of new shell gaps may be observed. This indicates that the nuclear shape can evolve with the angular momentum and that the deformed shapes that are not stable at low spins can become more stable as the spin is increased.

It is evident that the signature of a single-particle state can have values $\pm 1/2$. For odd mass systems, α can be $+1/2$ or -1/2 and for even-even or odd-odd system α can have values 0 or 1. The value of α is related to I through the relation $I = 2|\alpha|$. The energy difference between these two signature bands is known as the signature splitting. The definition of the favored signature (α_f) is given as [11].

$$\alpha_f = \frac{1}{2}\left[(-1)^{j_p-\frac{1}{2}} + (-1)^{j_n-\frac{1}{2}}\right] \tag{2.26}$$

Thus, from a single Nilsson configuration two rotational bands having different signatures can be obtained. The Fig. 2.7, shows such an example where two signature partners in ^{163}Dy, are built on the $5/2^+[642]i_{13/2}$ neutron configuration.

Since the only good quantum numbers remaining are the parity and signature (π, α), the basis state for a deformed rotating nucleus can be completely described in terms of $|\pi, \alpha\rangle$. The energy eigen-value (e^{ω}_{μ}) is given as,

$$e^{\omega}_{\mu} = \langle\mu|h_{\omega}|\mu\rangle$$

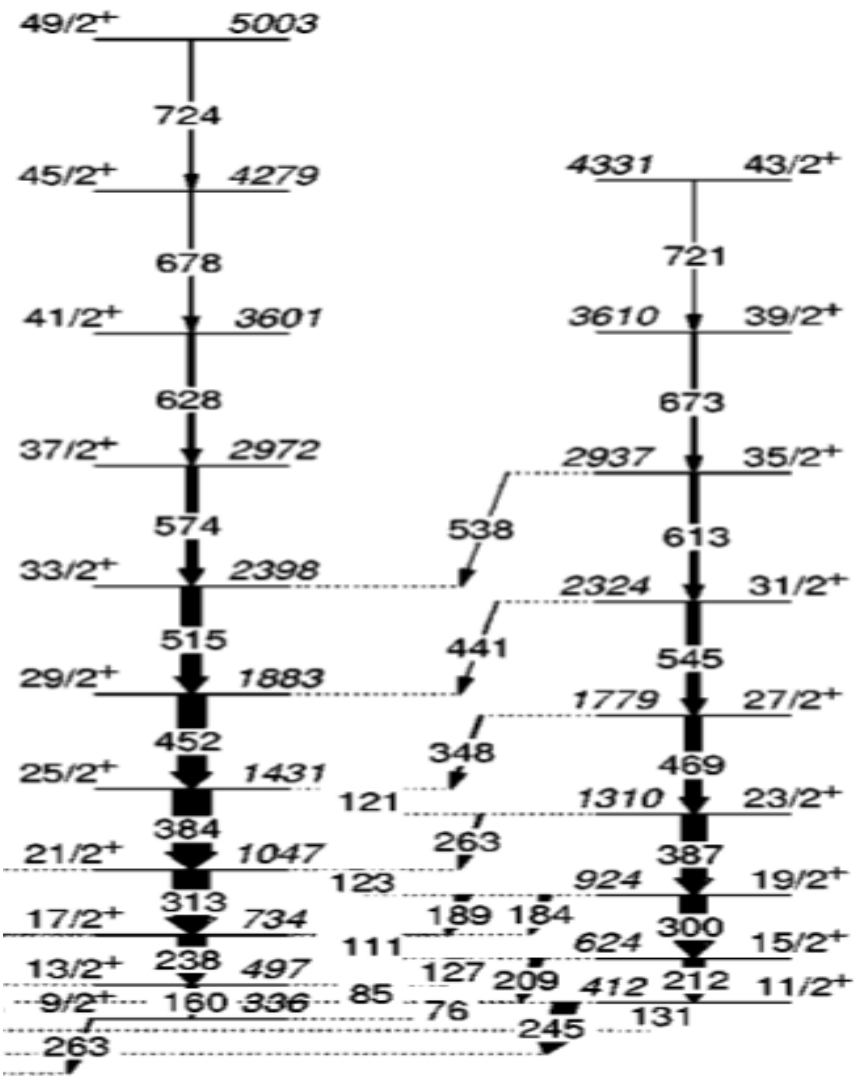

Figure 2.7: Two signature partner band in ^{163}Dy [12]. According to the definition of favored signature, ($\alpha_f = \frac{1}{2}\left[(-1)^{13/2-1/2}\right] = \frac{1}{2}$), the favored sequence of angular momentum are 1/2, 5/2, 9/2, 13/2, ... which is in accordance with the observed level scheme.

$$= \langle\mu|h_0|\mu\rangle - \omega\langle\mu|i_x|\mu\rangle \tag{2.27}$$

The above equation implies that the expectation value of the angular momentum operator i_x , is equal to the negative gradient of the single particle routhian,

$$\frac{de^{\omega}_{\mu}}{d\omega} = -\langle\mu|i_x|\mu\rangle \tag{2.28}$$

Thus, in the cranking model, the four possible configurations are, $\pi = (+,-) \otimes \alpha = (1/2,-1/2)$. The Fig. 2.8 shows the routhian plot for N=60. The spins and signatures in this figure are represented in the following way: (+,+1/2) by solid lines; (+,-1/2) by dotted line; (-,+1/2) by dot-dashed line and (-,-1/2) by dashed line. The nomenclature of the levels is given in the following table. In case of a nucleus

Table 2.1: Notation for routhian identification.

π, α	label	π, α	label
-,-1/2	E,G,...	+,-1/2	B,D,...
-,+1/2	F,H,...	+,+1/2	A,C,...

containing N number of nucleons, the total routhian (E^{ω}) and the total angular momentum projection along the rotational axis (I_x) can be calculated using eqn. 2.27 and 2.28. Thus, the total routhian for the yrast configuration is

$$E^{\omega} = \sum_{\mu=1}^{N} \langle \mu | H_{\omega} | \mu \rangle = \sum_{\mu=1}^{N} e_{\mu}^{\omega} \tag{2.29}$$

where μ runs over all the occupied states and for yrast configurations, the lowest N routhians are considered. The total energy E in the laboratory coordinate system can be calculated as

$$E = \sum_{\mu=1}^{N} \langle \mu | H_0 | \mu \rangle = E^{\omega} + \omega I_x \tag{2.30}$$

and the total angular momentum projection along the rotational axis is

$$I_x = \sum_{\mu=1}^{N} \langle \mu | i_x | \mu \rangle \tag{2.31}$$

It is to be remembered that I_x is a measure of the aligned quasi-particle angular momentum in the body fixed frame.

In the Fig. 2.8, the Fermi surface for N=60, is shown by the solid horizontal

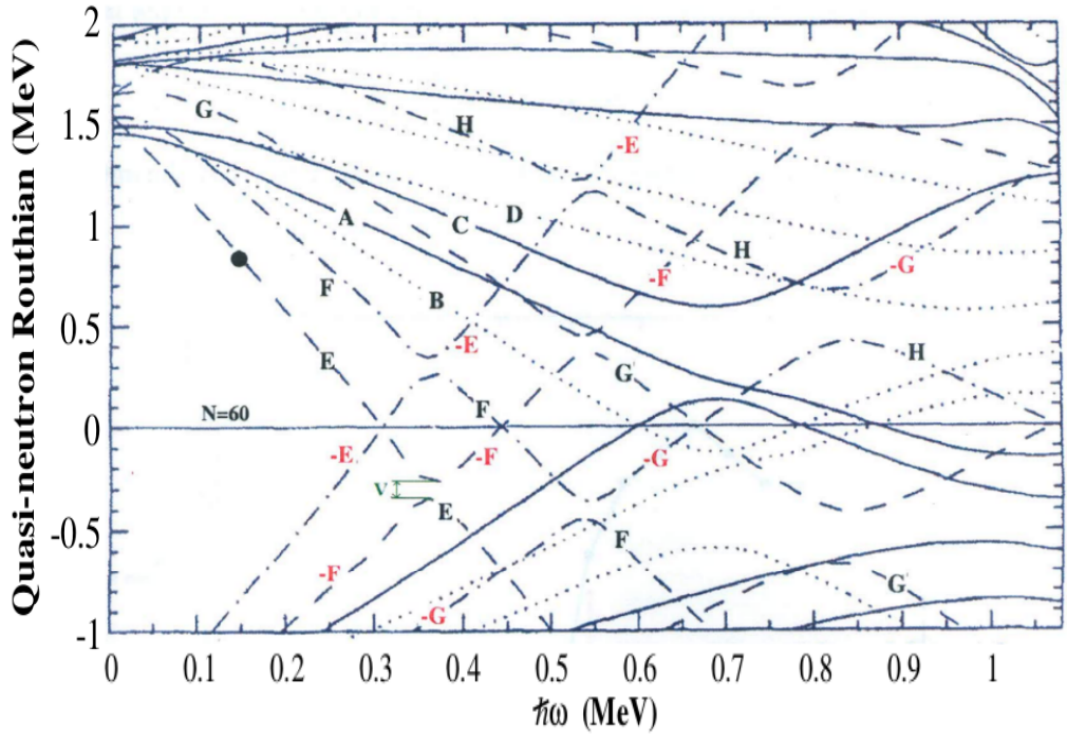

Figure 2.8: Quasi-particle routhian for 60 neutrons. The parameters for the calculation are β_2=0.15, β_4=0.0 and $\gamma = 0°$. The pairing strength $\Delta_\nu = 1.08$ MeV. In case of 61 neutrons, one neutron is placed at E (shown by dot)

line. For the reference configuration all the levels below this line are filled and it corresponds to the ground stand band. In the Fig. 2.8 the highest filled levels are -E and -F. According to this quasi-particle routhian, the first crossing is predicted $\hbar\omega \sim 0.37$ MeV where the quasi-particle move from the hole levels (-E and -F) to particle levels (E and F). This is illustrated in the fig. 2.8 by tracing their course and marking the hole states by red color. Their crossing is known as EF crossing. The effect of such crossing on the aligned angular momentum i_x also calculated from change in the slopes of the filled routhians and the i_x versus $\hbar\omega$ plot in Fig. 2.9 shows the characteristic increases in i_x ($\sim 10\hbar$) at ω=0.37 MeV/$\hbar$. It should be noted that the observed gain in the aligned angular momentum, is a measure of the interaction strength between the interacting routhians. This interaction strength, V, depends on the gap between the two routhians at crossing frequency. If the interaction strength,

V, is weak, then the gap between the two routhians, $2V$, is small. This leads to large alignment gain i_x whereas the strong interaction results in relatively lower gain in i_x. However, such a crossing of routhians is allowed only when one of the interacting levels is occupied and the other one is empty.

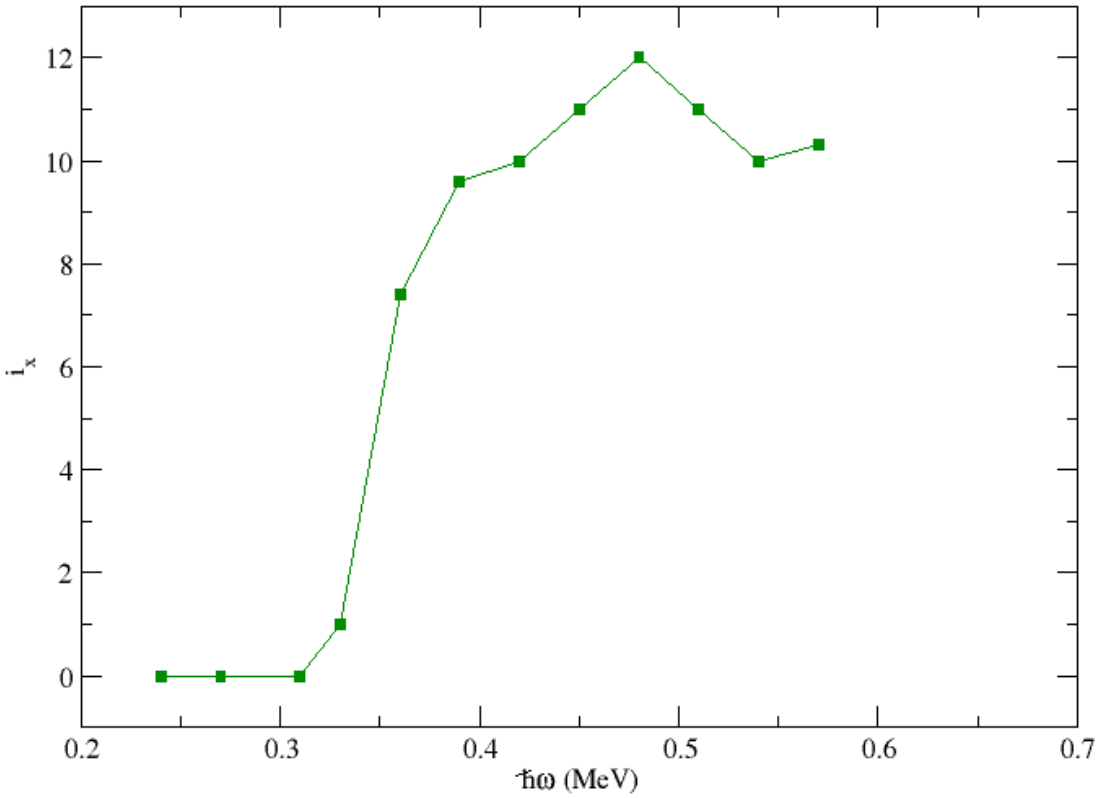

Figure 2.9: The alignment angular momentum plot extracted from the Fig. 2.8. The figure shows that the approximate gain in $i_x \sim 10\hbar$.

For two decades, it was believed that these are the only two ways (single particle excitation and collective rotation) to generate the high angular momentum states in atomic nuclei. However, in early 1990's regular band structures were observed in near spherical Pb nuclei [13, 14, 15, 16] where the intra band transitions are predominantly

$M1$ in nature as shown in Fig. 2.17. Later this type of structures were found in other mass regions [17, 18, 19, 20]. The other features associated with these bands are:

1. Large $B(M1)/B(E2)$ ratios with values ∼10-100 $(\mu_N/eb)^2$. For a normal deformed band these values are about 1 $(\mu_N/eb)^2$.

2. These bands show a falling trend in $B(M1)$ rates with increasing rotational frequency.

3. The $\mathcal{J}^2$ values for these bands ∼10-25 $\hbar^2 MeV^{-1}$ which is smaller than the normal deformed bands. Since the crossover $E2$ transitions are either weak or absent, the ratio of $\mathcal{J}/B(E2)$ become larger than 100 $\hbar^2 MeV^{-1}(eb)^{-2}$.

These properties establish the fact that the bands don't arise from the collective rotation. On the other hand, the presence of regular band structure rules out the single particle excitations. A satisfactory explanation to these bands was given by Frauendrof [21, 22] by introducing the concept of tilted axis cranking (TAC). It was pointed out that in these nuclei, some of the valence nucleons are aligned along the symmetry axis while the others are aligned perpendicular to the symmetry axis. A geometrical picture of this configuration is shown in Fig. 2.11 where a shears-like system is formed by the valence nucleons and the high angular momentum states are generated by the simultaneous closing of the two blades of the shear. In this situation, the total angular momentum becomes tilted with respect to the rotational axis. Thus, the π -rotational symmetry is broken and the signature is no longer a good quantum number. So, the staggering in the magnetic transition rates $(B(M1))$, observed in cases of Principal Axis Rotation (PAR), are absent in Tilted Axis Rotation (TAR). In this case instead, the $B(M1)$ transition rates show a steady decrease with increasing angular momentum. This happens because the $B(M1)$ rates are proportional to the perpendicular component of the magnetic moment vector $(\mu_\perp)$ which decreases as the

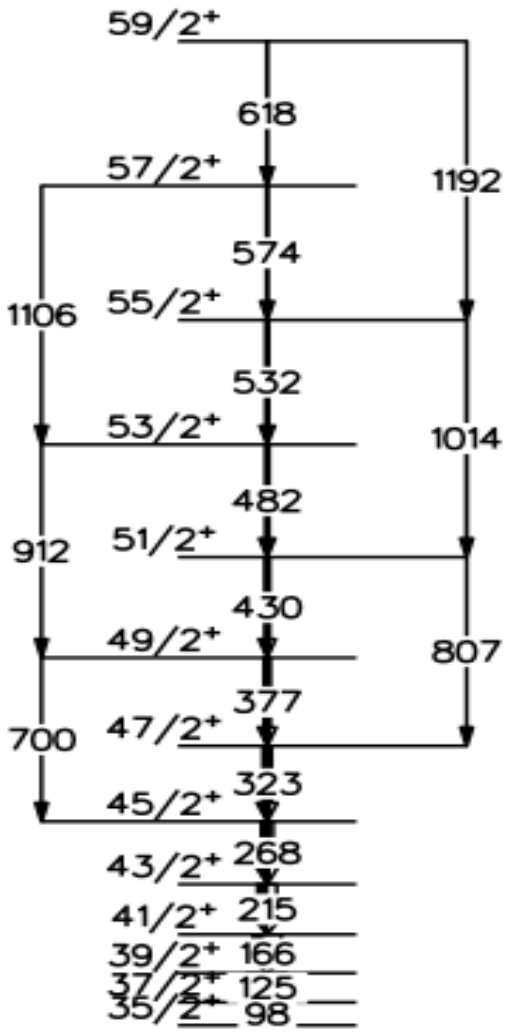

Figure 2.10: Typical example of a shears band observed in ^{199}Pb.

two blades of the shear close. The Tilted Axis Cranking (TAC) used to model this angular momentum generation mode is discussed below.

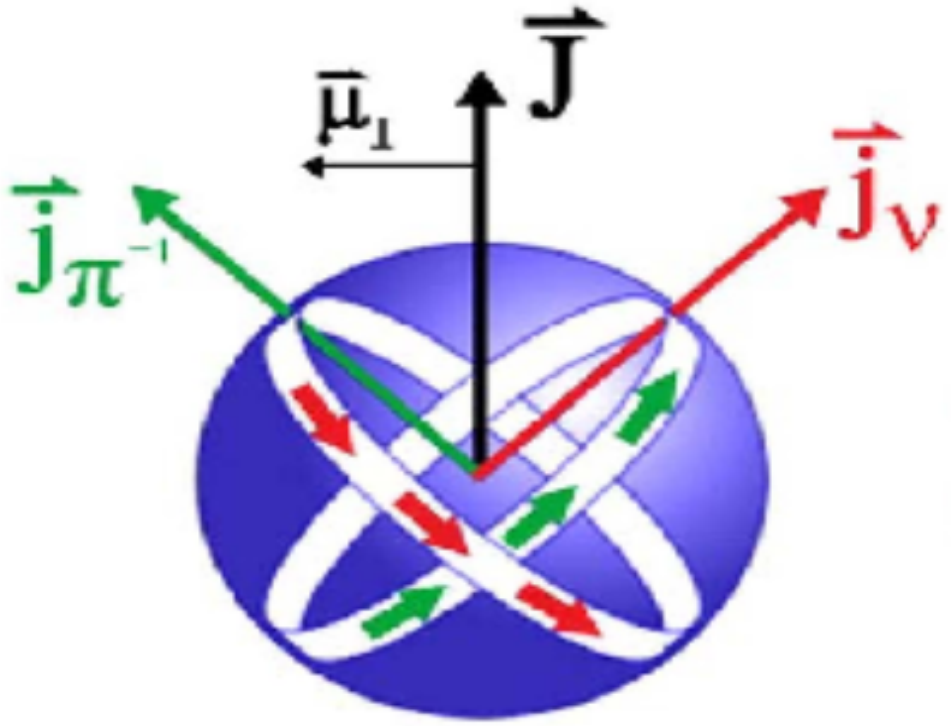

Figure 2.11: Depiction of the coupling of angular momentum vectors due to the rotation of current loops of proton particles and neutron holes in Magnetic Rotation.

2.5 Tilted Axis Cranking (TAC)

In this mode the axis of rotation of the nucleus does not coincide with any of the Principal axis of the nucleus. However, the $E(I)$ can be expressed as a function of I and exhibits $I(I+1)$ dependency. The presence of small deformation implies that the E vs. I behavior has a origin different from regular rotation. It was later demonstrated that this phenomenon is a manifestation of the an-isotropic current distribution of a few nucleon near the Fermi surface [11-13]. New symmetries results from the combination of spatial symmetries of the density distribution with the vector of the angular momentum. Due to the participation of limited number of particles contributing to the angular momentum, the band terminates early unlike in the case

of regular rotation. The general TAC routhian can be written as,

$$h'_{TAC} = h_0 - \Delta(P^+ + P) - \lambda N - \omega(j_1 \sin\theta\cos\phi + j_2 \sin\theta\sin\phi + j_3\cos\theta) \quad (2.32)$$

where h_0 is the single particle Hamiltonian of a deformed potential. We denote the intrinsic frame (body fixed axes) by 1, 2, 3 and the laboratory frame by *x, y, z*. The angles θ and ϕ denote the orientation angles of the total angular momentum J (*z-axis*) with respect to the intrinsic frame of reference and so there are the Euler's angles (Fig. 2.12). The choice of $\phi = 0$ corresponds to the planer tilt where J lies in one of the principal planes (1-3 plane). When, both ϕ= 0 and $\theta = 0$, the TAC routhian reduces to the PAC. In this section we shall restrict our discussion to $\phi = 0$ case *i.e* planer TAC solution.

In TAC, the spherical part of the single particle energies can be calculated from the spherical Woods-Saxon potential and combined with the deformed part of the an-isotropic harmonic oscillator potential. In this modified version the TAC solution can be rewritten as,

$$h'_{TAC} = h_{sph} + V_{def}(\epsilon_2, \gamma, \epsilon_4) - \Delta(P^+ + P) - \lambda N - \omega(j_1 \sin\theta + j_3\cos\theta) \quad (2.33)$$

where the h_{sph} represents the spherical part which also includes the $l.s$ interaction and V_{def} which is the deformed part of the Nilsson single particle Hamiltonian [14]. This routhian provides quasi-particle energies and quasi-particle states which is, in turn, used to construct the many-body configuration $|\omega, \epsilon_2, \gamma, \epsilon_4, \theta\rangle$ representing the band of interest. For a given configuration and frequency ω, the routhian is minimized with respect to the deformation parameters $\epsilon_2, \gamma, \epsilon_4, \theta$.

$$e'(\omega, \epsilon_2, \gamma, \epsilon_4, \theta) = \langle\omega, \epsilon_2, \gamma, \epsilon_4, \theta|h'|\omega, \epsilon_2, \gamma, \epsilon_4, \theta\rangle \quad (2.34)$$

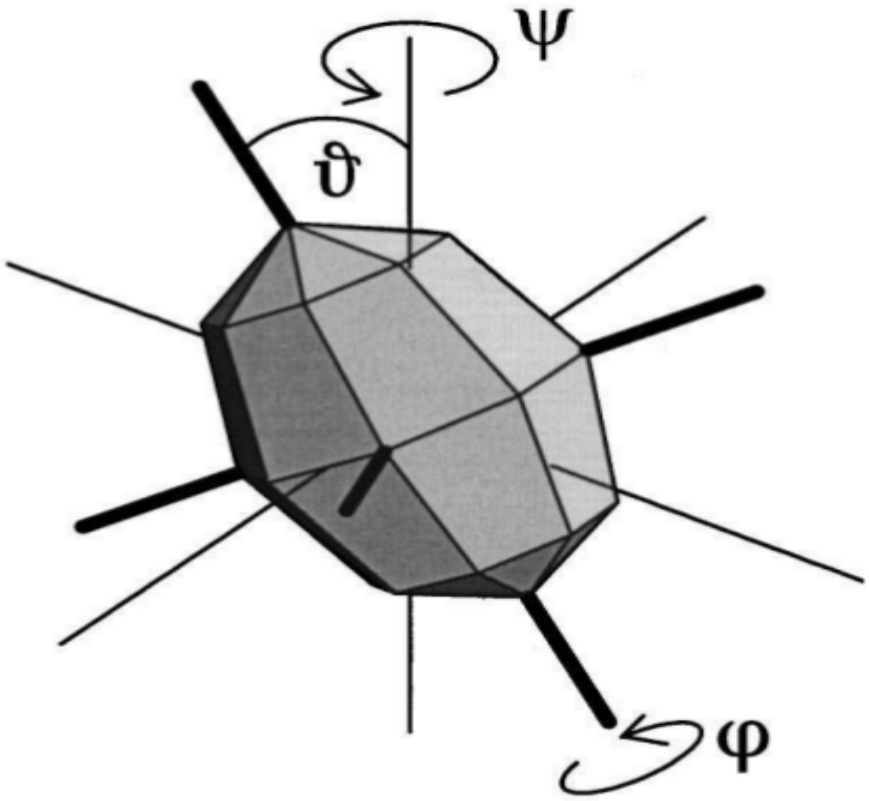

Figure 2.12: The Euler angles describing the orientation of the reflection symmetric deformed shape.

At the equilibrium angle θ, the cranking axis is parallel to the direction of **J**. That is

$$\tan\theta = \frac{\omega_1}{\omega_3} = \frac{J_1}{J_3} \tag{2.35}$$

Once the parameters are fixed through the energy minimization, the corresponding routhian is expressed by $|\omega, \epsilon_2, \gamma, \epsilon_4, \theta\rangle$. The electromagnetic transitional rates can be calculated using the expression [13, 15].

$$\langle (I-2)(I-2)|\mathcal{M}_{-2}(E2)|II\rangle = \langle \mathcal{M}_{-2}(E2)\rangle =$$

$$\sqrt{\frac{5}{4\pi}}\left(\frac{eZ}{A}\right)\left[\sqrt{\frac{3}{8}}\langle Q'_0\rangle \sin^2\theta + \frac{1}{4}\langle Q'_2 + Q'_{-2}\rangle(1+\cos\theta)^2\right] \tag{2.36}$$

where, Q'_ν are the intrinsic quadrupole moments and calculated with respect to the principal axes (1, 2, 3). The reduced $E2$ transition probability becomes

$$B(E2, I \to I-2) = \langle \mathcal{M}_{-2}(E2)\rangle^2 \tag{2.37}$$

The intra-band M1 transition matrix element is

$$\langle (I-1)(I-1)|\mathcal{M}_{-1}(M1)|II\rangle = \langle \mathcal{M}_{-1}(M1)\rangle =$$

$$\sqrt{\frac{3}{8\pi}}[\mu_3 \sin\theta - \mu_1 \cos\theta] \tag{2.38}$$

Hence, the reduced M1 transition probability becomes

$$B(M1, I \to I-1) = \langle \mathcal{M}_{-1}(M1)\rangle^2 \tag{2.39}$$

The components of the magnetic moments with respect to the principal axes is calculated using the expressions

$$\mu_i = \mu_N(J_{i,p} + (\eta 5.58 - 1)S_{i,p} - \eta 3.82 S_{i,n}) \tag{2.40}$$

where the components of J and spin $S(= \langle s\rangle)$ are calculated using the TAC configuration $|\omega, \epsilon_2, \gamma, \epsilon_4, \theta\rangle$ and η is the attenuation factor to the free spin magnetic moments. The components of the electromagnetic transition operator $\mathcal{M}_\nu$ refer to the lab system where as $\langle \mathcal{M}_\nu\rangle$ is calculated for the TAC configuration $|\omega, \epsilon_2, \gamma, \epsilon_4, \theta\rangle$. These theoretically obtained transition probabilities can be compared with the

experimentally observed values and are the most crucial signatures of tilted axis rotation. As mentioned before, this model successfully describes the origin of the $M1$ bands and it also predicts the possibility of alternative angular momentum generation mechanisms such as the Anti-magnetic rotation.

The development from the spherical shell model to the tilted axis cranking can be summarized as follows: The spherical shell model results from the single-particle mean field Hamiltonian, which gives the single-particle energies of nuclear orbits in a spherical potential. Fig. 2.13 illustrates the case of the $g_{9/2}$ level. When the potential is deformed the $g_{9/2}$ level splits according to the projection of the single-particle angular momenta, Ω, on the symmetry axis. In this case Ω is a good quantum number. For a rotating deformed potential about the symmetry axis, Ω is no longer a good quantum number and the signature becomes the new constant of motion. The single particle levels split linearly as $\omega\Omega$ if the pairing interaction is not considered. Finally when the the rotation is tilted with respect to the principal axis, then the splitting is non-linear as shown in the last column of the figure and the signature is no longer a good quantum number.

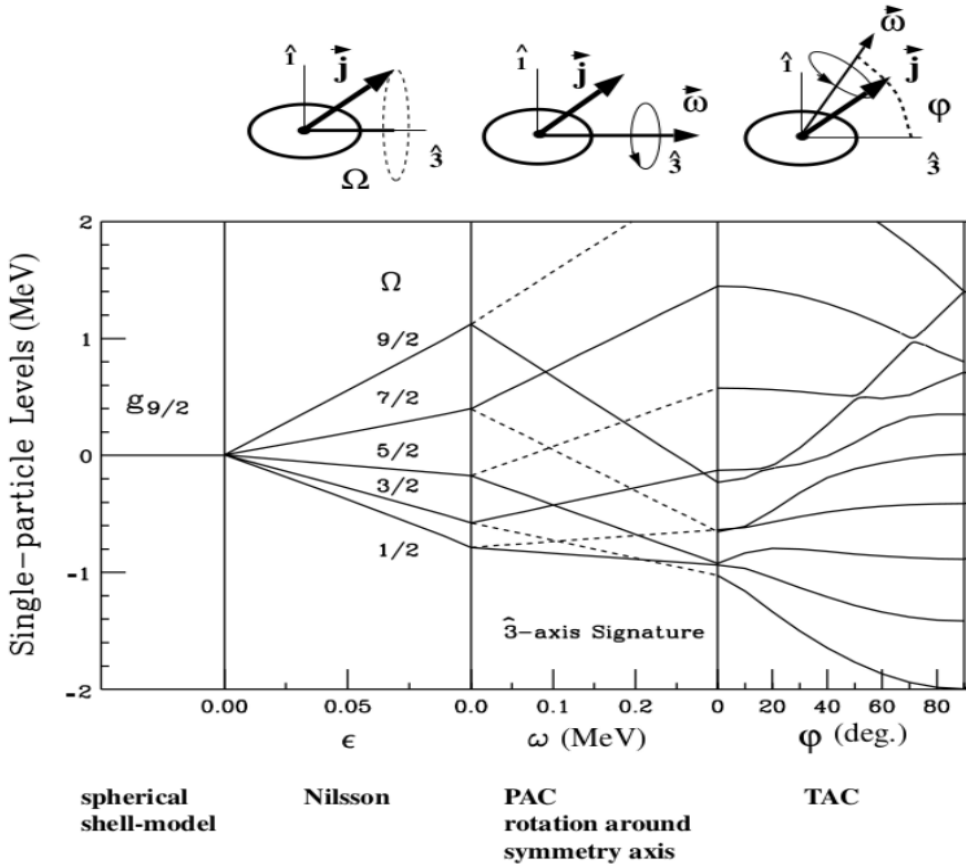

Figure 2.13: The effect on a spherical shell model single-particle orbital (in this case a $g_{9/2}$ level, as shown in the first panel) as the nuclear potential is deformed (second panel, labeled Nilsson), undergoes rotation around the symmetry axis (third panel, labeled PAC rotation around the symmetry axis), rotates about a tilted axis (fourth panel, labeled TAC).

2.6 Semi-Classical-Shears Model (SCSM)

Tilted Axis Cranking (TAC) was introduced to explain the occurrence of the magnetic bands initially found in Pb region. However, these calculations indicate that most of the angular momentum was generated by the single particle motion. Thus, Clark and Macchiavelli proposed the semi-classical model [23] for TAR where the angular momentum of the quasi-particles are represented as vectors aligned to either rotation or deformation axis. The magnitude of the vector is set equal to maximum aligned value of their nuclear state. The angular momentum in this model

is generated through the reorientation of the two vectors.

The only degree of freedom in the Shears scheme is the angle θ between the two vectors, known as the Shears angle. The total angular momentum is given by $I = \sqrt{j_\pi^2 + j_\nu^2 + 2j_\pi j_\nu \cos\theta}$ (as shown in Fig. 2.14). At the band head the neutrons

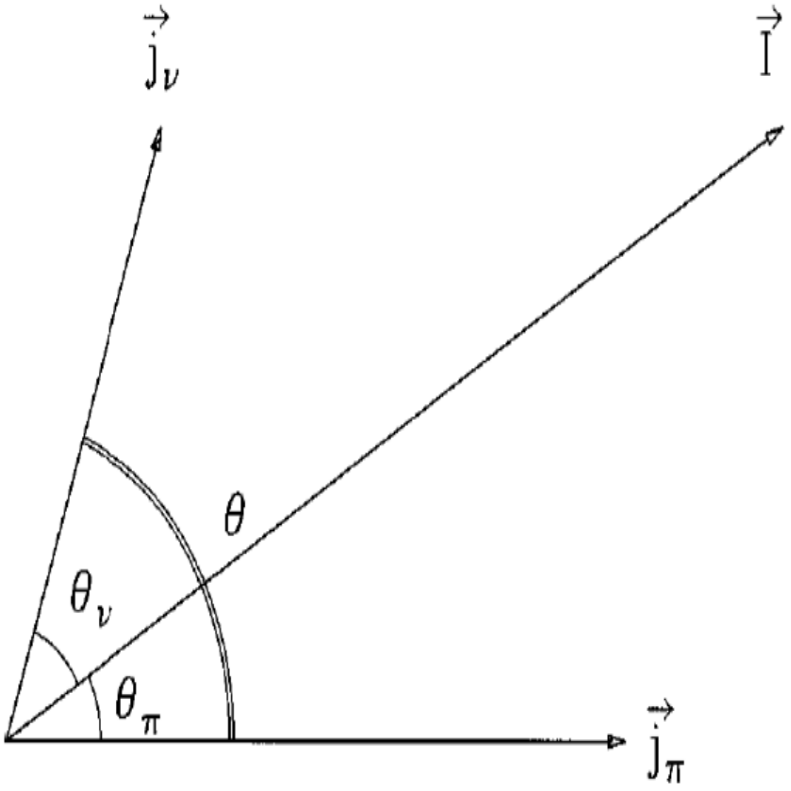

Figure 2.14: Schematic drawing of the angular momentum coupling of neutrons and protons in an $M1$ band.

(protons) are approximately parallel to the rotation axis and protons (neutrons) are parallel to the symmetry axis. Thus, the minimum and maximum value of I are given as $I = \sqrt{j_\pi^2 + j_\nu^2}$ and $I = \sqrt{j_\pi + j_\nu}$, respectively. Therefore, the number of possible integral values of I is approximately $I = j_\pi + j_\nu - \sqrt{j_\pi^2 + j_\nu^2}$. The excitation energy E(I) along the Shears band is given by the change in the potential energy caused by

re-coupling of the angular momenta of the blades,

$$E(I) = V_2 P_2(\theta) \tag{2.41}$$

where the sign of V_2 describes the attractive particle-particle (negative) or the repulsive particle-hole (positive) interactions. The parabolic behavior of the $E(\theta)$ vs. I is plotted in the Fig. 2.15. It is apparent that the resulting rotational like properties can be characterized by an effective moment of inertia given by, $\mathcal{J} = j_\pi j_\nu / 3V_2$.

In order to study the competition between the shears mechanism and the rotation of the core, the rotational energy is introduced by hand, such that the energy $E(I)$ is given by

$$E(I) = \frac{R^2}{2\mathcal{J}} + V_2 P_2(\theta) \tag{2.42}$$

where the rotational angular momentum, R is equal to $I - j_\pi - j_\nu$ and $\mathcal{J}$ is the rotational momentum of inertia. The above equation is solved through energy minimization w.r.t θ. For an accurate comparison with the experimental data the angular frequency ω plays an important role and is given as,

$$\omega = \frac{dE}{dI} = \frac{dE}{d\theta} \times \frac{d\theta}{dI} = 3V_2 \times \frac{I}{j_\pi j_\nu} \times cos\theta \tag{2.43}$$

The fit to the experimental $I(\omega)$ values fixes the value of the shears potential.

The microscopic origin of the $P_2(\theta)$-type of force between the protons and the neutrons is attributed to the particle-vibrational coupling of the valance quasi-particle to the core. To understand this aspect, the two body potential can be expanded in

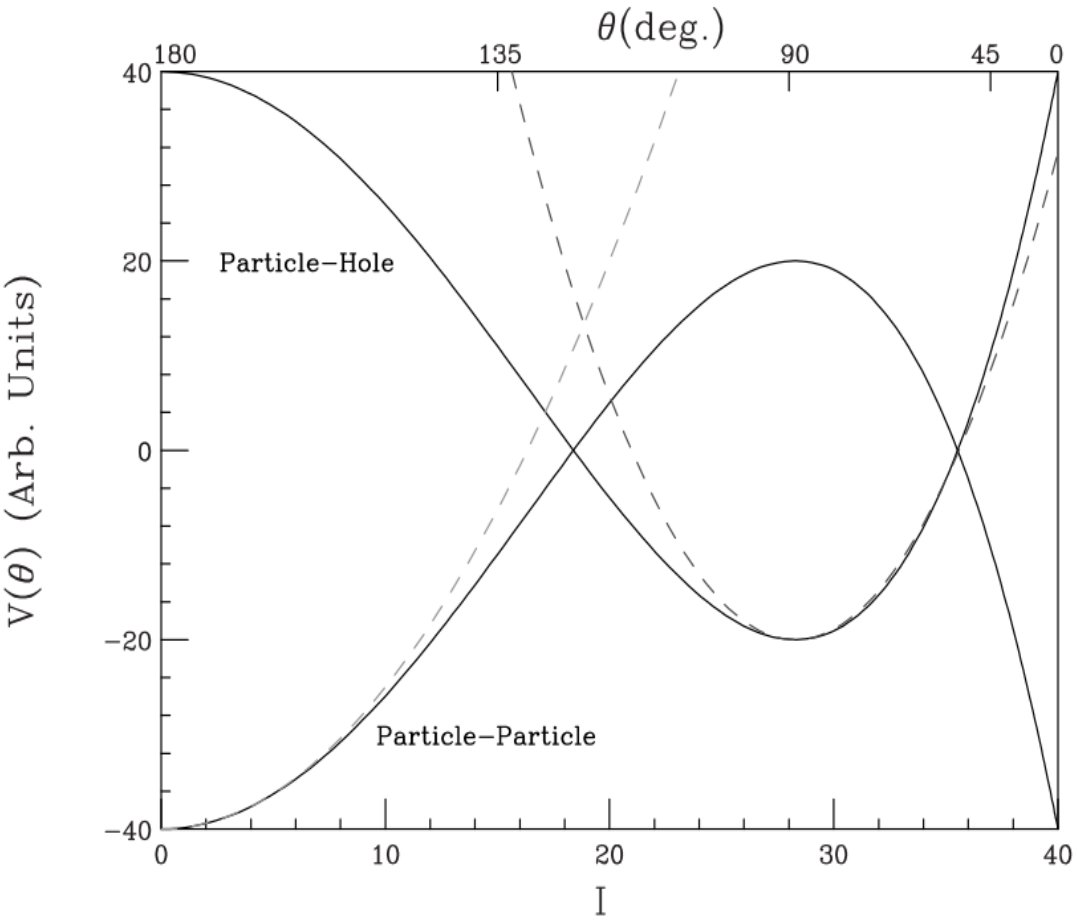

Figure 2.15: Particle-particle/hole potential as a function of angular momentum and θ for an interaction of the form $V_2P_2(cos\theta)$. The dashed lines corresponds to a rotational approximation. The energy is given as $EE_b = V_2P_2(cos\theta)$, where E_b is the band head energy. Generally only particle-hole interaction (repulsive) is observed experimentally.

terms of even multipoles as,

$$V_{\pi\nu}(\theta) = V_0 + V_2P_2(\theta) + ... \tag{2.44}$$

The P_2 term may be positive or negative depending on particle-hole or particle(hole)-particle(hole) combination respectively. At this point one may be tempted to consider a spin dependent force term like $j_\pi.j_\nu$ or a delta type force. A spin dependent force naturally gives rise to a rotational spectra. However, this term favors 0° or 180°

coupling depending on the sign and it's contribution to the band head (perpendicular coupling) configuration is small. On the other hand the delta type force does not give rise to a rotational spectrum. Thus, to explain this phenomena, particle-vibration picture is invoked. The interaction Hamiltonian between a particle and a phonon of order λ arises from the variation in the single-particle potential δV included by the collective vibration. In a spherical nucleus it is given by

$$H_{int} = \delta V = -k_\lambda \sum_\mu Y^*_{\lambda\mu}(\theta, \phi)\alpha_{\lambda\mu} \tag{2.45}$$

where $k_\lambda = R_0(\partial V/\partial r)$ is the particle form factor and $\alpha_{\lambda\mu}$ is the phonon amplitude and r, θ, ϕ are the particle polar coordinates. The significance of this coupling is as follows.

The first order coupling gives rise to scattering effects of a particle in state $\mathbf{j_1}$ to a state $\mathbf{j_2}$ through a phonon of order 1. Similarly in the second order interaction the scattering is between a particle and hole in state $\mathbf{j_1}$ and $\mathbf{j_2}$, respectively. The representative Feynman diagram of these two types of couplings are shown in Fig. 2.16 The interaction between particle-hole case is given by,

$$V_\lambda = \frac{2\lambda + 1}{4\pi C_\lambda} k_\lambda(r_1)k_\lambda(r_2)P_\lambda(\theta_{12}) \tag{2.46}$$

where θ_{12} is the angle between the position vectors of particles 1 and 2. The effective interaction is of a P_λ type and it's magnitude depends on the particle form factor k_λ and restoring force parameter C_λ. The restoring force parameter is in turn directly proportional to the amplitude and energy of the phonon,

$$C_\lambda = \frac{(2\lambda + 1)\hbar\omega_\lambda}{|\langle 1|\alpha_\lambda|0\rangle|^2} \tag{2.47}$$

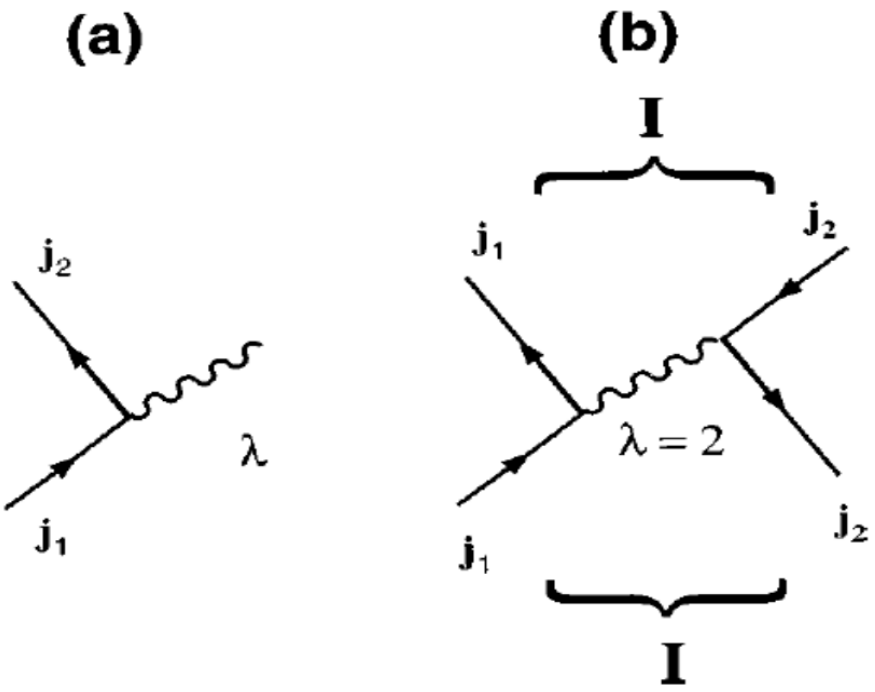

Figure 2.16: Representation of particle-vibration coupling in (a) first and (b) second order coupling.

To compare the above result with the experiment the expectation value of the interaction potential in the angular momentum coupled state $|j_1 j_2 I\rangle$ is calculated. For large values of j the we have,

$$\langle j_1 j_2 I|V_2|j_1 j_2 I\rangle = \frac{1}{4}\frac{5}{4\pi C}\langle k_1(1)\rangle\langle k_2(1)\rangle P_2(\theta) \tag{2.48}$$

For $C_2 = 500$ MeV and $\langle k_1\rangle = \langle k_2\rangle = 50$ MeV we obtain $V_2 \sim 500$ keV, which is near to the value of experimental V_2 in the mass ~ 200 region.

Since the $B(M1)$ rates are proportional to the square of the perpendicular component of the magnetic moment, they should show a characteristic drop as the shears close ($\theta \approx 90^\circ \rightarrow 0^\circ$). From the simple geometry specified in Fig. 2.14, this

dependence is given by [23]

$$B(M1, I \rightarrow I-1) = \frac{3}{8\pi}\vec{\mu}_{\perp}^{2} = \frac{3}{8\pi} g_{eff}^{2} j_{\pi}^{2} \sin^{2}\theta_{\pi} \left[\mu_{N}^{2}\right] \tag{2.49}$$

Thus, SCSM provides a convenient theoretical tool to calculate the energy for a given angular momentum state for a given configuration and the corresponding $B(M1)$ rates in the observed magnetic bands.

This theoretical description of the observation of these shears or magnetic bands as a result of TAR led to the prediction of an alternate configuration possible in even-even nuclei (Fig. 2.17), where a double symmetric shears structure can be formed where the high-j deformation aligned proton-holes in time reverse orbit are coupled with rotation aligned neutron particles or vice-versa. In this picture, two shears like structures will be formed whose magnetic moments are anti aligned. Hence, the net magnetic moment is zero resulting in the absence of dipole transitions between the levels of the band. Thus, the geometry is identified as Anti-magnetic Rotation (AMR). But, as this geometry retains the $R_z(\pi)$ symmetry, the rotational structure is expected to decays by weak $E2$ transitions with a falling $B(E2)$ rates with increasing spin. The higher angular momentum states, in this scenario, will be generated by simultaneous closing of the two shears and is represented by $I = j_p + 2j_h cos\theta$. This behavior can be described by the Semi Classical Particle-Rotor Model for AMR which incorporates the interplay between the collective rotation and the anti-magnetic rotation. This model is described below.

2.6.1 SEMI CLASSICAL PARTICLE-ROTOR MODEL (SCPRM)

In this model the energy E(I) is given by [24],

$$E(I) = \frac{(\boldsymbol{I} - \boldsymbol{j_\pi} - \boldsymbol{j_\nu})^2}{2\mathcal{J}} + \frac{V_{\pi\nu}}{2}\left(\frac{3\cos^2\theta - 1}{2}\right) + \frac{V_{\pi\nu}}{2}\left(\frac{3\cos^2(-\theta) - 1}{2}\right) - \frac{V_{\pi\pi}}{n}\left(\frac{3\cos^2(2\theta) - 3}{2}\right) \tag{2.50}$$

where the first term is the rotational contribution and the rest of the terms are the shear contributions, $V_{\pi\nu}$ = 1.2 MeV and $V_{\pi\pi}$ = 0.2 MeV. 'n' is the scaling factor between $V_{\pi\nu}$ and $V_{\pi\pi}$ and is determined by the actual number of particle-hole pairs for a given single-particle configuration.

The corresponding total angular momentum can be evaluated by imposing the energy minimization condition as a function of θ and is given by,

$$I = aj + 2j\cos\theta + \frac{1.5\mathcal{J}V_{\pi\nu}\cos\theta}{j} - \frac{6\mathcal{J}V_{\pi\pi}\cos 2\theta\ \cos\theta}{nj} \tag{2.51}$$

The first two terms represents the contribution from shears mechanism (I_{sh}). At the band head ($\theta = 90°$), I = j_ν = aj, which corresponds to the aligned angular momentum of the neutrons due to core rotation. This implies that there is a band head frequency which corresponds to the alignment frequency of the neutrons which is essential for the formation of the shear structure. The higher momentum states are formed by gradual closing of the shears angle and the maximum angular momentum (${I_{sh}}^{max}$) that can be generated through AMR due to complete alignment of the two proton holes ($\theta = 0°$). For example when the protons occupy the $g_{9/2}$ orbital ($A \sim 100$ mass region)

$${I_{sh}}^{max} = j_\nu + \frac{9}{2} + \frac{7}{2} \tag{2.52}$$

The significance of the third and fourth terms of Eq. 2.51 becomes apparent if we determine the expression for the frequency associated with the shears mechanism (ω_{sh}). This can be computed through $\left(\frac{dE_{sh}}{d\theta}\right)/\left(\frac{dI_{sh}}{d\theta}\right)$ and is given by,

$$\omega_{sh} = \ (1.5V_{\pi\nu}/j)\cos\theta - (6V_{\pi\pi}/nj)\cos 2\theta \ \cos\theta \tag{2.53}$$

Thus, the third and fourth terms of the Eq. 2.51 are equal to the product of rotational moment of inertia $\mathcal{J}$ and shears frequency (ω_{sh}). They represent the interplay between collective and shears mechanism and Eq. 2.51 can be re-written as

$$I = I_{sh} + \mathcal{J}\omega_{sh} \tag{2.54}$$

It is to be noted that the magnitude of $\mathcal{J}$ determines the extent of the interplay in generation of angular momentum in AMR+rotation model. This value can be estimated from Eq. 2.54

$$\mathcal{J}\omega_{sh}|_{(\theta=0^\circ)} = I_{max} - {I_{sh}}^{max} \tag{2.55}$$

where, I_{max} is the highest observed angular momentum state, ${I_{sh}}^{max}$ is given by Eq. 2.52 and

$$\omega_{sh}|_{\theta=0^\circ} = \left(\frac{1.5V_{\pi\nu}}{j}\right) - \left(\frac{6V_{\pi\pi}}{nj}\right) \tag{2.56}$$

In case of the SCPRM model, the rotational frequency (ω) is given by

$$\omega = \omega_{rot} - \omega_{sh} \tag{2.57}$$

where $\omega_{rot} = \frac{1}{2\mathcal{J}_{rot}}(2I+1)$ is the core rotational frequency and $\mathcal{J}_{rot}$ is the core

moment of inertia, whose value can be estimated from the slope of the $I(\omega)$ plot for the ground state band (before the neutron alignment). The relative negative sign in Eq. 2.56 indicates that a given angular momentum state for AMR+rotation will be formed at a lower frequency as compared to that due to pure rotation.

In this model, the electric quadrupole transition rate $B(E2)$ in the units of $(eb)^2$ is given by [23]

$$B(E2) = \frac{15}{32\pi}(eQ_{eff})^2 \sin^4\theta \tag{2.58}$$

Since the electric quadrupole transition rate $B(E2)$ is proportional to $\sin^4\theta$. Therefore, as the two shears close symmetrically, the $B(E2)$ rates will show a characteristic drop with increasing angular momentum, which will distinguish an AMR band from a band arising due to collective rotation. Apart from the falling trends in $B(E2)$ values, AMR can also be characterized by large $\mathcal{J}^{(2)}/B(E2)$ ratio [$\sim$100 MeV$^{-1}(eb)^{-2}$] which for a well-deformed nucleus is $\sim$10 MeV$^1(eb)^2$. Thus, the characteristic features of AMR can be summarized as follows:

1. Rotational bands with $\Delta I = 2$.
2. Near spherical nuclei; weak $E2$ transitions.
3. No $M1$ transitions present.
4. $B(E2)$ rates fall as a function of spin.
5. The $\mathcal{J}^2/B(E2)$ ratios are large $\sim$100 $\hbar^2$MeV$^{-1}(eb)^{-2}$.

This mode of generating the high angular momentum has been experimentally reported to occur in various Cd isotopes [25, 26]. The present thesis has established this mode to be present in ^{104}Pd [27].

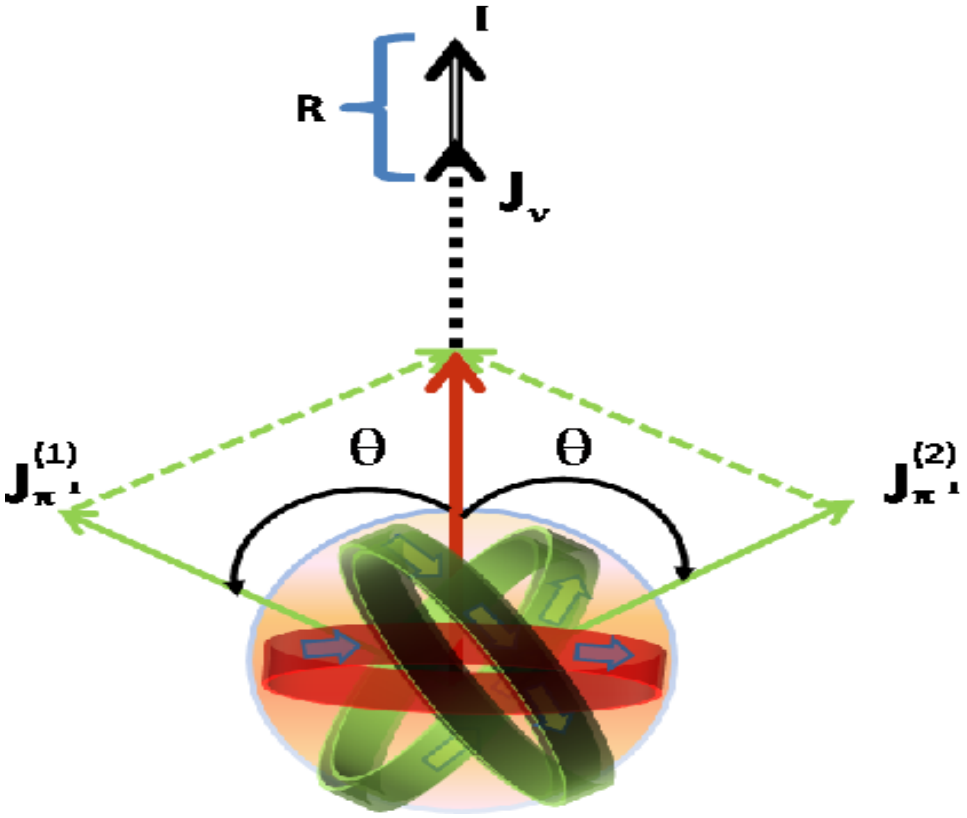

Figure 2.17: The coupling of angular momentum vectors in Anti-magnetic Rotation.

2.7 Particle Rotor Model

In this section we shall discuss the Particle Rotor Model (PRM). There is a definite advantage of using this phenomenological model over the Cranking model. The PRM describes the nucleus in the lab frame, hence, the total angular momentum $\vec{I}$ is a good quantum number and the experimental values can be directly compared with the PRM predictions. However, the main disadvantage of this model is that it becomes computationally extremely involved to describe the multi-particle (valence particles three or more) configurations.

This model is used to study the ground state band structures in odd or odd-odd nucleus. The valence nucleon(s) is(are) coupled to the even-even core and the total angular momentum is the vector addition of the rotational angular momentum $\vec{R}$

and the intrinsic angular momentum $\vec{j}$. This coupling scheme is the same as the one shown in Fig. 2.2. Thus, the PRM Hamiltonian is expressed as

$$H = H_{int} + T_{rot} \tag{2.59}$$

where H_{int} is the deformed Nilsson potential. If the rotation is considered along the z axis and the T_{rot} assumed to be for an axially symmetric system then

$$T_{rot} = \frac{\hbar^2}{2\mathcal{J}}[(I^2 - I_z^2) + (j^2 - j_z^2 - I_+ j_- + I_- j_+)] \tag{2.60}$$

The first term represents the core contribution. The second term is the contribution of the intrinsic motion of the valence nucleon and the last term is responsible for the particle-rotation coupling which is the equivalent Coriolis term. In this model, the total wave function is written as

$$\Psi_{I,M,K} = \sqrt{\frac{2I+1}{16\pi^2}}\Phi_K(q)\mathcal{D}^I_{MK}(\phi,\theta,\psi) + (-1)^{I-j}\Phi_{-K}(q)\mathcal{D}^I_{M-K}(\phi,\theta,\psi) \tag{2.61}$$

where the single particle wave function Φ_K is calculated from the Nilsson model and can be expressed as

$$\phi_{-K} = \sum_j (-1)^{j+K} C_{jK}|j-K\rangle \tag{2.62}$$

where C_{jK} are the mixing amplitudes calculated from the Nilsson model. The Hamiltonian is diagonal without the Coriolis term and the energy eigenvalue is given by

$$E_{I,K} = \frac{\hbar^2}{2\mathcal{J}}[I(I+1) - K^2] + E_{sp}(K) \tag{2.63}$$

where the total single particle energy (contribution of Φ_K) E_sp(K) incorporates the effects of j^2 and j_z^2. The effect of the Coriolis term can be treated as the perturbation and there can be two limiting situations: (a) the strong coupling limit (DAL) where the valence particles are aligned along the deformation axis (low j and high Ω) (b) the decoupled limit (RAL) where the valence particles are aligned along the rotational axis. The angular momentum coupling scheme are shown in Fig. 2.18. The rotational bands arising from DAL have a small signature splitting with the level sequence as

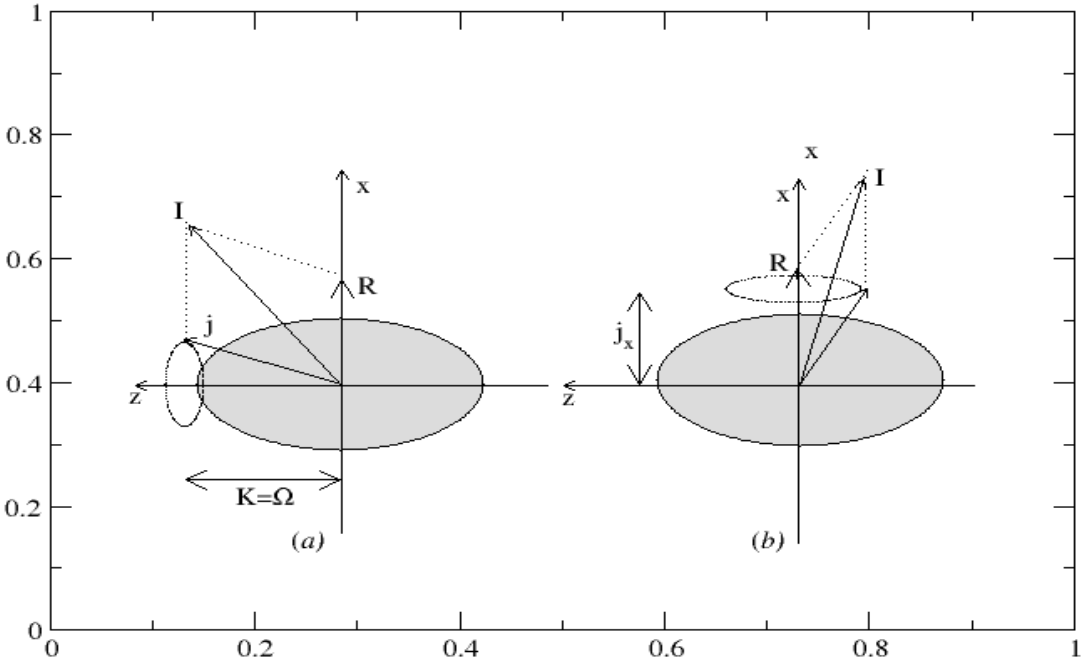

Figure 2.18: The angular momentum coupling schemes for DAL (strong coupling) and RAL (weak coupling).

$I = K, K+1, K+2, \ldots$ while in the case of RAL the effect of Coriolis interaction is significant and the coupling between the nucleon and the core is minimal. The inclusion of Coriolis interaction mixes the states having the same I and the K values

differing by one unit. The lowest order change in the energy because of the Coriolis term is

$$\Delta E(I,K) = \frac{\hbar^2}{2\mathcal{J}}\langle\Psi_{I,M,K}|(I_+j_- + I_-j_+)|\Psi_{I,M,K}\rangle \tag{2.64}$$

Since $j_\pm$ has no diagonal element in K, Coriolis interaction contributes through second order but for the $K{=}\frac{1}{2}$ value, it has the first order effect. The, the expression for $\Delta E(I,K)$ for $K=\frac{1}{2}$ can be written as

$$\Delta E(I,K) = -2\frac{\hbar^2}{2\mathcal{J}}(-1)^{I+\frac{1}{2}}\langle\mathcal{D}^I_{M\frac{1}{2}}|I_-|\mathcal{D}^I_{M-\frac{1}{2}}\rangle(-1)^{-j-\frac{1}{2}}\langle\phi_{\frac{1}{2}}|j_+|\phi_{-\frac{1}{2}}\rangle$$

$$= (-1)^{1+\frac{1}{2}}\left(I+\frac{1}{2}\right)a \tag{2.65}$$

where a is known as the decoupling parameter and is responsible for the staggering in level energies known as the *signature splitting* in the rotational bands.

2.8 Triaxial Particle Rotor Model (TPRM)

In this model we assume that the unpaired neutron and proton are coupled to an triaxial core. The total Hamiltonian is given as [28, 29]

$$\hat{H} = \hat{H}_{core} + \hat{H}_{s.p} + \hat{H}_{pair} \tag{2.66}$$

In the case of triaxial deformation, the Hamiltonian of the even-even core is given as,

$$\hat{H}_{core} = \sum_{i=1}^{3}\frac{\hbar^2 R_i^2}{2\mathcal{J}_i} = \sum_{i=1}^{3}\frac{\hbar^2(I_i-j_i)^2}{2\mathcal{J}_i} \tag{2.67}$$

where R, I and j are the angular momentum of the core, the nucleus and the single particle, respectively. For the triaxial shape, the rotation is possible around any of the three axes. The corresponding three rotational moments of inertia are assumed to be connected by a relation of hydro-dynamical type

$$\mathcal{J}_\kappa = \frac{4}{3}\mathcal{J}_0(I)\sin^2\left(\gamma + \frac{2\pi}{3}\kappa\right) \tag{2.68}$$

where $\mathcal{J}_0(I) = \mathcal{J}_0\sqrt{1+bI(I+1)}$ is the variable moment of inertia [30] of the core. The value of $b = 0.013$ can be fixed from that in Ref. [31].

$\hat{H}_{s.p}$ describes the Hamiltonian of the unpaired single particle. In the triaxial deformed field of the even-even core, $\hat{H}_{s.p.}$ is given by

$$\begin{aligned}\hat{H}_{s.p} = &-\frac{\hbar^2}{2m}\nabla^2 + \frac{1}{2}m\omega_0^2\{1 - 2\beta[Y_{20}\cos\gamma + \frac{1}{\sqrt{2}}(Y_{22}+Y_{2-2})\sin\gamma]\} \\ &- \kappa\hbar\omega_0\{2l.s + \mu(l^2 - \langle l_N\rangle^2)\}\end{aligned} \tag{2.69}$$

where κ and μ are Nilsson parameters, Y_{2q}, is the rank-2 spherical harmonic function. $\hat{H}$ pair is the Hamiltonian to represent the pairing correlation which can be treated in the Bardeen-Cooper-Schrieffer (BCS) formalism. The single-particle wave function can be expressed as,

$$|\nu\rangle = \sum_{Nlj\Omega} C^{(\nu)}_{Nlj\Omega}|Nlj\Omega\rangle \tag{2.70}$$

where ν is the sequence number of the single-particle orbitals, $|Nlj\Omega\rangle$ represents the corresponding Nilsson state, $C^{(\nu)}_{Nlj\Omega}$ is the coefficient to identify the configuration mixing. Diagonalizing the single-particle Hamiltonian in the basis $|Nlj\Omega\rangle$, we can obtain the $C^{(\nu)}_{Nlj\Omega}$ and the single-particle eigenvalue ϵ_ν . The corresponding quasi-particle energy can then be determined by $E_\nu = \sqrt{(\epsilon_\nu - \lambda)^2 + \Delta^2}$, with λ and Δ

being the Fermi energy and the energy gap, respectively. The total Hamiltonian in Eq. 2.66 can be diagonalized in the symmetrically strong coupling basis

$$|IKM\nu\rangle = \sqrt{\frac{2I+1}{16\pi^2}}\left[D^I_{MK\alpha^\dagger_\nu}|\tilde{0}\rangle + (-1)^{I-K}D^I_{M-K\alpha^\dagger_\nu}|\tilde{0}\rangle\right] \tag{2.71}$$

where $\alpha^\dagger_\nu$ is creation operator of the single nucleon in the orbital $|\nu\rangle$, D^I_{MK} is the rotational matrix. This model has been successfully used in $A \sim$100 region to describe the experimental routhians and transition rates in ^{110}Ag [32].

2.9 The Doublet Bands

Recently, a series of bands have been observed experimentally that form doublets as they lie very close in energy. Fig. 2.19 shows a typical example of such doublet bands as observed in ^{128}Cs. It has been suggested that the vanishing energy splitting between these bands arises due to the possible existence of chiral symmetry breaking of the nucleus. The chiral bands are observed mainly in well-deformed nuclei, in which there are valence particles and valence holes in orbitals of high angular momentum. The former drives the nucleus towards elongated shapes, while the latter towards oblate ones. The interplay of these opposite tendencies may result in a shape resembling a triaxial ellipsoid. In the triaxially deformed nucleus, the particle and hole align their angular momenta along the short and long axes of the density distribution, respectively (Fig. 2.20). Moreover, the moment of inertia with respect to the medium axis is the largest, which favors the collective rotation around that axis. Thus, the total angular momentum vector has non-zero components on all the three axes, and these vectors can form either a left-handed or a right-handed system. Such doublet bands are expected to have similar moments of inertia, alignment behavior and transition rates, besides the similar routhians.

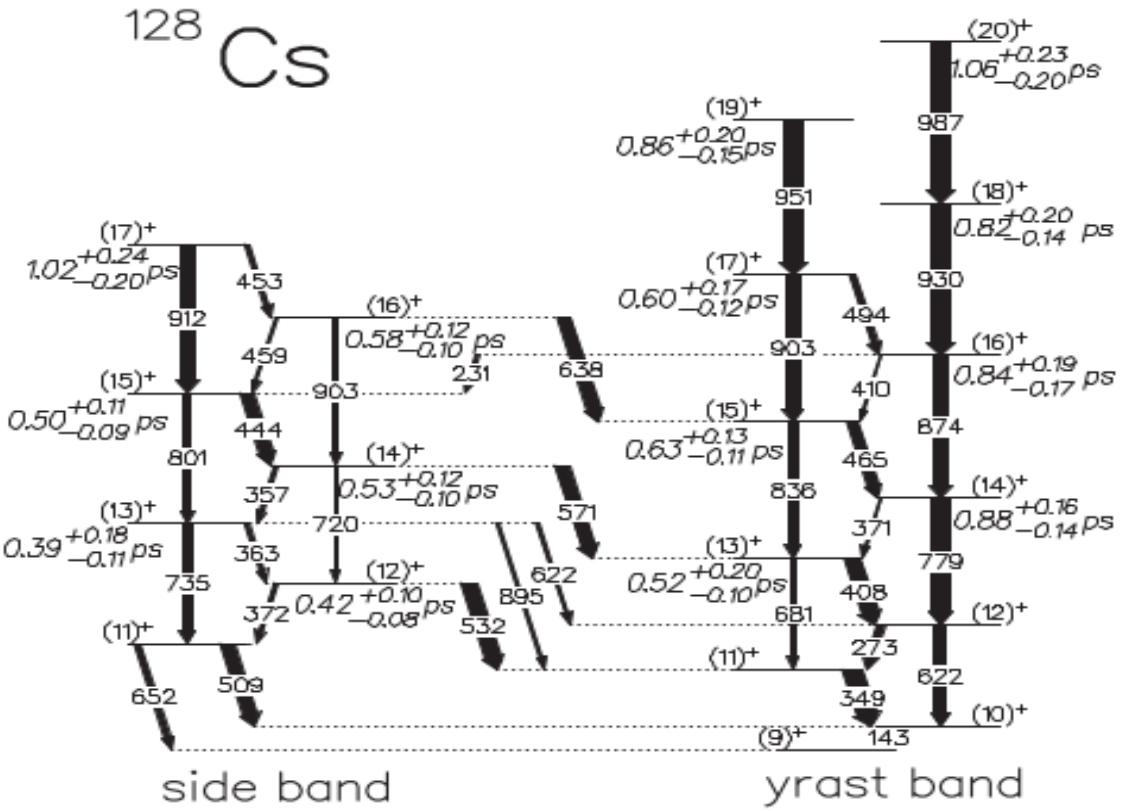

Figure 2.19: An example of the chiral bands as observed in ^{128}Cs. (Figure taken from [33])

Thus, the spin chirality is an interesting phenomenon in high spin physics. The tilted axis cranking calculations also support the occurrence of the chiral bands. To the date, many experiments have reported the observation of the possible chiral doublets in mass regions of $A \sim 100$ and $A \sim 130$. However, in most of the cases the transition rates were found to be different in the two bands. This rules out the interpretation based on spin charility for these doublet bands. However, the doublet bands in ^{128}Cs exhibit all the requisite properties of a chiral doublet. The triaxial projected shell model (TPSM) calculations have been have been successful in describing the behavior of ^{128}Cs and does not assume the spin charility as a pre-requisite. This model was also used to understand the doublet bands of ^{106}Ag studied

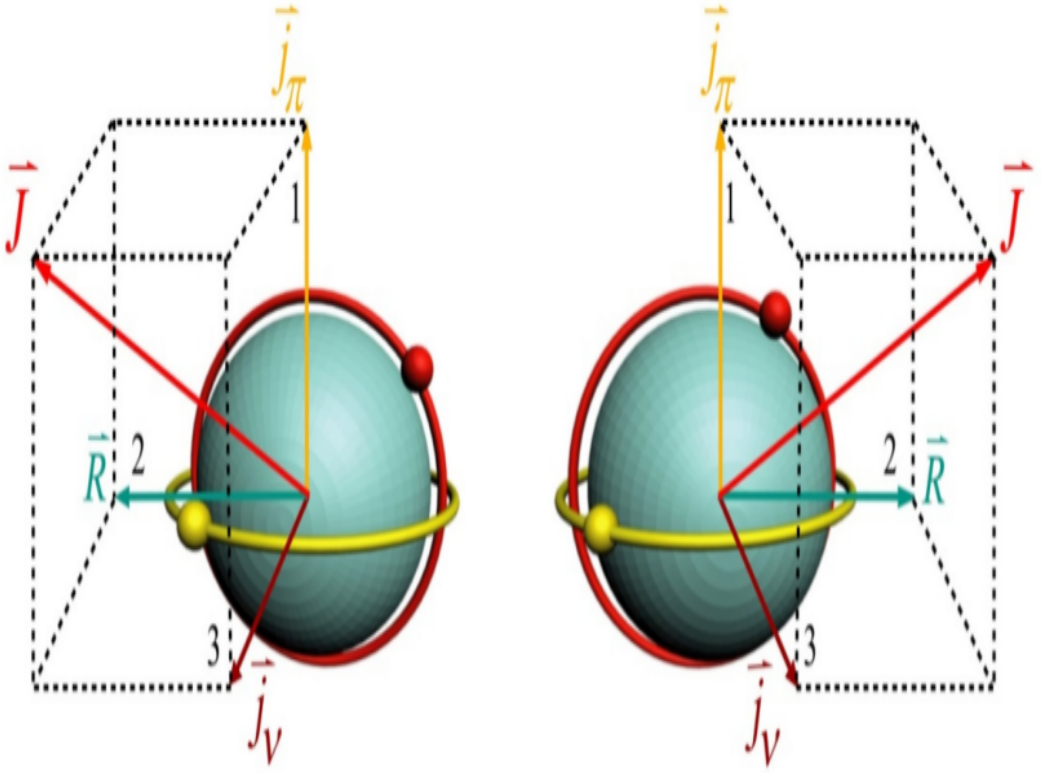

Figure 2.20: A schematic diagram of two chiral configurations of an odd-odd triaxial nucleus where the angular momenta of the valence proton, the valence neutron and the core are mutually perpendicular.

during the present work. The salient aspects of this model are discussed below.

2.10 Triaxial Projected Shell Model (TPSM)

The basic philosophy in the TPSM approach is similar to that of spherical shell model with the only exception that deformed basis is employed rather than the spherical one. This allows to investigate heavier deformed nuclei with a small number of basis states. The basis space of the TPSM approach for odd-odd nuclei is composed of one-neutron and one-proton quasiparticle configurations:

$$|\phi_\kappa\rangle = a^\dagger_\nu a^\dagger_\pi |0\rangle \tag{2.72}$$

The above basis space is adequate to describe the chiral bands in odd-odd nuclei, which are based on one-proton and one-neutron quasiparticle configurations. The triaxial quasi-particle (qp)-vacuum $|0\rangle$ in Eq. (2.72) is determined by diagonalization of the deformed Nilsson Hamiltonian and a subsequent BCS calculations. The number of basis configurations depend on the number of levels near the respective Fermi levels of protons and neutrons [34].

The states $|\phi_\kappa\rangle$ obtained from the deformed Nilsson calculations don't conserve rotational symmetry. To restore this symmetry, three-dimensional angular-momentum projection technique is applied. From each intrinsic state, , in (2.72) a band is generated through projection technique. The interaction between different bands with a given spin is taken into account by diagonalizing the shell model Hamiltonian in the projected basis. The TPSM wave function is written in the form of

$$|IM\rangle = \sum_{K,\kappa} f^I_{K,\kappa} P^I_{M,K} |\kappa\rangle \tag{2.73}$$

where, P^I_{IM} is the angular momentum- projection operator,

$$P^I_{MK} = \frac{2I+1}{8\pi^2} \int d\Omega D^I_{MK}(\Omega) R(\Omega) \tag{2.74}$$

The rotational band energies together with wave functions can be obtained by solving the eigenvalue-equation,

$$\sum_{K,\kappa} f^I_{K,\kappa} (\langle \kappa' | H P^I_{K'K} | \kappa \rangle - E^I \langle \kappa' | P^I_{K'K} | \kappa \rangle) = 0 \tag{2.75}$$

The Hamiltonian is written as,

$$H = H_0 - \frac{1}{2}\chi \sum_{\mu} \hat{Q}^+_{\mu} \hat{Q}_{\mu} - G_M \hat{P}^+ \hat{P} - G_Q \sum_{\mu} \hat{P}^+_{\mu} \hat{P}_{\mu} \tag{2.76}$$

where, the first term is the spherical Nilsson hamiltonian, the second term denotes multipole-multipole interactions, the third and fourth terms stand for the monopole and quadrupole pairings, respectively. The operators $\hat{P}$ and $\hat{Q}$ are defined as

$$\hat{Q}_{\mu} = \sum_{\alpha,\beta} Q_{\mu\alpha\beta} c^{\dagger}_{\alpha} c_{\beta} \tag{2.77}$$

$$\hat{P}^{\dagger} = \frac{1}{2} \sum_{\alpha} c_{\dagger} c^{\dagger}_{\bar{\alpha}} \tag{2.78}$$

$$\hat{P}^{\dagger}_{\mu} = \frac{1}{2} \sum_{\alpha\beta} Q_{\mu\alpha\beta} c^{\dagger}_{\alpha} c^{\dagger}_{\bar{\beta}} \tag{2.79}$$

where the quadrupole matrix elements are given by

$$Q_{\mu\alpha\alpha'} = \delta_{NN'} \langle Njm | Q_{\mu} | N'j'm' \rangle \tag{2.80}$$

Also, $\alpha = \{Njm\}$ while $\bar{\alpha}$ represents the time reversed states of α. The details of this model can be found in Ref. [34].

In this chapter, I have described in brief, the theoretical frameworks which have been employed to describe the observed features of ^{104,105}Pd and ^{106}Ag. The next chapter is devoted to the different experimental and analysis methods which were used to establish the high spin behaviors of these nuclei.

Bibliography

[1] P. Navràtil and W. E. Ormand, Phys. Rev. C **68**, 034305 (2003).

[2] M. G. Meyer, Phys. Rev. **74**, 235 (1948).

[3] O. Haxell, J. H. D. Jensen, and H. E. Suess, Phys. Rev. **75**, 1766L (1949).

[4] B. A. Brown. The nuclear shell model towards the drip lines. *Prog. Part. Nucl. Phys.*, 47:517âĂŞ599, (2001).

[5] https://universe-review.ca/F14-nucleus02.htm.

[6] A. Bohr, Phys. Rev. **81** 134 (1951).

[7] S. G. Nilsson, Kgl. Danske Videnskab Selskab Mat -fys Medd, 29(16) (1955).

[8] E. Paul *Nuclear Models*, Private communication.

[9] Richard F. Casten *Nuclear Structure from a Simple Perspective*. Oxford Science Publications, 1990.

[10] R. Bengtsson et al., Physics Letters B **57**, 301 (1975).

[11] I. Hamamoto, Phys. Lett. B **235** 221 (1990).

[12] B. Binder *et al.,* Phys. Rev. C **67** 034302 (2003).

[13] B. Fant *et al.,* J. Phys. G **17** 319 (1991).

[14] R. M. Clark *et al.,* Phys. Lett. B **275** 247 (1992).

[15] G. Baldsiefen *et al.,* Phys. Lett. B **275** 252 (1992).

[16] A. Kunhnert *et al.,* Phys. Rev. C **46** 133 (1992).

[17] I. Thorslund *et al.,* NUcl. Phys. A **564** 285 (1993).

[18] R. H. Regan *et al.,* Phys. Rev. C **49** 1885 (1994).

[19] P. Datta *et al.,* Phys. Rev. C **67** 014325 (2003).

[20] H. Schnare *et al.,* Phys. Rev. Lett. **82** 4408 (1999).

[21] S. Frauendorf, Rev. of Mod. Phys. **73** 463 (2001).

[22] S. Frauendorf, Nucl. Phys. A **557** 259c (1993).

[23] R. M. Clark and A. O. Macchiavelli, Annu. Rev. Nucl. Part. Sci. 2000. 50:1-36.

[24] Santosh Roy *et al.*, Phys. Lett. B **694** 322 (2011).

[25] A. J. Simons *et al.,* Phys. Rev. Lett. **91** 162501 (2003).

[26] P. Datta *et al.,* Phys. Rev. C **71** 041305(R) (2005).

[27] N. Rather *et al.,* Phys. Rev. C **89** 061303(R) (2014).

[28] A. Bohr and B. R. Mottelson, *Nuclear structure*, Vol **II** (Benjamin, New York, 1975).

[29] I. Hamamoto and H. Sagawa, Phys. Lett. B **201**, Issue 4, 415 (1988).

[30] S. M. Abecasis and E. S. Hernndez, Nucl. Phys. A **180**, Issue 2, (1972).

[31] K. Mki-Kuutti and E. Hammarn, Nucl. Phys. A **411**, Issue 1, 125 (1983).

[32] Santosh Roy *et al.*, Phys. Lett. B **710** 587 (2012).

[33] E. Grodner *et al.,* Phys. Rev. Lett. **97** 172501 (2006).

[34] J. A. Sheikh and K. Hara, Phys. Rev. Lett. **82** 3968 (1999).

Chapter 3

Experimental Techniques and The Data Analysis

3.1 Fusion Evaporation Reactions

A nucleus does not naturally exist in high-spin states, it has to be excited or prepared in these states. The fusion-evaporation reaction is the best experimental technique to produce high spin states with large cross-sections. In such a reaction, the kinetic energy of the collision in the center of mass frame is converted into excitation energy of the compound system.

Depending on the energy of the incident nucleus, various reaction mechanisms can occur. These range from Coulomb excitation to fragmentation of the incident/-target nucleus. A schematic diagram of various reactions at near Coulomb barrier energies, is shown in Figure 3.1.

The fusion-evaporation technique has many other advantages such as to either

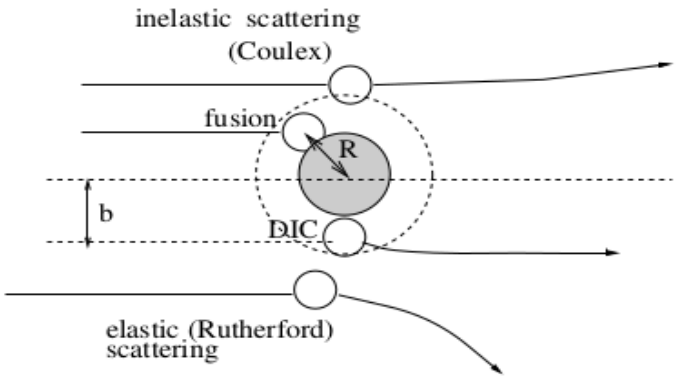

Figure 3.1: Various types of heavy-ion collisions as a function of impact parameter.

specifically populate certain energy levels, achieve an exotic configuration of protons or neutrons, transfer a certain amount of angular momentum or a combination of all the above. This in turn enables us to study various structural phenomena associated with the nucleus according to our interest. The linear momentum of the

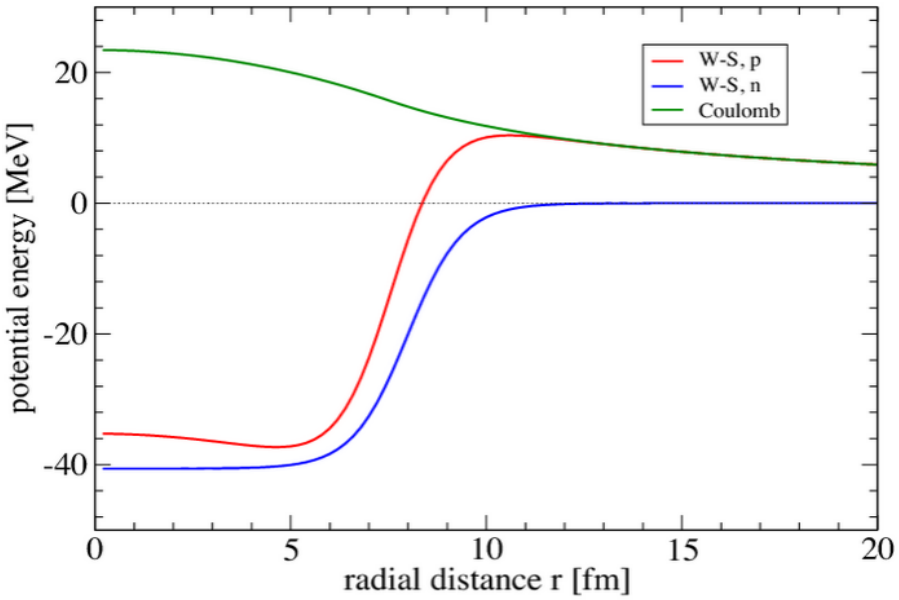

Figure 3.2: The Coulomb and Woods-Saxons potentials that contribute to the effective potential between two nucleons.

projectile, mv, increases with the projectile mass and beam energy. For a given

impact parameter, the angular momentum imparted is proportional to mv. However, this quantity (angular momentum) is limited by competition with fission such that the maximum angular momentum increases with beam energy up to a critical value [1]. This critical value, in its turn, reaches a maximum of around 77 $\hbar$ at A $\sim$ 140 [2] (for higher masses, Coulomb repulsion makes fission more favorable and the critical angular momentum is lowered).

For a nuclear-fusion reaction to occur the projectile nuclei must collide with the target nuclei with sufficient energy to overcome the fusion barrier and come into the range of the nuclear force. The fusion barrier can be approximated to the Coulomb barrier which is the energy required for the incident nuclei to overcome their mutual electrostatic repulsion. Fig. 3.2 shows the repulsive Coulomb potential and attractive Wood-Saxon potential for nucleons. In sufficiently heavy systems the combination of nuclear and Coulomb forces is still repulsive within the range of the nuclear force and additional energy is required for fusion to occur [3].

When fusion occurs, it takes about 10^{-20} s for the compound nucleus to reach thermodynamic equilibrium, after which its formation history has no influence on its behavior. This is followed by particle evaporation effectively 'cooling' the nucleus, until a low enough excitation energy is reached for γ-ray emission to become energetically more favorable. Initially a sequence of competing quadrupole and dipole γ rays are emitted from a quasi-continuum of high-energy states [4]. These γ rays have a continuous range of energies and therefore cannot be resolved experimentally and they appear as a continuous background. Eventually, the quasi-continuum transitions start to populate the discrete yrast (lowest energy for a given spin) or near-yrast states as shown in Fig. 3.3. As stated by the Bohr assumption, the following decays will provide information about the nuclear structure of the compound nuclei which is independent of the initial nuclei [5] that collided.

The production cross-section calculations for the different residues can be performed using the fusion-evaporation simulation program PACE [6]. These calculations served as a guide to choose an appropriate beam energy for the reaction. In the present thesis the reactions were chosen such that mostly only two nuclei with comparable reaction cross-section were populated which accounted for $\sim 85\%$ of the fusion cross-section.

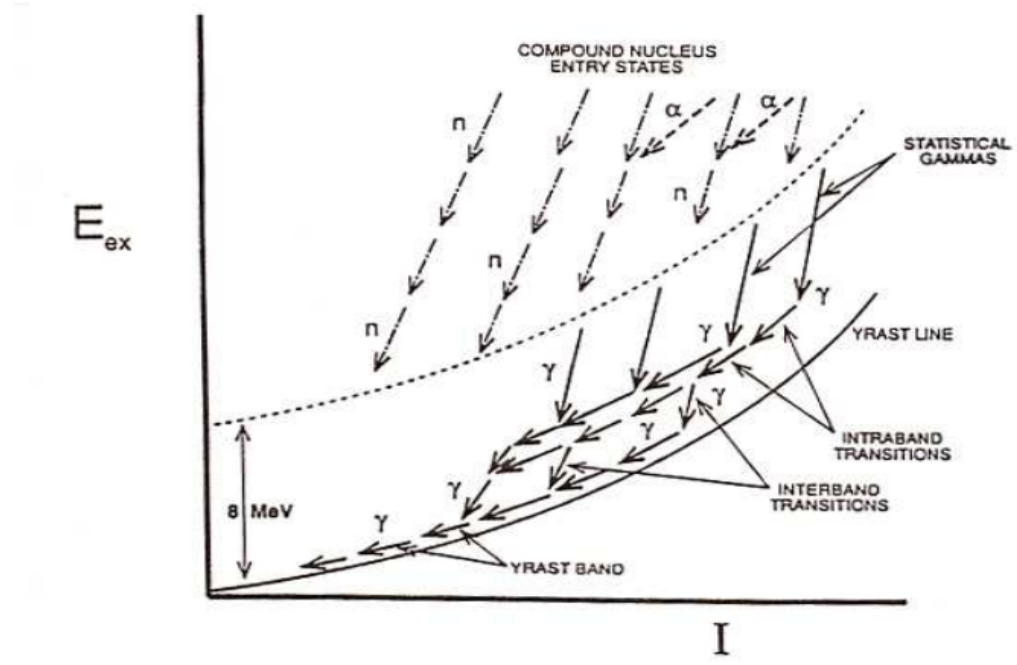

Figure 3.3: A schematic representation of the formation of high-spin residual nuclei from compound nucleus decay.

3.2 Target

The target used in the two experiments was 1 mg/cm^2 ^{96}Zr with ^{206}Pb backing of 9 mg/cm^2 thickness. The backed target was used to stop the recoiling nuclei. An advantage of using the backed target is that the transitions occurring between high-spin states are emitted before the recoiling nuclei stop in the backing material

and are, therefore, Doppler broadened. This Doppler broadening is used as a tool to estimate the level lifetimes of these high spin states. The choice of Pb as backing was mainly due to two reasons viz. It is a high Z material which would, therefore, facilitate an efficient stopping of the recoil and thus enable a subpicosecond lifetime measurements. Pb also has a higher Coulomb barrier than the target material which would prevent the fusion-evaporation reaction between the Pb and the beam nuclei. The currents of ^{13}C and ^{14}N beams used in the experiments were of the order of 8-10 nano-amps.

3.3 Excitation Energy and Maximum Angular Momentum.

By conservation of energy, the compound nucleus will be formed at an excitation energy which depends on the center of mass kinetic energy of the collision and the Q-value (Q_{fus}) for compound nucleus formation such that

$$E_{ex} = E_{cm} + Q_{fus} \tag{3.1}$$

Where the Q_{fus} of the reaction is given by

$$Q_{fus} = [M_P + M_T - M_{CN}]c^2 \tag{3.2}$$

and the energy of the nucleus in the centre of mass frame, E_{cm}, is given by

$$E_{cm} = \frac{M_T}{M_P + M_T} E_b \tag{3.3}$$

where E_b is the beam energy and $M_{P,T,CN}$ are the masses of the projectile, target and the compound nucleus, respectively.

As the excitation of the compound nucleus is higher than the particle emission energy threshold, it will undergo particle evaporation to cool down and remove excitation energy from the compound system.

The maximum angular momentum, l_{max}, of the fusion-evaporation can be given by [1]

$$l_{max}^2 = \frac{2\mu R^2}{\hbar^2}(E_{cm} - V_c) \tag{3.4}$$

Where μ is the reduced mass of the system, given by

$$\mu = \frac{M_P M_T}{M_T + M_P} \tag{3.5}$$

R is the maximum distance at which the collision leads to any contact. An empirical relation for R, derived from [7], is given by:

$$R = 1.36(A_1^{1/3} + A_2^{1/3}) + 0.5fm \tag{3.6}$$

V_c , in units of MeV, is the Coulomb barrier between the target and projectile in the centre of mass frame, which can be estimated using the expression [1]:

$$V_c \approx 1.44\frac{Z_T Z_P}{R} \tag{3.7}$$

It is clear from Eqn. 3.4 that those collisions which maximize the value of the reduced mass ($i, e.$ symmetric reactions) will have the largest input angular momentum for a given center of mass energy. Thus, the symmetric target-projectile combination is the most favorable to produce the high angular momentum states in the residual nuclei.

3.4 Gamma-ray detection

After preparing a nucleus of interest at high angular momentum utilizing a suitable fusion-evaporation reaction, an efficient γ-ray detection system is essential to detect the discrete γ-rays. In the present work, this was achieved by using the Indian National Gamma Array (INGA) (photograph shown in Fig. 3.4). It is a spherical array of Compton-suppressed, high-purity germanium (HPGe) detectors [8] with clover geometry. The INGA can accommodate up to 24 detectors with solid

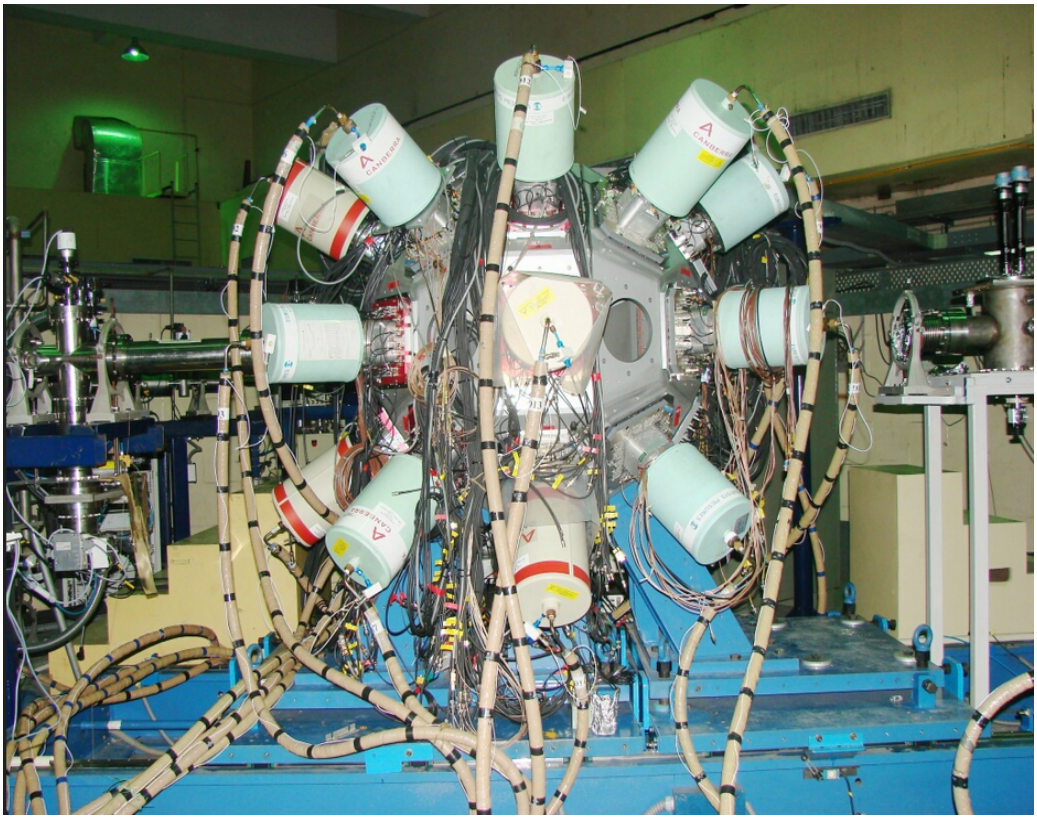

Figure 3.4: Photograph of the INGA detector array. It consisted of 20 Compton suppressed clover detectors spread over a solid angle of 4π.

angle coverage of 25% of 4π. The 'Compton suppression' is the reduction of unwanted background events resulting from a γ ray Compton scattering out of the Ge detector, thereby failing to deposit its full energy. Each clover detector is surrounded by

bismuth germinate (BGO) scintillation detectors (Fig. 3.5) that detect the Compton scattered γ rays out of the clover detector. A γ ray recorded simultaneously in the Ge detector and in the BGO shield can be assumed not to have deposited its full energy and is excluded from the recorded data. This substantially improves the peak-to-background ratio of resulting spectra [9].

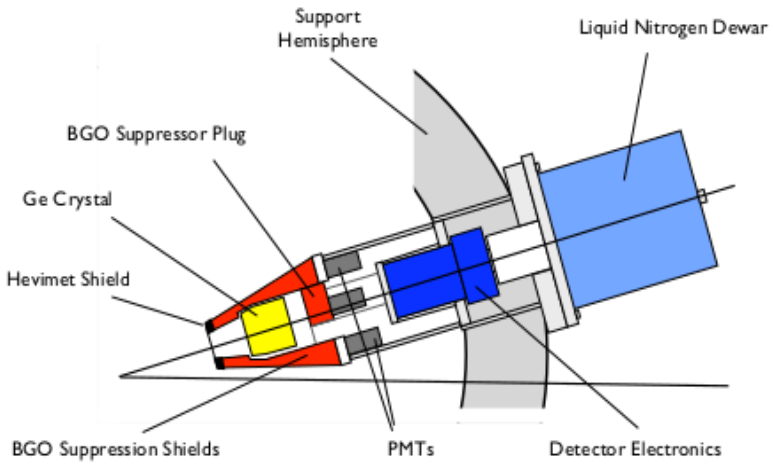

Figure 3.5: Schematic diagram of a single HPGe detector module, adapted from [11]

A total of 20 Compton suppressed clover detectors were in use during the present thesis work. The two- and higher-fold coincidence data were recorded in the fast digital data acquisition system based on Pixie-16 modules [10]. The time-stamped data were sorted in a γ-γ-γ cube and seven angle-dependent γ-γ matrices with a time window of 150 ns using the multiparameter time-stamped based coincidence search (MARCOS) program, developed at TIFR. The working principle and functioning of a HPGe clover detector is briefly discussed below.

3.4.1 Advantages of using HPGe detectors.

In order to resolve the large number of γ-rays from a fusion evaporation reaction, the gamma detector should have an excellent energy resolution. This implies that it should be a semi-conductor detector. Fig. 3.6 shows the mean free path of a photon in Silicon and Germanium. It is obvious that a depletion depth of at least

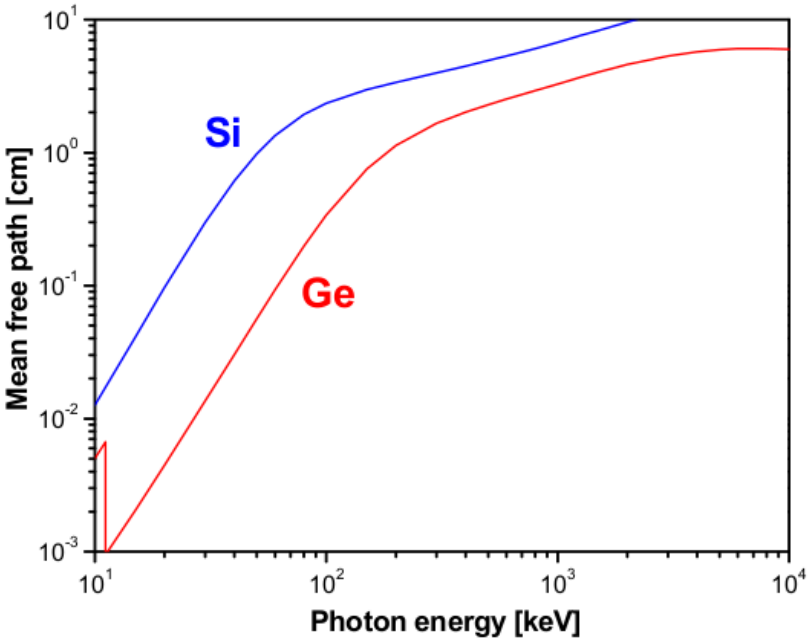

Figure 3.6: Photon mean free paths in Si and Ge.

several cm is required. Due to its higher atomic number, Ge has a much lager linear attenuation coefficient, which leads to a shorter mean free path. Thus, Ge is preferred for high gamma-ray detection ($\sim$ 1 MeV) to achieve higher detection efficiency. For a semiconductor detector, the depletion depth d is given by

$$d \approx \left(\frac{2\varepsilon V_0}{eN}\right)^{1/2} \tag{3.8}$$

where, V_0 is the reverse bias voltage and N represents the net impurity concentration in the initial semiconductor material. If Silicon or Germanium of normal semiconduc-

tor purity is employed, the maximum achievable depletion depth is a few mm even at bias voltages close to the breakdown level. Thus, the impurity concentration should be reduced down to 10^{10} atoms/cm^3 in order to realize intended depletion depths of cm order. At this impurity concentration, a reverse bias voltage of 1 kV can produce a depletion depth of 1 cm. However, the required impurity concentration corresponds to levels less than 1 part in 10^{12}, which is quite challenging.

One way to further improve the net impurity concentration is to compensate the residual impurities with an opposite type impurity material. However, the semoconductor detectors develped by this method are not very stable with temperature and are thus now obsolete.

The other way to improve the net impurity concentration is to add additional refining processes so that the intended purity of the crystal can be met. Techniques have been developed to achieve high purity Ge crystals in this approach and such high-purity Ge (HPGe) detectors are now commercially available. However, no equivalent technique is available for Si yet. As already mentioned, the HPGe detectors were used in our experiments.

3.4.2 HPGe Detector Configuration

An HPGe detector normally comes in planer or co-axial geometry. However, from the photon mean free path in germanium, a detector thickness of the order of 5 cm is required for efficient detection of MeV photons. The maximum depletion depth for the planar detectors is limited to less than 1 or 2 cm. To produce a detector with a thicker depletion depth, a different electrode configuration must be employed. The HPGe detectors dedicated for the detection of MeV photons are, therefore, constructed in coaxial geometry. In this configuration, one electrode is

fabricated at the outer surface of a cylindrical crystal and the other electrode is located at the inner surface of the central hole. In this way, much larger active volumes can be achieved. A close-ended configuration is one in which only part of the central core is removed and the outer electrode is extended over one flat side surface. This configuration is the most common type of commercial HPGe detector.

The electric field in HPGe detectors governs the charge carrier collection process. The signal pulse shape and the timing behavior are consequently dependent on the variation of the electric field strength. The governing equation in a semi-conductor detector is the Poisson's equation:

$$\nabla^2 V = -\frac{\rho}{\varepsilon} \tag{3.9}$$

The charge density ρ is given as ρ = -eN_A for p-type crystals and as $\rho = eN_D$ for n-type crystals. Assuming p-type crystals and true coaxial geometry, Poisson's equation becomes

$$\frac{d^2V}{dr^2} + \frac{1}{r}\frac{dV}{dr} = -\frac{\rho}{\varepsilon} = \frac{eN_A}{\varepsilon} \tag{3.10}$$

It is complicated to solve this equation for partial depletion conditions, so the bias voltage is assumed to be larger than the depletion voltage. Then the boundary conditions can be set as

$$V(r_2) - V(r_1) = V_0 \tag{3.11}$$

where r_1 and r_2 represent inner and outer radii. This leads to the following solution for the magnitude of the electric field

$$E(r) = \frac{eN_A}{2\varepsilon}r + \frac{V_0 - (eN_A/4\varepsilon)(r_2^2 - r_1^2)}{rln(r_2/r_1)} \tag{3.12}$$

the depletion voltage V_d can be calculated from the condition $E(r_1) = 0$, and is given by

$$V_d = \frac{eN_A}{2\varepsilon}\left[\frac{r_2^2 - r_1^2}{2} - r_1^2 ln(r_2/r_1)\right] \tag{3.13}$$

Fig. 3.7 shows the variation of the electric field for an ideal coaxial HPGe detector. The capacitance per unit length of a fully depleted ideal coaxial detector is

$$C = \frac{2\pi\varepsilon}{ln(r_2/r_1)} \tag{3.14}$$

To make the capacitance as low as possible, the radius of the center core r_1 is kept to a minimum.

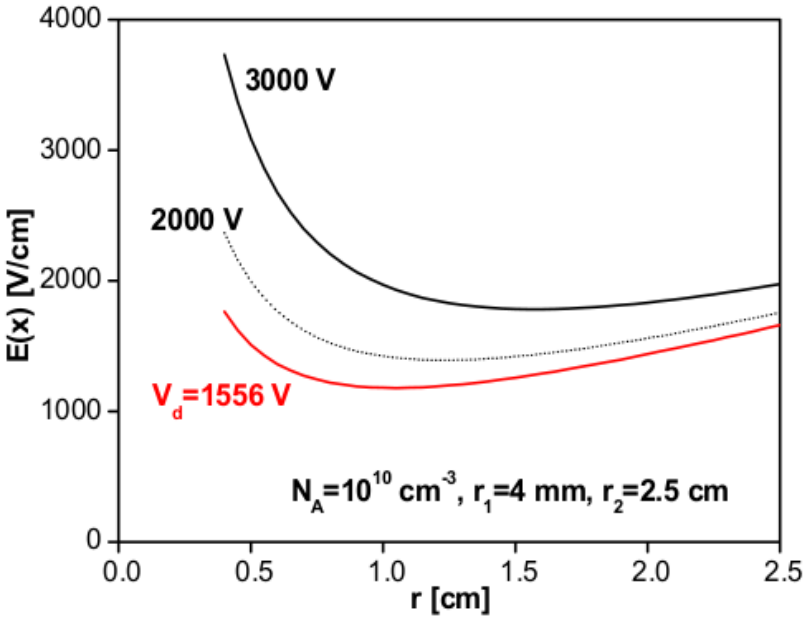

Figure 3.7: Electric field variation of a true coaxial detector. This Fig. is taken from Ref. [12].

For the practical closed-ended coaxial detectors, the Poisson's equation is hard to solve analytically and therefore a numerical method must be employed. An example

of the potential variation and the electric field direction is shown in Fig. 3.8.

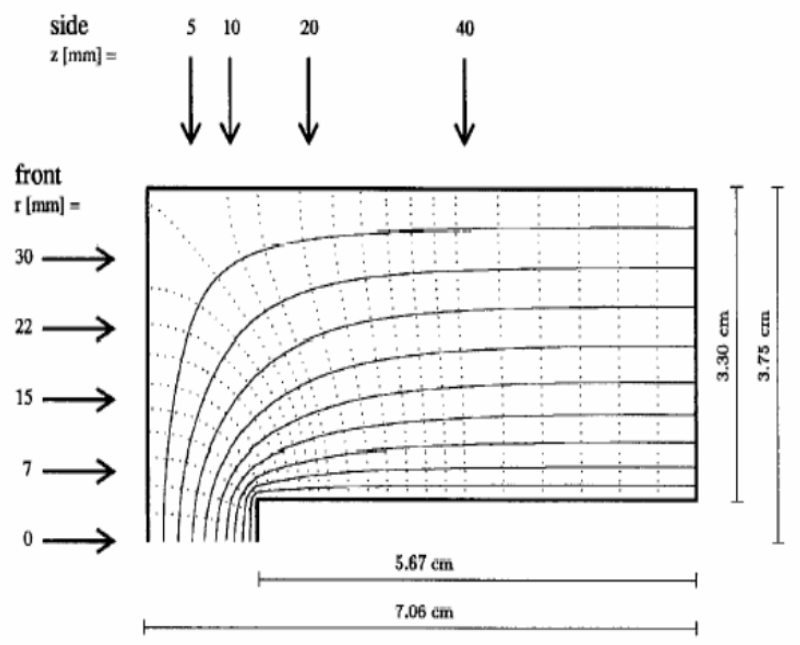

Figure 3.8: Potential and electric field distribution of a close-ended coaxial detector [13].

3.4.3 Mechanism of radiation detection by HPGe detector

In a semiconductor detector, the energy of a γ photon is measured by the number of charge carriers set free in the detector material (here HPGe crystal). The number of electron-hole pairs is proportional to the energy of photon. This happens when the γ photon interacts with the material of the detector through three distinct processes. The relative importance and efficiency of each of these processes is strongly dependent upon the energy of the photon and upon the density and atomic number of the absorbing (detector) medium. These processes are briefly discussed below.

1. **Photoelectric Absorption**: The most probable fate of a photon having energy slightly higher than the binding energy of atomic electrons is photoelectric

absorption. In this process, the photon transfers all of its energy to the electron. The electron will escape its orbit with a kinetic energy equal to the difference between the photon energy and its own binding energy. The electron is absorbed through the ionization process.

2. **Compton Scattering**: The Compton effect is usually the predominant type of interaction for the γ energy between 300 keV to 3 MeV. In this process the photon scatters with an atomic electron and eject it from orbit. The photon retains a portion of its original energy and continues moving in a different direction. Thus, the Compton effect has an absorption component and scattering component. The amount of energy lost by the photon can be related to the angle at which the scattered photon travels relative to the original direction of travel.

   The scattered photon will interact again, but since its energy has decreased, it becomes more probable that it will enter into a photoelectric interaction. The free electron produced by the Compton process may be quite energetic and behave like a beta particle of similar energy, producing secondary ionization and excitation before coming to rest.

   As with ionization produced by any process, secondary radiation are initiated, in this case, by the photo-electron which may have sufficient energy to produce additional ionization and excitation of orbital electrons. Also, filling of the electron vacancy left by the photo-electron results in characteristic X-rays.

3. **Pair Production**: The photons with energy greater than 1.02 MeV, under the influence of the electromagnetic field of a nucleus, may be converted into an electron and a positron. The threshold of 1.02 MeV is equivalent to the rest mass of the electron and positron which is 0.51 MeV each. The Pair production is not a dominant energy loss mechanism for the usual domain of descrete

gamma spectroscopy. The probability of pair production increases with Z of the absorber and with the photon energy.

3.5 Clover detector

The usefulness of a gamma spectrometer is characterized by its energy resolution, efficiency of detection and ability to discriminate gamma rays of interest against the background radiations. In heavy ion induced compound nucleus reactions, the energy resolution is affected by Doppler broadening. So, besides having large efficiency, the gamma detectors should have small opening angle to reduce this broadening. A concept of Clover detectors , consisting of an assembly of four crystals in a common cryostat, have been designed to overcome this problem and yet preserve the high efficiency for the gamma energies in MeV domain. The electrical segmentation of the individual crystals of the Clover detector, a technique reported in Ref. [14, 15], lowers the opening angle and thereby improves the performance of these detectors further.

3.5.1 Clover detector geometry

The Clover detector (from Eurisys Mesures) consists of four closely-packed N-type hyper-pure germanium crystals. The geometry of the crystals inside the vacuum chamber is shown in Fig. 3.9. Each crystal has a quasi-square front face with round edges obtained by tapering the two adjacent faces with an angle of 7° starting at about half of length, and by cutting the two other faces, parallel to the crystal axis, along the whole length. The starting dimensions of the Germanium crystals are 51 mm diameter and 71 mm length. The active volume of the Clover detector is about 470

cm^3 ; which is nearly ∼89% of the original crystal volume. The detector is inserted in a BGO Compton suppressor. These crystals are cooled through a common cold finger. Each crystal has separate outputs for energy and timing.

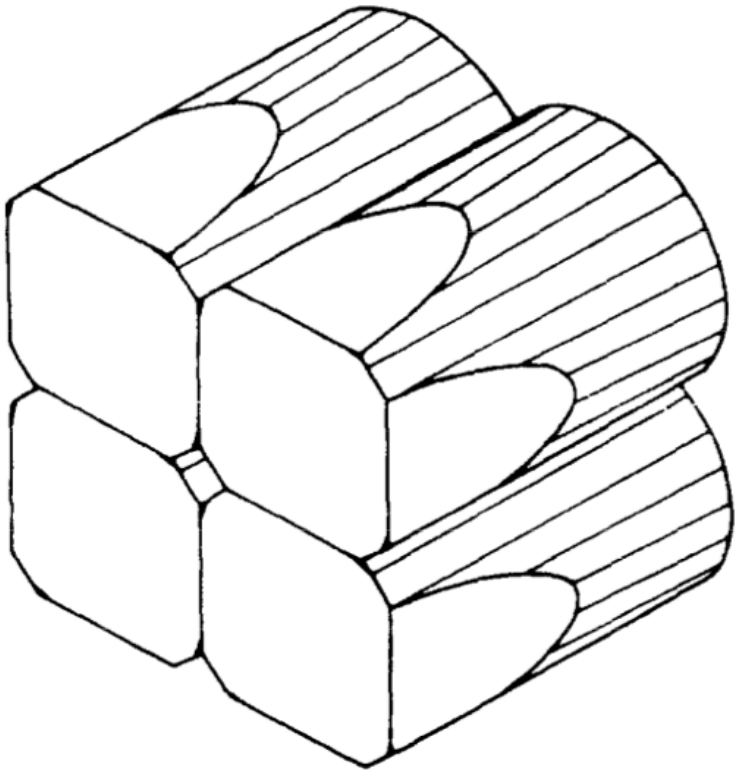

Figure 3.9: Schematic view of the geometrical arrangement of the four individual HPGe crystals inside a clover detector.

Advantages of the clover detector

1. In a clover detector, the four crystals are electrically isolated and there is no physical medium where a gamma ray can lose energy when it is scattered from one crystal to the other. So, a gamma ray may deposit its full energy in a single crystal or a fraction of its energy may be Compton scattered out of the detector or into another crystal of the detector. Thus, by calibrating and adding these energy depositions, it is possible to estimate the total energy of the Compton

scattered gamma ray. The total "full energy peak" efficiency of the Clover detector with the four crystals can be determined by summing the individual contributions in two different ways. There is a finite probability that by adding two simultaneous counts in the background, it is possible to generate a count in the photo-peak. This method of time correlated addition is referred to as the addback mode and the corresponding spectrum is called the *Addback spectrum*. On the other hand, if the spectra from the four crystals are added with out any time correlation, then the resultant spectrum is called the *sum spectrum*. This corresponds to a situation where there are four independent HPGe crystals as there is no photo-peak recovery possible in this case. A typical *sum* and *Addback spectrum* are shown in Fig. 3.10. It is clear from the figure that in case of the *Addback spectrum*, the general background spectrum is lowered and the photo-peak counts are increased with respect to the sum spectrum. This indicates the power of the Addback concept and the utility of a clover detector.

2. In the Clover detector, each crystal is small. So the timing characteristics are much better than that of a single large HPGe crystal of equivalent volume ∼440 cc.

3. The background in the *Addback spectrum* at higher energies will be less than that recorded by a single large volume detector. This is due to the fact a large HPGe detector will detect the higher energy gamma rays as well as the background with same efficiencies while in the Clover detector the background at higher energy is detected with lower efficiency but the photo-peak is reproduced by adding the smaller energies detected at larger efficiency.

4. Since the Clover detector consists of four individual crystals housed in a single cryostat, each of the individual crystals can be considered as a scatterer and the two adjacent crystals as absorbers. This makes Clover detectors sensitive

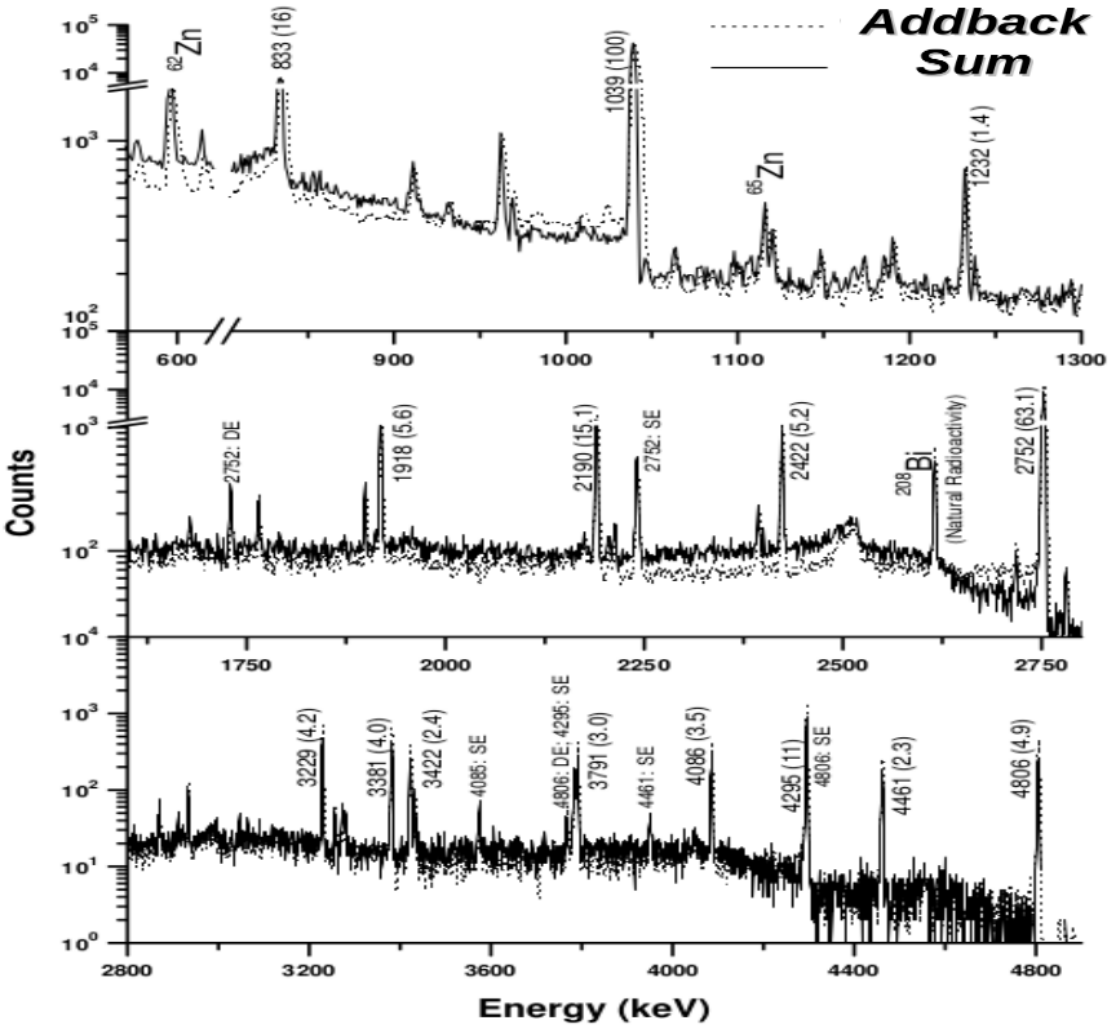

Figure 3.10: The gamma ray spectra (both in addback and direct sum modes) obtained after the irradiation of a sample of natural Cr with 55 MeV ^{16}O beam. The energies of the gamma rays from ^{66}Ga decay are indicated. The relative intensities of these gamma rays are also shown in parentheses. (taken from Ref. [17])

to the polarization of the gamma transitions. Thus, a clover detector can act as a polarimeter, distinguishing the electric or the magnetic nature of the incident photons [16].

In order to further demonstrate the advantages of the addback mode over the direct sum, the relative full energy peak efficiencies for the sum and addback modes have been studied. Fig. 3.11 shows the plots for the two cases. Although these two modes

show more or less similar efficiencies for gamma rays of energies below ∼500 keV; for higher energies, the addback mode shows considerable increase in the efficiency at higher energies due to Compton compensation.

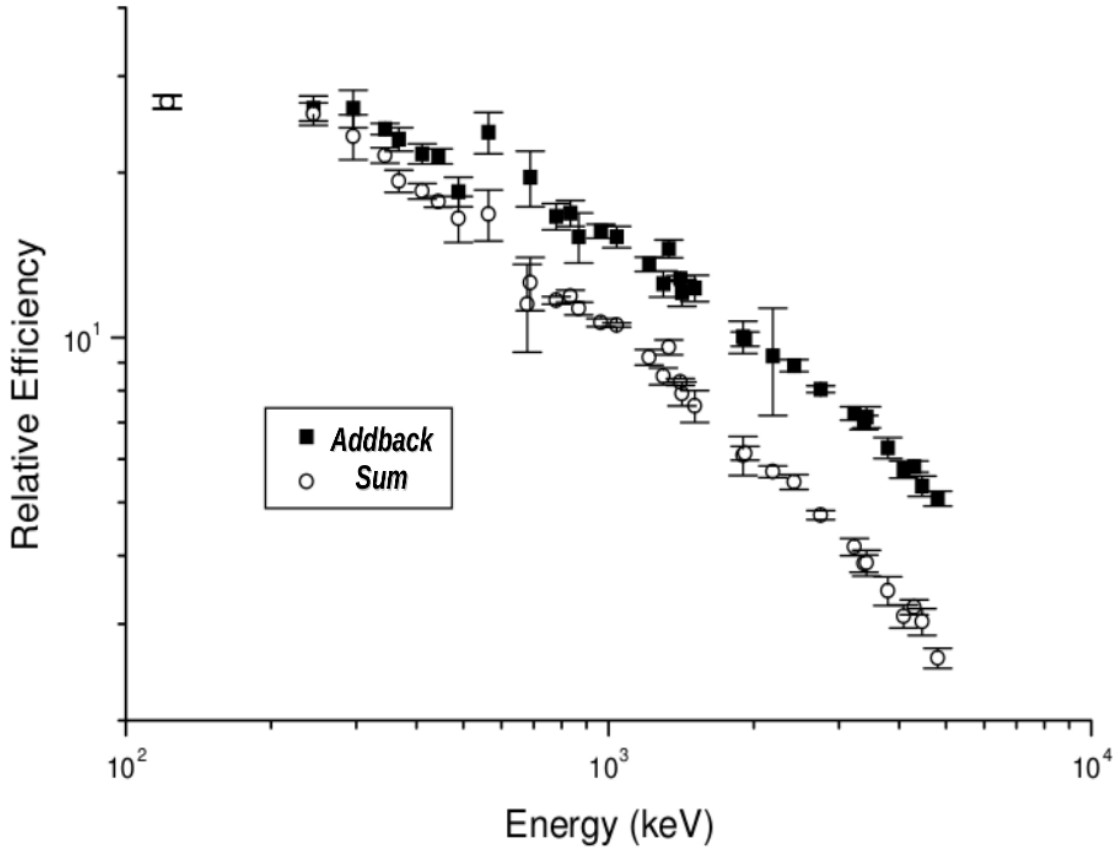

Figure 3.11: Variation of relative efficiency with energy in direct sum and addback modes. (taken from Ref. [17])

The addback factor F, defined as the ratio of the full efficiency in add-back mode over the efficiency in sum mode, is also plotted in Fig. 3.12. The factor at low energies starts from ∼1.0 indicating that the direct and total modes do not differ at low gamma ray energies (≤300 keV) since most of these gamma rays deposit their full energy in one of the crystals only. The factor then increases sharply till ∼2 MeV; where the add-back mode contribution becomes appreciable. The rate of increase is less for higher energy gamma rays although the factor continues to increase steadily

for energies up to 5 MeV.

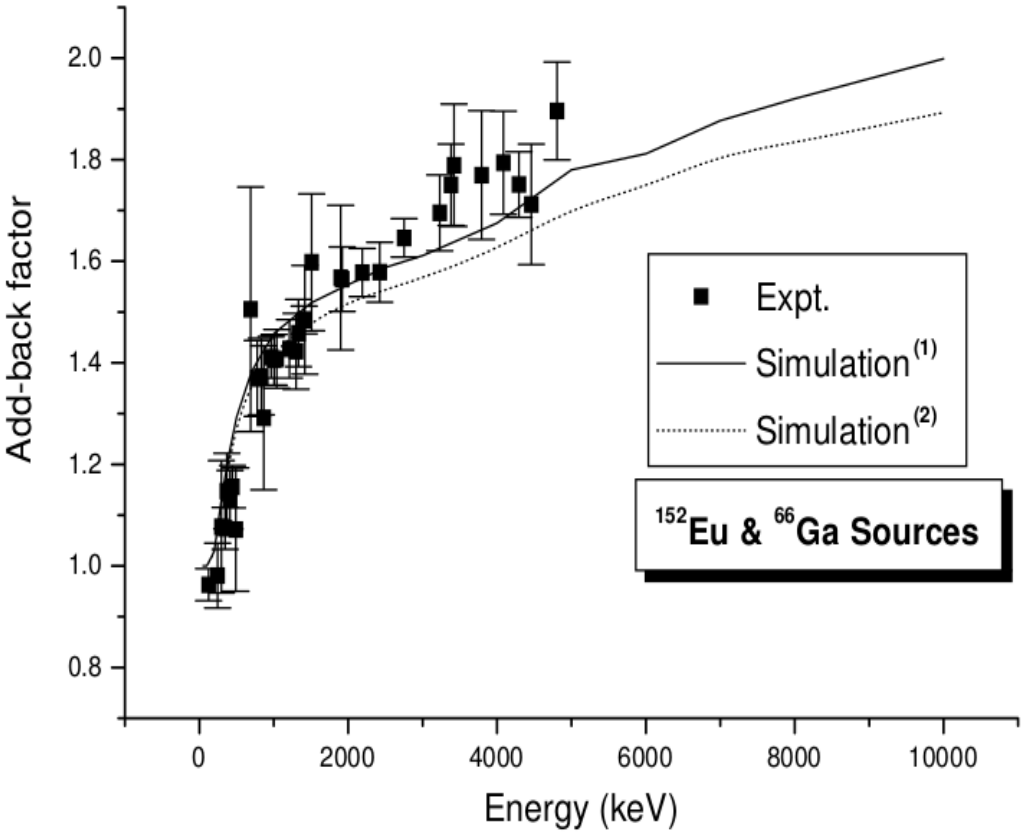

Figure 3.12: Variation of addback factor with energy. (taken from Ref. [17])

3.6 γ ray Spectroscopic Techniques

The HPGe clover detectors of the INGA array generate raw data from the detection of γ rays emitted by the de-exciting nuclei populated during the fusion-evaporation reaction. The various analysis techniques are used to process this raw data in order to generate meaningful spectra and to extract the various spectroscopic information required to understand the nuclear structure of the intended nucleus. These include the initial precise calibrations of the data needed for the addback

procedure and the processes used to create multidimensional data histograms from which spectra are produced and level schemes are built. There are methods to determine the spin and the parity of the excited levels and to measure their lifetimes which are crucial to any physical interpretation. All these techniques were used during the course of this thesis and are discussed below.

3.6.1 Level Scheme Building

The various detectors used in an experiment are first "gain matched", "energy calibrated" and "efficiency corrected" in order to generate useful spectra. As the data recorded are time-stamped, different time windows can be used to define a coincident event and a time correlated data set is generated. This data is stored in matrices or cubes in order to construct the level scheme of the nucleus populated in the experiment. In a 2-dimensional $\gamma\gamma$ matrix, the two gamma energy bins are defined along the x and y-axis (typically 0.5 keV per ADC channel), and is incremented by the number of counts at the energy coordinates for coincident γ-ray pairs. However, in case of backed targets (as in our experiments) where the high spin γ transitions are usually Doppler-broadened and a special matrix is formed by placing an E_γ detected by detectors at 90° along one axis and the other co-incident E_γ from any other detector along the other axis. Then the 90° spectrum obtained with a gate on the all-detector axis, enables us to detect and place these transitions in a level scheme. Fig. 3.13 shows two γ-gated spectra for 90°-vs-all and all-vs-all coincidence. From this figure one can easily appreciate the above argument. This matrix is also used to find the true intensities of the gamma rays which are Doppler shifted.

A 3-dimensional $\gamma\gamma\gamma$ cube contains an additional E_γ axis. For a bin in the cube to be incremented three γ rays must be detected in coincidence. In this case , the

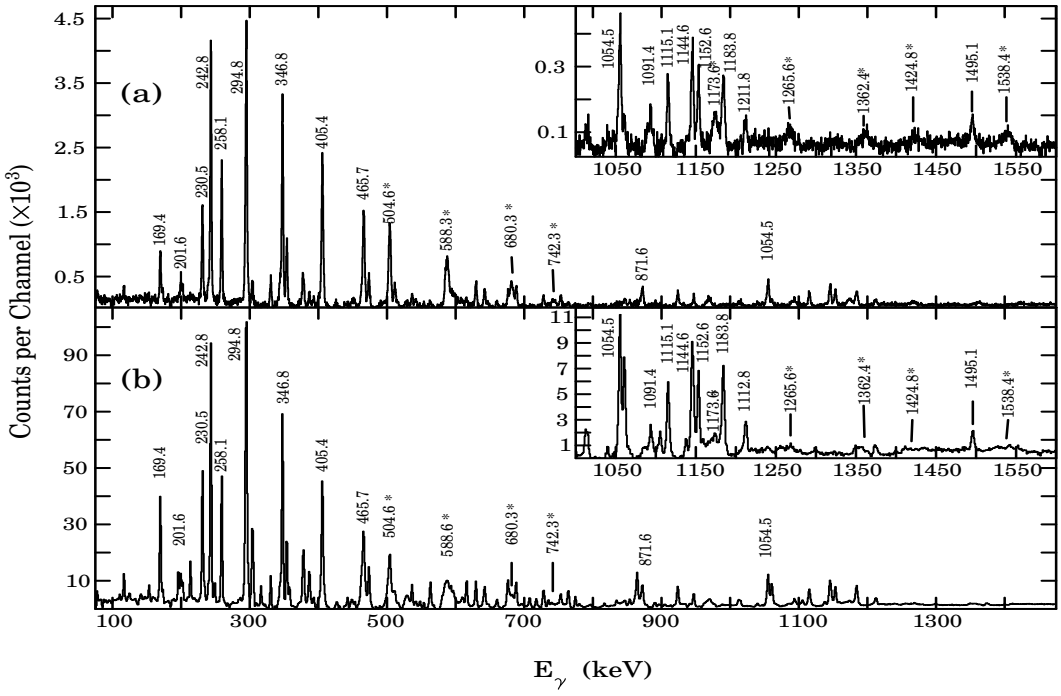

Figure 3.13: Gated spectra for all-vs-all and 90-vs-all ("all" means any detector of the array) detectors are shown. The lines with line-shapes are identifiable only for the 90° projected spectrum (**a**) from 90-vs-all matrix. Lines with asterisk marks are the lines with line-shapes. The gates are placed at 230.5 keV and 258.6 keV in each case which belong to Band 3 of ^{106}Ag (chapter 6).

gamma gates can be set on the two axes of a cube (a double gate) to project a spectrum containing only those γ-ray transitions in coincidence with the both of the γ rays. This multiple gating condition removes the contamination from the gamma-rays coming from the other residual nuclei. In the present thesis work, the 2-dimensional matrices are analyzed using the softwares such as DAMM which is a part of the UPAK software suite [18] while the RadWare [19] was mostly used for the analysis of the cubes. This software allows double gates to be set to study three-fold coincidences. The continuum background is subtracted within the RadWare program using algorithms based on

subtracting multiple background gates in the region of the Compton background [20].

3.6.2 Spin Assignment

The fusion-evaporation reaction makes it possible to measure the *angular distribution* of the de-exciting γ ray transitions since the angular momentum vector ($l = r \times p$) of a compound nucleus is in a direction perpendicular to the reaction plane. Thus, angular distribution can be measured with respect to this quantization axis. However, as the particles evaporate from the compound nucleus, this alignment is perturbed resulting in a Gaussian distribution of the m substate population, centered at $m = 0$ [21]. In the case of an orientated substate population, the probability of a γ ray being emitted at an angle, θ relative to the beam direction is given by [1, 22]

$$W(\theta) = \sum_k a_k P_k(cos\theta) \tag{3.15}$$

where $W(\theta)$ is the gamma-ray intensity measured at angle θ to the beam direction. Here k takes even values less than $2l$ where l is the angular momentum taken away by the emitted photon, $P_k(cos\theta)$ are the standard Legendre polynomials. a_k is called the angular distribution coefficient. This value depends on the substate or m-population distribution and the values of the initial and final state spins [22]. The a_k values can be used to experimentally distinguish between transitions of different multipolarities [22, 23]. In discrete gamma ray spectroscopy, the transition multipolarities are mostly restricted to angular momentum values of 2 or less (mostly $E2$, $M1$ or $E1$ decays are observed). Thus, in this case the Eq. 3.15 takes the form

$$W(\theta) = a_0 \left(1 + a_2 P_2(\cos\theta) + a_4 P_4(\cos\theta)\right) \tag{3.16}$$

where $a_4 = 0$ for a pure dipole transition. By measuring the intensity of a gamma-ray transition as a function of detector angle about the beam direction, a full angular distribution can be obtained from which the values of a_2 and a_4 can be obtained by fitting the distribution to Eqn. 3.16. Similarly, fitting the experimentally observed a_2 and a_4 coefficients for transitions of known multipolarity gives a measure of the degree of substate alignment for that spin. However, the fixed (and often limited) angular granularity of modern gamma-ray arrays coupled to the complexity of the singles spectra, a full angular distribution analysis may not be always possible. Therefore, several techniques have been devised over time to exploit the difference between the dipole and the quadrupole angular distributions so as to assign the spin to the discrete levels of a given nucleus.

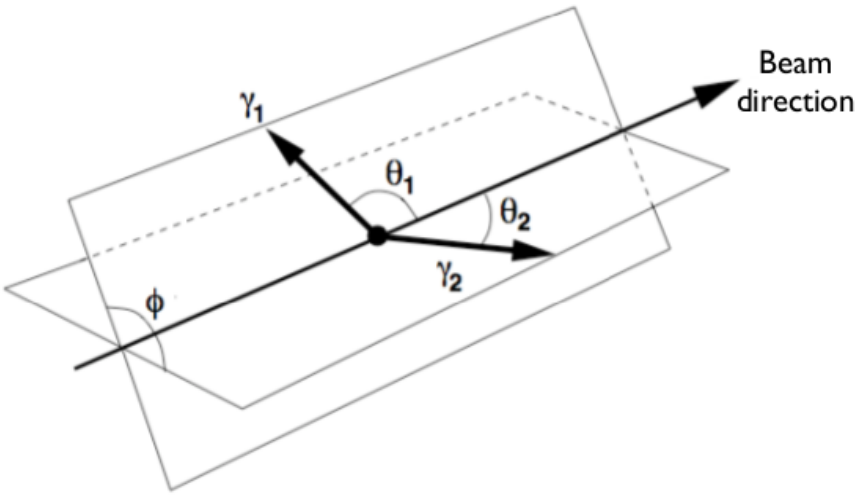

Figure 3.14: Geometry of the γ rays used in DCO ratios.

1. **DCO Ratios:** The Directional Correlations from Oriented states (DCO) is a method that is used to infer the spin differences between states observed by the measurement of the gamma-decay between them [24]. The angular correlation between the two coincident γ rays is shown in the Fig. 3.14 which illustrates

the emission of two coincident γ rays at different angles, θ_1 and θ_2 relative to the beam direction. The angle ϕ is the angle between the two planes defined by θ_1 and θ_2 and the beam axis. The DCO ratio is calculated from experimental data by

$$R_{DCO} = \frac{I^{\gamma 2}_{\theta 1}(gate^{\gamma 1}_{\theta 2})}{I^{\gamma 1}_{\theta 2}(gate^{\gamma 2}_{\theta 1})} \tag{3.17}$$

where $I^{\gamma 2}_{\theta 1}(gate^{\gamma 1}_{\theta 2})$ is the intensity of the coincident gamma (γ_2) measured at angle θ_1, when a gate is placed on the gating transition (γ_1) at an angle θ_2 and vice-versa. A detail discussion of DCO ratio is given in Ref. [25]. In this thesis work, the detectors of the INGA at 90° and 23° rings have been used for DCO measurements. This method for the spin assignment was extensively used during my studies barring certain weak lower level transitions of ^{106}Ag where gated angular distribution method was used which is discussed later.

2. **Anisotropies:** In order to differentiate between the transitions of ΔI=$\pm$1 and ΔI=2 type, measuring the difference between anisotropies is another commonly employed method. The anisotropy A for our detector geometry can be defined by

$$A = 2\left(\frac{W(157^\circ) - W(90^\circ)}{W(157^\circ) + W(90^\circ)}\right) \tag{3.18}$$

where the angles correspond to detector positions. Fig. 3.15 illustrates the theoretically expected value for this anistropy for the three possible multipolarities. Note that the different values of anisotropy (A) for ΔI=$\pm$1 decays depends on the value of the $E2/M1$ mixing ratio (δ).

3. γ **gated angular distribution:** In the case of the INGA array, the γ ray detectors are positioned at various angles with respect to the beam direction,

and thus, the full angular distribution measurements are also possible. But the distribution from the singles data where no coincidence criteria is considered can be obtained only for a few strong transitions. It is not possible to measure directly the angular distributions for the relatively weak γ-ray transitions due to the high density of photopeaks and inadequate single to background ratio in singles spectra. In order to isolate the photopeaks of interest γ ray coincidence gates are used [26]. In this method the angle-dependent matrices were formed by placing gammas detected at a given angle on one axis and the corresponding coincident gamma detected at any other angle on the other axis. This method may be used for the spin assignment of very weak transitions as it employs many detectors than used for R_{DCO} measurements (two angles only). The details of this analysis method as we used it are as follows.

The background subtracted gamma-gated spectra were extracted from the seven angle-dependent matrices. The peak areas were normalized by the number of detectors and efficiencies at each angle. These distributions ($w(\theta)$) were fitted to the angular distribution function given by Eq. 3.16 as shown in Fig. 3.16. In order to establish the validity of this technique for the present INGA geometry, we have determined the angular distribution coefficients from the singles spectra for the lowest strong transitions in ^{105,106}Ag. The results from the two methods were found to agree within $\pm 1\sigma$. Thus, we established the gamma gated angular distribution technique as a valid analysis method for the present INGA geometry. However, it may be noted that this method is not suitable for gamma transitions which exhibit line-shapes.

Fig. 3.16 shows the gated angular distribution of 506, 932 and 1170 keV transitions of ^{106}Ag. It may be noted that no specific bias on the angular distribution has been introduced due to the gamma gating. This is due to the fact that the gating transition is detected in twenty detectors at seven angles

which are evenly spaced over 23°, 40°, 65°, 90°, 115°, 140° and 157° angles. Thus, any angular correlation effect is washed away.

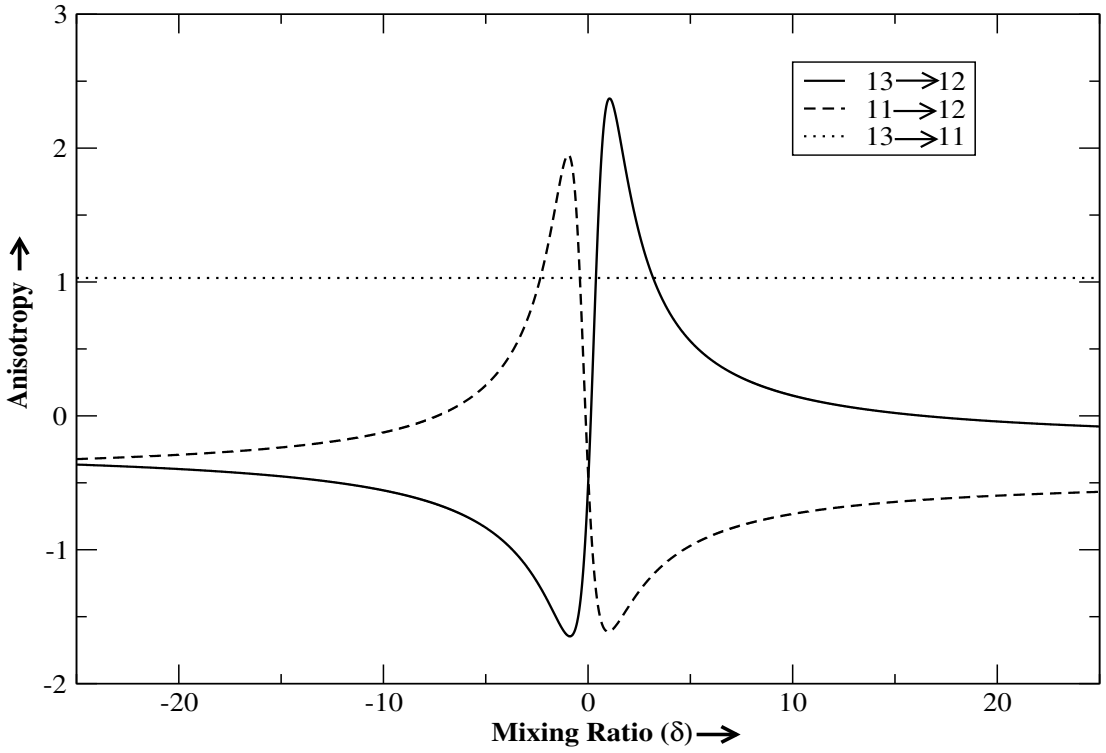

Figure 3.15: Possible theoretical values of the gamma-ray anisotropy as a function of mixing ratio between dipole and quadrupole (δ) for various transitions as indicate in the figure.

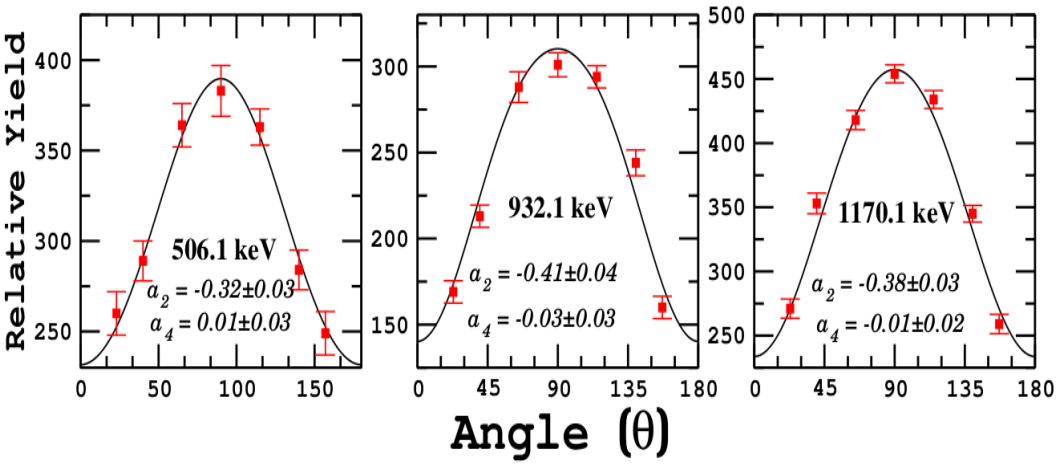

Figure 3.16: Gamma gated angular distribution for the three transitions of ^{106}Ag.

3.6.3 Parity Assignment

The parity of a level can be determined if the polarization of the gamma ray which de-excites that level can be measured and the parity of the final state is known. It has been stated in section 3.5.1 that the HPGe clover detector can be used as a polarimeter [27]. The large total efficiency of the INGA array allows one to carry out coincidence measurements between the 90° CLOVER detectors and the remaining detectors. This method of the Polarizational-Directional Correlation from Oriented nuclei (PDCO) has been described in ref. [28]. This type of analysis uses the fact that the direction of Compton scattering is different for electric and magnetic type transitions. Thus, by comparing the efficiency corrected photo-peak intensities from the 'added-back' spectra for the horizontal and the vertical combinations of the four crystals, the electric or magnetic (or mixed) nature of the transition can be determined. The polarization (P) of a gamma radiation depends on the polarization sensitivity (Q) and the polarization asymmetry (A) through the relation, $P = A/Q$. The polarization asymmetry of a Compton scattered photon has been defined as

[29, 30]

$$A = \frac{a(E_\gamma)N_\perp - N_\parallel}{a(E_\gamma)N_\perp + N_\parallel} \tag{3.19}$$

where $N_\perp$ and $N_\parallel$ denote the number of events scattered in perpendicular and parallel directions to the reaction plane, respectively. The asymmetry correction factor $a(E_\gamma)$ indicates the geometrical asymmetry in the detection system and in our case was determined by

$$a(E_\gamma) = \frac{N_\parallel}{N_\perp} \tag{3.20}$$

using gamma-ray transitions from an unpolarized radioactive source. The asymmetry correction factor $a(E_\gamma)$ as a function of energy has been measured for the INGA geometry using the radioactive ^{152}Eu and ^{133}Ba sources. The factor was observed to remain at an almost constant value of 0.98 over an energy range from 300 to 1400 keV as shown in Fig. 3.17.

The experimental asymmetry, A, for the transitions of interest, is evaluated from the two E_γ - E_γ matrices. One matrix contains events in which one of the gamma rays was scattered inside the clover detector between crystals placed at 90° with respect to the beam axis while a coincident gamma ray are registered in any clover placed at the other angles. The other matrix is almost similar, except for the fact that the gamma rays which are scattered inside the clover between crystals in the direction parallel to the beam axis, are considered.

The polarization detection efficiency Q is determined at each transition energy by using the measured asymmetries A and the theoretically calculated values P_{cal}. In our analysis we calculated the theoretical values of polarization (P_{cal}) from the Eqn.

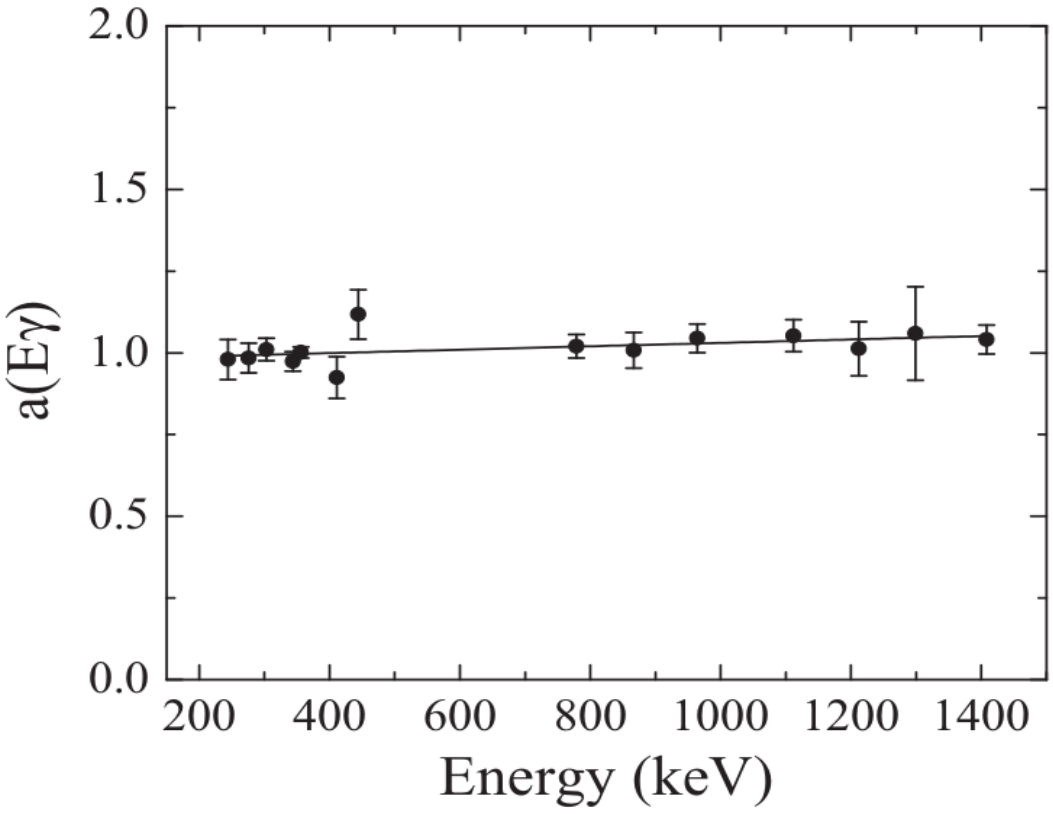

Figure 3.17: The asymmetry correction factor $a(E_\gamma)$ for the clover detector placed at 90° with respect to the beam direction. The solid line shows a linear fit of the data points.

[30]

$$P_{cal} = \pm \frac{3A_{22}H_2 - 7.5A_{44}H_4}{2 - A_{22} + 0.75A_{44}} \tag{3.21}$$

where ± is taken for a transition without (with) a parity change . For a dipole-quadrupole mixed transition, the functions H_λ are given explicitly by

$$H_2 = \frac{F_2(11) - 1.5\delta F_2(12) + \delta^2 F_2(22)}{F_2(11) + 2\delta F_2(12) + \delta^2 F_2(22)} \tag{3.22}$$

and

$$H_4 = -\frac{1}{6} \tag{3.23}$$

The values of the coefficients F_λ are tabulated in the Ref. [31].

The polarization sensitivity Q which was obtained for the present INGA array is plotted as a function of photon energy in Fig. 3.18.

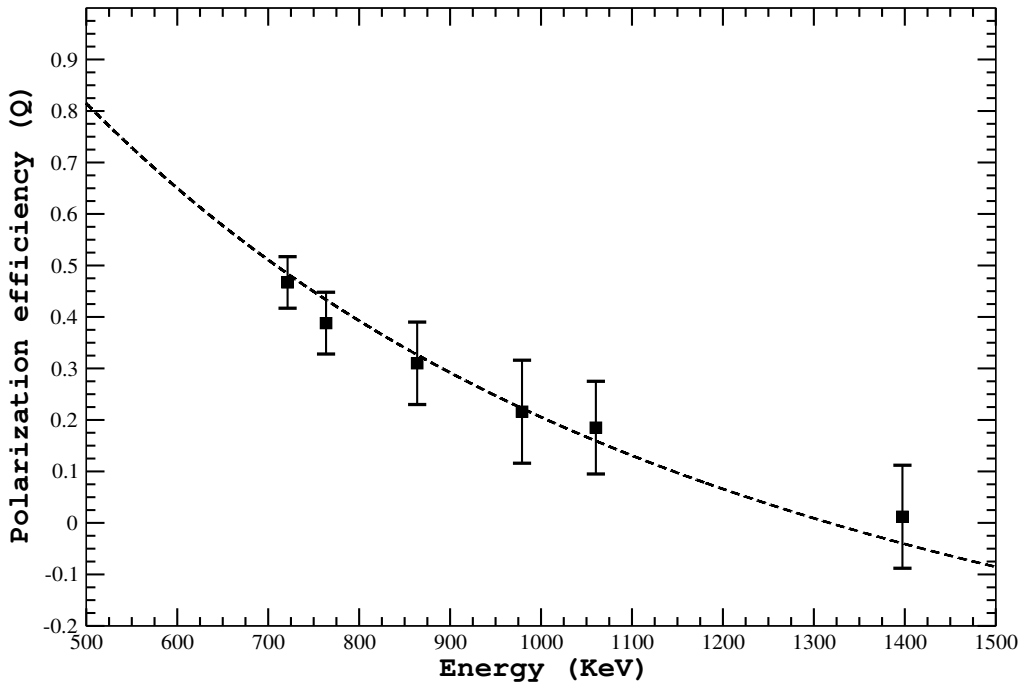

Figure 3.18: The polarization sensitivity as a function of energy for detectors which acted as porimeters in our experiments.

The fit to the experimental values are obtained by using [30]

$$Q(E_\gamma) = Q_0(a + b \times E_\gamma) \tag{3.24}$$

where Q_0 is called the polarization sensitivity for the ideal Compton polarimeter and is defined as

$$Q_0 = \frac{1+\alpha}{1+\alpha+\alpha^2} \tag{3.25}$$

where

$$\alpha = \frac{E_\gamma(\text{keV})}{511}$$

The least-squares fitting of experimental polarization sensitivity $Q(E_\gamma)$ gave $a = 2.0(9)$ and $b = -1.3 \times 10^{-3}$ in keV^{-1}. A positive value of linear polarization (P) is indicative of electric character whereas a negative value indicates magnetic character of the transitions. The linear polarization for a mixed transition is expected to be close to zero.

In a situation where there is an ambiguity between whether a given dipole transition is actually ΔI=+1 or ΔI=$-$1, the results from angular distribution and polarization can be used simultaneously to resolve this issue. Such a situation occurred during the spin assignment of an excited level in ^{106}Ag. The band head spin for Band 3 (chapter 6) was assigned by plotting theoretical values for A_2 from the gated angular distribution and polarization for the possible spin values and were compared with the experimental values. This leads to an unambiguous spin assignment to the band head. This case has been discussed in detail in chapter 6.

3.7 Nuclear Lifetime measurements: Doppler-Shift Attenuation Method

The measurement of the lifetimes of the excited levels populated during the fusion-evaporation reaction are often very crucial for nuclear structure studies. This is because there are only a few observables available that can experimentally be determined in a model-independent way which include the energies of the excited nuclear levels, the gyro-magnetic ratios and the level lifetimes. Various techniques have been developed to measure the level lifetimes ranging from 10^{-14} to 10^{-7} sec. Each method is suitable for a specific time scale. The two common methods used for de-exciting recoiling reaction products include "Recoil Distance Method" and "Doppler Shift Attenuation Method" (DSAM). The DSAM method is useful if the level lifetimes are $\sim 10^{-14} - 10^{-12}$ sec and has been extensively used during this thesis. Thus, this method is discussed in detail.

Principle: The Doppler Shift Attenuation Method exploits the stopping time of the energetic recoiling ions in the high-Z solid backing as a clock for the γ-emitting de-exciting nuclear states. Ideally, we have an ensemble of nuclei excited at t=0 to a state with a sub-picosecond lifetime entering the backing with an initial velocity $v_0/c \sim 10^{-4} - 10^{-1}$. As the recoil velocity gradually decreases with time as a result of electronic and atomic collisions in the backing material, the emitted γ-ray is Doppler-shifted covering an energy range from E_0 to $E_0+\Delta E_\gamma$. The resulting Doppler-broadened line profile thus reflects the correlation between the decay processes and the velocity attenuation of the recoiling ions in the backing. Thus, knowing the stopping power $dE/dx = -M_1(dv/dt)$, one can estimate the nuclear lifetime from the line-shape profile. The simulation of this stopping power is a crucial input to DSAM analysis and should be modeled as realistic as possible since this is identified as one

of the principal sources of uncertainty on the measured level lifetimes.

The Doppler-shifted energy E_s of a γ ray emitted by a recoiling nucleus at velocity v as observed by a detector at an angle θ with respect to the recoil velocity is given by

$$E_s \approx E_0 \left(1 + \frac{v}{c} cos\theta\right) \tag{3.26}$$

where E_0 is the energy of the γ ray in the inertial frame of the recoil. The gamma-ray photo-peak thus has a line-shape depending on the velocity (between v_0 and zero) of the recoil. Measuring the centroid of the total line-shape gives a measure of the average velocity at which the gamma-ray was emitted. The centroid results are usually expressed in terms of a Doppler Shift Attenuation Factor F(τ), where

$$F(\tau) = \frac{v_{av}}{v_0} = \frac{1}{v_0 \tau} \int_0^\infty v(t) exp\left(-\frac{t}{\tau}\right) dt \tag{3.27}$$

where v_0 is the initial recoil velocity and v_{av} is the average recoil velocity when the gamma-ray is emitted.

The slowing down of the recoil as a function of time ($v(t)$) is usually taken from tables of stopping powers such as those by Northcliffe and Schilling or Ziegler [32].

The stopping power is usually separated into two components, electronic and nuclear stopping. In electronic stopping, the recoil slows down due to interactions with atomic electrons in the stopping material. Since the mass of the recoil is much larger than the mass of the electrons, many collisions are required to stop the recoil.

In the nuclear stopping process, the recoils lose energy in a small number of discrete steps due to nuclear collisions. These can cause the nucleus to scatter and alter its direction, which must be accounted for (since a change in direction will alter

the measured, Doppler shifted energy). This is usually modeled by using Monte Carlo simulations of the recoil velocity profiles [33, 34].

In practice, however, it's not just one level but a cascade of excited levels whose lifetime is measured simultaneously by the technique. This introduces lot more complexity to the process of actual measurement. Besides knowing the details of stopping mechanisms that a recoiling nucleus undergoes in the backing, side-feeding intensity at various levels and side-feeding times have to be considered as well. Each of these steps are crucial for an accurate lifetime measurement and are discussed below.

(1) Stopping Power Mechanism: As mentioned above, the recoil looses energy by interactions in the backing which can be classified in two processes. Out of the two processes, electronic and nuclear stopping, which will dominate the total energy loss per unit path length (the *stopping-power*), depends on the moving ion's velocity relative to the medium and thus on its kinetic energy. For high velocities, the electronic stopping dominates the energy loss. The nuclear stopping becomes significant below the Bohr velocity, $v_0 = \alpha c \approx c/137$.

For the interaction with electrons, the charge state of the ion is important, which in turn depends on its velocity in the medium. For velocities $v \approx v_0$, it can be excepted that the ion is completely ionized (fully stripped) and thus has no bound electrons. In this case, the description of the system as the motion of a point charge in an infinite free electron gas is appropriate. The estimation of the stopping-power in this regime can be done with the use of dielectric functions proposed by Lindhard [35, 36] or Mermin [37]. For very low ion velocities, the projectile is not ionized and the energy loss mainly takes place by collisions with weakly bound electrons of the medium. For the calculation of the stopping-power in this regime, an effective density of free electrons is usually assumed.

For velocities between these two extremes, the ion will pick up electrons from the medium and will loose electrons to it in a continuous interplay. Expressions for the stopping-power in this regime have, inter alia, been derived by Lindhard and Scharff [38].

For the nuclear stopping-power, there are also theoretical considerations describing the average behavior of the ions. In combination with the electronic stopping, the Lindhard-Scharøff-Schitt (LSS) theory [39] has been discussed here. This description is usually formulated in scaled, dimensionless variables.

$$\epsilon = \frac{6.49 \times 10^{12} a_f A_1}{Z_1 Z_2 (A_1 + A_2)} E \tag{3.28}$$

$$\rho = \frac{4\pi a_f^2 A_1 A_2}{(A_1 + A_2)^2} N x \tag{3.29}$$

where $a_f = 0.8853 a_b$, with $a_b = 0.529 \times 10^{-10} m$ being the Bohr radius, N denotes the number of atoms per cm^3 in the stopper material, $A_{1(2)}$ and $Z_{1(2)}$ denote the charge and mass number of the projectile (the target material), respectively, and x is the traveled path. The dimension of x is cm and the dimension of E is MeV. The total stopping-power is given by the sum of electronic and nuclear stopping-power. In the limit of low velocities $v < 2Z_1 v_0$, the LSS theory can be approximated by

$$\frac{d\epsilon}{d\rho} = \left(\frac{d\epsilon}{d\rho}\right)_e + \left(\frac{d\epsilon}{d\rho}\right)_n = f_e \kappa \epsilon^{1/2} + \frac{f_n \epsilon^{1/2}}{0.67\phi_n + 2.07\epsilon} \tag{3.30}$$

here, κ is the Lindhard stopping coefficient, f_n , f_e and ϕ_n are fit parameters used to match the LSS theory with experimental findings. Fig. 3.19 shows the evolution of the stopping-power according to equ. 3.30. The empirically determined parameters f_n , f_e and ϕ_n for various target-projectile combinations are tabulated and are provided

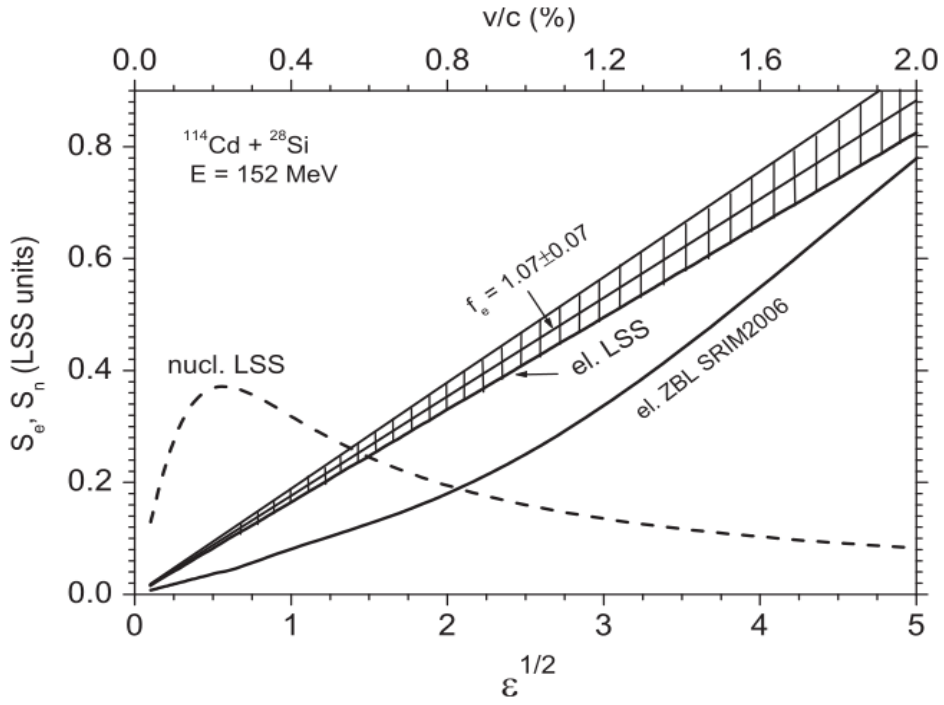

Figure 3.19: Stopping-power of ^{114}Cd in ^{28}Si in dimensionless units of LSS-theory (compare eqs. 3.28, 3.29). The solid lines display the values for the electronic stopping from the Ziegler-Biersack parametrization and from LSS-theory, the dashed line shows the contribution of the nuclear stopping as described by the LSS-theory. The graph with the label "$f_e = 1.07 \pm 0.07$" shows experimental findings for the scaling factor f_e . The figure is taken from [40].

in form of different stopping-power parametrizations, such as those by Northcliff and Schilling in [41] Ziegler and Biersack (SRIM-Codes) [42].

On the other hand, the single collisions of nuclear stopping power induce significant changes in the motion of the ion and the treatment as a continuous processes is a poor approximation. In this case the results are obtained by considering these "hard" collisions as statistical processes with theoretical distributions of energy loss and lateral deflection ("staggering"). An effective treatment of these processes can be achieved with a Monte-Carlo simulation. Detailed description of the models treating the stopping of the ions in matter are given by [43, 44, 40]. An extensive

description of a Monte-Carlo simulation of the stopping processes can be found in the GEANT4 *Physics Reference Manual* [45]. In the present work, the LINESHAPE code by Wells and Johnson [46] has been employed which uses the Monte-Carlo simulation.

(2) Feeding from Higher Levels: When a given level of interest is populated directly without being fed by any other level with comparable lifetime, the rate of decay of the population is given by [47]

$$\frac{dN}{dt} = -(N_0/\tau)e^{-t/\tau} \tag{3.31}$$

where N_0 is the number of nuclei in this state at time $t = 0$ and τ is it's decay lifetime. However, if the state of interest is partially populated in a reaction, then it is not possible to distinguish between γ-decays due to direct population and due to the feed from higher levels. If the lifetimes of the higher levels are comparable or if the higher-lying states are formed with significantly different initial recoil velocities, then the shape of the Doppler-broadened line-shape will be modified for the level of interest.

Fig. 3.20 shows a generalized feeding scheme to a level of interest with lifetime τ_1. The fraction of nuclei that decay per unit time from this level, is

$$f_1(t) = \frac{1}{\tau_1}\left[f_1 e^{-t/\tau_1} + \sum_i 2^n f_i^0 \frac{\tau_1}{\tau_i - \tau_1}(e^{-t/\tau_i} - e^{-t/\tau_1})\right] \tag{3.32}$$

where $f_1^0 = N_1^0/N_0$ is the fraction of nuclei directly populated in the observed state and $f_i^0 = N_i^0/N_0$ for $i = 2$ to n are the fractions that populate the observed state by a single decay from higher-lying levels with lifetimes τ_i. Thus, the calculation of a Doppler-broadened γ-ray line-shape requires a modification of Eq. 3.31 to take account of the feeds coming from other levels.

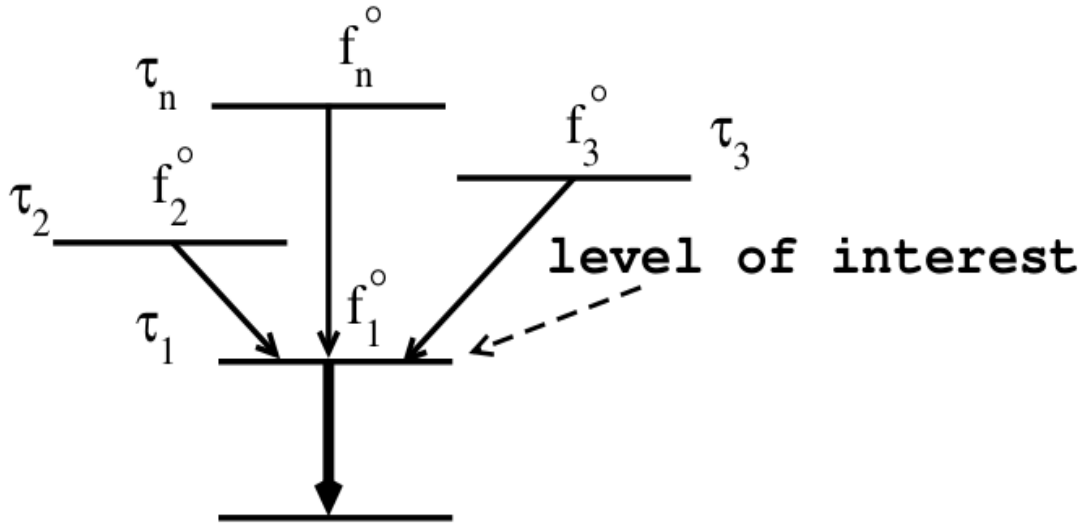

Figure 3.20: A decay scheme to illustrate feeding from higher levels as well as direct feeding of a nuclear level.

The generalized form of eq. 3.27 is

$$F(\tau_1, \tau_2, ..., \tau_n) = \int_0^\infty \left[f_1^0 e^{-t/\tau_1} v(t) + \sum_{i=2}^{n} \frac{e^{-t/\tau_i} - e^{-t/\tau_1}}{\tau_i - \tau_1} v(t) \right] \frac{dt}{v(0)\tau_1}$$

$$= f_1^0 F(\tau_1) + \sum_{i=2}^{n} \frac{\tau_i F(\tau_i) - \tau_1 F(\tau_1)}{\tau_i - \tau_1} f_i^0 \tag{3.33}$$

where

$$F(\tau_i) = \int_0^\infty \frac{v(t)}{v_0 \tau_i} e^{-t/\tau_i} dt$$

$$f_1 + \sum_{i=2}^{n} f_i = 1$$

The lifetimes of the state of interest can be determined provided the lifetimes τ_i and the branching fractions f_i^0 for all levels involved are known. It is assumed that the angular distributions and initial recoil velocities are the same whether the level is fed directly or from another level.

(3) Side feeding, Fit to Q_t and Error estimation: For an excited level of a band, the unobserved intensity (difference of the intensity at the level of interest and at the immediate higher level) is assumed to originate from a band with an average transition quadrupole moment Q_{sf} . Energies in the side-feeding bands are calculated from the following equation.

$$\mathcal{J}^{(2)} = I\left[\frac{d^2E}{dI^2}\right]^{-1} = \frac{dI}{d\omega} = \mathcal{J}^{(1)} + \omega\frac{d\mathcal{J}^{(1)}}{d\omega} \tag{3.34}$$

$$\approx \frac{4}{E_\gamma(I+2 \longrightarrow I) - E_\gamma(I \longrightarrow I-2)}$$

where $\mathcal{J}^{(2)}$ is the Kinematic moment of inertia and is assumed to be the same as the band of interest. The trial value of the transition quadrupole moment (Q_t) for the level of interest together with the input information on the transition energies and relative intensities within the band are used to calculate τ for each state using the following equation.

$$\tau = B_r\frac{821.0565}{Q_t^2E_\gamma^5\langle IK_{20}|I-2K\rangle^2} \tag{3.35}$$

where τ is in femtoseconds, B_r is the branching ratio of the level, $\langle IK20|I2K\rangle$ is the Clebsch-Gordan coefficient for the transition with a value of roughly $(3/8)^{1/2}$, for high spin levels Q_t is in electron-barns and E_γ is in MeV. To simulate decay times in an individual nucleus, the side-feeding band is chosen to generate a random decay time

for each consecutive state based on its average lifetime τ. In this way, the program is able to calculate an average F(τ) curve for a large set of nuclei with realistic formation and decay properties for the initial trial values of Q_t. This is done for each level of the band concerned. When the calculation is complete, the χ^2 for the trial parameters is

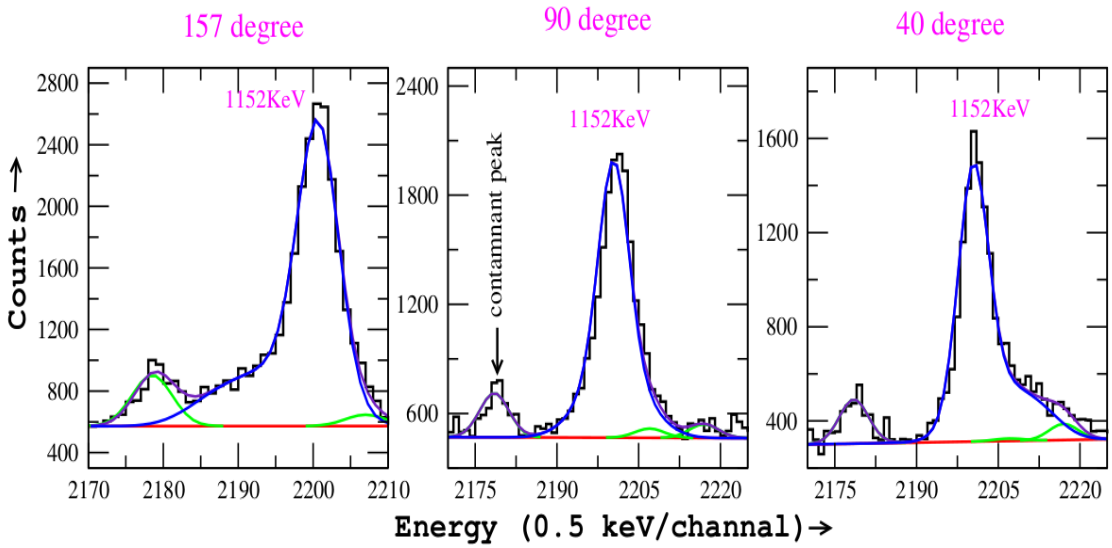

Figure 3.21: Typical experimental line-shapes and the respective fits using the LINESHAPE code by Wells and Johnson. The Red color represents the backgroung, blue is the fit to the line-shape, green to the contaminant peak(s) and the brown is the fit to the total experimental data.

calculated for the experimental and simulated F(τ). The calculation is then repeated with different set of parameter values while a χ^2 minimization algorithm attempts to find the best fit for Q_t and Q_{sf} values. Both the SIMPLEX and MIGRAD algorithms from the MINUIT statistical analysis package [48] are used for this purpose.

Fig. 3.21 shows the results of a typical line-shape analysis for a 1152 keV transition. The left, middle and the right panels show the line-shapes at backward (157°), 90° and forward 40° angles, respectively. The solid line is the best fit to the observed line-shape. These fits are carried out simultaneously so as to minimize the error on the estimated Q_t

Once the best-fit parameters have been obtained, their uncertainties are estimated. The uncertainties in the lifetime measurements are derived from the behavior of the χ^2 in the vicinity of the minimum (second column in Table 3.1). The second source of uncertainty in this measurement are due to the uncertainty in the side-feeding intensity which originate from the uncertainties in the intensities of the top-feeding and the feedout γ-transitions for the level of interest (third column). This is estimated by finding the level lifetimes for the extremum values of side-feeding intensities. The third source is the estimation of the side-feeding time (fourth column). This uncertainty has been estimated by varying the side-feeding time by $\pm$20%. The total statistical uncertainty (fifth column) is calculated by adding the uncertainties due to line-shape fitting, side-feeding intensity and the side-feeding lifetime in quadrature. However, it should be noted that this uncertainity does not include the systematic uncertainty which arises due to the choice of the stopping powers used for the present target-backing combination. This uncertainty varies between 1% to 15% depending on the extant of line-shape that a given gamma photon experiences. These error contributions in a typical quadrupole band of ^{105}Pd studied during this work is tabulated in the table below.

Table 3.1: The contribution to error from various sources which include level lifetime, side-feeding quadrupole moment, intensity and from the choice of stopping-power for ^{105}Pd. For a magnetic band, the contribution to statistical error also comes from the mixing ratio between $E2$ and $M1$ contributions to a $\Delta I = 1$ transition.

I^π	τ(%error)	I_γ(%*error*)	Q_{sf}(% error)	stas. (% error)	sys. (% error)
$33/2^+$	2.4	1.0	1.4	3.0	1.3
$37/2^+$	4.2	1.3	1.0	4.3	2.3
$41/2^+$	5.6	1.5	6.3	8.4	4.7
$45/2^+$	6.2	2.9	9.6	11.7	6.8
$49/2^+$	7.2	9.3	8.7	14.6	9.7
$53/2^+$	8.0	13.3	11.3	19.2	14.3

It is to be noted that if a line-shape can be extracted from a top gate, then the uncertainties due to the side-feed vanishes. Thus, this leads to more accurate

estimation of level lifetime. However, in most of the cases this extraction for the high spin levels is limited by statistics.

The following three chapters report the experimental results on ^{104,105}Pd and ^{106}Ag which have been obtained by the techniques described in this chapter.

Bibliography

[1] H. Ejiri and M. J. A. de Voigt, *Gamma-Ray and Electron Spectroscopy in Nuclear Physics*, Oxford University Press, New York, (1989).

[2] S. Cohen, F. Plasil, and W. Swiatecki, Annals of Physics **82**, 557 (1974).

[3] R. Bass, Nucl. Phys. A **231**, 45 (1974).

[4] T. Lauritsen et al., Phys. Rev. C **62**, 1 (2000).

[5] J. M. Blatt and V. F. Weisskopf, Theoretical Nuclear Physics (Dover, ADDRESS, 1991).

[6] A. Gavron, Phys. Rev. C **21**, 230 (1980).

[7] J. Wilcyński, Nucl. Phys. A, **216**, 386 (1973).

[8] S. Muralithar et al., Nucl. Instrum. Methods A **622**, 281 (2010).

[9] D. M. Cullen, 'EFFIT', private communcation.

[10] R. Palit et al., Nucl. Instrum. Methods Phys. Res., Sect. A **680**, 90 (2012).

[11] P. J. Nolan, F. A. Beck, and D. B. Fossan, Annual Review of Nuclear and Particle Science **44**, 561 (1994).

[12] G. F. Knoll, Radiation detection and Measurement (Third Edition, 2012), page 412.

[13] Th. Kröll et al., Nucl. Intstr. and Meth. A **371**, 489 (1996).

[14] S.L. Shepherd et al., Nucl. Instr. and Meth. A **434** 373 (1999).

[15] S. Bouneau et al., Nucl. Instr. and Meth. A **443** 287 (2000).

[16] Jones, P.M. Nucl. Instr. Meth. Phys. A **362**, 556 (1985).

[17] M. Saha Sarkar et al., Nucl. Instr. and Meth. in Physics Research A **491** 113 (2002).

[18] W. T. Milner,"UPA" The Oak Ridge Data Analysis Package, private communcation.

[19] D. C. Radford, Nucl. Instr. and Meth. in Physics Research A **361**, 297 (1995).

[20] D. C. Radford, Nucl. Instr. and Meth. in Physics Research A **361**, 306 (1995).

[21] T. Yamazaki, Nuclear Data Sheets. Section A **3**, 1 (1967).

[22] E Der Mateosian and A.W. Sunyar, Atomic Data and Nuclear Data Tables 13 407 (1974).

[23] B. Crowell et al, Phys. Rev. C **45** 1564 (1992).

[24] K.S. Krane, R.M. Steffen and R.M. Wheeler, Nuclear Data Tables **11** 351 (1973).

[25] A. Krämer-Flecken et al., Nucl. Inst. and Meth. in Physics Research Section A: Accelerators, Spectrometers, Detectors and Associated Equipment **275**, 333 (1989).

[26] E. Ideguchi et al., Phys. Rev. C **81**, 034303 (2010).

[27] P.J. Nolan, F.A. Beck, D.B. Fossan, Ann. Rev. Nucl. Part. Sci. **44** 561 (1994).

[28] Ch. Droste, S.G. Rohozinski, K. Starosta, T. Morek, J. Srebrny, P. Magierski, Nucl. Instr. and Meth. A **378** 518 (1996).

[29] K. Starosta et al., Nucl. Instrum. Methods Phys. Res. A **423**, 16 (1999).

[30] J. K. Deng et. al., Nucl. Instrum. Methods Phys. Res. A **317**, 242 (1992).

[31] Muri naga's book.

[32] J.F. Ziegler, Handbook of Stopping Cross-Sections For Energetic Ions in All Elements (Pergamon, New York, 1980).

[33] W.M. Currie, Nucl Inst. Meth. **73** 173 (1969).

[34] J. Bacelar et al. Phys. Rev. Lett. **57** 3019 (1986).

[35] On the properties of a gas of charged particles, J. Lindhard, Mat. Fys. Medd. Dan. Vid. Selsk. **28** (8) (1954).

[36] Stopping power of electron gas and equipartition rule, J. Lindhard, A. Winther, Mat. Fys. Medd. Dan. Vid. Selsk. **34** (4) (1964).

[37] Lindhard Dielectric Function in the Relaxation-Time Approximation, N.D. Mermin, Phys. Rev. B **1** 2362 (1970).

[38] Energy Dissipation by Ions in the keV Region, J. Lindhard, M. Scharff, Phys. Rev. **124**, 128 (1961).

[39] Range Concepts and Heavy Ion Ranges, J. Lindhard, M. Scharff and H. E. Schiøtt, Mat. Fys. Medd. Dan. Vid. Selsk. **33** (14) (1963).

[40] E. O. Lieder *et al.*, Nucl. Inst. and Meth. in Physics Research A **607**, 591-599 (2009).

[41] Range and Stopping-Power Tables for Heavy Ions, L.C. Northcliffe, R.F. Schilling, Nuclear Data Tables A **7** 233 (1970).

[42] The Stopping Power and Range of Ions in Matter, vol. 1, J.F. Ziegler, J.P. Biersack, V. Littmark, Pergamon Press, New York (1985).

[43] Lifetime Measurements of excited nuclear Levels by Doppler-shift Methods, T. K. Alexander, J. S. Foster in Advances in Nuclear Physics vol. 10, M. Banger and E. Vogt (Hrsg.), Plenum Press, New York (1978)

[44] Stopping power in perspective, P. Simgund, Nuclear Instruments and Methods in Physics Research B **135**, 1 (1998). lineshape analysis, E. O. Lieder et al., Nuclear Instruments and Methods in Physics Research A **607**, 591 (2009).

[45] Physics Reference Manual, Version:geant4 9.4, http://geant4.web.cern.ch/geant4/support/userdocuments.shtml (2010).

[46] J. C. Wells and N. R. Johnson, Oak Ridge National Laboratory Report No. ORNL-6689, 1991.

[47] Erich Vogt and Michel Baranger, ADVANCES IN NUCLEAR PHYSICS (Springer Science+ Business Media, LLC, 1968).

[48] F. James and M. Winkler, MINUIT User's Guide, (2004).

Chapter 4

Anti-magnetic Rotations in ^{104}Pd

4.1 Introduction

The even-even ^{104}Pd has 46 protons and 58 neutrons. Thus, the valence protons are in $g_{9/2}$ orbital and the neutrons are in $g_{7/2}$, $d_{5/2}$ and $h_{11/2}$ orbitals if we assume ^{90}Zr as the core.

The ground state (GS) band of this nucleus is a 0-qp positive parity band but at higher spins, the neutron and proton alignments are expected. But these alignments will not change the parity of the GS band. However, the two quasi-neutron bands of ^{104}Pd can have negative parity as they might arise from $h^1_{11/2} \times (d_{5/2}, g_{7/2})^1$ configuration. It may be noted that ^{104}Pd is the isotone of ^{106}Cd where the antimagnetic rotation was identified for the first time [1] and was later also established as a mode of excitation in ^{108,110}Cd [2, 3]. In all the three cases, the yrast states above $I^\pi = 16^+$ originate due to AMR. For this mode of excitation, two magnetic subsystems are formed by $\pi g^{-2}_{9/2} \times \nu[h^2_{11/2}, g^2_{7/2}]$ configuration and the transverse magnetic moments of the two subsystems are anti-aligned. This same configuration can lead to the high

spin states in the positive parity yrast band of ^{104}Pd. Thus, this is the best case to search for AMR in a nucleus other than Cadmium. In previous searches, the indications of AMR bands have been found in ^{100}Pd [4], ^{101}Pd [5] and ^{144}Dy [6]. But due to the absence of the lifetime measurements, the bands in these nuclei could not be identified with AMR.

In a recent publication, D. Sohler *et. al.* [7] have reported the detailed high spin level structure of ^{104}Pd. The positive parity yrast band was established up to $I^{\pi} = 26^{+}$. In addition, four more high spin negative parity bands were also reported. However, none of the level lifetimes were measured.

This chapter reports the lifetime measurements of the high spin levels of ^{104}Pd. These measurements are essential to understand the mechanisms of angular momentum generation in these bands.

4.2 Experiment

In order to populate the high spin states of ^{104}Pd, the 63 MeV ^{13}C beam delivered by 14-UD Pelletron at Tata Institute of Fundamental Research (TIFR), was bombarded onto a 1 mg/cm^2 enriched ^{96}Zr target with ^{206}Pb backing of 9 mg/cm^2 thickness. The de-exciting γ rays were detected using the Indian National Gamma Array (INGA) [8] which consisted of 18 Compton suppressed clover detectors. The two and higher fold coincidence data were recorded by fast digital data acquisition system based on Pixie-16 modules [9]. The corresponding time stamped data were sorted in a γ-γ-γ cube and the various types of γ-γ matrices as discussed in the chapter 3. The count rate of the INGA array was about 850 Hz. The peak-to-Compton ratio with BGO was measured to be about 0.41.

4.3 Experimental Methods

The $\gamma - \gamma - \gamma$ cube was used to established the low lying levels of ^{104}Pd with the help of the RADWARE program LEVIT8R [10]. It was also used to determine their relative intensities. The two samples of double gamma gated spectra are shown in Fig. 4.1. However, the $\gamma - \gamma - \gamma$ data were not useful to establish high spin

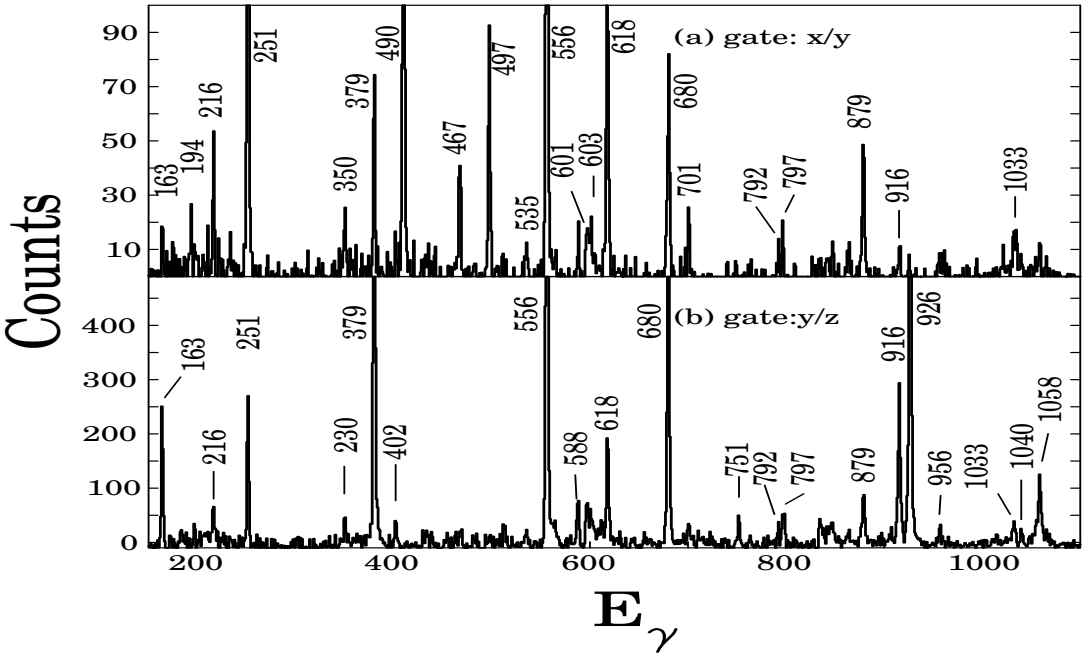

Figure 4.1: Double gated spectra from cube. The gates lists used are denoted by x,y and z such that x = 768 keV, y = 1168 keV and z = 739 keV + 651 keV for each spectrum. The high spin transitions for the bands D, E and F can be identified from spectrum (a), while for bands C, D and E from spectrum (b). A x/y gating condition demands a triple coincidence of a gamma with the gammas in the list x and in the list y.

states which de-excite through γ-rays which exhibit Doppler-shifted line-shapes. An asymmetric 90°-vs-all γ-γ matrix was constructed by placing the γ-energy detected

at 90° along one axis and the coincident γ-energy detected at any other angle along the other axis. The 90° projections of different γ-gates on this matrix were used to extend the level scheme to higher spins and to measure the corresponding relative intensities. Fig. 4.2 shows three typical gated spectra from this matrix and a number of high energy transitions are identified.

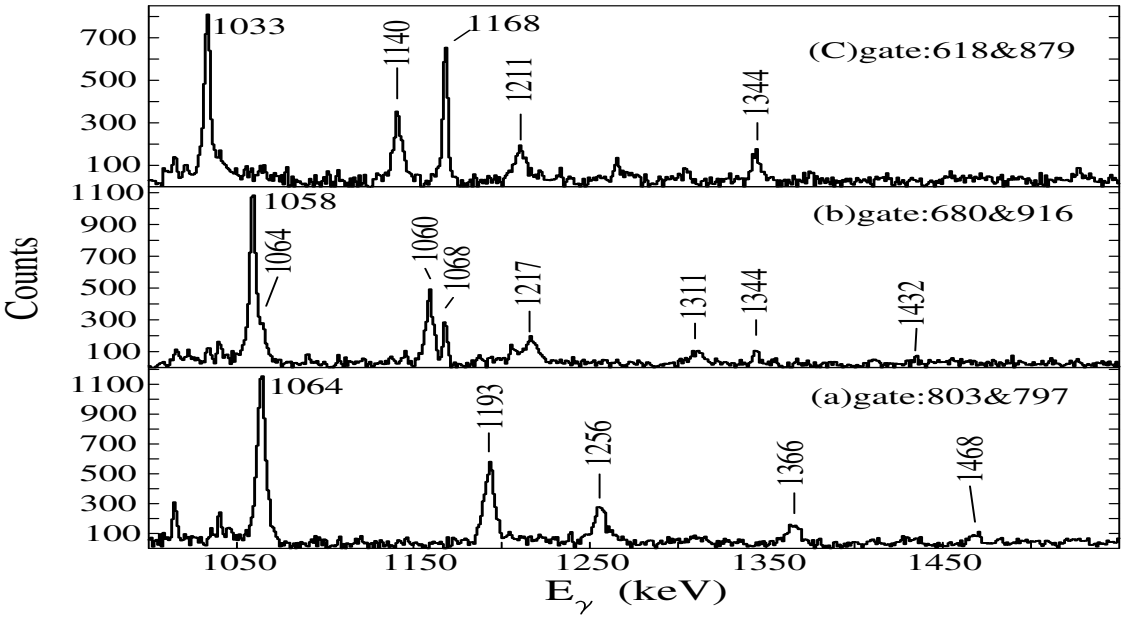

Figure 4.2: The 90° projected gamma gated spectra for Band 1, Band 2 and Band 3 (Fig. 4.5).

The intensities, DCO and polarization values of the different transitions are given in Table 4.2. The details of these analysis techniques have been discussed in chapter 3. A plot of the measured DCO and PDCO values as a function of the gamma energies are shown in Fig. 4.3 and 4.4, respectively. The partial level scheme of ^{104}Pd is shown in Fig. 4.5 where the widths of the transitions are proportional to their

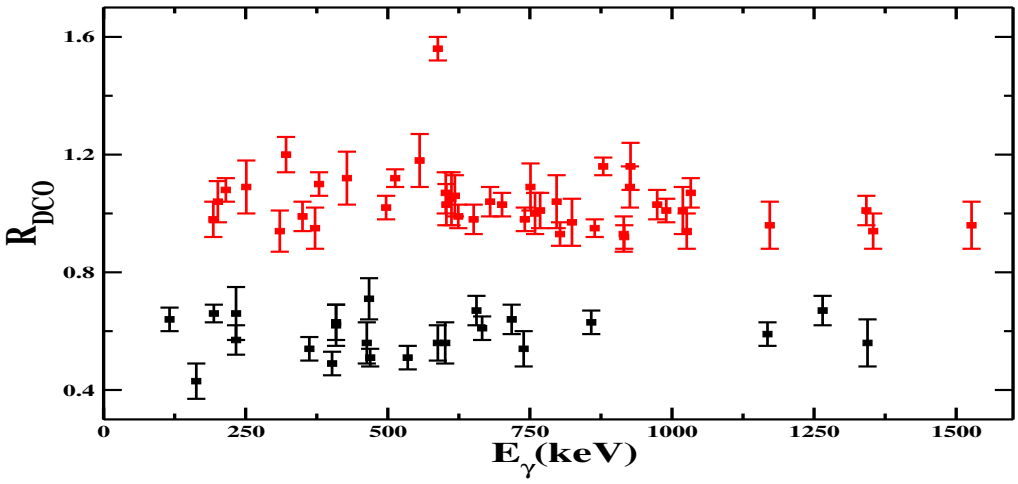

Figure 4.3: The DCO ratio values as a function of the gamma energy as measured for the various transitions of ^{104}Pd. The red color corresponds to transitions with quadrupole nature while the black color corresponds to the transitions with dipole nature.

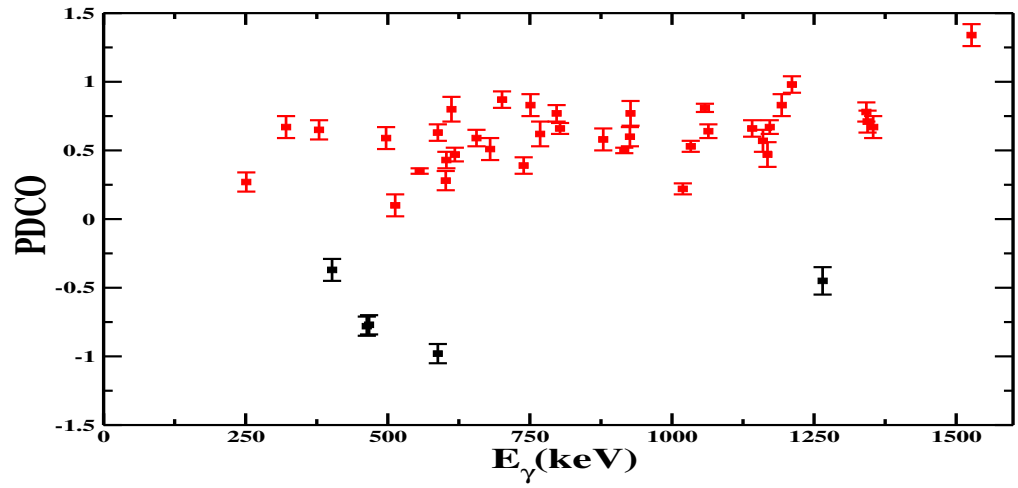

Figure 4.4: The PDCO values as a function of the gamma energy for the various transitions of ^{104}Pd. The red color corresponds to transitions with electric nature while the black color corresponds to the transitions with magnetic nature.

relative intensities. The present level scheme is in a good agreement with the earlier report [7].

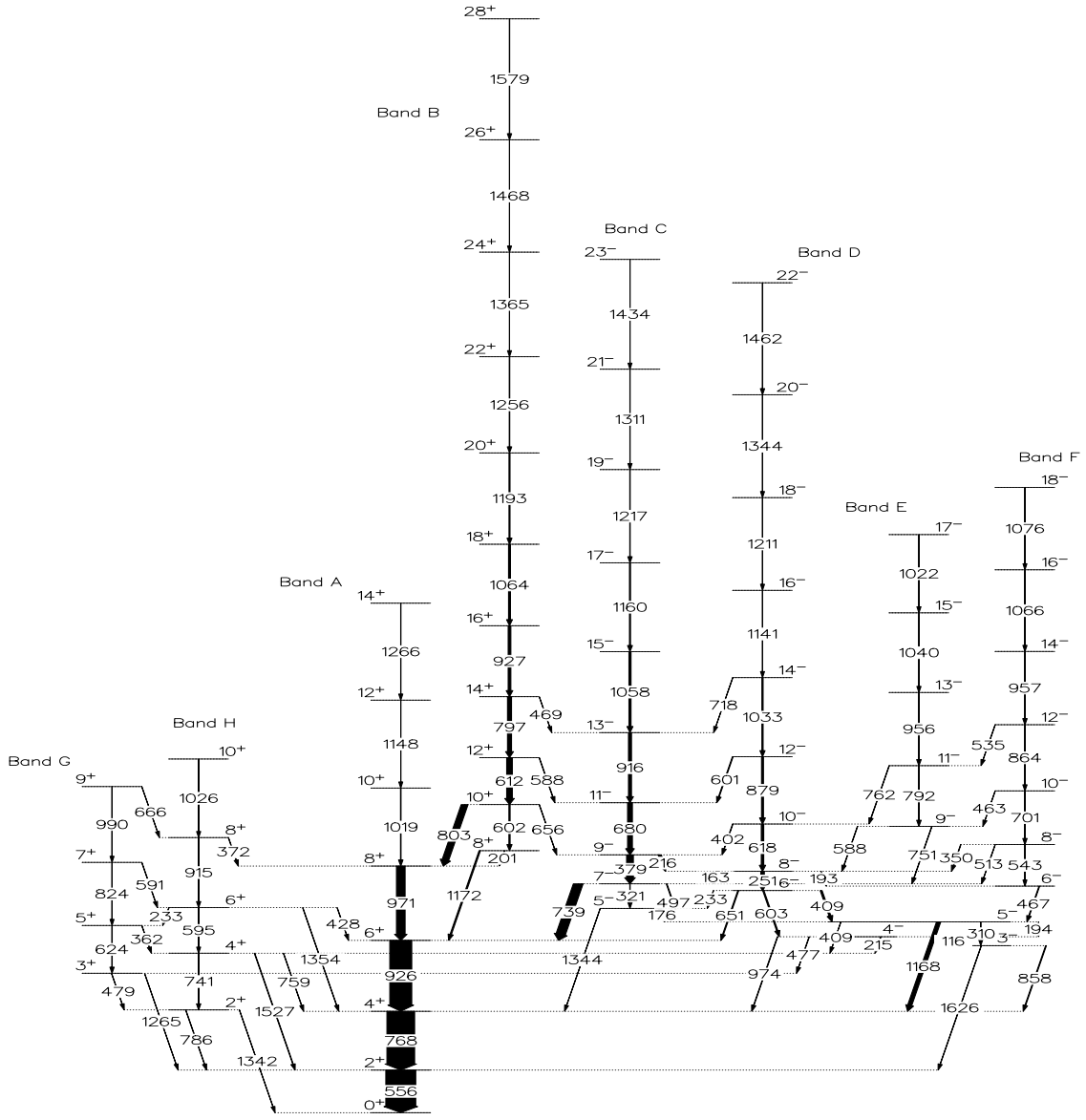

Figure 4.5: The partial level scheme of ^{104}Pd established by the present work. The γ transitions are in keV.

The MARCOS (referred in chapter 3) was also used to construct two more angle-dependent γ-γ asymmetric matrices for the 40° and 157° angles. These two matrices were used to extract the line-shapes for Band 2, Band 3 and Band 4. These line-shapes of different high spin states of ^{104}Pd were fitted by the theoretical line-shapes generated using the LINESHAPE analysis code developed by Wells and Johnson [11]. The procedure of this technique involves the simulation of the stopping power of the

various recoils in the backing, handling the side-feed to each level concerned and the side-feeding Q_t's. The procedure adopted in the present case and the associated uncertainties have been discussed in detail in chapter 3.

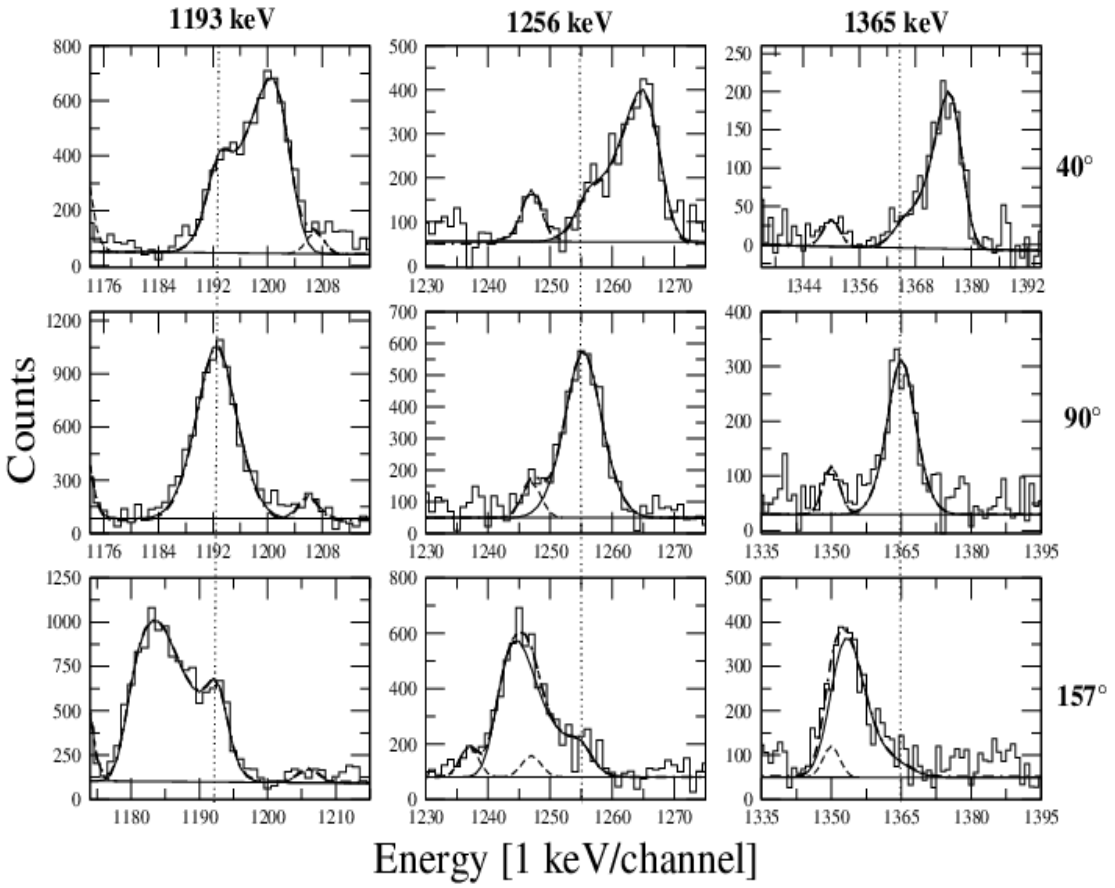

Figure 4.6: Examples of the line-shape fits for 1193 ($20^+ \rightarrow 18^+$) keV, 1256 ($22^+ \rightarrow 20^+$) keV and 1365 ($24^+ \rightarrow 22^+$) keV transitions of Band B at 40°, 90° and 157° with respect to the beam direction. The fitted Doppler broadened line-shapes are drawn in solid lines while the contaminant peaks are shown in dashed lines. The result of the fit to the experimental data is shown in dot-dashed lines.

For Band B the topmost transition of 1468 ($26^+ \rightarrow 24^+$) keV was assumed to have 100% side-feed. The other parameters were allowed to vary until the minimum χ^2 value was reached. This led to the estimation of the effective lifetime for the 26^+ level. For the 24^+ level decaying through 1365 keV transition, the effective lifetime of the 26^+ level and the side-feeding lifetime were considered as the input parameters.

In this way, each lower level was added one by one and fitted until all of the observed line-shapes of the yrast cascade of ^{104}Pd were included into a global fit where only the in-band and the side-feeding lifetimes were allowed to vary. This procedure of global fit was carried out simultaneously for the forward and the backward angles. The uncertainties in the lifetime measurements were derived from the behavior of the χ^2 in the vicinity of the minimum for the simultaneous fit at the two angles. The other source of error in the level lifetime measurement was due to the uncertainty in the side-feeding intensity which originated from the uncertainties in the intensities of the top-feeding and the feed-out γ-transitions for the level of interest. This was estimated by finding the level lifetimes for the minimum and maximum values of side-feeding intensities. The final statistical uncertainty was calculated by adding the uncertainties due to line-shape fitting and side-feeding intensity in quadrature.

In the present analysis, all the line-shapes for Band B were extracted from the 803 keV γ-gated spectrum. In this gate the line-shape of 927 ($16^+ \rightarrow 14^+$) keV transition was strongly contaminated by 926 ($6^+ \rightarrow 4^+$) keV transition. However, it was found from the data that the γ-transitions below 10^+ state did not exhibit line-shapes. Thus, the 926 keV transition could be treated as a contaminant peak. The intensity of this stopped peak was estimated from the efficiency corrected areas of 556 ($2^+ \rightarrow 0^+$), 768 ($4^+ \rightarrow 2^+$) and 971 ($8^+ \rightarrow 6^+$) keV transitions in the 803 keV γ-gate. These areas were found to be equal within $\pm$1%. So a stopped peak at 926 keV with this averaged area was used to determine the true line-shape of 927 keV transition. The examples of the line-shape fits for the three top transitions for Band B in ^{104}Pd are shown in Fig. 4.6. The level lifetime values and the corresponding statistical and systematic uncertainties are given in table. 4.1.

The line-shapes for the Band C and Band D were extracted from the sum gate of 680 keV and 379 keV and the sum gate of 618 keV and 251 keV, respectively. The

line-shape fits for 1160 keV and 1141 keV transitions belonging to Band C and Band D respectively, are shown in Fig. 4.7.

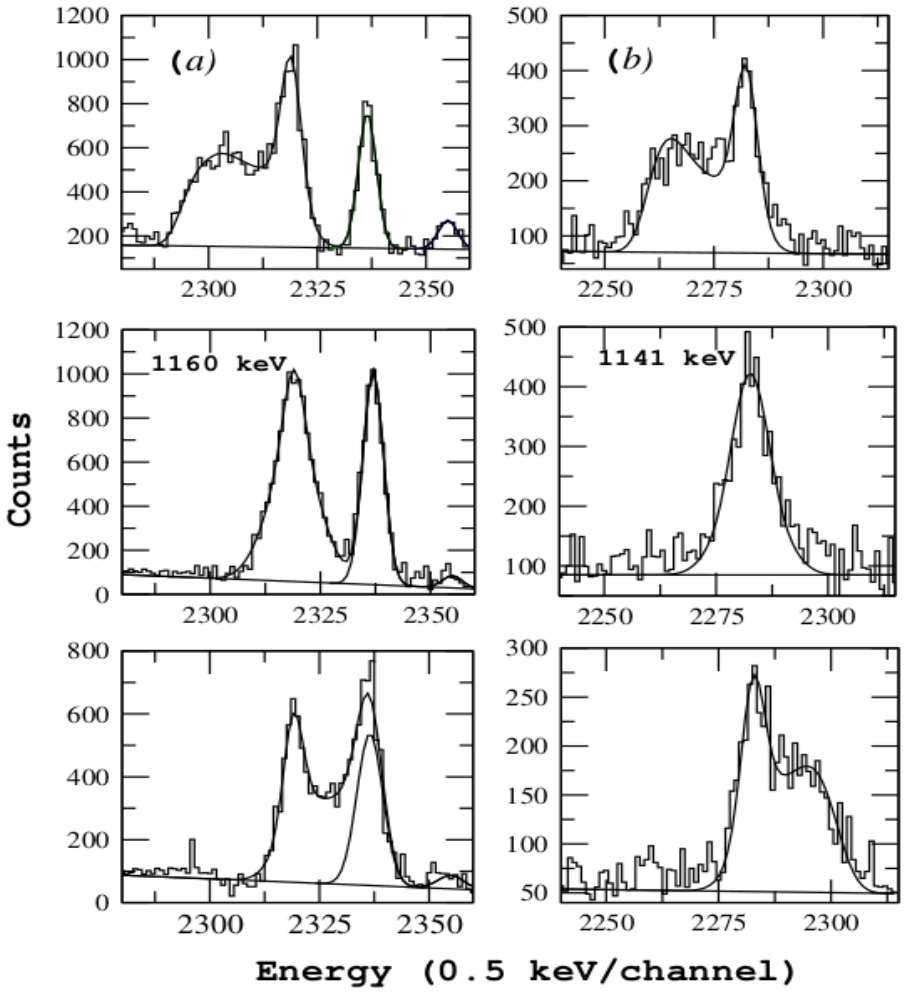

Figure 4.7: Examples of the line-shape fits for (a)1160 ($17^- \rightarrow 15^-$) keV (Band C), (b)1141 ($16^- \rightarrow 14^-$) keV (Band D) and transitions at 157°, 90° and 40° with respect to the beam direction. The fitted Doppler broadened line-shapes are drawn along with the contaminant peaks.

The B(E2) transition rates were extracted from the measured level lifetimes using the formula

$$B(E2) = \frac{0.0816}{E_\gamma^5 \times \tau} \tag{4.1}$$

where E_γ is the energy in MeV of a pure E2 transition, τ is the level lifetime in pico-

seconds and B(E2) is in the units of $(eb)^2$. The extracted B(E2) values are tabulated in Table 4.1.

4.4 RESULTS

4.4.1 Level Scheme

Band A: It is the positive parity GS band which was extended upto the value of 14^+ by placing an additional level to the previously known one [7]. The deduced multipolarity of its de-exciting 1266 keV gamma is such that it was assigned a stretched $E2$ character.

Band B: This band was also extended by placing an additional transition to the known value of Ref. [7]. The DCO and the PDCO measurements confirm the previous spin and the parity assignments. The gamma de-exciting the $I^\pi = 28^+$ level was assigned to be an $E2$ transition based on the same assumption that it continues to be the part of the existing rotational sequence. This band originates from the GS band and gets connected through 803 keV transition.

Band C: Like the Band A and Band B, the spin-parity assignments from our analysis were in agreement with the Ref. [7]. However, the levels $I^\pi = 21^-$ and $I^\pi = 23^-$ were found to de-excite by gamma energies 1311 keV and 1434 keV, respectively which were reported to be 1313 keV and 1386 keV in Ref. [7]. The 1434 keV transition was attributed a stretched $E2$ based on its PDCO value of 0.37(18) which is consistent with it's electric nature. The DCO measurement for this transition was not possible because of the considerable line-shape.

Bands D, E and F: These three non-yrast negative parity bands were reported

earlier. These bands were confirmed from the present data. They could not be extended further from the present analysis.

Bands G and H: These bands were also established in the previous study and have been confirmed by us. The multipolarity assignments are also in agreement with our measurements.

Table 4.1: The measured lifetimes for the levels of ^{104}Pd for band C, band D and band E. It should be noted that the quoted errors are the statistical and the systematic respectively. The statistical error on each level is obtained by adding in quadrature the errors on intensity, intrinsic quadrupole moment of the level and the corresponding side-feeding quadrupole moment.

I_i^π	E_γ	$\tau \pm stat. \pm syst.$	B(E2)$\pm stat. \pm syst.$	$\mathcal{J}^{(2)}/B(E2)$
($\hbar$)	(keV)	(ps)	$(eb)^2$	$\hbar^2 MeV^{-1}(eb)^{-1}$
		Band B		
16^-	927	0.452±.04 ± .03	0.259±.02 ± .02	112(9)
18^-	1064	0.271±.02 ± .02	0.222±.02 ± .02	141(13)
20^-	1193	0.178±.02 ± .02	0.193±.02 ± .02	334(35)
22^-	1256	0.203±.02 ± .03	0.131±.02 ± .02	283(22)
24^-	1365	0.241±.03 ± .04	0.072±.01 ± .01	554(80)
26^-	1468	0.661	0.021	
		Band C		
13^-	916	0.473±.05 ± .03	0.268±.03 ± .02	104.5(12)
15^-	1058	0.210±.01 ± .01	0.292±.02 ± .02	133.6(9)
17^-	1160	0.142±.01 ± .01	0.274±.02 ± .03	259.1(19)
19^-	1217	0.112±.01 ± .01	0.272±.02 ± .03	156.9(12)
21^-	1311	0.057±.01 ± .02	0.376±.02 ± .04	85.1(5)
23^-	1434	0.043	0.313	
		Band D		
12^-	879	0.576±.01 ± .01	0.269±.03 ± .02	96.6(11)
14^-	1033	0.292±.02 ± .01	0.237±.02 ± .02	156.1(13)
16^-	1141	0.176±.01 ± .02	0.239±.02 ± .03	238.5(20)
18^-	1211	0.136±.01 ± .02	0.230±.02 ± .03	130.4(11)
20^-	1344	0.052±.01 ± .03	0.356±.02 ± .04	95.5(5)
22^-	1462	0.038	0.321	

4.5 Discussions

4.5.1 Band A

This is the GS band of the even-even ^{104}Pd. However, from the alignment plot (Fig. 4.8) it seems that the lower five levels probably arise due to the quadrupole vibrations. The GS collective band (0-qp) consists of 1019 keV, 1148 keV and 1266 keV transitions and the quasi-particle alignment is nearly zero since all the nucleons are paired. However, since this band becomes non-yrast after $I^{\pi} = 8^{+}$, it cannot be extended beyond 14^{+}.

4.5.2 Band B

It is observed from the alignment plot (Fig. 4.8) that this band corresponds to $i_x \sim 8\hbar$. This is the characteristic quasi-particle alignment of two $h_{11/2}$ neutrons in this mass region. At higher spins the i_x values seem to remain constant with a slow increase around $\hbar\omega$=0.5 MeV. In addition, the $\mathcal{J}^{(2)}/B(E2)$ values for Band B are considerably higher than those for bands C and D and is found to increase with spin (table 4.1). This is expected for an AMR band as the B(E2) values are small and decrease with spin while the $\mathcal{J}^{(2)}$ remains nearly constant [1]. Thus, the high spin levels of Band B of ^{104}Pd seem to originate due to anti-magnetic rotation.

This possibility has been further investigated in the framework of SCPRM. For these calculations, the configuration for Band B was assumed to be $\pi g_{9/2}^{-2} \otimes \nu[h_{11/2}^{2}, (g_{7/2}/d_{5/2})^{2}]$ which is the same as for the AMR band of its isotone, namely ^{106}Cd. For this configuration, the symmetric shears is formed between $j_h{}^{(1)} = j_h{}^{(2)} = j_\pi = 9/2$ and $j_p = j_\nu = 16$. There are eight possible particle - hole and one hole -

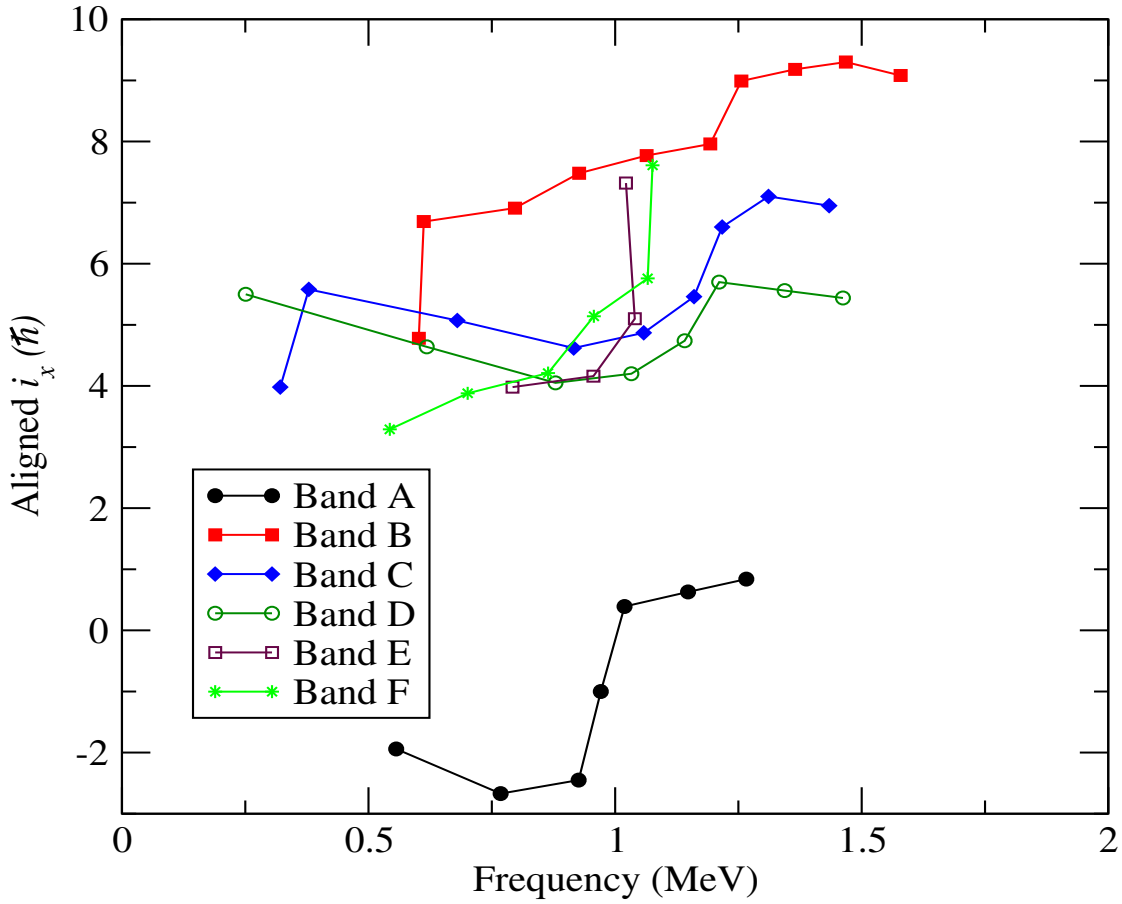

Figure 4.8: Alignment plots for the various bands of ^{104}Pd as indicated. The Harris parameters used for the calculation are $\mathcal{J}^{(1)} = 14\hbar$ and $\mathcal{J}^{(2)} = 15\hbar$.

hole pairs which imply that $n = 8$. Thus, the shears parameters used in the present calculation were $j = 4.5\ \hbar$, $a = 3.55$, $V_{\pi\nu} = 1.2$ MeV and $V_{\pi\pi} = 0.2$ MeV. For ^{104}Pd, $I_{sh}^{max} = j_\nu + 9/2 + 7/2 = 24\ \hbar$ and from the experiment I^{max}= 26 $\hbar$. Using these values in Eq. (8), $\mathcal{J}$ was estimated to be 5 MeV$^{-1}\hbar^2$. $\mathcal{J}_{rot}$ was found to be 17 MeV$^{-1}\hbar^2$ from the slope of the ground state band of ^{104}Pd before the neutron alignment. With these fixed set of parameters, the numerical values of I(ω) were calculated and have

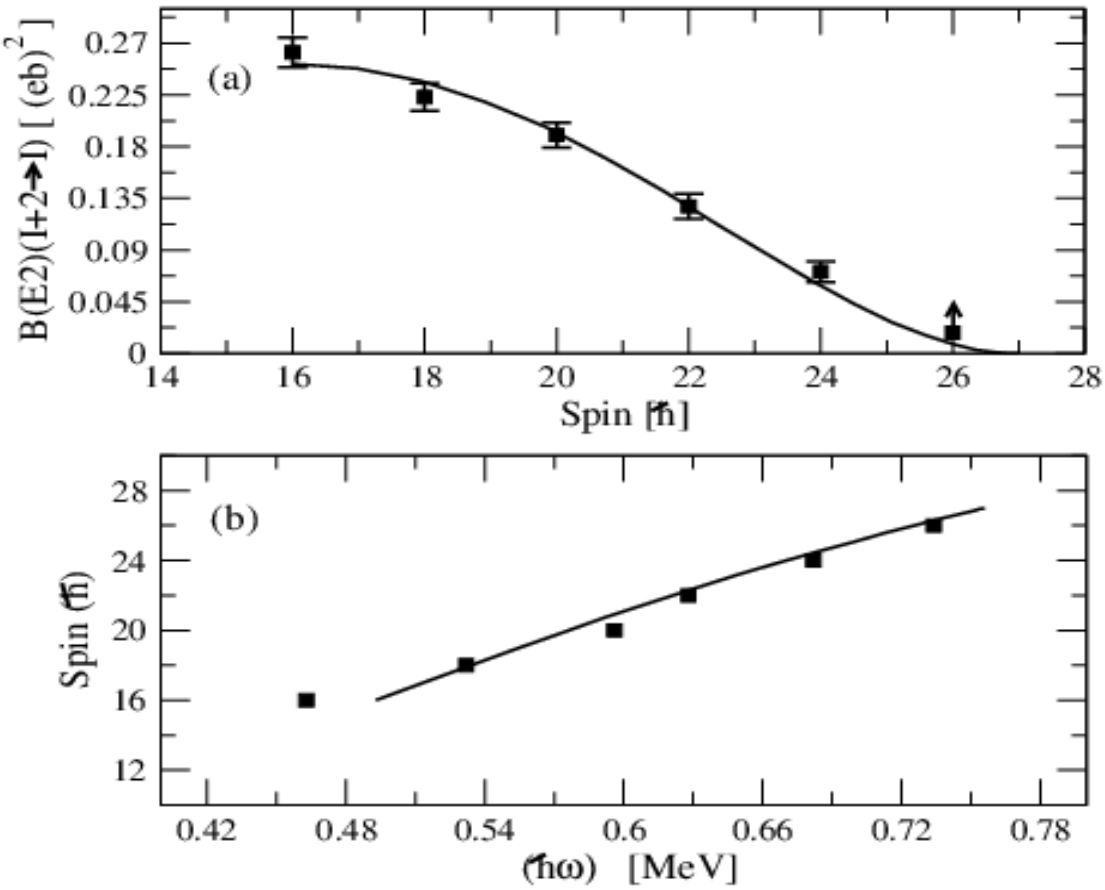

Figure 4.9: The observed B(E2) rates (a) and the I(ω) plot (b) in ^{104}Pd. The lines represent the numerical values obtained from the semi-classical particle rotor model for the parameter set as given in the text. The error bars given in (a) correspond to statistical error only.

been shown by the solid line in Fig. 4.9(b) while the experimental values are shown as filled squares. The calculated values were shifted by the experimental bandhead frequency of 0.46 MeV. The comparison plot shows that the numerical values obtained from semi-classical particle rotor model are in good agreement with the experimental values. It is worth noting that in the present model, the shears angle (θ) is the only variable and every angular momentum state corresponds to a unique θ which is determined from 2.50. However, from the Eq. $I_{sh} = j_p + 2j_h \cos\theta$, the complete closure of the two proton blades ($\theta = 0°$) leads to an angular momentum gain of 9 $\hbar$ (corresponding to I = 27 $\hbar$) which is inconsistent with Pauli exclusion principle. A

pictorial representation of the evolution of the shears structure in ^{104}Pd as a function angular momentum is shown in Fig. 4.10 where the highest observed level of I = 26 $\hbar$ corresponds to $\theta = 25°$ as calculated from Eq. 2.50.

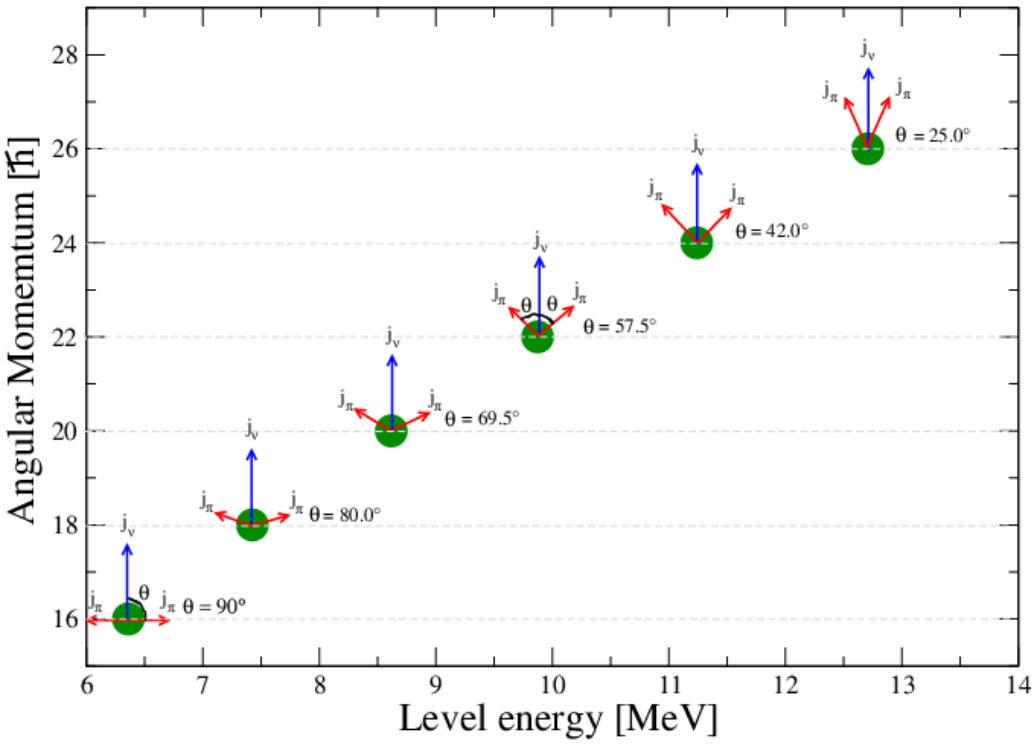

Figure 4.10: A pictorial representation of the symmetric shears structure in ^{104}Pd. The higher spin states are generated by the gradual closing of the shears angle.

These θ values were used to calculate the B(E2) transition rates from Eq. 2.58. The eQ_{eff} for ^{104}Pd was found to be 1.3 eb from the single particle quadrupole moments of the Nilsson states with Woods-Saxon potential at $\beta_2 = 0.15$ [7]. This prescription has been described in detail in Ref. [2]. The experimental and calculated values have been shown in Fig. 4.9(a). The good agreement provided the essential consistency check for the numerical calculations since both the I(ω) and the B(E2) values for the observed AMR band of ^{104}Pd were well reproduced for same set of values for the shears angle. It is worth noting that though these calculations involved a number of parameters but none of them was left free to obtain the good agreement

between the experimental and calculated values. Thus, AMR has been conclusively established in a nucleus other than Cadmium for the first time which extends the domain of AMR in A ∼100 region. This result has induced further experimental investigation in neighboring ^{105}Pd which is reported in the next chapter.

4.5.3 Band C and D

The measured $B(E2)$ values for the high spin levels of Band C and Band D are plotted in Fig. 4.11. It may be observed from the figures that the $B(E2)$ are constant in each band and the average values are similar. This average value of 0.26±0.06 corresponds to a β value of 0.20. Thus, both the bands originate due to collective rotation of a prolate shape with β ∼0.20. In Fig. 4.12, the energy staggering between Bands C and D, using equation $S(I) = E(I) - E(I-1)$, has been plotted. This shows a characteristic energy splitting of two signature partner bands. This observation is consistent with the quasi-neutron configuration of $h^1_{11/2} \otimes (d_{5/2},\ g_{7/2})^1$ where the $h_{11/2}$ neutron is expected to occupy the low Ω orbitals thereby leading to signature splitting. It may also be noted that this configuration is also consistent with the quasi-particle alignment value of $\sim 5\hbar$ (Fig. 4.8).

4.5.4 Bands E and F

These are the other set of negative parity partner bands. They are more non-yrast as compared to Band C and Band D and thus, are populated with substantially lower intensity. For this reason it was not possible to measure the lifetimes of the high spin levels of these two bands. In order to investigate further, the energy staggering between these bands is plotted in Fig. 4.12. It may be noted that the energy splitting pattern is very similar to that of bands C and D and in both cases, the odd spins are

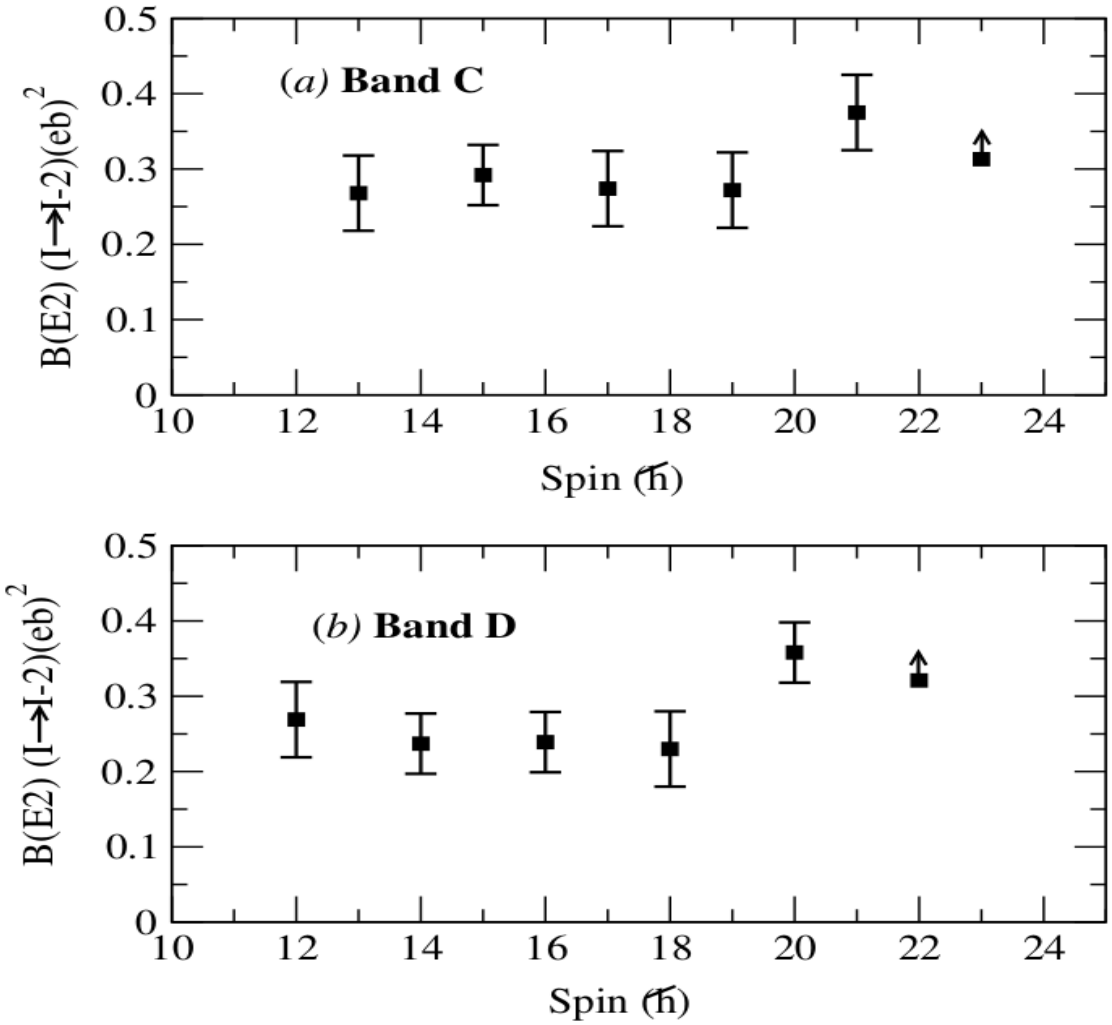

Figure 4.11: The $B(E2)$ rates for the Band C (a) and Band D (b) as a function of spin.

the favored signature. Thus, it seems plausible that these are signature partners with the same quasi-neutron configuration of $h^1_{11/2} \times (d_{5/2}/g_{7/2})^1$.

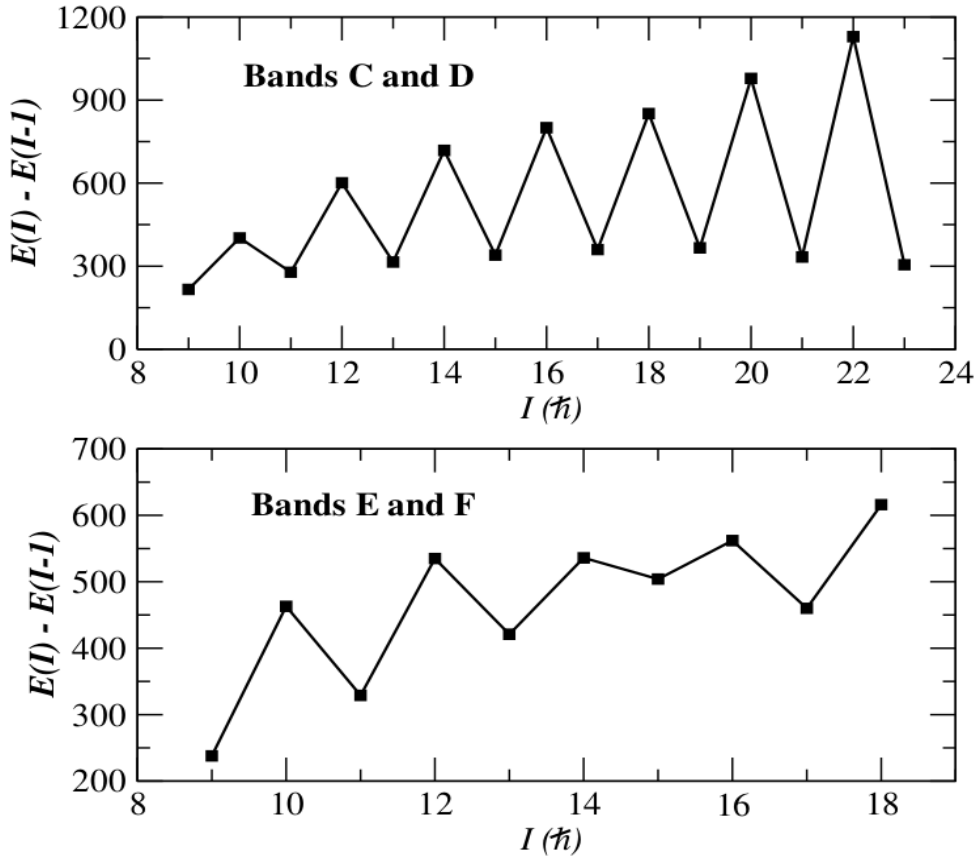

Figure 4.12: The energy staggering plots for the two pairs of bands, bands C and D and bands E and F.

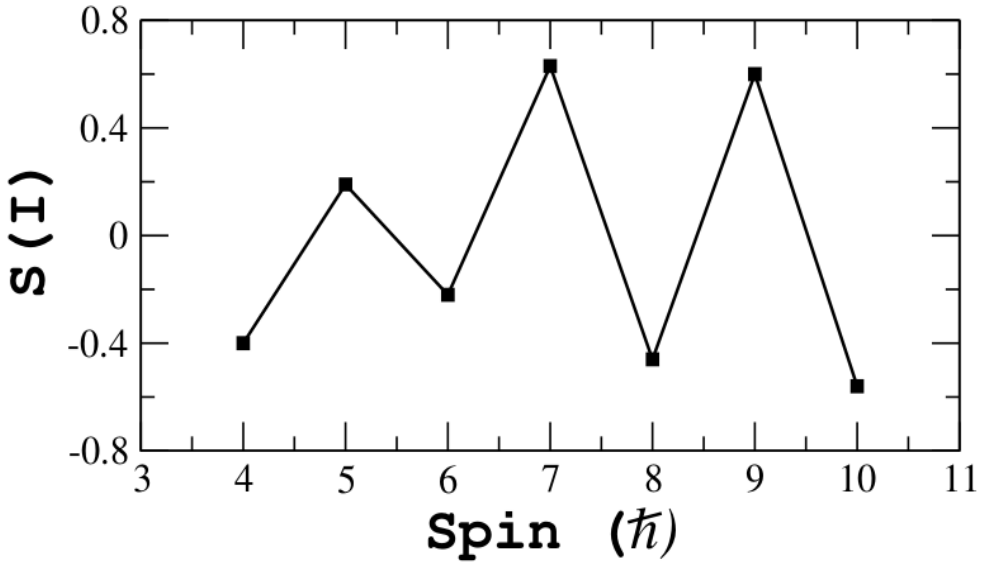

Figure 4.13: A plot for the experimentally observed odd-even spin energy staggering for the bands G and H.

4.5.5 Bands G and H

These are the two positive parity γ-soft bands built on the 2^+ level. The distinction between a γ-soft and a γ-rigid energy sequence is expressed in terms of the odd-even spin energy staggering function [12]

$$S(I) = \frac{E(I) + E(I-2) - 2E(I-1)}{E(2_g^+)} \tag{4.2}$$

such that for a rigid triaxial rotor this staggering function gives positive values for the even spins and the negative values for the odd spins. However, the sign between the even and the odd spins is reversed for the γ soft rotor. This staggering plot for the Bands G and H is shown in Fig 4.13 which seems to establish the γ softness of this sequence.

Thus, the present data seems to indicate that the high spin states of ^{104}Pd are generated by the principal axis rotation (Bands C, D, E and F) as well as antimagnetic rotation (Band B). This is a novel observation of co-existence of collective and antimagnetic rotation which has been established through the measurement of electric quadrupole transition rates of the high spin states of ^{104}Pd.

Table 4.2: Energies, relative intensities, DCO ratios, linear polarizations and the deduced multi-polarities of transitions assigned to the ^{104}Pd in the present work.

$I_i^\pi \rightarrow I_f^\pi(\hbar)$	$E_\gamma(KeV)$	I_γ	R_{DCO}	P	$Mult.$
$4^- \rightarrow 3^-$	116	0.5(1)	0.64(22)		D
$8^- \rightarrow 7^-$	163	3.9(2)	0.43(6)		D
$5^- \rightarrow 4^-$	194	2.1(3)	0.66(10)		D
$8^- \rightarrow 6^-$	193	0.4(1)	0.98(16)		Q
$8^+ \rightarrow 8^+$	201	1.2(2)	1.04(12)		D
$4^- \rightarrow 4^+$	215	1.5(2)	1.08(14)		D
$9^- \rightarrow 8^-$	216	1.6(1)			
$6^- \rightarrow 5^-$	233	0.3(1)	0.57(13)		D

Table 4.2 – *Continued from previous page*

$I_i^\pi \rightarrow I_f^\pi(\hbar)$	$E_\gamma(KeV)$	I_γ	R_{DCO}	P	$Mult.$
$6^+ \rightarrow 5^+$	233	0.4(2)	0.66(9)		D
$8^- \rightarrow 6^-$	251	7.5(7)	1.09(9)	0.27(7)	E2
$5^- \rightarrow 3^-$	310	1.0(3)	0.94(7)		Q
$7^- \rightarrow 5^-$	321	1.2(5)	1.2(4)	0.67(8)	E2
$8^- \rightarrow 8^-$	350	1.3(4)	0.99(5)		D
$5^+ \rightarrow 4^+$	362	0.7(5)	0.54(4)		D
$8^+ \rightarrow 8^+$	372	0.2(2)	0.95(7)		D
$9^- \rightarrow 7^-$	379	21.6(14)	1.1(4)	0.65(7)	E2
$10^- \rightarrow 9^-$	402	1.2(3)	0.49(4)	-0.37(8)	M1
$5^- \rightarrow 4^+$	409	0.3(2)	0.63(6)		
$6^- \rightarrow 5^-$	409	6.6(5)	0.62(7)		D
$6^+ \rightarrow 6^+$	428	0.8(4)	1.12(9)		D
$10^- \rightarrow 9^-$	463	0.4(3)	0.56(7)	-0.78(7)	M1
$6^- \rightarrow 5^-$	467	2.4(4)	0.71(6)	-0.77(8)	M1
$14^+ \rightarrow 13^-$	469	0.4(3)	0.51(3)		D
$4^- \rightarrow 3^+$	477	1.1(3)			
$3^+ \rightarrow 2^+$	479	0.6(4)			
$7^- \rightarrow 5^-$	497	1.9(5)	1.02(4)	0.59(8)	E2
$8^- \rightarrow 7^-$	513	0.6(2)	1.12(3)	0.10(2)	E2
$12^- \rightarrow 11^-$	535	0.7(2)	0.51(4)		
$8^- \rightarrow 6^-$	543	0.2(2)			
$2^+ \rightarrow 0^+$	556	100	1.18(1)	0.35(6)	E2
$12^+ \rightarrow 11^-$	588	1.2(3)	0.56(6)	0.63(7)	E1
$9^- \rightarrow 8^-$	588	1.8(4)	1.56(4)	-0.98(7)	M1
$7^+ \rightarrow 6^+$	591	0.9(3)			
$22^+ \rightarrow 22^+$	595	0.3(3)			
$6^+ \rightarrow 4^+$	595	1.7(3)			
$12^- \rightarrow 11^-$	601	1.2(2)	0.56(7)		D
$10^+ \rightarrow 8^+$	602	2.6(5)	1.07(7)	0.28(6)	E2
$6^- \rightarrow 4^-$	603	3.8(1)	1.03(5)	0.43(9)	E2
$12^+ \rightarrow 10^+$	612	17.9(6)	1.05(10)	0.8(5)	E2
$10^- \rightarrow 8^-$	618	8.3(4)	1.06(7)	0.47(6)	E2
$5^+ \rightarrow 3^+$	624	1.2(2)	0.99(4)		Q
$6^- \rightarrow 6^+$	651	2.8(4)	0.98(5)		D
$10^+ \rightarrow 9^-$	656	0.7(4)	0.67(5)	0.59(8)	E1
$9^+ \rightarrow 8^+$	666	0.4(2)	0.61(4)		D
$11^- \rightarrow 9^-$	680	14.9(5)	1.04(5)	0.51(6)	E2
$10^- \rightarrow 8^-$	701	1.4(3)	1.03(4)	0.87(6)	E2
$14^- \rightarrow 13^-$	718	0.2(2)	0.64(2)		D
$7^- \rightarrow 6^+$	739	32.2(4)	0.54(5)	0.39(8)	E1
$4^+ \rightarrow 2^+$	741	1.5(2)	0.98(3)		Q
$9^- \rightarrow 7^-$	751	1.0(1)	1.09(5)	0.83(9)	E2

Table 4.2 – *Continued from previous page*

$I_i^\pi \rightarrow I_f^\pi(\hbar)$	$E_\gamma(KeV)$	I_γ	R_{DCO}	P	$Mult.$
$4^+ \rightarrow 4^+$	759	0.9(4)	1.00(4)		D
$11^- \rightarrow 10^-$	762	1.2(2)			
$4^+ \rightarrow 2^+$	768	92.1(23)	1.01(3)	0.62(6)	E2
$2^+ \rightarrow 2^+$	786	1.3(2)			
$11^- \rightarrow 9^-$	792	1.7(2)			
$14^+ \rightarrow 12^+$	797	12.7(7)	1.04(9)	0.77(4)	E2
$10^+ \rightarrow 8^+$	803	22.0(6)	0.93(4)	0.66(8)	E2
$7^+ \rightarrow 5^+$	824	0.4(3)	0.97(8)		Q
$3^- \rightarrow 4^+$	858	2.4(3)	0.63(4)		D
$12^- \rightarrow 10^-$	864	1.2(3)	0.95(3)		Q
$12^- \rightarrow 10^-$	879	6.1(3)	1.16(3)	0.58(2)	E2
$8^+ \rightarrow 6^+$	915	1.2(2)	0.93(6)		Q
$13^- \rightarrow 11^-$	916	10.5(2)	0.92(3)	0.50(7)	E2
$6^+ \rightarrow 4^+$	926	74.2(1)	1.09(3)	0.60(9)	E2
$16^+ \rightarrow 14^+$	927	8.8(2)	1.16(8)	0.77(3)	E2
$13^- \rightarrow 11^-$	956	0.9(4)			
$14^- \rightarrow 12^-$	957	1.5(2)			
$8^+ \rightarrow 6^+$	971	27.6(9)			
$4^- \rightarrow 4^+$	974	1.6(3)	1.03(5)		D
$9^+ \rightarrow 7^+$	990	0.4(2)	1.01(4)		Q
$10^+ \rightarrow 8^+$	1019	1.5(2)	1.01(4)	0.22(4)	E2
$17^- \rightarrow 15^-$	1022	0.6(2)			
$10^+ \rightarrow 8^+$	1026	0.6(2)	0.94(6)		Q
$14^- \rightarrow 12^-$	1033	3.6(3)	1.07(5)	0.53(3)	E2
$15^- \rightarrow 13^-$	1040	0.7(2)			
$15^- \rightarrow 13^-$	1058	7.0(3)		0.81(5)	E2
$18^+ \rightarrow 16^+$	1064	6.4(3)		0.64(6)	E2
$16^- \rightarrow 14^-$	1066	0.6(2)			
$18^- \rightarrow 16^-$	1076	0.4(2)			
$16^- \rightarrow 14^-$	1141	2.2(2)		0.66(8)	E2
$12^+ \rightarrow 10^+$	1148	0.5(3)			
$17^- \rightarrow 15^-$	1160	3.3(2)		0.57(9)	E2
$5^- \rightarrow 4^+$	1168	13.8(5)	0.59(4)	0.47(5)	E1
$8^+ \rightarrow 6^+$	1172	4.5(4)	0.96(8)	0.67(8)	E2
$20^+ \rightarrow 18^+$	1193	3.4(3)			E2
$18^- \rightarrow 16^-$	1211	1.0(2)		0.98(9)	E2
$19^- \rightarrow 17^-$	1217	1.3(3)			E2
$22^+ \rightarrow 20^+$	1256	1.6(2)			E2
$3^+ \rightarrow 2^+$	1265	2.2(2)	0.67(5)	-0.45(6)	M1
$21^- \rightarrow 19^-$	1311	0.6(2)			E2
$2^+ \rightarrow 0^+$	1342	0.4(1)	1.01(5)	0.78(9)	E2
$20^- \rightarrow 18^-$	1344	0.2(1)			E2

Table 4.2 – *Continued from previous page*

$I_i^{\pi} \rightarrow I_f^{\pi}(\hbar)$	$E_{\gamma}(KeV)$	I_{γ}	R_{DCO}	P	$Mult.$
$5^- \rightarrow 4^+$	1344	2.8(3)	0.56(8)	0.71(8)	E1
$6^+ \rightarrow 4^+$	1354	1.1(2)	0.94(4)	0.67(9)	E2
$24^+ \rightarrow 22^+$	1366	0.3(2)			Q
$23^- \rightarrow 21^-$	1434	0.2(1)		0.37(18)	
$26^+ \rightarrow 24^+$	1468	0.2(1)			
$4^+ \rightarrow 2^+$	1527	1.6(4)	0.96(8)	1.34(7)	E2
$28^+ \rightarrow 26^+$	1579	0.6(3)			E2
$3^- \rightarrow 2^+$	1626	0.8(2)			

Bibliography

[1] A. J. Simons, *et al.*, Phys. Rev. Lett. **91** 162501 (2003).

[2] P. Datta *et al.*,Phys. Rev. C **71**, 041305 (R) (2005).

[3] S. Roy *et al.*, Phys. Rev. C **81**, 054311 (2010).

[4] S. Zhu, *et al.* Phys. Rev C **64** 041302(R) (2001).

[5] M. Sugawara *et al.*, Phys. Rev. C **86**, 034326 (2012).

[6] M. Sugawara *et al.*, Phys. Rev. C **79**, 064321 (2009).

[7] D. Sohler *et al.*, Phys. Rev. C **85**, 044303 (2012).

[8] S. Muralithar *et al.*, Nucl. Instrum. Methods A **622**, 281 (2010).

[9] R. Palit *et al.*, Nucl. Instrum. Methods A **680**, 90 (2012).

[10] D. C. Radford, Nucl. Instrum. Methods A **361**, 297 (1995).

[11] J. C. Wells and N. R. Johnson, Oak Ridge National Laboratory Report No. ORNL-6689, **44** (1991).

[12] McCutchan E A, Bonatsos Dennis, Zamfir N V and Casten R F 2007 Phys. Rev. C **76** 024306.

Chapter 5

High Spin Level Structure in ^{105}Pd

5.1 Introduction

The first observation of the AMR outside the Cd-isotopes in ^{104}Pd induced the similar search in ^{105}Pd. The isotone of this nucleus, ^{107}Cd, has two positive parity AMR bands [1]. Such a partner of AMR bands is expected in odd mass nuclei due to the presence of the odd neutron in $(d_{5/2}, g_{7/2})$ orbitals. In addition, it was also interesting to explore the possibility of the co-existence of antimagnetic and collective rotations in ^{105}Pd.

5.2 Experiment

The high spin states of ^{105}Pd were populated by ^{96}Zr $(^{13}C, 4n)$ reaction using the 63 MeV ^{13}C beam from the 14-UD Pelletron at TIFR. The target was made of 1 mg/cm^2 85% enriched ^{96}Zr on 9 mg/cm^2 ^{206}Pb backing. The beam current was about 9 nA. The γ rays were detected in the upgraded Indian National Gamma Array

(INGA) [2] which consisted of 20 Compton suppressed clover detectors arranged in six rings with three at 23°, two at 40°, two at 60°, four at 90°, three at 120°, three at 140° and three at 157° with respect to the beam direction. Two or higher fold coincidences were collected by a fast data acquisition system based on Pixie-16 modules of XIA LLS [3]. A total of 5×10^8 $\gamma - \gamma - \gamma$ coincidences were collected. The time stamped data were sorted using the data sorting routine, MARCOS, developed at TIFR with a time window of 200 ns to construct $\gamma - \gamma$ matrices and $\gamma - \gamma - \gamma$ cube.

5.3 Analysis Method

A number of matrices were formed by unfolding each of the three fold events in order to analyze the data. The various matrices created are:

(1) The symmetrized $\gamma - \gamma$ matrix: This matrix was used to create various gates in order to build the level scheme upto spin values whose gamma transitions did not exhibit any Doppler broadened line-shape. In addition, the $\gamma - \gamma - \gamma$ cube was used to establish the relatively weak transitions in this spin regime.

(2) 90°-vs-All matrix: A special matrix is formed by placing an E_γ fired by detectors at 90° along one axis and the other co-incident E_γ from any other detector along the other axis. Then projecting the 90° spectrum with a gate on the all-detector axis enables us to place all the high spin transitions in the level scheme that are otherwise Doppler Shifted. This matrix was also used for the relative intensity measurements.

(3) The angular correlation matrix: This matrix was formed by placing the gamma energies detected at 90° and 157° along the two axes respectively. This matrix was used to determine the DCO ratio. A plot of the measured DCO values as

a function of energy for ^{105}Pd is shown in Fig. 5.1. The values are also tabulated in table 4.2 and were used to determine the spins of the excited levels.

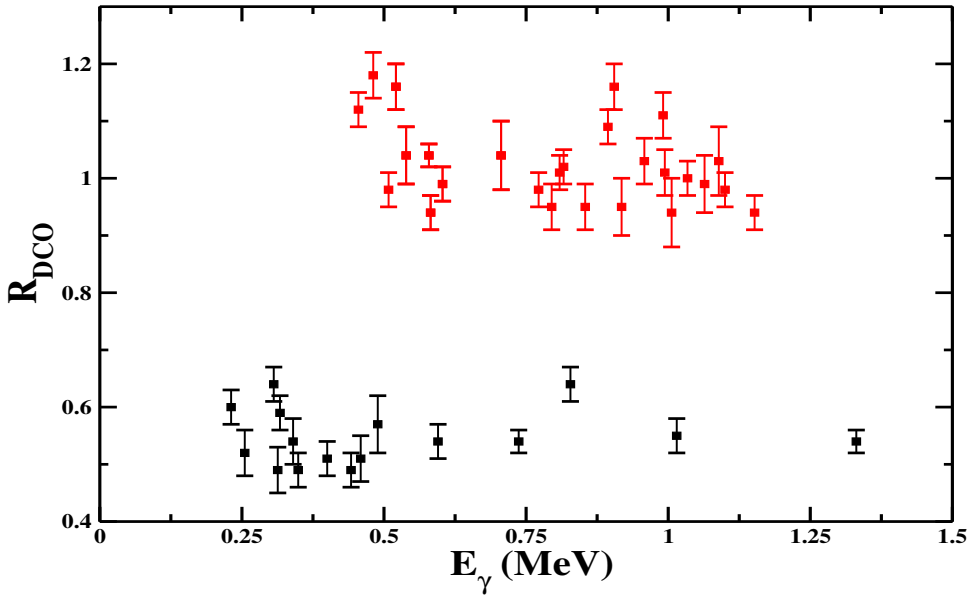

Figure 5.1: The measured DCO ratios vs energy for ^{105}Pd. The DCO values for the dipole and the quadrupole transitions are clearly separated. The red color corresponds to transitions with quadrupole nature while the black color corresponds to the transitions with dipole nature.

(4) The PDCO matrix: Two asymmetric matrices were formed to determine the electromagnetic nature (electric or magnetic) of the observed gamma transition by the method of PDCO [4]. The measured PDCO values for ^{105}Pd have been plotted in Fig. 5.2. It can be observed from the figure that the electric and magnetic transitions are well separated in terms of their PDCO ratios. These values are given in table 5.2 and are essential to fix the parities of the observed bands of ^{105}Pd.

(5) The asymmetric Doppler-Shift attenuation method (DSAM) matrices: Three asymmetric DSAM matrices were constructed to perform the line-shape analysis. These matrices were constructed by placing events recorded at a

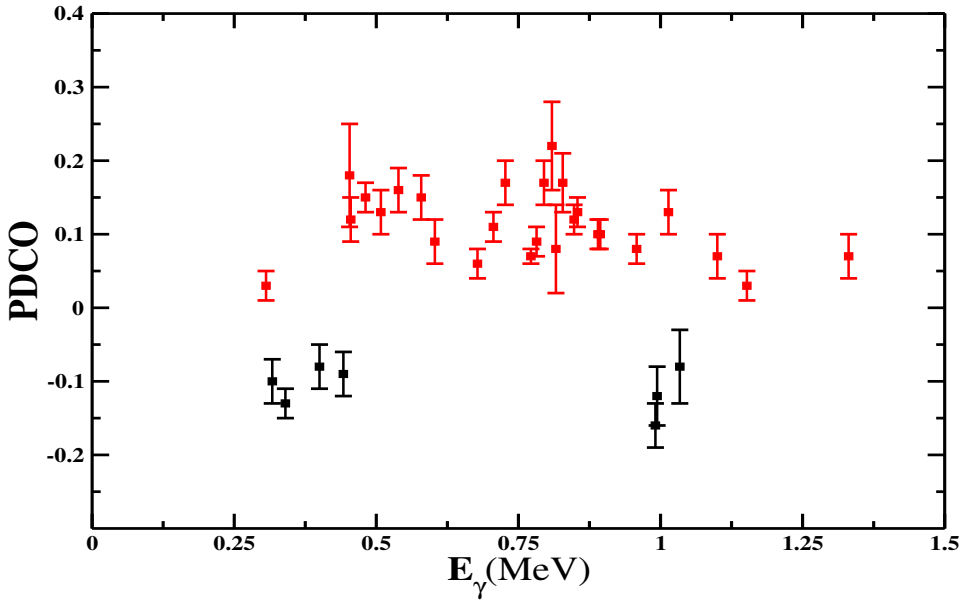

Figure 5.2: The measured PDCO ratios vs energy for ^{105}Pd. The electric and the magnetic transitions can be easily identified. The red color corresponds to transitions with electric nature while the black color corresponds to the transitions with magnetic nature.

specific angle (23°, 157°, and 90°) on x axis while events recorded at all other angles were placed on y axis. The line-shapes were observed for high spin states at both forward, backward and 90° angles by putting gates on the y axis and projecting the spectra on the x axis. The lifetimes of different states of ^{105}Pd were measured by fitting these experimental line-shapes with the LINESHAPE analysis code developed by Wells and Johnson [5].

5.4 RESULTS

5.4.1 Level Scheme

The partial level scheme of ^{105}Pd (shown in Fig. 5.3) has been established using (a) coincidence information of the γ rays. (b) the DCO ratios and (c) the PDCO ratios. The present work confirms the low spin level scheme established in the earlier work [6]. The DCO and PDCO values for 306 keV transition were extracted from 706 keV gate. The intensities of different γ -transitions have been obtained from the gated spectra at 90° and normalized with the intensity of 481 keV γ ray which has been assumed to be 100%. These relative intensities have been tabulated in table I. The true intensities of 183 keV and 306 keV transitions could not be established due to the isomeric $11/2^-$ level which has a long lifetime of about 35 μsec. However, the relative observed intensities of all the other γ rays de-exciting the low spin levels match with the reported values [6] within $\pm 1\sigma$. The DCO and PDCO ratios of different γ-transitions have also been tabulated in table I.

Band 1: It is a positive parity band with bandhead at $I^\pi = 7/2^+$ which decays to the ground state $5/2^+$ through 319 keV γ-transition. This band is built on $\nu(g_{7/2}, d_{5/2})^1$ configuration which shows a sharp alignment with a large gain of $8\hbar$ (Fig. 5.7). This is consistent with the two $h_{11/2}$ neutron alignment in this mass region and thus the high spin states beyond $27/2^+$ level has a neutron configuration of $\nu[(g_{7/2}, d_{5/2})^1 \times h^2_{11/2}]$. It should be noted that AMR band in ^{107}Cd has been reproduced with similar neutron configuration with two proton holes in $g_{9/2}$ [1]. Thus, it was interesting to investigate whether ^{105}Pd can exhibit AMR with four proton holes in $g_{9/2}$. This band has been extended to $I = 55/2\hbar$ through the placement of six new $E2$ transitions. All these transitions exhibit appreciable line-shapes at forward and backward angles. The gated 90° spectrum is shown in Fig 5.4 (b) where these six

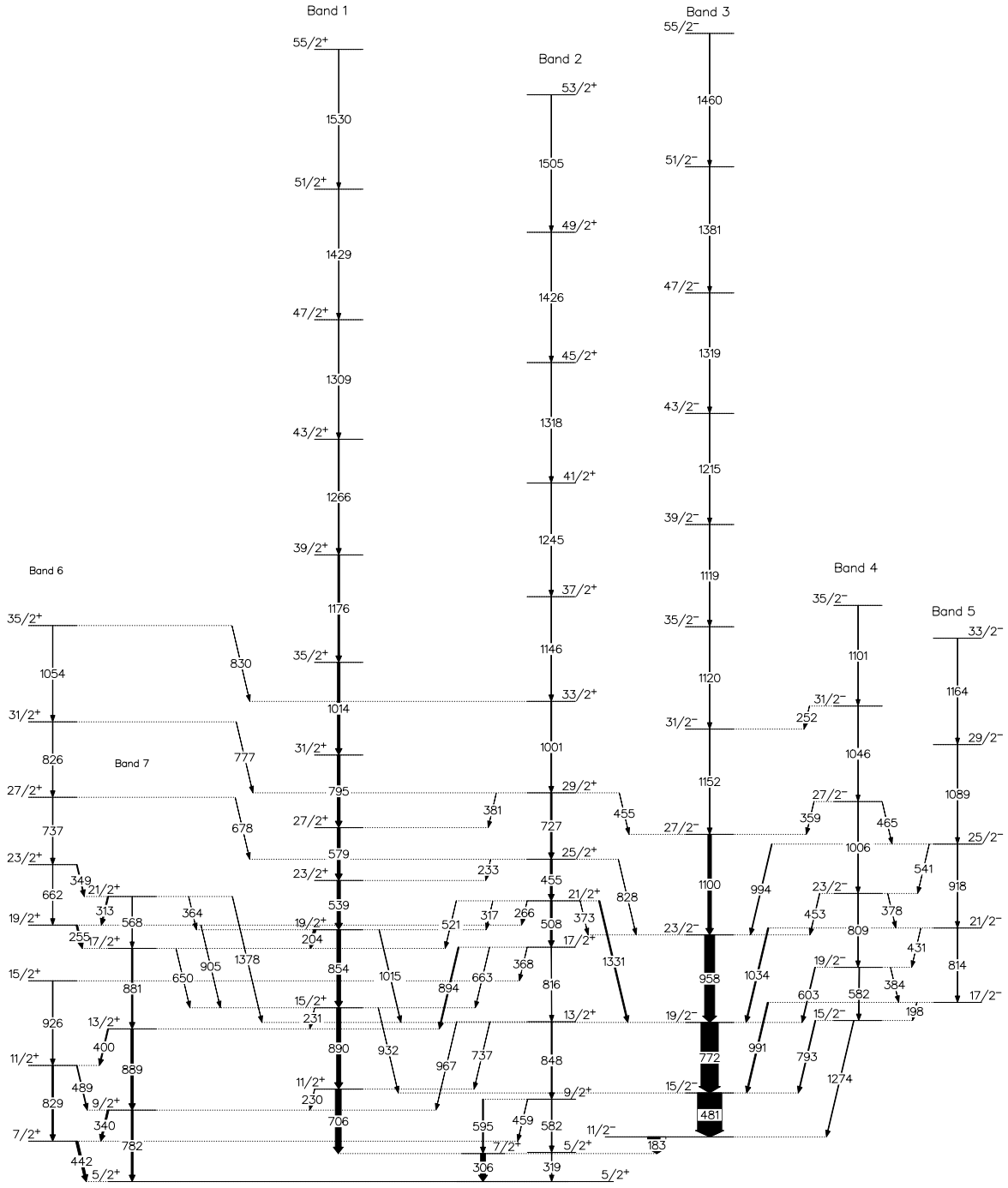

Figure 5.3: The partial level scheme of ^{105}Pd established by the present work. The γ transitions are in keV.

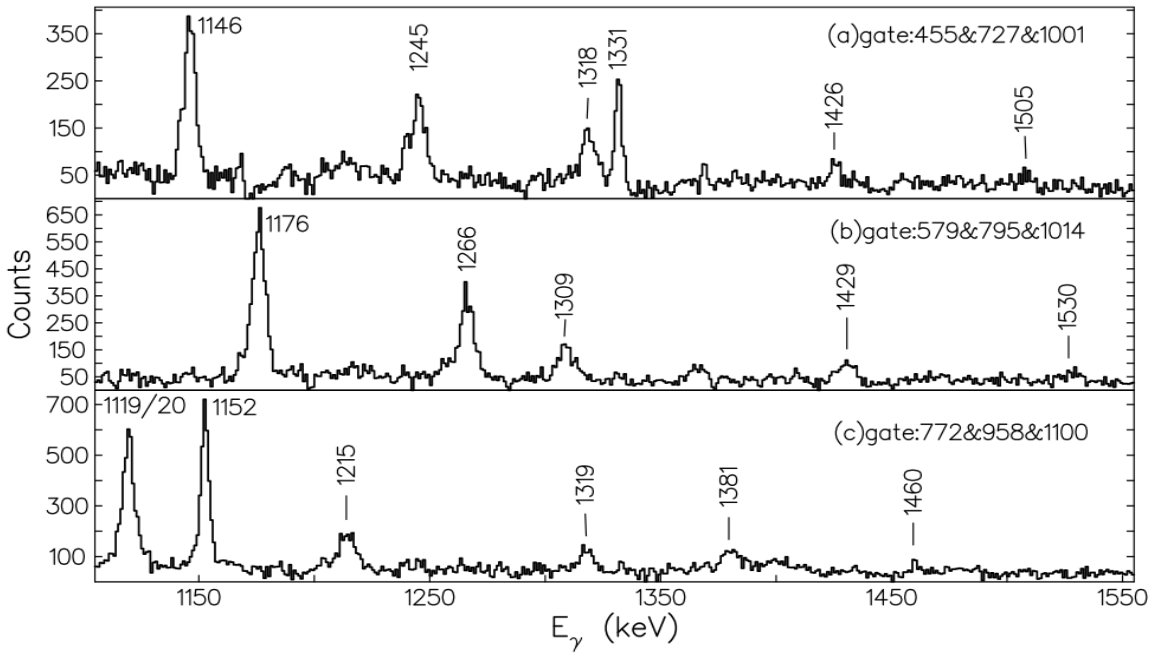

Figure 5.4: The 90° projected gamma gated spectra for Band 1 (b), Band 2 (a) and Band 3 (c). The corresponding γ gates have been indicated in the figure.

new $E2$ transitions can be observed. The corresponding gates are indicated in the figure. The low spin levels were established with the help of cube. A typical gated spectrum from cube for this band is shown in Fig. 5.5 (c). The various transitions which belong to this band can be clearly identified from this spectrum.

Band 2: It is a positive parity non yrast band which predominantly decays to the ground state by Band 1 and Band 2. This band has been extended up to $I^\pi = 53/2^+$. The newly placed transitions are shown in Fig. 5.4 (a) which is a gated 90° spectrum. Fig. 5.5 (a) shows a γ gated spectrum from the cube where the other γ rays belonging to this band can be identified. The Band 2 exhibits a band crossing around $\hbar\omega \sim 0.4$ MeV and the behavior is identical to Band 1. Thus, both the bands are expected to have the same configuration and are the signature partners of each other. Thus, in the nomenclature of CSM, Band 1 and Band 2 have AEF and BEF configurations, respectively. Both the two bands at higher spins may exhibit AMR

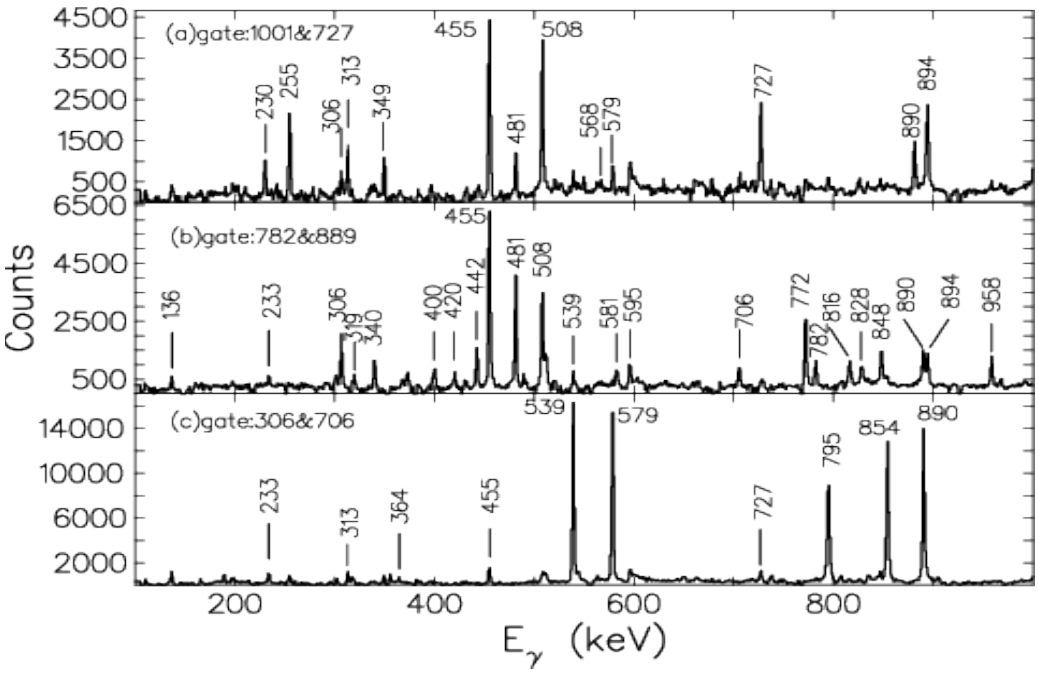

Figure 5.5: Examples of background subtracted coincidence spectra obtained from cube. These spectra show the placement of Band 1 (c), Band 2 (a) and Bands 6 and 7 (b). The γ gates have been indicated in the figure.

which can only be established through lifetime measurements.

Band 3: It is a negative parity band built on $I^\pi = 11/2^-$ level. This is an isomeric level of about 35 μsec which decays to a $7/2^+$ level through a 183 keV $M2$ transition. This band was known up to $I = 31/2$ and has been extended up to $I = 55/2$. The gated 90° spectrum (Fig. 5.4 (c)) shows the newly placed high energy $E2$ transitions. The negative parity Band 3 is built on $\nu h^1_{11/2}$ configuration and it exhibits a delayed crossing at $\omega \sim 0.5$ MeV as compared to Band 1 as shown in Fig. 5.7. The observed alignment gain of $6\hbar$ is lower than Band 1 and Band 2. This gain, however, is higher than the observed alignment gain of $4\hbar$ which corresponds to neutron AB crossing in this mass region. Thus, this alignment has been associated with the FG crossing.

Bands 4 and 5: These two non-yrast bands are of negative parity and have

been established for the first time. Due to the small relative intensities, they could not be extended to higher spins. These bands decay to Band 2 through $M1$ or $E2$ transitions. The inter and intra transitions of these bands have been shown in the double γ-gated spectra in Fig. 5.6.

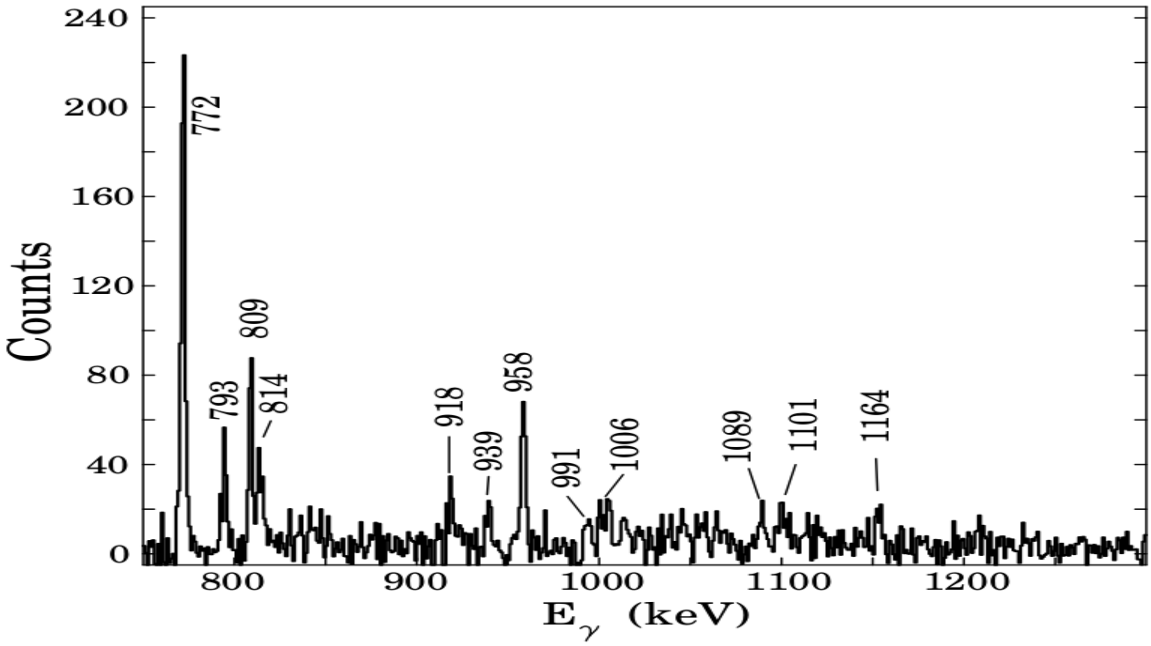

Figure 5.6: Example of γ gated spectrum from cube which established the Bands 4 and 5. The gates used are 991 keV + 603 keV and 481 keV.

Bands 6 and 7: These bands consist of low spin cascades built on the ground state. These levels have been established in the previous work [6]. The γ gated spectrum from the cube was used to identify the levels of these two bands as shown in Fig. 5.5 (b). In the present work the missing crossover $E2$ transitions could be identified. It is interesting to note that although the excited levels of this band lie quite close to those of the yrast band (Band 1), it could not be extended further.

All the transitions which are consistent with the earlier work [6] or the newly established ones, are placed in the level scheme of ^{105}Pd as shown in the Fig. 5.3. The low lying levels were placed using the $\gamma - \gamma - \gamma$ cube. The cube analysis was

necessary for low spin levels in order to suppress the contaminant γ rays from the other evaporation channels.

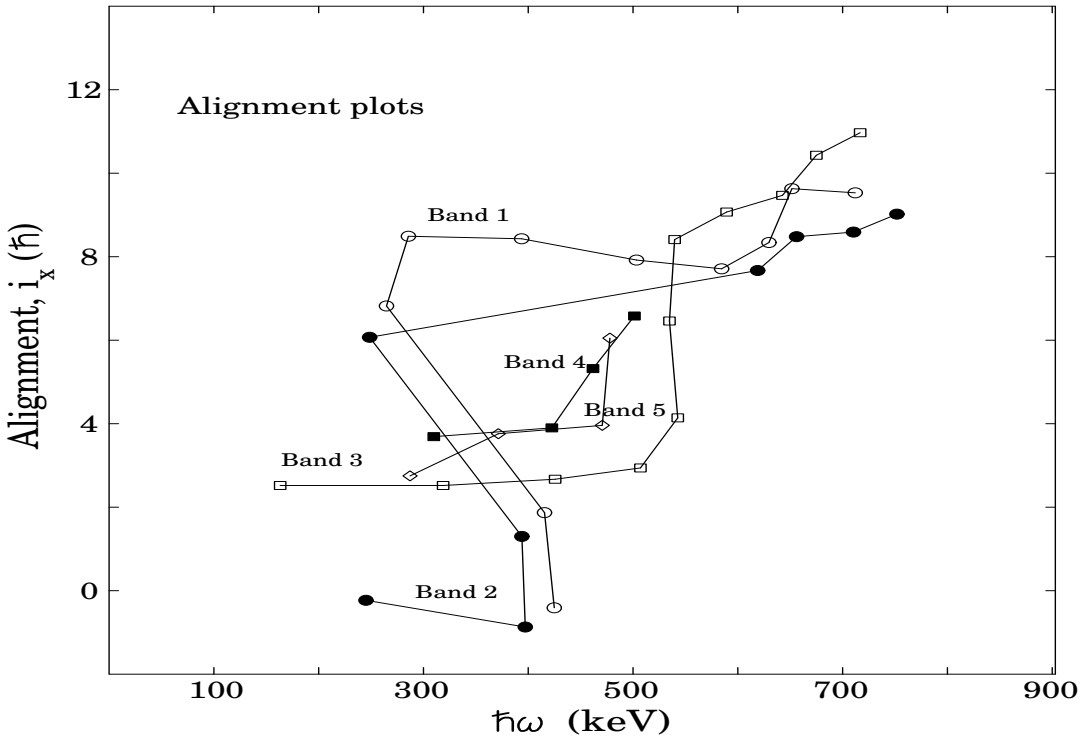

Figure 5.7: The alignment plots for the various bands of ^{105}Pd as shown in Fig. 5.3.

5.5 DSAM Analysis

The line-shapes were extracted from the projected γ-spectrum at forward (23°), backward (157°) and 90° angles by putting gates on the three asymmetric DSAM matrices. For bands Band 1, Band 2 and Band 3, the gamma gates were 539 keV, the sum gates of 727 and 455 keV and 772 keV, respectively and the line-shapes were observed from $I^{\pi} = 31/2^{+}$, $29/2^{+}$ and $19/2^{-}$ levels. As mentioned before, the level

lifetimes of the excited states of the three bands were measured using LINESHAPE analysis codes of Wells and Johnson. These codes were used to generate the velocity profiles of the recoiling nuclei using the Monte Carlo technique with a time step of 0.001 ps for 5000 histories. These profiles were generated at 23°, 90° and 157° angles. The electronic stopping power given by Northcliff and Shilling [7] with shell corrections were used for calculating energy loss of the recoiling ^{105}Pd nuclei.

The energies of the γ-transitions and the side feeding intensities were extracted from the γ-gated 90° spectra. These values have been as input parameters for the line-shape analysis. The side feeding intensity of each level and the feeding to the top most level of each band have been modeled as a cascade of five transitions with a moment of inertia which is comparable to that of the band of interest. The quadrupole moments of the side-feeding sequences were allowed to vary which when combined with the moment of inertia gave an effective side feeding lifetime for each level. For each observed line-shape, in-band and side-feeding lifetimes, background shape parameters and the intensities of the contaminant peaks (if present), were allowed to vary. The energy of the contaminant peaks were fixed from γ-gated 90° spectra. For each set of parameters the simulated line-shapes were fitted to experimental spectra using χ^2-minimization routine of MINUIT [8].

For each of the three bands, the lifetime of the topmost transition was found by assuming 100% side-feed. The other parameters were allowed to vary until the minimum χ^2 was reached. Thus the line-shape analysis for the topmost transition led to the estimation of the effective lifetime for the topmost level. For the next lower level, the effective lifetime of the topmost level and the side-feeding lifetime were considered as input parameters. In this way, each lower level was added one by one and fitted, until all the observed line-shapes of the band were included into a global fit where only the in-band and side-feeding lifetimes were allowed to vary.

This procedure of global fit was done for the three angles simultaneously.

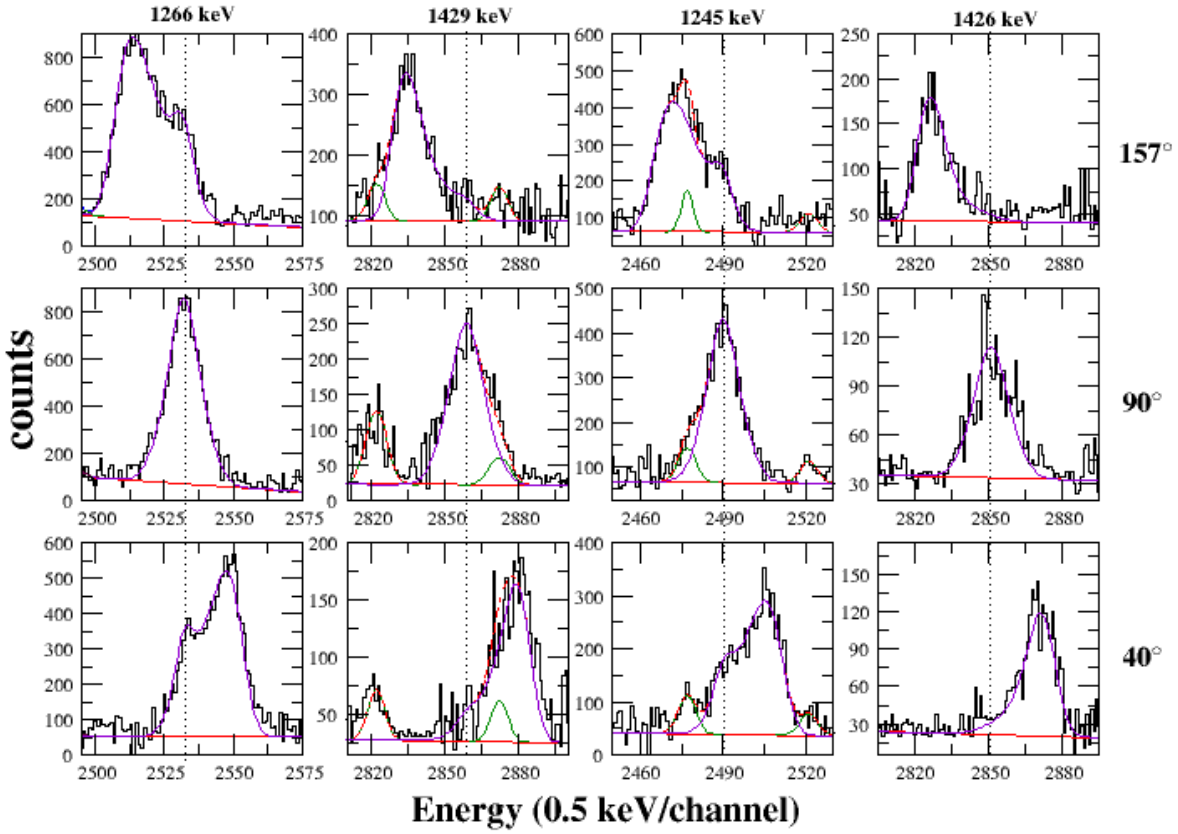

Figure 5.8: Examples of line-shape fits observed by the forward, backward and 90° detectors for ^{105}Pd. Here magenta color represents the fit to the Doppler-broadened line-shapes, green is the fit to the contaminant peak(s), and red is the fit to the total experimantal data.

The error bar on the lifetime values includes the fitting error, error in the side-feeding intensity and the side feeding lifetimes added in quadrature to constitute the net statistical error. However, there is also a systematic error contribution from the choice of stopping power used to simulate the energy loss of the recoil. The contribution of this error for ^{105}Pd is tabulated in table 5.1. The examples of the

line-shape fits are shown in Fig. 5.8. The fitted line-shapes are drawn in magenta color while the contaminant peaks are shown in green. The 90° spectra have been shown as references in order to identify the line-shapes at the forward and backward angles. The level lifetimes and the corresponding B(E2) transition rates have been listed in table 5.1.

Table 5.1: The measured lifetimes for the levels of ^{105}Pd for band 1, band 2 and band 3. It should be noted that the quoted errors are the statistical and the systematic respectively. The statistical error on each level is obtained by adding in quadrature the errors on intensity, intrinsic quadrupole moment of the level and the corresponding side-feeding quadrupole moment.

I_i^π	E_γ	I_γ	$\tau \pm stat. \pm syst.$	B(E2)$\pm stat. \pm syst.$	$\mathcal{J}^{(2)}$/B(E2)$\pm stat.$
($\hbar$)	(keV)		(ps)	$(eb)^2$	$\hbar^2 MeV^{-1}(eb)^{-2}$
			Band 1		
$35/2^+$	1014	25.3(4)	0.37±.01 ± .01	0.20±.01 ± .01	123±6
$39/2^+$	1176	16.7(4)	0.18±.01 ± .01	0.20±.01 ± .01	224±11
$43/2^+$	1266	9.3(3)	0.13±.01 ± .01	0.19±.02 ± .01	495±52
$47/2^+$	1309	4.8(2)	0.13±.01 ± .01	0.16±.02 ± .01	207±26
$51/2^+$	1429	2.4(1)	0.15±.02 ± .02	0.09±.01 ± .01	443±49
$55/2^+$	1530	1.2(1)	0.13	0.05	
			Band 2		
$33/2^+$	1001	9.1(2)	0.43±.02 ± .01	0.19±.01 ± .01	145±8
$37/2^+$	1146	7.2(2)	0.22±.01 ± .01	0.19±.01 ± .01	214±11
$41/2^+$	1245	4.3(2)	0.15±.01 ± .01	0.18±.02 ± .01	299±33
$45/2^+$	1318	1.9(1)	0.13±.01 ± .01	0.16±.01 ± .01	234±15
$49/2^+$	1426	1.0(1)	0.18±.02 ± .02	0.08±.01 ± .01	617±77
$53/2^+$	1505		0.14	0.04	
			Band 3		
$23/2^-$	958	100.0	0.58±.01 ± .01	0.17±.01 ± .01	166±10
$27/2^-$	1100	35.3(6)	0.27±.01 ± .01	0.19±.01 ± .01	406±21
$31/2^-$	1152	20.0(6)	0.22±.01 ± .01	0.18±.01 ± .01	654±36
$43/2^-$	1215	9.8(5)	0.13±.01 ± .01	0.24±.01 ± .01	161±7
$47/2^-$	1319	5.0(3)	0.09±.01 ± .01	0.23±.02 ± .02	283±25
$51/2^-$	1381	2.6(1)	0.07±.01 ± .01	0.23±.03 ± .03	218±28
$55/2^-$	1460	1.2(1)	0.07	0.18	

In Band 3, the line-shapes of 1119 keV and 1120 keV transitions overlap. Thus, it was not possible to estimate the lifetimes of $I^\pi = 35/2^-$ and $39/2^-$ levels.

The lifetimes of the lower levels ($31/2^-$, $27/2^-$ and $23/2^-$) have been estimated by assuming feeding lifetime which was estimated by fitting the collective line-shapes of 1119 and 1120 transitions with 100% side-feed. Thus, for Band 3, the fitting procedure described above has been used in two segments, one for 1381, 1319 and 1215 keV transitions where the top feeding lifetime is the effective lifetime corresponding to 1460 keV transition and the other for 1152, 1100 and 958 keV transition where the top feeding lifetime corresponds to the effective lifetime estimated from the collective line-shapes of 1119 and 1120 keV transitions.

5.6 Discussions

5.6.1 Band 1

The positive parity Band 1 is built on the single particle configuration $\nu[(g_{7/2}, d_{5/2})^1 \otimes h^2_{11/2}]$ after the neutron $h_{11/2}$ alignment. The table 5.1 shows that the $B(E2)$ values fall steadily with increasing spin. The $B(E2)$ rates were deduced from the measured level lifetimes using the equation

$$B(E2) = \frac{0.0816}{E^5_\gamma \times \tau} \tag{5.1}$$

where E_γ is the energy in MeV of a pure $E2$ transition, τ is the level lifetime in picoseconds, and $B(E2)$ is in units of $(eb)^2$. These extracted $B(E2)$ values are tabulated in Table 5.1 and have been plotted as a function of angular momentum in Fig. 5.9. In addition, the $\mathcal{J}^{(2)}/B(E2)$ values of Table 5.1 are found to be an order of magnitude larger than those for a well-deformed collective rotor [$\sim 10^2 MeV^1(eb)^2$] and increases with spin. This is expected for an antimagnetic rotation (AMR) band as the B(E2) values are small and decrease with spin while $\mathcal{J}^{(2)}$ remains nearly

constant [9]. In order to explore this possibility further, model calculations were done using SCPRM discussed in chapter 2. In this calculation for Band 1 with the above configuration $j_h^{(1)} = j_h^{(2)} = j_\pi = 9/2$ and $j_p = j_\nu = 31/2$. Thus, the shears parameters used in the present calculation were $j = 4.5\hbar$, a = 3.444, $V_{\pi\nu}$ = 1.2 MeV, and $V_{\pi\pi}$ = 0.15 MeV. It may be noted that the $V_{\pi\nu}$ and $V_{\pi\pi}$ values have been taken to be the same as in Cd isotopes [10] of the same mass region.

The good agreement of experimental and calculated $I(\omega)$ values in Fig. 5.9(b) indicates that the high spin states above 35/2 may originate due to AMR. This possibility can further be explored by calculating the $B(E2)$ transition rates for these states which are characterized by the unique shears angle (θ) values. In the present calculation eQ_{eff} was taken as 1.3 eb which corresponds to β=0.13 which can be estimated from

$$Q_0 = \frac{3}{\sqrt{5\pi}} z R_0^2 \beta (1 + 0.16\beta) \tag{5.2}$$

The SCPRM calculations agree well with the observed $B(E2)$ values and reproduces the falling trend. This simultaneous agreement for $I(\omega)$ and $B(E2)$ values establishes that the high spin states of Band 1 originate from AMR.

5.6.2 Band 2

The $I(\omega)$ and $B(E2)$ behaviors of Band 2 are similar to those for Band 1. The SCPRM calculations are again in good agreement with the experimental values as shown in Fig. 5.10. Thus, the high spin states beyond $I = 33/2$ of Band 2 also originate due to AMR.

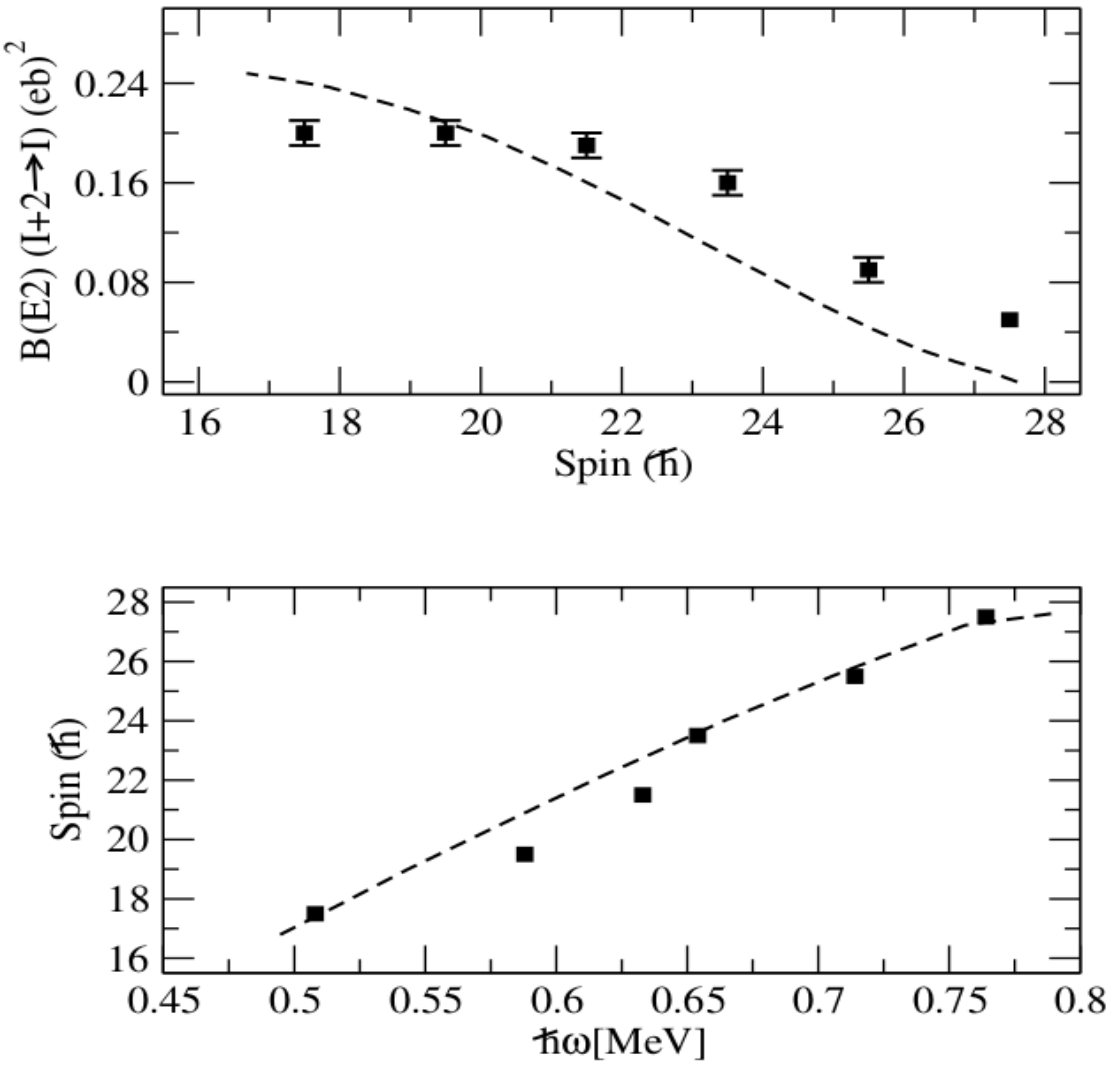

Figure 5.9: The observed $(a)B(E2)$ rates and the $(b)I(\omega)$ plot for Band 1 in ^{105}Pd. The dotted curves represent the numerical values obtained from the semi-classical particle rotor model for the parameter set as given in the text. The error bars correspond to statistical error only.

5.6.3 Band 3

It is obvious from the Fig. 5.12 that the variation of $B(E2)$ transition rate as a function of spin is completely different for this band from Band 1 and Band 2. The observed $B(E2)$ rates for this band remain nearly constant before and after the alignment of two $h_{11/2}$ neutrons (EFG configuration) which is the characteristic of

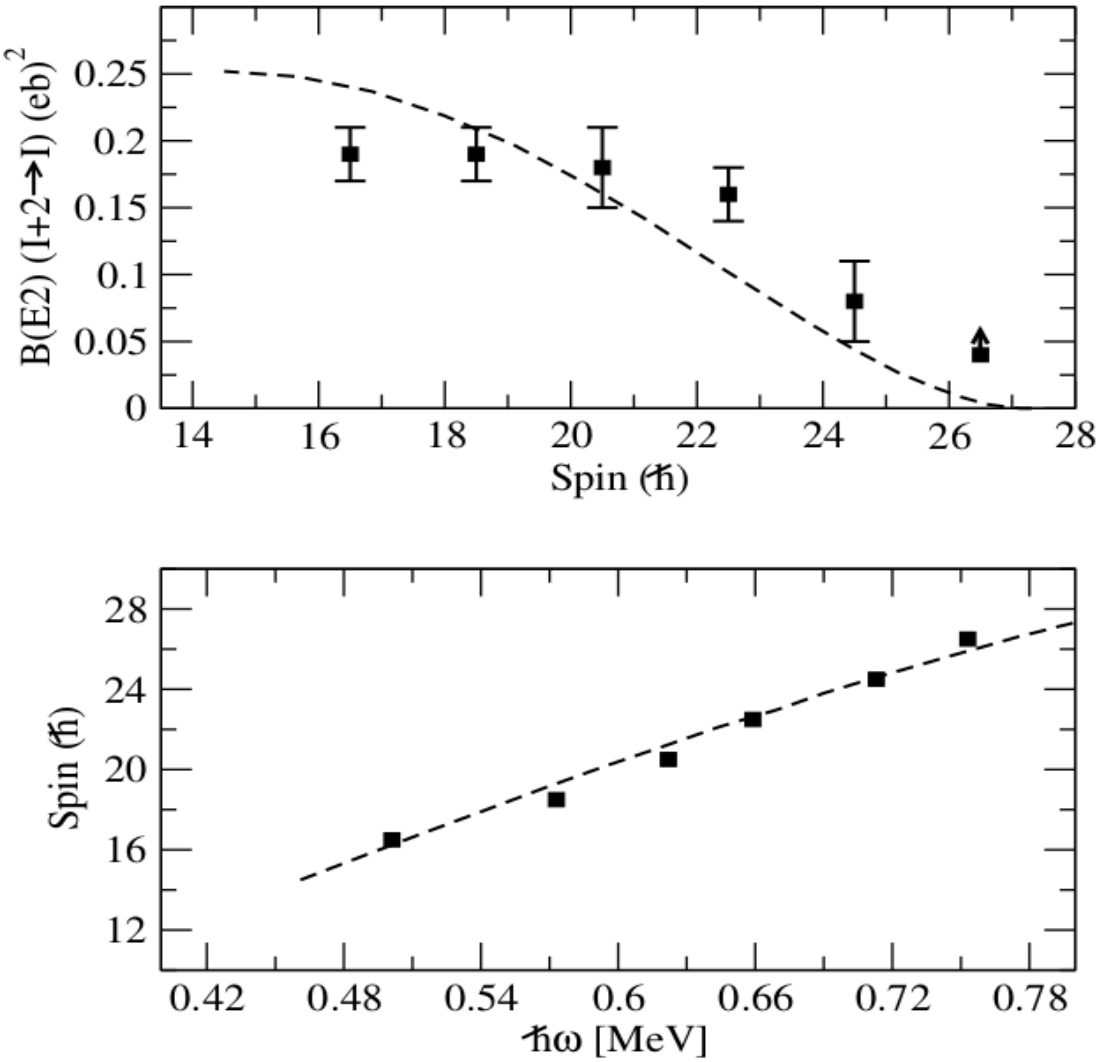

Figure 5.10: The observed $B(E2)$ rates and the $I(\omega)$ plot for Band 2 in ^{105}Pd. The lines represent the numerical values obtained from the semi-classical particle rotor model for the parameter set as given in the text. The error bars correspond to statistical error only.

collective rotation with a specific single particle configuration. The shape parameters corresponding to this collective rotation for this band can be estimated from the consistency of Q_t and $\mathcal{J}^{(1)}$ values in the spin interval of $16\hbar$ - $24\hbar$, where

$$Q_t(\beta,\gamma) = \frac{3}{\sqrt{(5\pi)}} \frac{ZeR_0^2\beta\cos(30+\gamma)}{\cos 30} \tag{5.3}$$

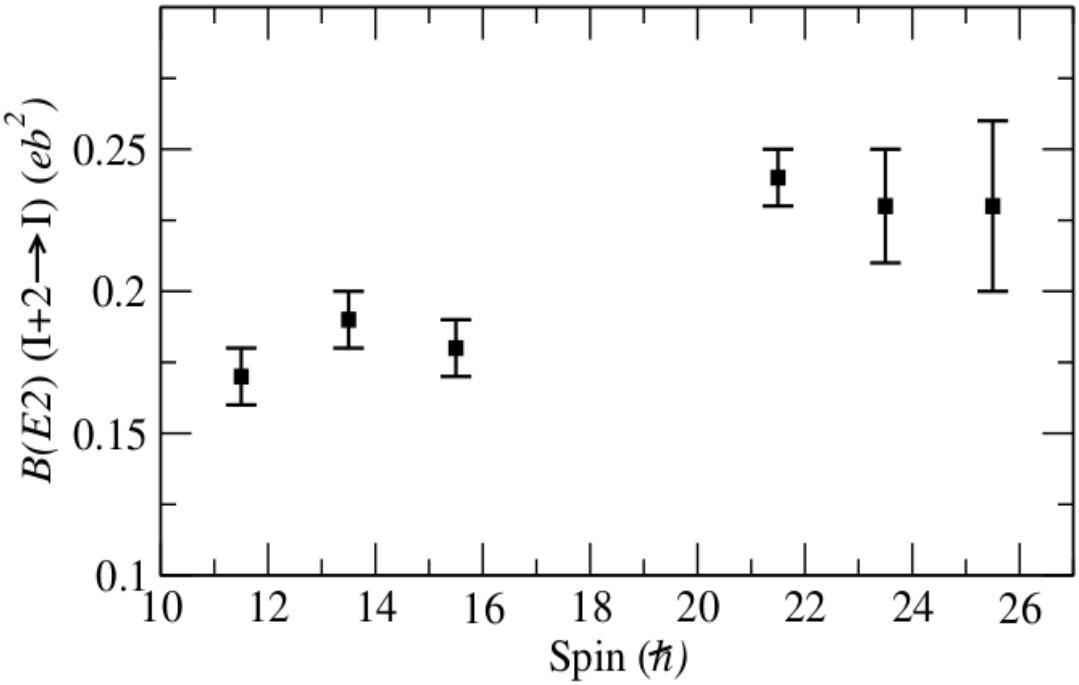

Figure 5.11: The observed $B(E2)$ rates for Band 3 in ^{105}Pd.

and,

$$\mathcal{J}^{(1)}(\beta,\gamma) = \frac{2}{5}AR_0^2\left[1-\sqrt{\frac{5}{4\pi}}\beta\cos(120+\gamma)\right] \tag{5.4}$$

The calculated values as a function of β and γ are shown in Fig. 5.12. The simultaneous consistency of the two values indicates an equilibrium deformation of $\beta = 0.19(3)$ and $\gamma = 6(4)$ for this band. Therefore, the high spin states of Band 3 between $16\hbar$ to $24\hbar$ seem to originate due to the collective rotation of a prolate shape with $\beta \sim 0.2$.

In summary, the structures of all the three bands of ^{105}Pd are quite similar and at intermediate spin, the two neutrons in $h_{11/2}$ orbital align with the rotational axis in all the bands. Thus, the neutron configuration for the Band 1 and Band 2 are AEF and BEF, respectively while Band 3 has EFG configuration. However, the

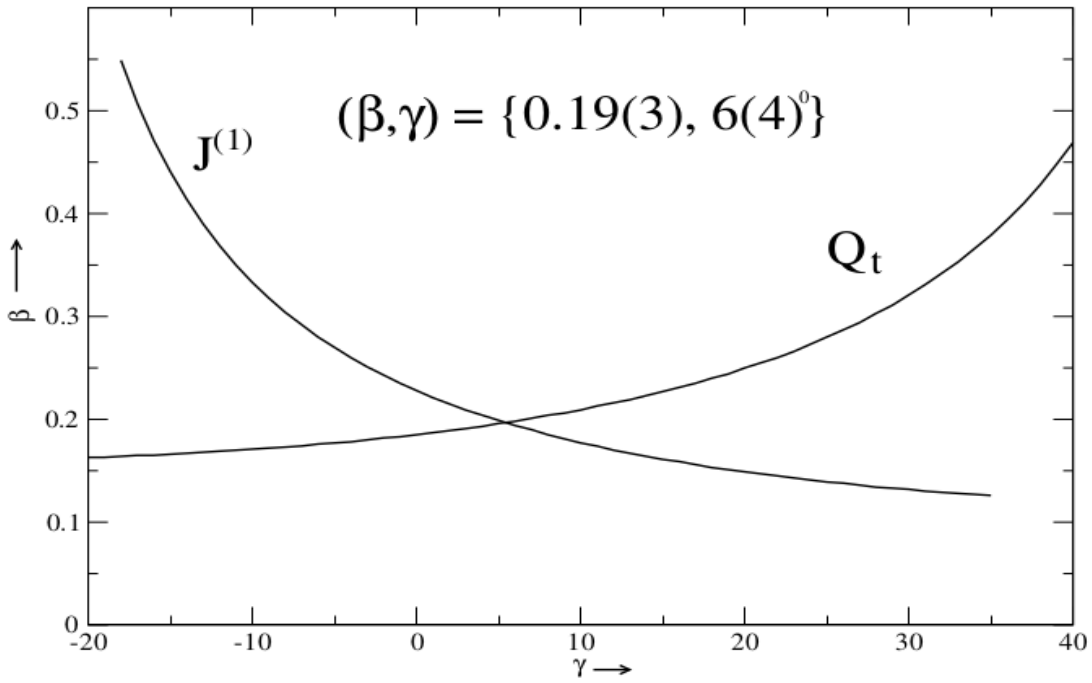

Figure 5.12: Plot of the shape parameters for the Band 3 of ^{105}Pd.

deduced electric quadrupole transition rates are significantly different for the levels of Band 1(2) and Band 3 beyond the neutron alignment. The measured $B(E2)$ values were found to decrease with the increase of angular momentum in Band 1 and 2 while they remain constant for Band 3. This experimental observation establishes the co-existence of two distinct angular momentum generation mechanisms in ^{105}Pd.

In the SCPRM model, the falling trend of $B(E2)$ is due to the simultaneous closing of the double shear which occurs due to the gradual alignment of the two proton holes along the rotational axis. The falling trend of the $B(E2)$ rates has also been explained within the framework of tilted axis cranking based on covariant density functional theory if the polarizaion effects are taken into account [11]. These calculations indicate the substantial increase in proton aligned angular momentum for the high spin states. Thus, the AMR phenomenon can be associated with the slow alignment of protons in the high Ω levels of a high-j orbital.

Thus, the reason of the co-existence can be can be associated with the alignment of proton holes (AB crossing) in Band 1 and Band 2 while for the Band 3, the proton AB crossing does not seem to take place. This difference in behavior, in turn, can be traced to tha fact that the estimated deformation for Band 3 is ∼0.19 while that for Band 1 and Band 2 is ∼0.13. This substantially large deformation may induce mixing for $g_{9/2}$ and $d_{5/2}$ proton orbitals for Band 3 which will delay the onset of proton alignment. However, these assumptions need to be tested within a model framework like Projected Shell Model (PSM) calculations.

Table 5.2: Energies, relative intensities, DCO ratios, linear polarizations and the deduced multi-polarities of transitions assigned to the ^{105}Pd in the present work.

$I_i^\pi \rightarrow I_f^\pi(\hbar)$	$E_\gamma(KeV)$	I_γ	$RDCO$	P	$Mult.$
$11/2^- \rightarrow 7/2^+$	183	...			
$17/2^- \rightarrow 15/2^-$	198	1.3(3)			
$19/2^+ \rightarrow 17/2^+$	204	1.0(2)			
$11/2^+ \rightarrow 9/2^+$	230	230	0.7(3)		
$15/2^+ \rightarrow 13/2^+$	231	0.5(3)	0.60(3)		D
$25/2^+ \rightarrow 23/2^+$	233	0.6(3)			
$31/2^- \rightarrow 31/2^-$	252	0.6(2)			
$19/2^+ \rightarrow 17/2^+$	255	6.5(2)	0.52(4)		D
$21/2^+ \rightarrow 19/2^+$	266	0.5(2)			
$7/2^+ \rightarrow 5/2^+$	306	...	0.64(1)	-0.04(3)	M1
$21/2^+ \rightarrow 19/2^+$	313	4.8(2)	0.49(4)		D
$21/2^+ \rightarrow 19/2^+$	317	0.3(2)	0.59(3)	-0.27(3)	M1
$5/2^+ \rightarrow 5/2^+$	319	...			
$9/2^+ \rightarrow 7/2^+$	340	7.1(2)	0.54(4)	-0.13(2)	M1
$23/2^+ \rightarrow 21/2^+$	349	3.6(2)	0.49(3)		D

Table 5.2 – *Continued from previous page*

$I_i^\pi \rightarrow I_f^\pi(\hbar)$	$E_\gamma(KeV)$	I_γ	$RDCO$	P	$Mult.$
$21/2^+ \rightarrow 19/2^+$	364	0.7(3)			
$27/2^- \rightarrow 27/2^-$	359	1.1(2)			
$17/2^+ \rightarrow 15/2^+$	368	0.6(2)			
$21/2^+ \rightarrow 23/2^-$	373	0.8(3)			
$23/2^- \rightarrow 21/2^-$	378	1.2(2)			
$29/2^+ \rightarrow 27/2^+$	381	0.4(3)			
$19/2^- \rightarrow 17/2^-$	384	0.6(2)			
$13/2^+ \rightarrow 11/2^+$	400	4.4(3)	0.51(3)	-0.08(3)	M1
$21/2^- \rightarrow 19/2^-$	431	0.3(3)			
$7/2^+ \rightarrow 5/2^+$	442	...	0.49(3)	-0.09(3)	M1
$23/2^- \rightarrow 23/2^-$	453	1.9(2)			
$29/2^+ \rightarrow 27/2^-$	455	0.7(3)	0.57(5)	0.12(3)	E1
$25/2^+ \rightarrow 21/2^+$	455	8.1(1)	1.12(3)	0.10(2)	E2
$9/2^+ \rightarrow 7/2^+$	459	1.2(2)	0.51(4)	-0.05(2)	M1
$27/2^- \rightarrow 25/2^-$	465	0.2(2)			
$15/2^- \rightarrow 11/2^-$	481	100	1.18(1)	0.15(2)	E2
$11/2^+ \rightarrow 9/2^+$	489	3.2(2)	0.57(5)	0.07(2)	M1
$21/2^+ \rightarrow 17/2^+$	508	7.7(3)	0.98(3)	0.13(3)	E2
$21/2^+ \rightarrow 17/2^+$	521	1.1(2)	1.16(4)	0.06(4)	E2
$23/2^+ \rightarrow 19/2^+$	539	14.0(1)	1.04(1)	0.16(3)	E2
$25/2^- \rightarrow 23/2^-$	541	0.7(3)			
$21/2^+ \rightarrow 17/2^+$	568	0.7(3)			

Table 5.2 – *Continued from previous page*

$I_i^\pi \rightarrow I_f^\pi(\hbar)$	$E_\gamma(KeV)$	I_γ	$RDCO$	P	$Mult.$
$27/2^+ \rightarrow 23/2^+$	579	12.5(2)	1.04(1)	0.15(3)	E2
$9/2^+ \rightarrow 5/2^+$	582	1.8(2)	0.94(3)	0.08(3)	E2
$19/2^- \rightarrow 15/2^-$	582	3.2(1)			
$9/2^+ \rightarrow 7/2^+$	595	4.4(2)	0.54(1)	-0.08(5)	M1
$23/2^+ \rightarrow 23/2^-$	595	1.6(2)			
$19/2^- \rightarrow 19/2^-$	603	3.2(2)	0.99(1)	0.09(3)	E2
$17/2^+ \rightarrow 15/2^+$	650	0.7(2)			
$23/2^+ \rightarrow 19/2^+$	662	1.4(2)			
$17/2^+ \rightarrow 15/2^+$	663	0.7(2)			
$27/2^+ \rightarrow 25/2^+$	678	0.4(2)	0.56(5)	-0.06(2)	M1
$11/2^+ \rightarrow 7/2^+$	706	24.4(1)	1.04(1)	0.11(2)	E2
$29/2^+ \rightarrow 25/2^+$	727	6.6(1)	1.03(1)	0.17(3)	E2
$13/2^+ \rightarrow 11/2^+$	737	0.9(2)	0.54(2)	-0.07(2)	M1
$27/2^+ \rightarrow 23/2^+$	737	2.2(2)			
$19/2^- \rightarrow 15/2^-$	772	71.8(1)	0.98(1)	0.07(1)	E2
$31/2^+ \rightarrow 29/2^+$	777	0.5(3)	0.54(3)	-0.04(2)	M1
$9/2^+ \rightarrow 5/2^+$	782	8.0(1)	1.09(2)	0.08(2)	E2
$15/2^- \rightarrow 15/2^-$	793	3.7(1)			
$31/2^+ \rightarrow 27/2^+$	795	11.6(1)	0.95(1)	0.17(3)	E2
$23/2^- \rightarrow 19/2^-$	809	2.1(2)	1.01(3)	0.22(6)	E2
$21/2^- \rightarrow 17/2^-$	814	2.3(2)			
$17/2^+ \rightarrow 13/2^+$	816	1.7(2)	1.02(1)	0.08(6)	E2

Table 5.2 – *Continued from previous page*

$I_i^\pi \rightarrow I_f^\pi(\hbar)$	$E_\gamma(KeV)$	I_γ	$RDCO$	P	$Mult.$
$31/2^+ \rightarrow 27/2^+$	826	2.1(2)			
$25/2^+ \rightarrow 23/2^-$	828	2.3(1)	0.64(3)	0.17(4)	E1
$11/2^+ \rightarrow 7/2^+$	829	6.0(1)			
$35/2^+ \rightarrow 33/2^+$	830	0.4(3)			
$13/2^+ \rightarrow 9/2^+$	848	4.4(1)	0.93(4)	0.12(2)	E2
$19/2^+ \rightarrow 15/2^+$	854	15.7(2)	0.95(1)	0.13(2)	E2
$17/2^+ \rightarrow 13/2^+$	881	6.1(2)	1.16(3)	0.08(2)	E2
$13/2^+ \rightarrow 9/2^+$	889	10.2(1)			
$15/2^+ \rightarrow 11/2^+$	890	17.5(2)	0.92(3)	0.10(2)	E2
$17/2^+ \rightarrow 13/2^+$	894	5.1(1)	1.09(3)	0.10(2)	E2
$19/2^+ \rightarrow 15/2^+$	905	0.8(2)	1.16(8)	0.07(3)	E2
$25/2^- \rightarrow 21/2^-$	918	1.3(2)	0.95(5)	0.14(3)	E2
$15/2^+ \rightarrow 11/2^+$	926	2.8(2)			
$15/2^+ \rightarrow 15/2^+$	932	1.1(2)			
$23/2^- \rightarrow 19/2^-$	958	41.9(3)	1.03(1)	0.08(2)	E2
$13/2^+ \rightarrow 9/2^+$	967	1.0(2)			
$17/2^- \rightarrow 15/2^-$	991	5.7(2)	1.11(4)	-0.16(3)	Mx*
$25/2^- \rightarrow 23/2^-$	994	3.1(2)	1.01(4)	-0.12(4)	Mx
$33/2^+ \rightarrow 29/2^+$	1001	3.8(2)	0.83(4)	0.05(3)	E2
$27/2^- \rightarrow 23/2^-$	1006	1.7(2)	0.94(6)	0.11(3)	E2
$35/2^+ \rightarrow 31/2^+$	1014	10.6(1)	0.87(5)	0.13(3)	E2
$19/2^+ \rightarrow 13/2^+$	1015	2.1(2)	0.55(3)		

Table 5.2 – *Continued from previous page*

$I_i^\pi \rightarrow I_f^\pi(\hbar)$		$E_\gamma(KeV)$	I_γ	$RDCO$	P	$Mult.$
$21/2^-$	$\rightarrow$	1034	5.3(1)	1.00(3)	-0.08(5)	Mx
$19/2^-$						
$31/2^-$	$\rightarrow$	1046	0.4(3)			
$27/2^-$						
$35/2^+$	$\rightarrow$	1054	1.6(2)			
$31/2^+$						
$29/2^-$	$\rightarrow$	1089	0.6(2)	1.03(6)	0.06(4)	E2
$25/2^-$						
$27/2^-$	$\rightarrow$	1100	14.8(1)	0.98(3)	0.07(1)	E2
$23/2^-$						
$35/2^-$	$\rightarrow$	1101	0.3(2)			
$31/2^-$						
$35/2^-$	$\rightarrow$	1120	9.8(2)	0.79(4)	0.04(2)	E2
$31/2^-$						
$37/2^+$	$\rightarrow$	1146	2.7(2)			
$33/2^+$						
$31/2^-$	$\rightarrow$	1152	8.4(2)	0.94(3)	0.03(2)	E2
$27/2^-$						
$33/2^-$	$\rightarrow$	1164	0.4(2)	0.99(5)	0.05(3)	E2
$29/2^-$						
$39/2^+$	$\rightarrow$	1176	7.3(2)			
$35/2^+$						
$43/2^-$	$\rightarrow$	1215	3.0(3)			
$39/2^-$						
$41/2^+$	$\rightarrow$	1245	1.7(2)			
$37/2^+$						
$43/2^+$	$\rightarrow$	1266	4.6(2)			
$39/2^+$						
$15/2^-$	$\rightarrow$	1274	2.5(2)			
$11/2^-$						
$47/2^+$	$\rightarrow$	1309	2.5(3)			
$43/2^+$						
$45/2^+$	$\rightarrow$	1318	1.0(2)			
$41/2^+$						
$47/2^-$	$\rightarrow$	1319	1.9(2)			
$43/2^-$						
$21/2^+$	$\rightarrow$	1331	5.7(2)	0.54(2)	0.07(3)	E1
$19/2^-$						
$21/2^+$	$\rightarrow$	1378	1.3(3)			
$13/2^+$						

Table 5.2 – *Continued from previous page*

$I_i^\pi \rightarrow I_f^\pi(\hbar)$		$E_\gamma(KeV)$	I_γ	$RDCO$	P	$Mult.$
$51/2^-$	$\rightarrow$	1381	0.9(2)			
$47/2^-$						
$49/2^+$	$\rightarrow$	1426	0.6(2)			
$45/2^+$						
$51/2^+$	$\rightarrow$	1429	1.3(2)			
$47/2^+$						
$55/2^-$	$\rightarrow$	1460	0.5(3)			
$51/2^-$						
$53/2^+$	$\rightarrow$	1505	0.3(2)			
$49/2^+$						
$55/2^+$	$\rightarrow$	1530	0.6(2)			
$51/2^+$						

Bibliography

[1] Deepika Choudhury *et al.*, Phys. Rev. C **87**, 034304 (2013).

[2] S. Muralithar *et al.*, Nucl. Intrum. Methods A (2010).

[3] R. Palit *et al.*, Nucl. Instrum. Methods Phys. Res., Sect. A **680**, 90 (2012).

[4] Ch. Droste, S.G. Rohozinski, K. Starosta, T. Morek, J. Srebrny, P. Magierski, Nucl. Instr. and Meth. A **378** 518 (1996).

[5] J. C. Wells and N. R. Johnson, Oak Ridge National Laboratory Report No. ORNL-6689, (1991).

[6] F. A. Rickey *et al.*, Phys. Rev. C, **15**, No. 4, 1530 (1977).

[7] L. C. Northcliffe and R. F. Schilling, At. Data Nucl. Data Tables **7**, 233 (1970).

[8] F. James and M. Roos, Comput. Phys. Commun. **10**, 343 (1975).

[9] A. J. Simons, *et al.*, Phys. Rev. Lett. **91** 162501 (2003).

[10] S. Roy, *et al.*, Phys. Lett. **B** 694 322 (2011).

[11] P. W. Zhao, J. Peng, H. Z. Liang, P. Ring, J. Meng, Phys. Rev. Lett. **107**, 122501 (2011)

Chapter 6

Angular Momentum Generation Mechanism in ^{106}Ag

6.1 Introduction

In this chapter, the high spin level structure of ^{106}Ag has been discussed which is the odd-odd neighbor of ^{104,105}Pd. Since this nucleus is the isotone of ^{105}Pd, it will be interesting to explore the effect of the odd proton in $g_{9/2}$ orbital.

It has already been established that the observed signature splitting in ^{109,110}Ag can only be accounted by assuming triaxial deformation in these nuclei [1]. In addition, all the Ag isotopes have doublet bands and in most of the cases their moments of inertia are different. But in none of these bands, the transition rates have been measured. It may also be noted that the ground state band of ^{104}Ag was found to originate due to Shears mechanism [2] while the same band in ^{110}Ag originates due to collective rotation of a triaxial core [1]. So it is also interesting to measure the transition rates in the ground state band of ^{106}Ag in order to ascertain

whether it originates due to the Shears mechanism or due to the collective rotation.

With these motivations, the high spin states of ^{106}Ag were populated through ^{96}Zr(^{14}N, 4n) reaction using the 68 MeV ^{14}N beam from the 14-UD Pelletron at TIFR. The count rate in this experimrnt was about 760 Hz and the peak-to-Compton ratio for this experiment was similar to that for the previous experiment. The experimental details to establish its level scheme has already been discussed in chapter 3 in detail.

The partial level scheme of ^{106}Ag shown in Fig. 6.1, was built by analyzing the information from the different double γ gated spectra obtained from the $\gamma - \gamma - \gamma$ cube. The intensities of the γ rays de-exciting the high spin states were estimated from the 90°-vs-all matrix. The gated spectra at 90° corresponding to the Band 1 and Band 2 are shown in Fig. 6.2, while Fig. 6.3 shows such 90° projected spectra for the Band 3 and Band 4. It may be noted from the insets of these figures that the discrete γ transitions with energies up to 1500 keV are clearly visible in these gates.

The partial level scheme established from the present analysis has four high spin bands of which the positive parity ground state band has been established up to I^{π}=26^{+} while the three negative parity bands have been established up to I^{π}=19^{-} (Band 1), 22^{-} (Band 2) and 24^{-} (Band 3).

The intensities, multipolarities and the parities of the γ transitions determined from the present work are tabulated in Table 6.4. There is a high degree of correlation among the different excited levels of the four bands as each band de-excites to the low spin levels through multiple transitions and for all the high spin states, the cross over $E2$ transition corresponds to a pair of $M1$ transitions. Thus, the present partial level scheme has been well established.

In order to investigate the origin of these four bands, the lifetimes of all the

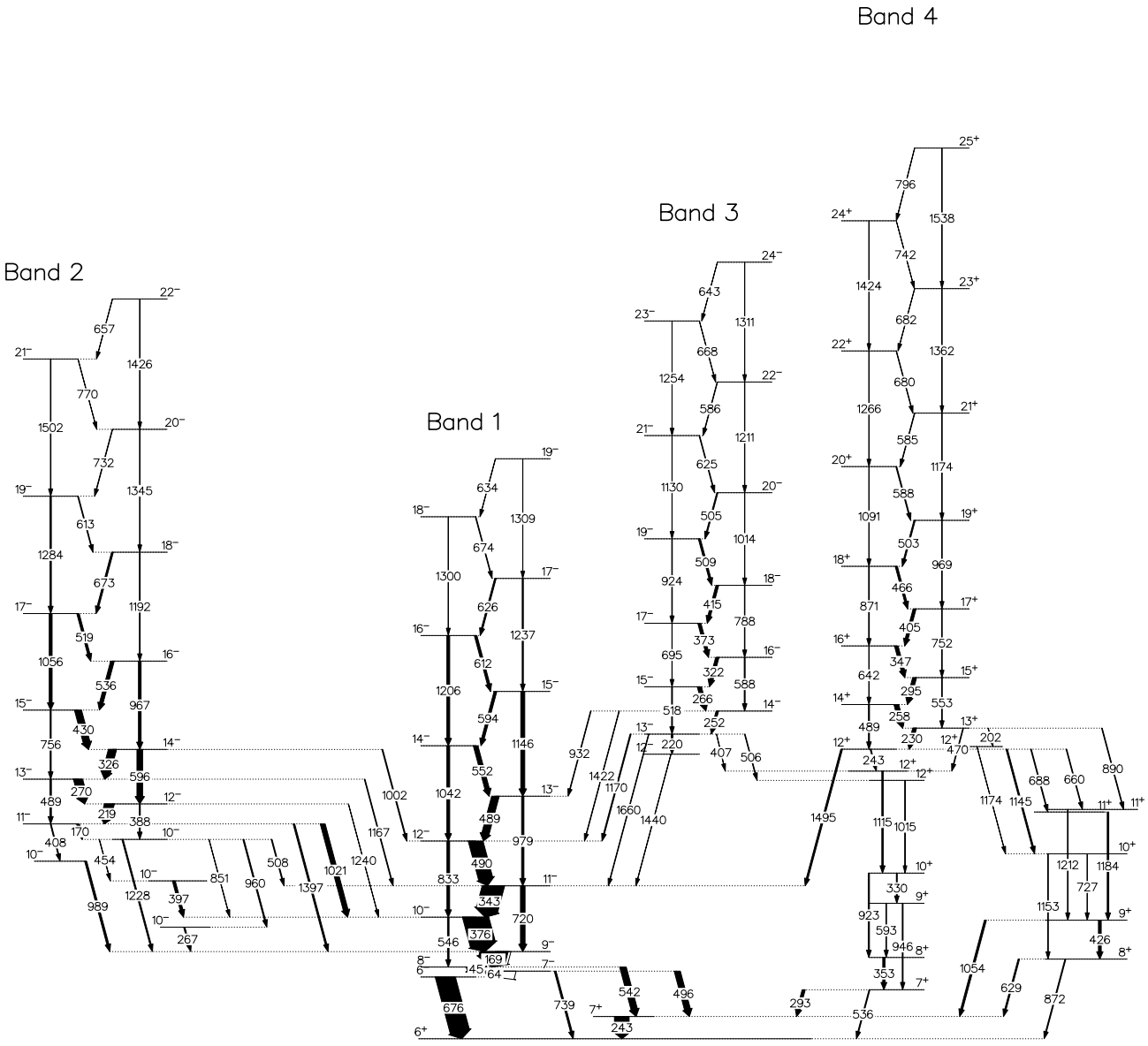

Figure 6.1: The partial level scheme of ^{106}Ag that was established from the present analysis.

excited levels have been measured through the DSAM technique. This technique of measuring the level lifetimes through line-shape fitting has been discussed in detail in chapter 3.

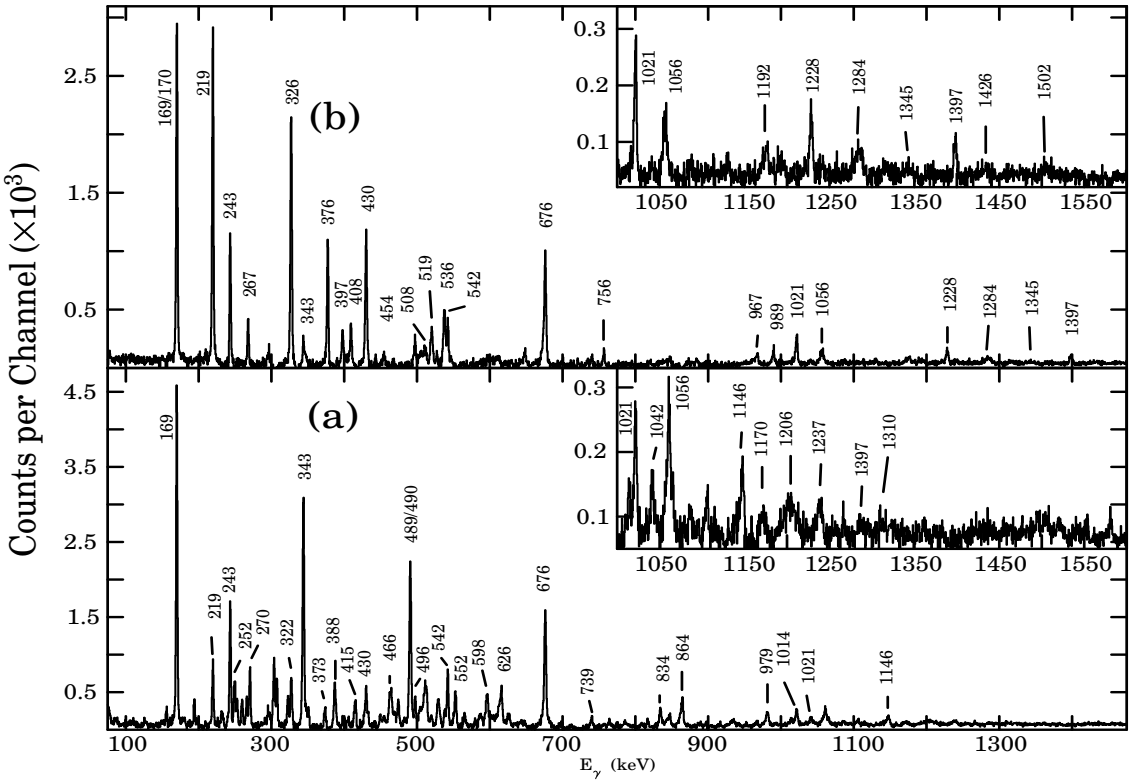

Figure 6.2: The 90° projected gamma gated spectra for Band 1 and Band 2 are shown in (a) and (b) respectively. The γ gates used are (a) 376 keV and (b) 270 keV. The high energy sectors of the spectra are shown in the insets.

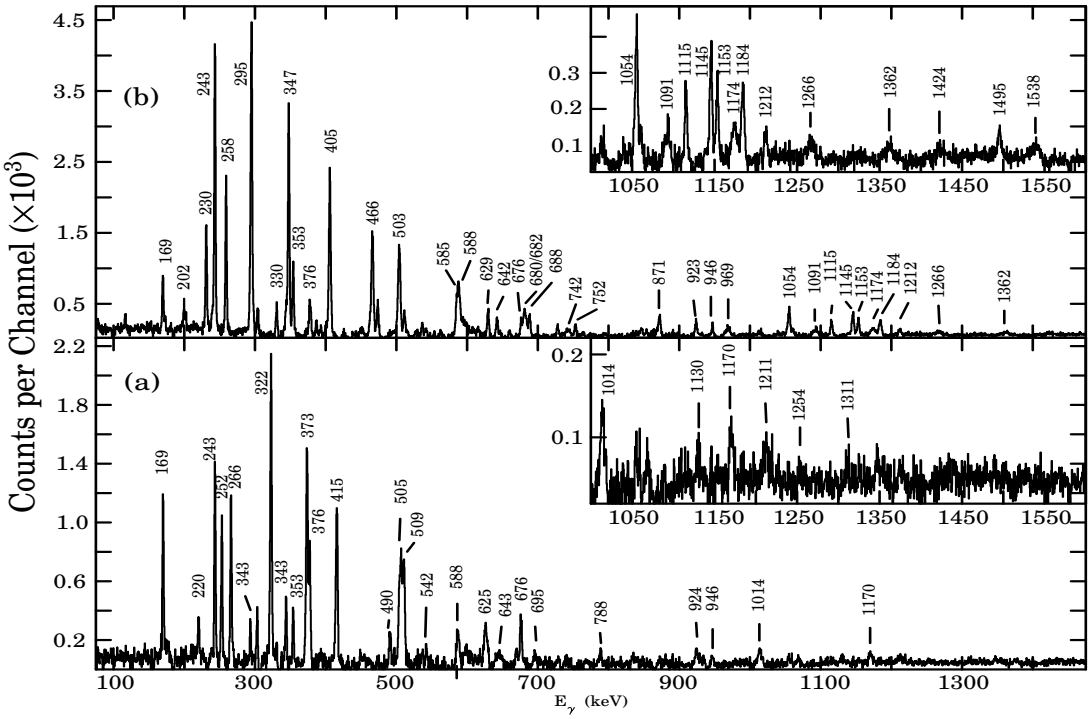

Figure 6.3: The 90° projected gamma gated spectra for Band 3 (a) and Band 4 (b). The γ gates used are (a) 252 keV + 266 keV and (b) 230 keV + 258 keV. The high energy sectors of the spectra are shown in the insets.

6.2 Band 1 and Band 2

Bands 1 and 2 are two well studied bands in recent times [3, 4, 5]. The present work confirms the placement of the γ-rays in these two bands along with their spin and parity assignments. Band 2 has been extended to I^{π}=22^{-} by adding two more $M1$ transitions of energy 772.9 and 658.9 keV, respectively. The corresponding cross-over $E2$ of energy 1431.8 keV has also been observed. These two bands form a doublet due to the near degeneracy in the level energy and the spin. The Band 1 is yrast at low spin and has been considered as the main band while the Band 2 is its partner.

The band structures of the doublet have been depicted in Fig. 6.4 through the $E(I)$ plot where the solid line is for the eye guidance. It is observed from the figure that the moments of inertia of the two bands are different as they cross diabetically around I = $14\hbar$. This crossing is an unique feature of ^{106}Ag among all the doublet bands reported in the A$\sim$100 [3, 6, 7, 8] region.

For two bands to be the chiral partners (spin chirality has been discussed in detail in chapter 2), these bands should exhibit nearly similar moment of inertia, quasi-particle alignment, signature staggering behavior and, more importantly, the transition probabilities. Indeed the nuclei of ^{134}Pr [9, 10] and ^{104}Rh [11] show the closest degeneracy in energy in the observed doublet bands over a wide angular momentum domain. However, in both cases the quasi-particle alignment behavior has been found to be different which indicates different shapes associated with the two bands. This has been supported by dissimilar behavior of the measured B(E2) rates in the two bands of ^{134}Pr [12] which rules out the possibility of static chirality. The experimental transition rates could, however, be reproduced within an interacting boson-fermion-fermion model (IBFFM) framework by assuming a triaxial equilibrium deformation with fluctuation in shape around this value. Such a model would imply

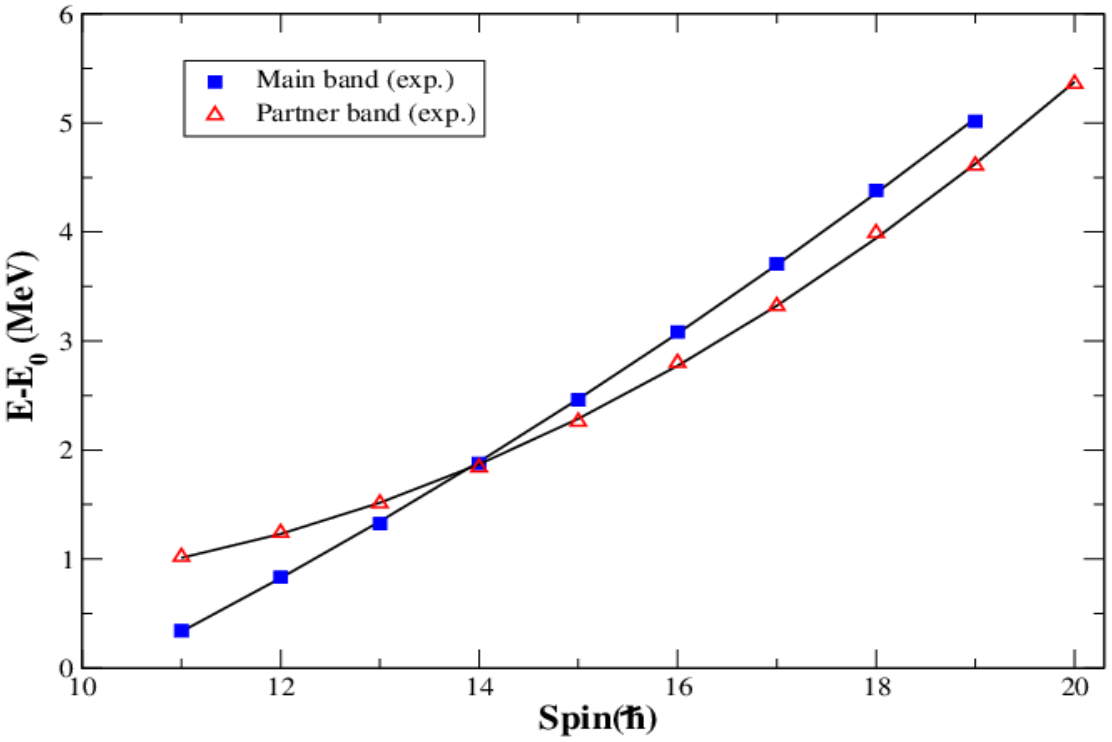

Figure 6.4: The experimental routhian plots for the doublet of ^{106}Ag (Bands 1 and 2). The solid lines connecting the points are for the eye guidance.

that the nuclear system will fluctuate between chiral and achiral configurations [12].

An alternate view on the origin of doublet bands has emerged based on the framework of the tilted axis cranking (TAC) model complemented by the random phase approximation (RPA) and its success in describing the experimental data in ^{135,136}Nd [13, 14]. In this model, the doublet bands correspond to zero RPA phonon and the one RPA phonon configurations, respectively. The lowest RPA phonon energy accounts for the energy difference between the two bands near the band head and originates due to fluctuation in the orientation of shape perpendicular to the plane of neutron and proton angular momenta. Such chiral vibrations decrease with increasing angular momentum which results in the decrease of energy spacing between the doublet bands. This situation has been realized in ^{128}Cs [15] and ^{135}Nd [13] which

may indicate the onset of chiral rotation at high spins. In both these nuclei, the transition rates for the doublet have been measured to be very similar and thus, are considered as the best candidates for chiral partner bands.

This picture opens up the possibility of a shape transformation in a γ-soft nucleus due to the chiral vibrations. In this case, the shape corresponding to the main band can be quite different from its partner band (one phonon configuration). The experimental data on the doublet bands in ^{106}Ag has been interpreted in this way where the possible deformation parameters for the main and the partner bands were found to be (β, γ) = (0.12, 28^0) and (0.20, 0^0), respectively, from Total Routhian Surface (TRS) calculations [3]. This picture gives an intuitive explanation for the existence of doublet bands with different moments of inertia and quasi-particle alignment behavior.

In a recent publication [16], Ma *et al*. have proposed that the doublet bands in ^{106}Ag may originate due to two different quasi-particle structures, namely $\pi(g_{9/2})^1 \otimes \nu(h_{11/2})^1$ for the main and $\pi(g_{9/2})^1 \otimes \nu(h_{11/2})^3$ for the partner band. However, the band crossing at $I = 18\ \hbar$ predicted by the Cranked Nilsson Strutinsky (CNS) calculations is substantially higher than the observed crossing at 14 $\hbar$. In addition, a preliminary B(E2) transition rates measurement [17] has been cited by Ma *et al*.. These reported B(E2) values for partner band have large uncertainty of $\gtrsim 50\%$. This measurement is consistent with both CNS prediction with fixed "K" value of 6 as well as with the previous interpretation [3] of triaxial and axial prolate shapes for the doublets. In addition, no B(M1) value has been reported which is essential to determine the quasi-particle structure of the doublet bands. Thus, the previous investigations [3, 16] on the origin of the doublet bands of ^{106}Ag have indicated two contrasting possibilities, namely, distinct shapes or distinct quasi-particle structures. In order to resolve this issue, the accurate measurement of transition rates in the doublet bands of the A$\sim$100

region in ^{106}Ag was necessary.

For the main band, the effective lifetimes for the 18^- and 19^- levels were found by fitting the line-shapes for 1309 ($19^- \rightarrow 17^-$) and 1300 ($18^- \rightarrow 16^-$) keV γ-transitions by assuming 100% side-feed. The top feed lifetime for 17^- level was assumed to be the intensity weighted average of the lifetimes for 18^- and 19^- levels since this level was fed by both 674 ($18^- \rightarrow 17^-$) and 1309 keV γ rays. The side feeding intensity at this level was fixed to reproduce the observed intensity pattern at 90° with respect to the beam direction. In this way each lower level was added one by one and fitted until all the observed line-shapes for 1206 ($16^- \rightarrow 14^-$), 1146 ($15^- \rightarrow 13^-$), 1042 ($14^- \rightarrow 12^-$) and 979 ($13^- \rightarrow 11^-$) keV γ rays were included into a global fit where only the in-band and feeding lifetimes were allowed to vary. The uncertainties in the measured lifetimes were derived from the behavior of χ^2 in the vicinity of the minimum for the simultaneous fit at the two angles. The lifetime for the 12^- level was measured by fitting the line-shape of 833 ($12^- \rightarrow 10^-$) keV γ ray extracted from the top gate of 490 keV. This was done to avoid the large feed to this level from other non-yrast states. In this case, the observed line-shape was fitted by taking into account the complete top cascade but no side feeding at 12^- level was considered. In order to cross-check the consistency of the level lifetime measurements from the top and the bottom gates in ^{106}Ag, the line-shape of 979 ($13^- \rightarrow 11^-$) keV transition was extracted from the 552 ($14^- \rightarrow 13^-$) keV gate and was fitted. The results from the top and the bottom gates were found to agree within $\pm$ 1 σ.

All these levels decay by ΔI=1 transitions also and their line-shapes were fitted following the same prescription except for 490 ($13^- \rightarrow 12^-$) and 489 ($12^- \rightarrow 11^-$) keV γ rays since their line-shapes overlapped. Thus, for most of the levels, the final values for the lifetimes were determined from the average of the values obtained from the independent fits to the two de-exciting transitions. The corresponding uncertainty

on a level lifetime has been calculated as the average of the uncertainties for the independent lifetime measurements for that level added in quadrature. However, it should be noted that the quoted errors do not include the systematic errors on the stopping power values which may be as large as 20%.

In an earlier work by Volkov *et al*. the lifetimes of the low spin levels from $8^{-}\hbar$ to $13^{-}\hbar$ of the main band of ^{106}Ag were measured using the Recoil-distance Doppler-shift Method (RDM) [18]. The reported value of lifetime for the 12^{-} level was 0.32(11) ps which has been the same as obtained in the present work. However, the reported value of 0.39(14) ps for the 13^{-} level was probably the effective lifetime and thus did not match with the present work.

The same method of line-shape analysis was followed for the levels of the partner band. The 14^{-} level lifetime was extracted from 326 keV ΔI=1 transition since the corresponding line-shape of cross-over $E2$ transition of 597 keV could be contaminated due to the presence of Ge(n, n$'\gamma$) reaction. The intensity ratio of the inter-band to the intra-band ΔI=1 transition for the 14^{-} level of the partner band was found to be 0.31(2). For the other levels whose lifetimes have been measured, the intensities of the inter-band ΔI=1 transitions could not be determined due to inadequate statistics in the 90° matrix. Examples of the line-shape fits in ^{106}Ag are shown in Fig. 6.5.

In order to deduce the $B(M1)$ rates from the measured level lifetimes, it was essential to estimate the mixing ratios (δ) for the ΔI = 1 transitions. For the present fusion evaporation reaction, the width of the sub-state population σ/j was estimated to be 0.3 from the DCO ratios of electric dipole and quadrupole transitions of ^{106}Ag. The mixing ratio for the ΔI=1 transitions were, then, estimated from the measured DCO values using $\sigma/j = 0.3$. These calculations were performed using the program ANGCOR [19]. It could be estimated that a 15% variation of σ/j value leads to a 10% systematic error on the mixing ratios. The values of the mixing ratio, along

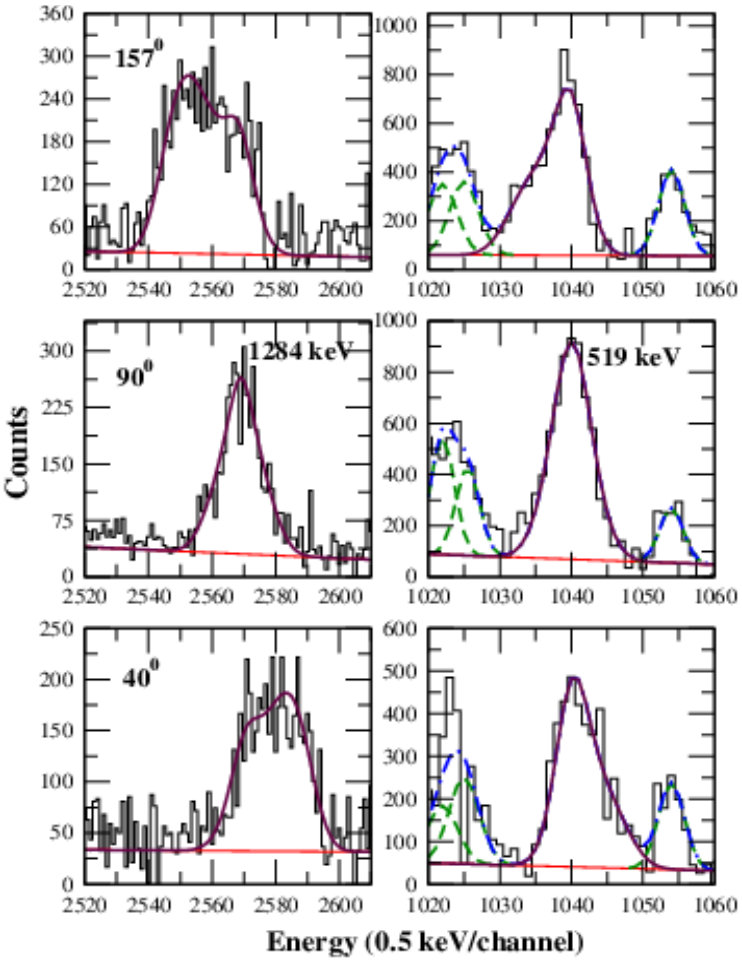

Figure 6.5: Examples of the line-shape fits for 1284 ($19^- \rightarrow 17^-$) keV and 519 ($17^- \rightarrow 16^-$) keV transitions at 40^0 and 157^0 with respect to the beam direction. The Doppler broadened line-shapes are drawn in solid lines while the contaminant peaks are shown in dotted lines. The result of the fit to the experimental data is shown in dashed lines.

with the level lifetime and the branching ratio for each level of the main and the partner bands have been tabulated in table 6.1. The uncertainties of the mixing ratios have been estimated by considering the extremum values of the uncertainties in the corresponding DCO values. It was found that the value of the mixing ratio doubles around the band crossing spin of I = $14\hbar$. The $B(M1)$ and $B(E2, I \rightarrow I-1)$ values of each level have been extracted from the corresponding level lifetime, branching and mixing ratios. The uncertainties on the deduced rates were calculated from the quadrature addition of the individual uncertainties on the rates due to these

three factors. For the three levels of the main band whose mixing ratios were not estimated, the maximum possible value for B(M1) rates corresponded to $\delta = 0$ while the minimum possible value was estimated by assuming the maximum observed value for $\delta = 0.25(6)$. On the other hand, the maximum and the minimum limits for the $B(E2, I \rightarrow I-1)$ values were found for $\delta = 0.25(6)$ and $\delta = 0$, respectively.

Table 6.1: The measured lifetimes for the levels of the doublet bands, the corresponding mixing ratios and the branching ratios of ^{106}Ag. The branching ratios are quoted for the ΔI=1 transitions. It should be noted that the quoted errors in the level lifetimes do not include the systematic errors in the stopping power values which may be as large as 20%.

Spin I ($\hbar$)	Lifetime (ps)	Mixing ratio (δ)	Bran. ratio $\frac{I_\gamma(\Delta I=1)}{I_\gamma(total)}$	$B(M1)$ μ_N
		Main Band		
12^-	0.32 (2)		0.84 (7)	1.22 (1)
13^-	0.20 (2)	0.12 (5)	0.76 (6)	1.70 (2)
14^-	0.23 (2)	0.23 (5)	0.61 (5)	0.80 (6)
15^-	0.22 (2)	0.25 (6)	0.40 (4)	0.45 (7)
16^-	0.17 (1)		0.47 (7)	0.67 (7)
17^-	0.10 (1)		0.57 (7)	1.12 (12)
		Partner Band		
14^-	1.77 (10)	0.09 (4)	0.58 (5)	0.68 (4)
15^-	0.31 (3)	0.21 (5)	0.87 (7)	2.02 (12)
16^-	0.40 (3)	0.24 (3)	0.57 (6)	0.49 (3)
17^-	0.27 (2)	0.11 (4)	0.45 (5)	0.69 (6)
18^-	0.10 (1)	0.14 (7)	0.70 (9)	1.42 (16)
19^-	0.11 (1)	0.18 (6)	0.36 (5)	0.79 (9)

The deduced transition rates have been plotted in Fig. 6.6. It is observed from this figure that within the experimental uncertainties, all the three transition rates for the two bands are essentially the same except at I=15$\hbar$ which probably originates due to the band crossing around this spin. The observation that the $B(E2, I \rightarrow I-2)$ are similar, does not support the two different quasi-particle picture of Ref. [20] since in that case the rates in the partner band are expected to be two times stronger than that of the main band. However, the explanation based on two different shapes

cannot be ruled out since the measured $B(E2, I \rightarrow I-2)$ values for the main and the partner band can be reproduced by different sets of (β, γ) values.

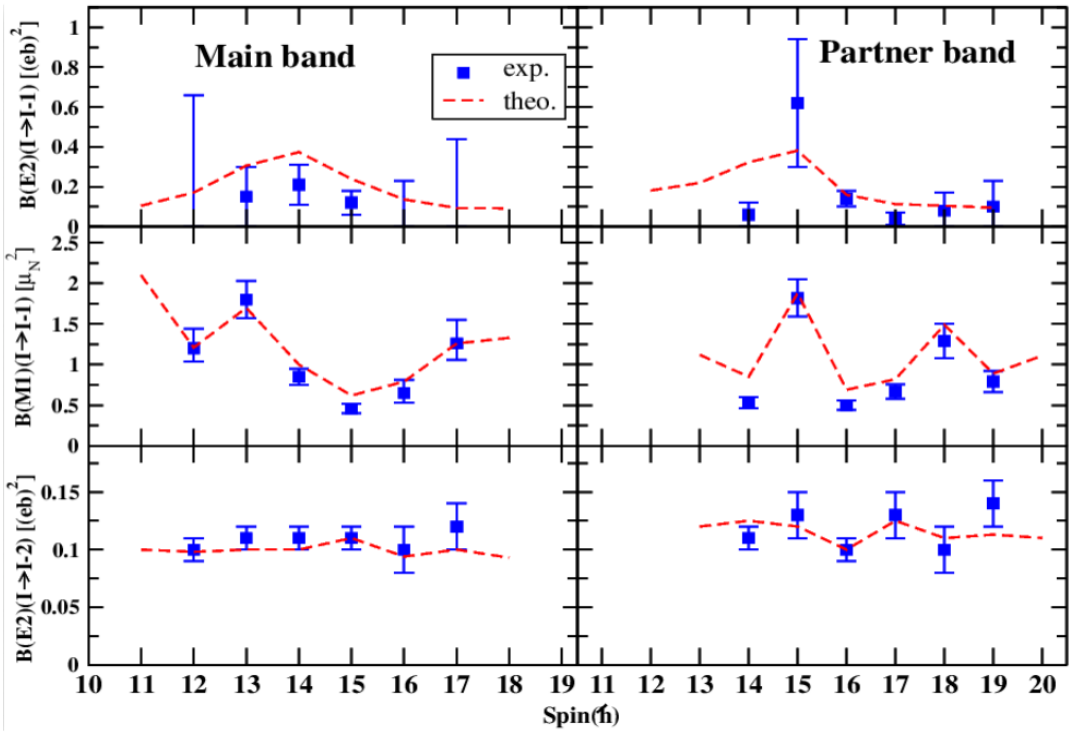

Figure 6.6: The deduced $B(E2, I \rightarrow I-1)$, $B(M1, I \rightarrow I-1)$ and $B(E2, I \rightarrow I-2)$ rates for the doublet bands of ^{106}Ag. The dashed lines represent the calculated values from TPSM.

The observed experimental band structure and transition rates of the doublet have been compared with the numerical results obtained using the TPSM approach. This model has been discussed in chapter 2. This model has been successful in describing the chiral band structure and transition rates in ^{128}Cs [21] and the level structure and branching ratios of the doublet bands in ^{108}Ag [7]. In the case of ^{106}Ag the same prescription had been followed where one neutron and one proton quasi-particle states were generated by the solving the triaxial Nilsson and pairing (monopole and quadrupole terms) Hamiltonian in the BCS approximation. The Nilsson potential with the deformation parameters $\epsilon = 0.15$ and $\gamma = 30^0$ have been used for ^{106}Ag which are consistent with the previous TRS calculation [3] and observed

systematic of Ag-isotopes [22]. In addition, it may be noted from Fig. 6.7 that the experimental routhians for the doublet can only be well reproduced by the numerical calculations based on TPSM corresponding to $\gamma = 30°$. In the present TPSM calculation, the configuration space consisted of N= $3, 4, 5$ major shells for neutrons and N= $2, 3, 4$ for protons. The lowest 28 K-bands were obtained through angular momentum projection within the energy window of 2.5 MeV. The projected bands (basis states) were employed to diagonalise the shell model Hamiltonian consisting of pairing and quadrupole-quadrupole interaction terms. The interaction strengths used in the present calculations were the same as those used in the previous studies [23, 21]. The energies for the doublet bands after the diagonalization are shown in Fig.6.8 (a). It is quite evident from the figure that calculated values are in good agreement with the experimental data and the band crossing spin is also well reproduced.

The calculated amplitude probabilities of the basis states (a^2_{ik}) for the main and the partner bands are plotted in Fig. 6.8(b) and (c) as a function of spin. It is observed from the figure that at low spins, the main band predominantly originates from K = 4 (quasi-particle energy=1.76 MeV) configuration while the partner band originates from K = 2 (2.12 MeV) configuration. However, beyond the observed band crossing spin of $14\hbar$, both the bands exhibit large K-mixing but the dominant amplitudes are now quite opposite to those before the crossing. Thus, the doublet bands in ^{106}Ag originate from the two quasi-particle states with different intrinsic configuration and cross each other at $14\hbar$.

The consistency of these calculations were performed by calculating the transition probabilities which are very sensitive to the eigen-vectors of the different angular momentum states. The transition probabilities for the present case had been calculated using free values of g_l while the g_s free values were attenuated by a 0.85 factor, i.e., $g^{\pi}_{l} = 1$, $g^{\nu}_{l} = 0$, $g^{\pi}_{s} = 5.59 \times 0.85$ and $g^{\nu}_{s} = -3.83 \times 0.85$. The

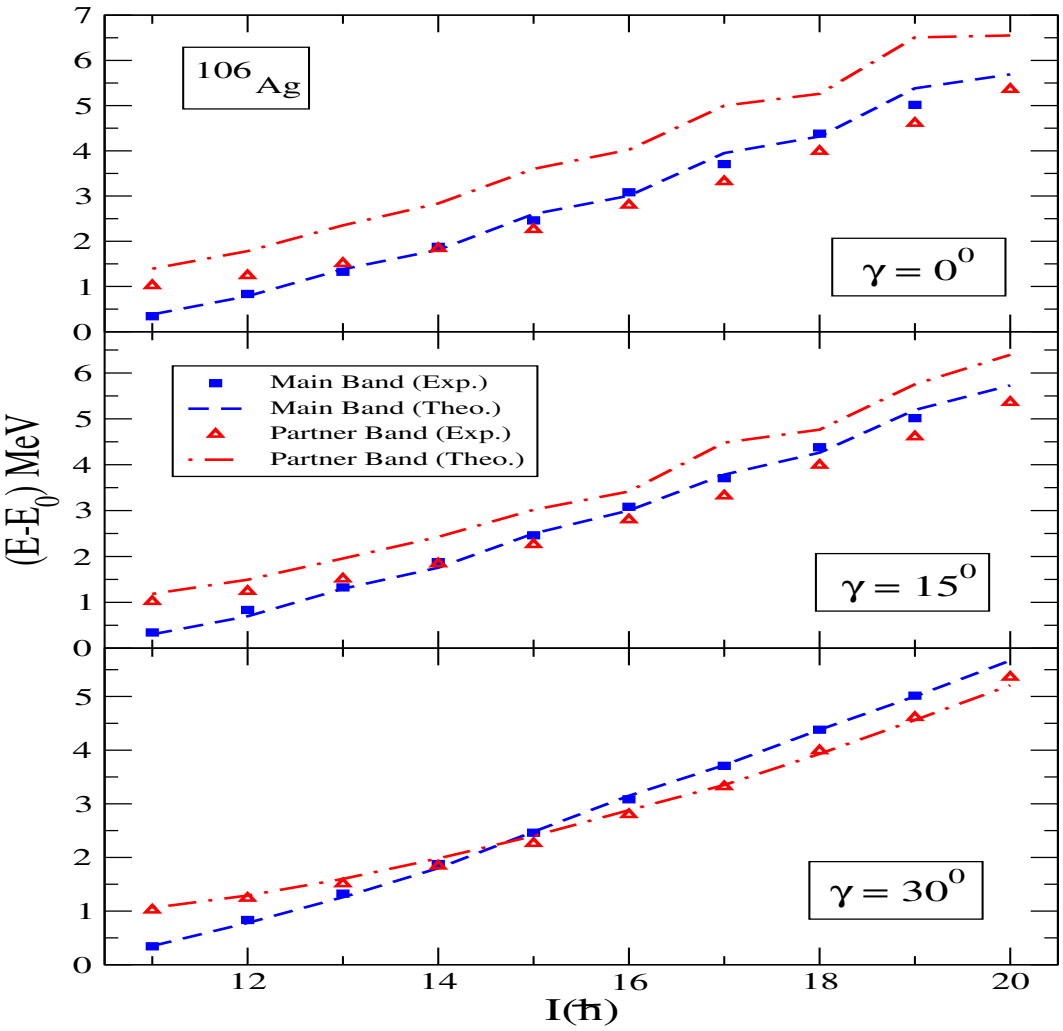

Figure 6.7: The comparison of theoretical and experimental routhians as a function of the γ parameter from TPSM calculations.

effective charges for the protons and the neutrons were assumed to be $1.5e$ and $0.5e$, respectively. Comparison of the experimental and the calculated transition probabilities for ^{106}Ag is shown in Fig. 6.6. It is observed from this figure that the numerical results obtained from TPSM with the present parameter set, are in good agreement with all the features of the experimental transition rates.

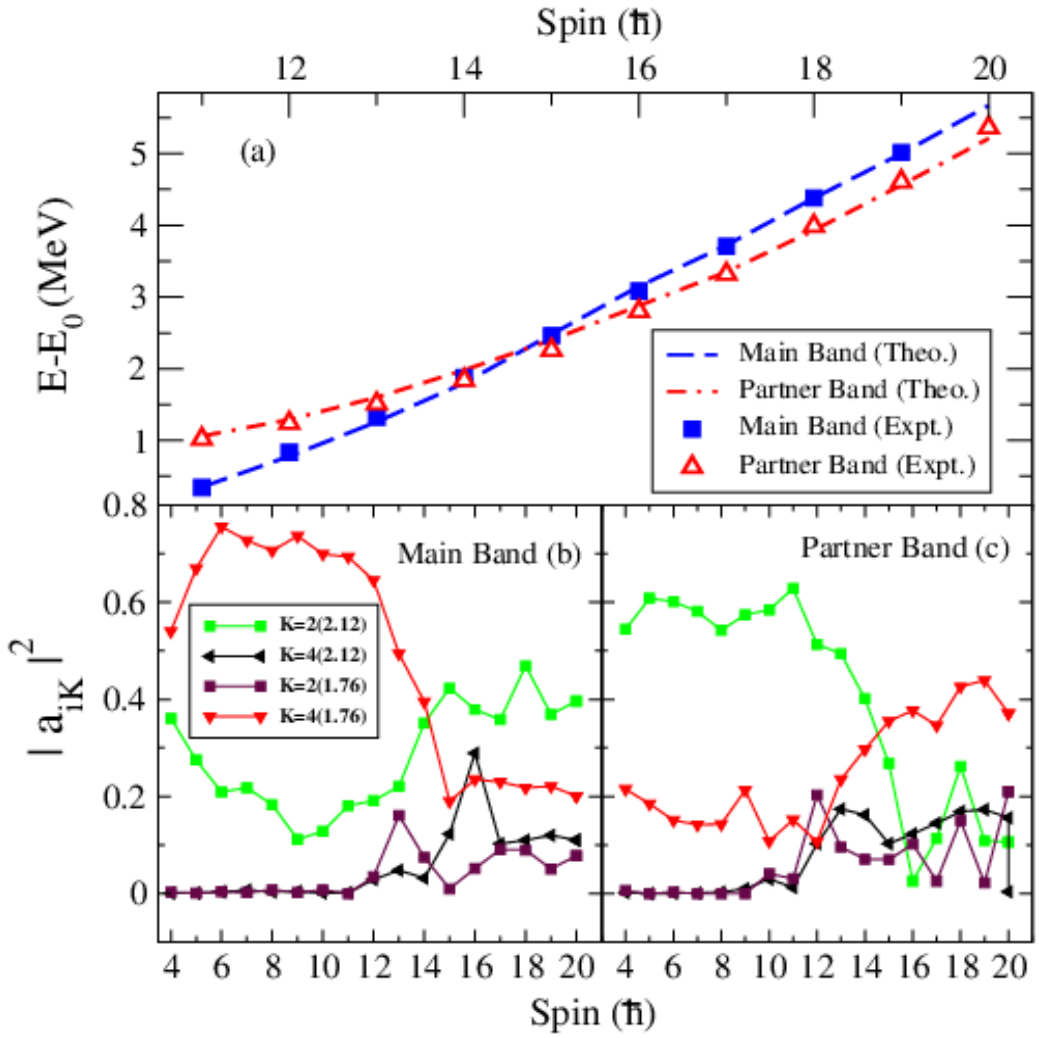

Figure 6.8: (a) Comparison of the measured energy levels of negative parity doublet bands of ^{106}Ag with those from TPSM calculation. The energies are relative to the band head E_0 taken to be the energy of $I^\pi = 10^- \hbar$ level of the main band. The calculated wavefunction amplitude probabilities from TPSM as a function of spin for the main and the partner bands are shown in (b) and (c), respectively. The numbers quoted in the parenthesis in the box of Fig. 6.8(b) are the quasi-particle energies in MeV.

It may be noted that similar precise level lifetime measurements in nearly degenerate doublet bands had only been performed in the A∼130 region for ^{128}Cs [7], ^{135,136}Nd [24, 25] and ^{134}Pr [21]. The MOI and transition rates were found to be very similar in ^{128}Cs and ^{135}Nd which established the doublet bands are chiral partners. On the other hand, the doublet bands of ^{134}Pr and ^{136}Nd exhibit the band crossing similar

to that observed in ^{106}Ag. In both the cases, the transition rates were found to be different and were interpreted within the frameworks of interacting boson-fermion-fermion model (IBFFM) and the tilted axis cranking (TAC) model complemented by the random phase approximation (RPA). These calculations indicated that the dissimilar transition rates in the doublet bands of ^{136}Nd and ^{134}Pr may originate due to chiral vibration [25] and chiral fluctuation [21], respectively. However, in the present work, similar transition rates have been observed in the doublet bands of ^{106}Ag. This novel feature of different MOI but similar transition rates can be reproduced by the calculation based on the TPSM. The success of this model in describing the doublet bands of mass-100 region seems to indicate that these bands are the consequence of triaxial deformation.

6.3 Band 3

Band 3 was completely revised by Leider *et. al.* [4] with respect to the previously reported work [26]. The present work, in general agrees with the γ-ray sequence in band 3 as published in Ref. [4], however, our work does not agree with their spin assignment. The band head spin was found to be I^{π}=12^{-} contradicting the 10^{-} assignment as reported in Ref.[4]. Band 3 feeds the band 1 through three $\Delta I = 1$ transitions of energies 932.0, 1170.1 and 1440.4 keV and two $\Delta I = 2$ transitions of 1422.3 and 1660.4 keV energy. Unlike band 1 and 2, this band interacts with the positive parity states and decays to the two 12^{+} levels through weak $E1$ transitions of energies 407.1 and 506.1 keV. The detailed angular distribution and polarization analysis were performed on the 506.1, 932.0 and 1170.1 keV transitions to assign the band head spin of band 3. The a_2 and a_4 coefficients extracted were -0.32 $\pm$ 0.03 and 0.01 $\pm$ 0.03 for 506.1 keV, -0.41 $\pm$ 0.04 and -0.03 $\pm$ 0.03 for 932.1 keV and -0.38 $\pm$ 0.03

and -0.01 ± 0.02 for 1170.1 keV transition. The linear polarization measurements of these gamma transitions were found to be 0.15 ± 0.11, -0.27 ± 0.11 and -0.23 ± 0.12 for 506.1 keV, 932.1 keV and 1170.1 keV, respectively. These measurements indicate that 506 keV gamma ray is an E1 transition. Thus, this transition was used to fix the spin parity of band 3 since the $M2$ mixing is expected to be negligible.

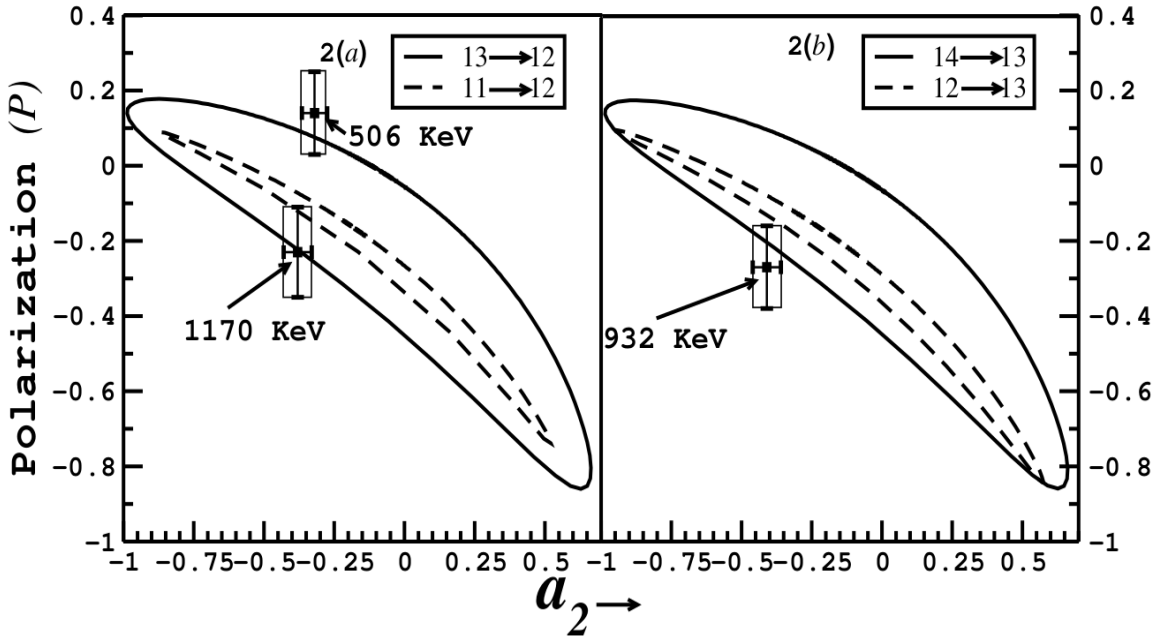

Figure 6.9: The contour plots for a_2 vs polarization for the two different spin assignments which are mentioned in the box.

The theoretical a_2 and P values have been plotted in Fig. 6.9 as a function of mixing ratio for two possible spin assignment schemes along with the experimental values. The boxes denote the simultaneous uncertainties in the values of a_2 and P. The dashed and the solid line correspond to the loci of the possible values of a_2 and P for the published in Ref. [4] and the proposed spin assignments, respectively. It is evident from the figure that the theoretical estimates are consistent with the experimental values for the spin assignment of 13^- to 12^+ for 506 keV transition and not with the previous assignment of 11^- to 12^+. It may also be noted from the figure

that the present spin assignment is consistent for 1170.1 keV (13^- to 12^-) and 932.1 keV (14^- to 13^-) transitions. This new spin-parity assignment is shown in Fig. 6.1 while the previously reported values are given in brackets. The corresponding mixing ratios are -0.05 ± 0.02, -0.14 ± 0.02 and -0.12 ± 0.03. Thus, the band head spin has been assigned to be 12^- for this band.

The lifetimes for the high spin levels of this band have been measured and are tabulated in table 6.2 The mixing ratios for each level have also been estimated in the

Table 6.2: The measured lifetimes, the corresponding mixing ratios and the branching ratios for the high spin levels of the Band 3 of ^{106}Ag. The branching ratios are quoted for the ΔI=1 transitions. It should be noted that the quoted errors in the level lifetimes include both the systematic and the statistical errors.

Spin I ($\hbar$)	Lifetime (ps)	Mixing ratio (δ)	Bran. ratio $\frac{I_\gamma(\Delta I=1)}{I_\gamma(total)}$	$B(M1)$ μ_N
		Band 3		
17^-	0.41 (2)	0.13 (5)	0.92 (4)	2.42(8)
18^-	0.37 (3)	0.19 (5)	0.84 (7)	1.74(5)
19^-	0.33 (4)	0.21 (6)	0.78 (9)	0.97(7)
20^-	0.16 (5)	0.18 (5)	0.77 (10)	2.06(14)
21^-	0.14 (4)	0.23 (6)	0.74 (11)	1.17(13)
22^-	0.21 (4)	0.19 (6)	0.57 (11)	0.74(10)

same way as described for Bands 1 and 2. Thus, The $B(M1)$ rates could be deduced and have also been tabulated as a function of spin in table 6.3. It is apparent from the table that the $B(M1)$ rates exhibit a characteristic fall of a shears band till $I = 19\hbar$ and beyond this value there is a sharp increase followed by another characteristic fall. Such a behavior has been reported in ^{108}Cd [27] and was identified with the band crossing phenomena in a shears band. The band crossing in the shears band is similar to that found in the case of the collective rotation. But the two similar phenomena need to be described in two different ways. In the case of collective rotation, the band crossing is associated with the alignment of the pair of quasi-particles to the rotational axis. In contrast, the band crossing in shears band happens due to new

single particle configuration which can reproduce the same angular momentum at large shears angles (at lower energies). This happens because the magnitude of the angular momentum vectors increases due to the participation of two more particles or holes in forming the new shears structure.

This observed behavior of the $B(M1)$ rates have prompted a numerical calculation based on the SPAC model [28] for the shears mechanism. It is similar to SCSM model which has been described in chapter 3. The basic difference between the two models is in geometrical picturization of the shears closing. In SCSM model, the shears blades are assumed to close around the total angular momentum (I) and thus, the tilt angle of I with respect to the symmetry axis remains constant. In SPAC model, the shears blade along the rotational axis remains fixed while the other blade closes towards the rotational axis. Thus, the tilt angle in this case does not remain constant. This modification is needed for those shears bands which have an appreciable collective contribution. For such bands it is natural to assume that the angular momentum of the rotationally aligned particles will not misalign with increasing angular momentum.

The aligned angular momentum for the quasi-particles in Bands 1, 2 and 3 have been shown in Fig. 6.10. It is apparent from the figure that the Band 3 has higher aligned angular momentum than the two-qp bands and thus originates from a four quasi-particle structure. A number of four quasi-particle structures are possible based on the $\pi g_{9/2}^{-1} \otimes \nu h_{11/2}^{1}$ configuration and the SPAC calculations were performed for all the configurations. The best agreement between the experimental and theoretical routhians was obtained for $\pi g_{9/2}^{-3} \otimes \nu h_{11/2}^{1}$ configuration before the band crossing and $\pi g_{9/2}^{-3} \otimes \nu h_{11/2}^{3}$ after the band crossing.

For the $\pi g_{9/2}^{-3} \otimes \nu h_{11/2}^{1}$ configuration, the rotational aligned angular momentum vector ($j_{\perp}$) is 5.5 $\hbar$ and the magnitude of the other vector ($j_{||}$) is assumed to be 9.5

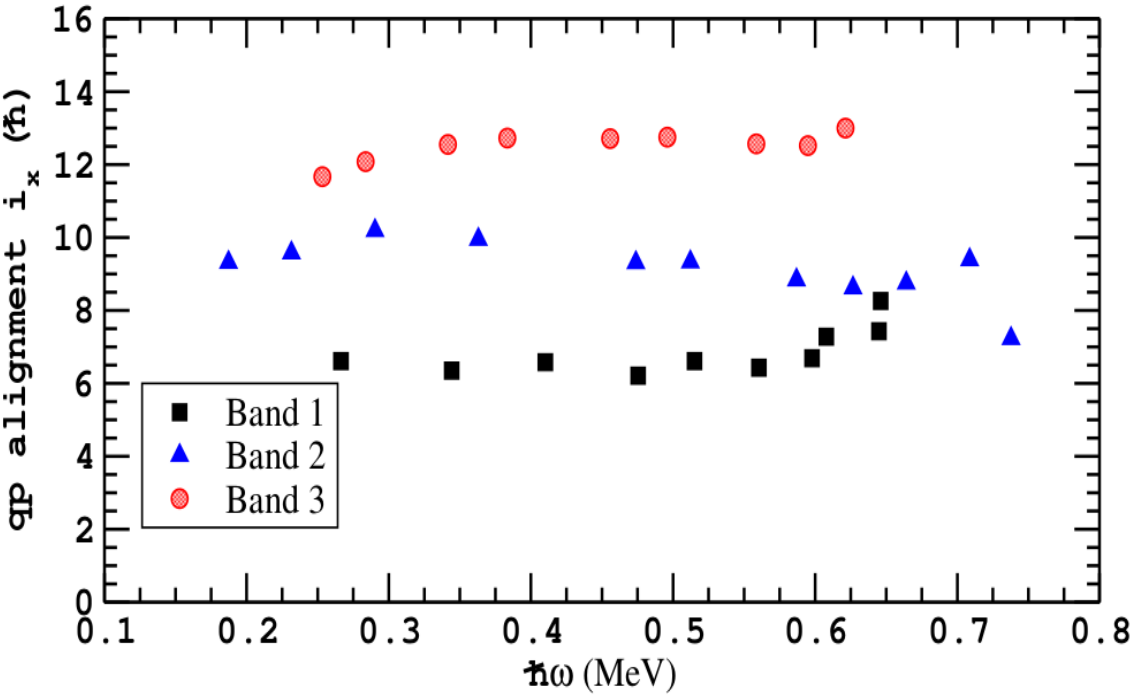

Figure 6.10: Experimental quasiparticle alignment i_x as function of rotational frequency for Bands 1, 2 and 3 in ^{106}Ag. The Harris parameters used are $\mathcal{J}_0$= 8.9$\hbar^2$/MeV and $\mathcal{J}_1$= 15.7$\hbar^4$/MeV^3.

$\hbar$ in order to reproduce the band head spin of 12 $\hbar$. For these calculations, a prolate deformation for this band has been assumed and the best values for the core moment of inertia ($\mathcal{J}$) and the particle-hole interaction ($V_{\pi\nu}$) were found to be 8.3 $\hbar$MeV^{-1} and 1.15 MeV, respectively. The comparison plot for the routhians is shown in Fig. 6.11, where the level energies have been normalized with respect to the band head energy of 12$^-$. In these calculations the band crossing has been assumed to occur at I=19 $\hbar$. It can be concluded from this figure that there is a good agreement between the experimental and the calculated routhians. However, the definitive cross-check for this configuration assignment can be obtained by comparing the experimental $B(M1)$ values with those obtained from the theoretical calculations using the equation

$$B(M1, I \rightarrow I-1) = \frac{3}{8\pi}\vec{\mu}_{\perp}^2 = \frac{3}{8\pi} g_{eff}^2 j_{\pi}^2 \sin^2\theta_{\pi} \left[\mu_N^2\right] \quad (6.1)$$

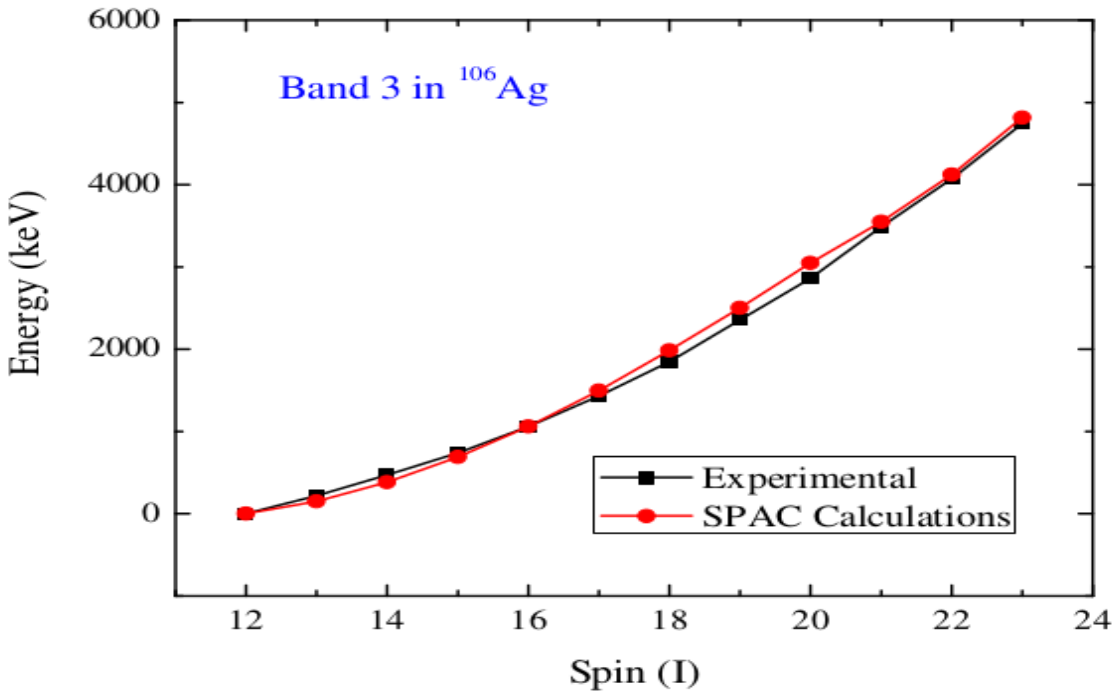

Figure 6.11: Comparison of the experimental routhian with the SPAC model calculations for the Band 3 in ^{106}Ag. The energies are normalized with respect to the 12^- state of the band.

where the shears angle (θ_π) corresponding to each level is the same which reproduces to the level energy. This comparison is shown in Fig. 6.12, where the single particle g-factor for the $g_{9/2}$ proton, the $g_{7/2}$ neutron and the $h_{11/2}$ neutron were taken to be 1.27, -0.21 and 0.21 respectively [2]. The good agreement of the numerical values confirms the configuration of Band 3 to be $\pi g_{9/2}^{-3} \otimes \nu h_{11/2}^{1}$ before the band crossing and $\pi g_{9/2}^{-3} \otimes \nu h_{11/2}^{3}$ after the band crossing with a collective contribution from the prolate core.

It is very interesting to note that in order to describe all the high spin characteristics of the three negative parity bands, we need to assume a triaxial deformation for Bands 1 and 2 and a prolate deformation for Band 3. This co-existence of shapes due to a broad TRS minimum has already been pointed out by Joshi *et al.* [3]. This TRS plot is shown in Fig. 6.13. The conclusion drawn from the

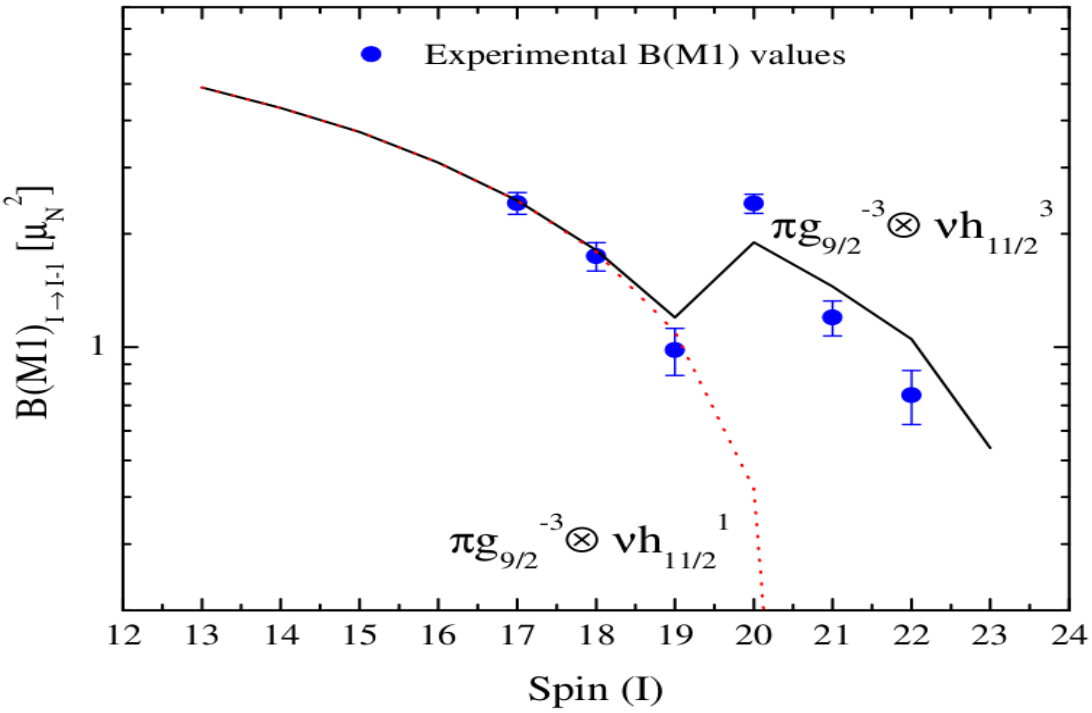

Figure 6.12: Comparison of the experimental $B(M1)$ values with the results obtained from the SPAC model calculations for the Band 3 of ^{106}Ag. The dotted red line is obtained from the calculations with $\pi g_{9/2}^{-3} \otimes \nu h_{11/2}^{1}$ configuration below the crossing. After the I=19 spin, the solid black line corresponds to the SPAC calculation using the configuration $\pi g_{9/2}^{-3} \otimes \nu h_{11/2}^{1}$.

present work on the co-existence of triaxial ($\gamma = 30°$) and axial ($\gamma = 0°$) deformations is consistent with this TRS picture for shape co-existence.

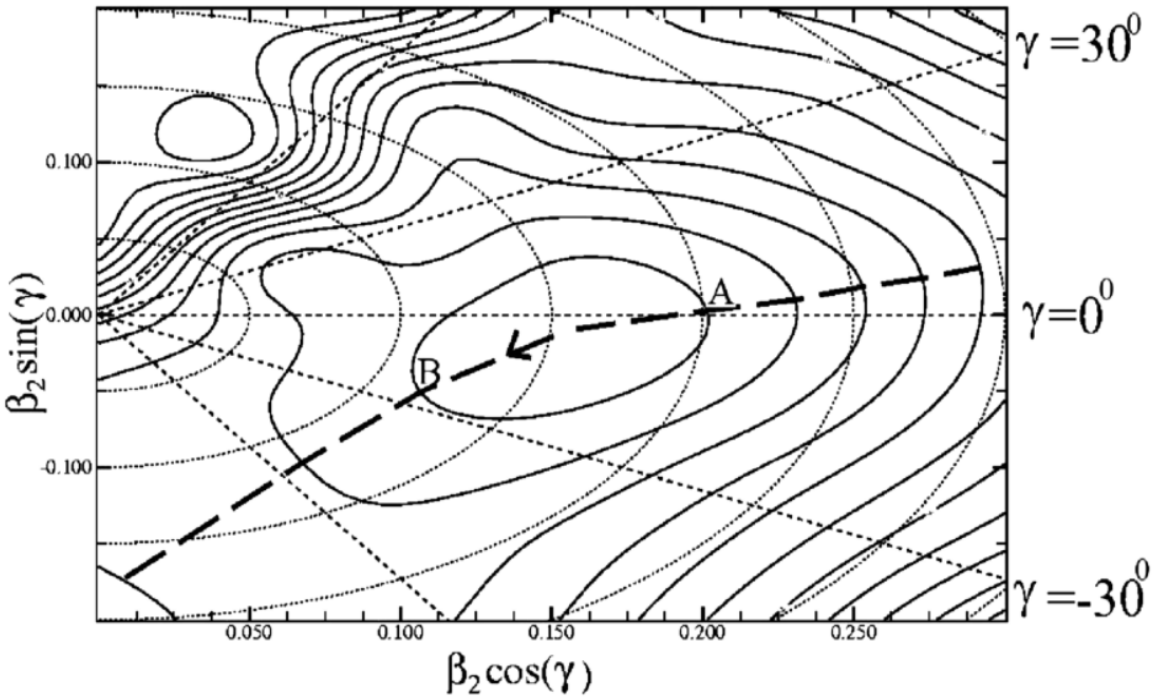

Figure 6.13: TRS plot for the yrast negative-parity configuration in ^{106}Ag at a rotational frequency of 0.40 MeV. The contour separation in this plot is 350 keV. This figure is taken from Ref. [3].

6.4 Band 4

The positive parity levels of ^{106}Ag were established by D. Jerrestam *at. al* [26] and the present level scheme (Fig. 6.1) agrees well with this report in the low spin domain. The band head spin of the high spin positive parity band was reported as 11^+. But the DCO and PDCO values obtained for 1145 keV from the present analysis are 1.11(15) and 0.35(11), respectively. Thus, the 1145 keV transition is an $E2$ transition which changes the band head spin to 12^+. The next higher level decays by 243 keV transition to the band head and by 1495 keV transition to 11^- level of Band 3. The DCO and PDCO values for the 1495 keV transition have been determined to be 0.48(17) and 0.21(13), respectively which indicates that it is an $E1$ transition. Thus, the second level of the band also has I^π=12^+. The assignment of γ

rays to high spin members of this band from the two works agree till the previously reported 19^+ level. Only the gamma transition energy between $19^+ \rightarrow 18^+$ has been changed from 586.3 to 588 keV. This band has been extended to I^π=25^+ in the present work (6.1). For all the levels, The $M1$ and the crossover $E2$ transitions have been identified. The DCO ratios for all the $M1$ transitions de-exciting the high spin levels of this band have been measured and tabulated in Table 6.4.

Table 6.3: The measured lifetimes, the corresponding mixing ratios and the branching ratios for the high spin levels of the Band 4 of ^{106}Ag. The branching ratios are quoted for the ΔI=1 transitions. It should be noted that the quoted errors in the level lifetimes include both the systematic and the statistical errors.

Spin I ($\hbar$)	Lifetime (ps)	Mixing ratio (δ)	Bran. ratio $\frac{I_\gamma(\Delta I=1)}{I_\gamma(total)}$	$B(M1)$ μ_N
		Band 4		
17^+	0.33 (3)	0.15 (4)	0.87 (5)	2.20(16)
18^+	0.21 (3)	0.18 (5)	0.76 (7)	1.98(17)
19^+	0.17 (3)	0.19 (6)	0.70 (7)	1.77(15)
20^+	0.12 (2)	0.24 (7)	0.69 (6)	1.52(18)
21^+	0.14 (3)	0.21 (7)	0.59 (6)	1.15(16)
22^+	0.17 (4)	0.18 (7)	0.67 (8)	0.69

The line-shapes could be observed for the γ transitions beyond I^π=16^+ and the lifetimes of levels from 16^+ to 22^+ have been measured. These values are tabulated in Table 6.3. It can be observed that the extracted $B(M1)$ rates decrease steadily with the increase of angular momentum.

This observation indicates that this band may also originates due to the shears mechanism. In order to explore this possibility further, the numerical calculations based on SPAC were carried out with $\pi g_{9/2}^{-1} \otimes \nu[(d_{5/2,g_{7/2}})^1, h_{11/2}^2]$ configuration. For this configuration $j_{||} = 4.5\ \hbar$ and $j_\perp = 10.5\ \hbar$ for a bandhead spin of 12 $\hbar$. The values for $V_{\pi\nu}$=1.2 MeV and $\mathcal{J}$=10.0 MeV^{-1} was assumed which were similar to those used for Band 3. Fig. 6.14 shows the experimental and the calculated routhians for Band 4. The agreement between values is reasonable upto I=25 $\hbar$.

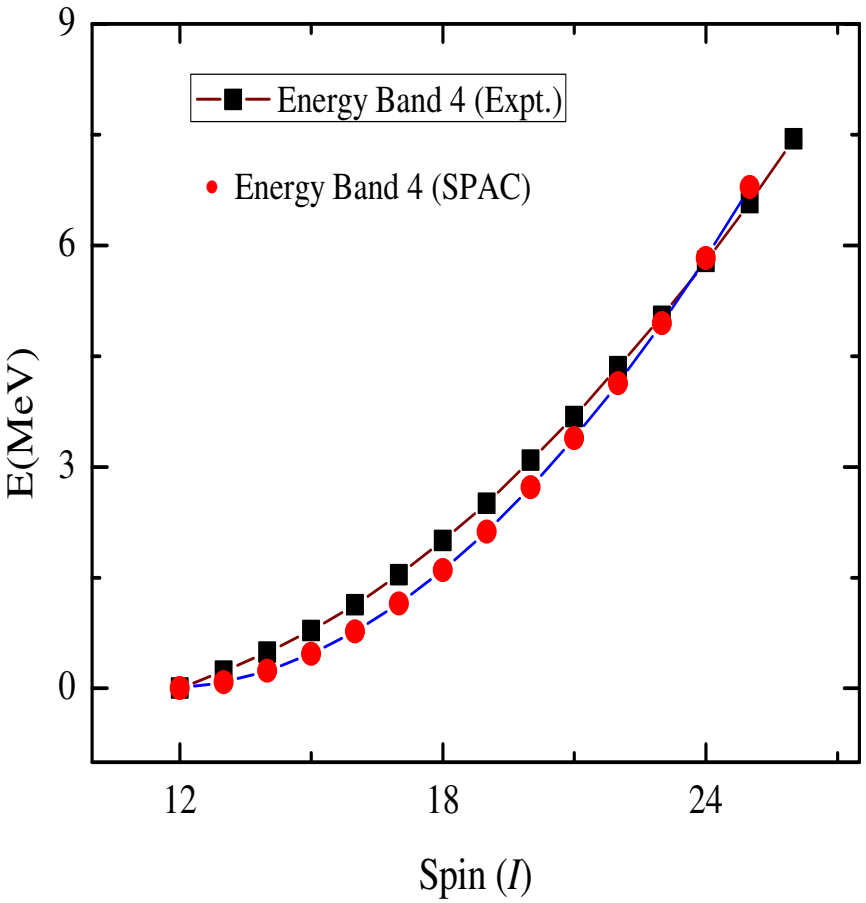

Figure 6.14: Comparison of the experimental routhian with the SPAC model calculations for the Band 4 in ^{106}Ag.

The $B(M1)$ transition rates were also calculated and compared with the experimental values. This comparison is shown in Fig. 6.15. It is apparent that both the $B(M1)$ rates and the routhians are well produced by the SPAC calculations. Thus, it may be inferred that the positive parity band of ^{106}Ag originates due to an interplay between shears mechanism and the collective rotation.

In summery, the partial level scheme of ^{106}Ag established in the present work has four high spin bands out of which three have negative parity while the fourth has positive parity. Bands 1 and 2 form a doublet and comparison with TPSM calculations

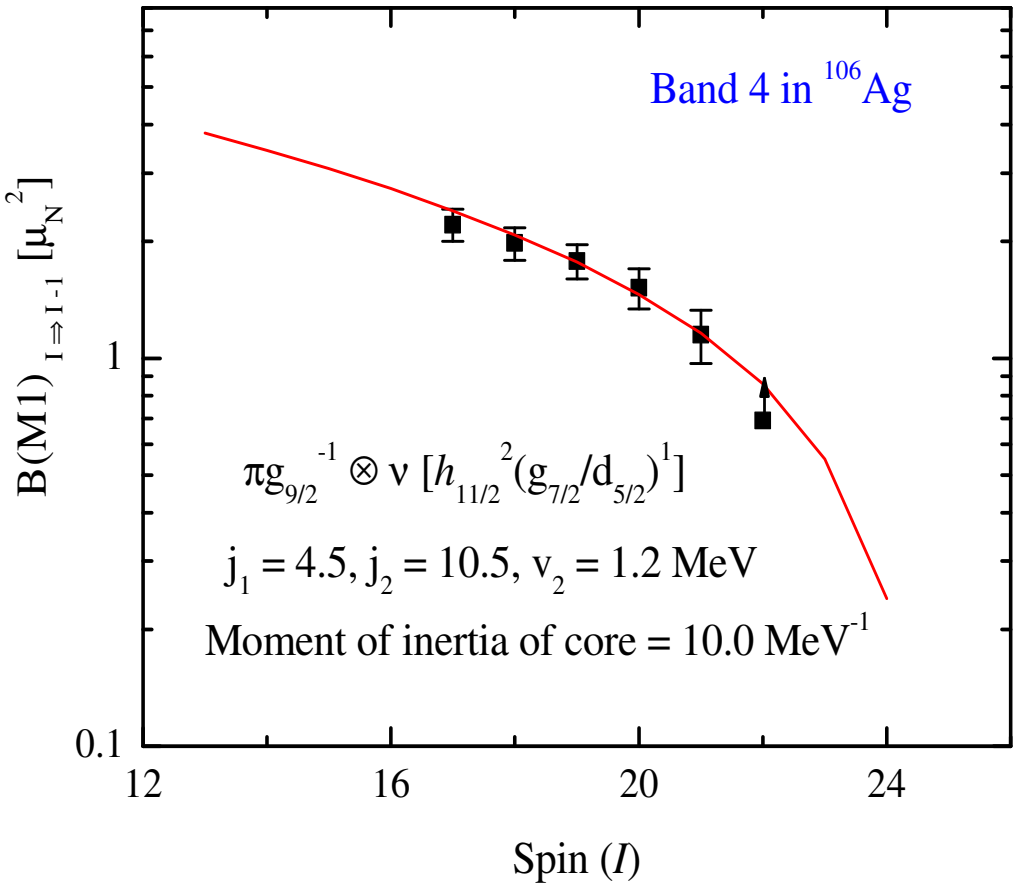

Figure 6.15: Comparison of the experimental $B(M1)$ values with the results obtained from the SPAC model calculations for the Band 4 of ^{106}Ag. The theoretical curve is obtained from the calculations with $\pi g_{9/2}^{-1} \otimes \nu[(d_{5/2}, g_{7/2})^1,\ h_{11/2}^2]$ configuration.

seem to indicate that these 2-*qp* bands arise due to a triaxial deformed core. The comparison with the numerical results of SPAC indicate that Band 3 originates due to an interplay of shears mechanism and the collective rotation. This band exhibits a band crossing at I=19 $\hbar$ which is also reproduced by SPAC calculations. The positive parity Band 4 also originates from this interplay but does not exhibit any band crossing till the observed spin 26 $\hbar$. For the SPAC calculations, a prolate core was assumed for both Band 3 and Band 4 which gives the collective contribution to

the angular momentum generation in these bands.

Table 6.4: Energies of the γ rays, The Spin, Parity and the relative intensities of transitions assigned to the ^{106}Ag in the present work.

E_γ (keV)	$I_i^\pi \rightarrow I_f^\pi(\hbar)$	I_γ	A_2/A_0	A_4/A_0	δ	R_{DCO}	PDCO
45	$8^- \rightarrow 7^-$						
64	$7^- \rightarrow 6^-$						
169	$9^- \rightarrow 8^-$	100			0.48(7)	1.1(4)	-0.33(11)
170	$11^- \rightarrow 10^-$	8.9(4)					
219	$12^- \rightarrow 11^-$	33.6(9)			0.34(6)	0.91(9)	-0.27(16)
220	$13^- \rightarrow 12^-$	5.8(4)					
230	$13^+ \rightarrow 12^+$	12.8(5)					
243	$7^+ \rightarrow 6^+$	51.8(1.4)					
243	$12^+ \rightarrow 12^+$	3.2(3)					
252	$14^- \rightarrow 13^-$	8.4(4)					
258	$14^+ \rightarrow 13^+$	16.3(5)					
266	$15^- \rightarrow 14^-$	14.5(5)					
267	$10^- \rightarrow 9^-$	4.3(3)					
270	$13^- \rightarrow 12^-$	31.8(6)			0.19(7)	0.73(9)	
293	$7^+ \rightarrow 7^+$	10.7(4)					
295	$15^+ \rightarrow 14^+$	13.7(3)				0.64(9)	-0.15(10)
322	$16^- \rightarrow 15^-$	11.5(4)			0.11(3)	0.64(5)	-0.13(8)
326	$14^- \rightarrow 13^-$	28.4(7)			0.09(4)	0.61(7)	-0.17(9)
330	$10^+ \rightarrow 9^+$	3.2(3)					
343	$11^- \rightarrow 10^-$	78.3(2.6)			0.15(3)	0.68(3)	-0.21(6)
347	$16^+ \rightarrow 15^+$	12.5(4)			0.12(4)	0.63(5)	-0.09(5)
353	$8^+ \rightarrow 7^+$	8.1(3)				0.62(6)	-0.19(9)
373	$17^- \rightarrow 16^-$	11.1(4)			0.13(5)	0.71(6)	-0.14(6)
376	$10^- \rightarrow 9^-$	92.1(3.2)	-0.31(3)	-0.05(4)	-0.08(3)	0.69(2)	-0.31(5)
388	$12^- \rightarrow 10^-$	3.7(5)					
397	$10^- \rightarrow 10^-$	1.5(2)					
405	$17^+ \rightarrow 16^+$	10.4(3)			0.15(4)	0.66(6)	-0.23(7)
407	$13^- \rightarrow 12^+$	1.2(2)					
408	$11^- \rightarrow 10^-$	3.2(3)					
415	$18^- \rightarrow 17^-$	9.6(3)			0.19(5)	0.62(6)	-0.28(9)
430	$15^- \rightarrow 14^-$	24.8(7)			0.21(5)	0.76(7)	-0.33(9)

Table 6.4 – *Continued from previous page*

E_γ (keV)	$I_i^\pi \rightarrow I_f^\pi(\hbar)$	I_γ	A_2/A_0	A_4/A_0	δ	R_{DCO}	PDCO
454	$10^- \rightarrow 10^-$	1.4(5)					
466	$18^+ \rightarrow 17^+$	7.8(4)			0.18(5)	0.71(6)	-0.18(9)
470	$13^+ \rightarrow 12^+$	2.4(3)					
489	$14^+ \rightarrow 12^+$	3.7(8)				0.96(8)	0.25(7)
489	$13^- \rightarrow 11^-$	5.3(5)					
490	$12^- \rightarrow 11^-$	52.1(1.3)					
489	$13^- \rightarrow 12^-$	26.7(1.2)			0.12(5)	0.65(8)	-0.23(14)
496	$7^- \rightarrow 7^+$	21.8(8)					
503	$19^+ \rightarrow 18^+$	4.6(3)			0.19(6)	0.71(7)	-0.17(10)
505	$20^- \rightarrow 19^-$	4.0(4)			0.18(5)	0.74(8)	-0.21(11)
506	$13^- \rightarrow 12^+$	2.3(3)	-0.32(3)	0.01(3)	-0.05(2)		0.15(11)
508	$10^- \rightarrow 11^-$	3.1(4)					
509	$19^- \rightarrow 18^-$	7.2(6)			0.21(6)	0.71(7)	-0.22(10)
518	$15^- \rightarrow 13^-$	2.8(5)				0.97(7)	0.29(9)
519	$17^- \rightarrow 16^-$	8.5(7)			0.11(4)	0.61(6)	-0.24(10)
536	$7^+ \rightarrow 6^+$	3.3(3)					
536	$16^- \rightarrow 15^-$	12.9(1.2)			0.24(3)	0.67(5)	-0.15(9)
542	$8^- \rightarrow 7^+$	23.4(9)				0.56(5)	0.13(6)
546	$10^- \rightarrow 8^-$	5.4(6)				1.07(11)	0.39(8)
552	$14^- \rightarrow 13^-$	16.3(1.5)			0.23(5)	0.80(7)	-0.33(9)
553	$15^+ \rightarrow 13^+$	.5(5)				0.97(8)	0.46(12)
585	$21^+ \rightarrow 20^+$	1.9(4)			0.21(7)	0.73(9)	-0.19(10)
586	$22^- \rightarrow 21^-$	1.7(3)			0.19(6)	0.74(9)	
588	$16^- \rightarrow 14^-$	3.2(3)				0.98(8)	0.47(8)
588	$20^+ \rightarrow 19^+$	3.2(4)			0.24(7)	0.77(9)	
593	$9^+ \rightarrow 8^+$	2.1(3)					
594	$15^- \rightarrow 14^-$	9.7(1.4)			0.25(6)	0.83(9)	-0.17(11)
596	$14^- \rightarrow 12^-$	20.6(2.2)					
612	$16^- \rightarrow 15^-$	9.2(9)					
613	$19^- \rightarrow 18^-$	2.7(5)			0.18(6)	0.71(6)	
626	$17^- \rightarrow 16^-$	5.4(8)					
625	$21^- \rightarrow 20^-$	2.3(4)			0.23(6)	0.70(9)	

Table 6.4 – *Continued from previous page*

E_γ (keV)	$I_i^\pi \rightarrow I_f^\pi(\hbar)$	I_γ	A_2/A_0	A_4/A_0	δ	R_{DCO}	PDCO
629	$8^+ \rightarrow 7^+$	5.0(7)				0.83(7)	- 0.16(11)
642	$16^+ \rightarrow 14^+$	1.2(3)				0.95(9)	0.37(12)
657	$22^- \rightarrow 21^-$	0.1(2)					
660	$12^+ \rightarrow 11^+$	2.5(5)					
673	$18^- \rightarrow 17^-$	6.3(7)			0.14(7)	0.65(9)	
674	$18^- \rightarrow 17^-$	2.3(9)					
676	$6^- \rightarrow 6^+$	71.4(2.3)					
695	$17^- \rightarrow 15^-$	1.0(3)					
680	$22^+ \rightarrow 21^+$	1.6(4)			0.18(7)	0.69(9)	
682	$23^+ \rightarrow 22^+$	0.8(3)					
688	$12^+ \rightarrow 11^+$	2.8(4)					
720	$11^- \rightarrow 9^-$	16.7(1.1)				0.93(8)	0.45(9)
727	$10^+ \rightarrow 9^+$	2.6(5)				0.61(9)	- 0.26(10)
732	$20^- \rightarrow 19^-$	1.8(4)					
739	$7^- \rightarrow 6^+$	6.3(6)					
742	$24^+ \rightarrow 23^+$	0.4(3)					
752	$17^+ \rightarrow 15^+$	1.6(3)				1.06(9)	0.29(12)
756	$15^- \rightarrow 13^-$	3.7(4)					
770	$21^- \rightarrow 20^-$	0.9(5)					
788	$18^- \rightarrow 16^-$	1.8(4)					
796	$25^+ \rightarrow 24^+$	0.2(2)					
833	$12^- \rightarrow 10^-$	9.9(7)				1.13(10)	0.36(10)
851	$10^- \rightarrow 10^-$	1.1(3)					
871	$18^+ \rightarrow 16^+$	2.5(3)					
872	$8^+ \rightarrow 6^+$	3.3(5)					
890	$13^+ \rightarrow 11^+$	2.4(3)					
923	$10^+ \rightarrow 8^+$	4.2(7)				1.07(10)	0.19(8)
924	$19^- \rightarrow 17^-$	2.0(3)					
932	$14^- \rightarrow 13^-$	2.1(3)	-0.41(4)	-0.03(3)	- 0.12(3)		- 0.27(11)
946	$9^+ \rightarrow 7^+$	3.0(6)				0.95(8)	0.15(9)
960	$10^- \rightarrow 10^-$	4.0(9)					
967	$16^- \rightarrow 14^-$	9.7(5)					
969	$19^+ \rightarrow 17^+$	2.0(4)					
979	$13^- \rightarrow 11^-$	8.4(5)				0.89(11)	0.33(9)
989	$10^- \rightarrow 9^-$	7.2(6)				0.57(5)	0.41(13)
1002	$14^- \rightarrow 12^-$	3.2(4)				0.94(8)	
1014	$20^- \rightarrow 18^-$	1.2(2)					
1015	$12^+ \rightarrow 10^+$	1.2(3)				0.92(13)	

Table 6.4 – *Continued from previous page*

E_γ (keV)	$I_i^\pi \rightarrow I_f^\pi(\hbar)$	I_γ	A_2/A_0	A_4/A_0	δ	R_{DCO}	PDCO
1021	$11^- \rightarrow 10^-$	17.5(1.4)	-0.43(30	-0.06(3)	-0.16(4)	0.64(8)	-0.33(8)
1042	$14^- \rightarrow 12^-$	10.4(5)				1.17(12)	0.49(13)
1054	$9^+ \rightarrow 7^+$	7.1(6)				1.06(11)	0.41(12)
1056	$17^- \rightarrow 15^-$	10.4(7)					
1091	$20^+ \rightarrow 18^+$	1.4(2)					
1115	$12^+ \rightarrow 10^+$	5.1(7)				1.07(9)	
1130	$21^- \rightarrow 19^-$	0.8(2)					
1145	$12^+ \rightarrow 10^+$	5.2(5)				1.11(15)	0.35(11)
1146	$15^- \rightarrow 13^-$	14.5(1.1)				0.95(12)	0.22(7)
1153	$10^+ \rightarrow 8^+$	1.8(4)				0.93(10)	
1167	$13^- \rightarrow 11^-$	2.6(8)					
1170	$13^- \rightarrow 12^-$	3.7(4)	-0.38(3)	-0.01(2)	-0.14(2)		-0.23(12)
1174	$21^+ \rightarrow 19^+$	1.3(2)					
1184	$11^+ \rightarrow 9^+$	5.5(7)				1.09(11)	
1192	$18^- \rightarrow 16^-$	2.7(3)					
1206	$16^- \rightarrow 14^-$	10.4(8)					
1211	$22^- \rightarrow 20^-$	1.3(2)					
1212	$11^+ \rightarrow 9^+$	2.3(4)				0.92(14)	
1228	$10^- \rightarrow 9^-$	3.2(5)				0.58(9)	-0.09(8)
1237	$17^- \rightarrow 15^-$	4.1(3)					
1240	$12^- \rightarrow 10^-$	0.7(2)				1.02(12)	
1254	$23^- \rightarrow 21^-$	0.5(4)					
1266	$22^+ \rightarrow 20^+$	0.8(2)					
1284	$19^- \rightarrow 17^-$	4.8(7)					
1300	$18^- \rightarrow 16^-$	1.2(4)					
1309	$19^- \rightarrow 17^-$	0.7(4)					
1345	$20^- \rightarrow 18^-$	1.0(5)					
1362	$23^+ \rightarrow 21^+$	0.4(5)					
1397	$11^- \rightarrow 9^-$	5.7(5)	0.25(4)	0.04(5)	-0.02(4)	1.09(13)	
1422	$14^- \rightarrow 12^-$	1.7(4)					
1424	$24^+ \rightarrow 22^+$	0.4(4)					
1426	$22^- \rightarrow 20^-$	0.5(4)					
1440	$12^- \rightarrow 11^-$	1.2(3)					
1495	$12^+ \rightarrow 11^-$	6.1(6)				0.48(17)	0.21(13))
1502	$21^- \rightarrow 19^-$	0.7(5)					
1499	$25^+ \rightarrow 23^+$	0.2(3)					
1538	$25^+ \rightarrow 23^+$	0.1(1)					

Bibliography

[1] S. Roy *et al.,* Phys. Lett. B **710** 587 (2012).

[2] P. Datta *et al.,* Phy. Rev. C **69** 044317 (2004).

[3] P. Joshi, et al., Phys. Rev. Lett. **98** 102501 (2007).

[4] E. O. Lieder *et al.,* Phys. Rev. Lett. **112**, 202502 (2014).

[5] N. Rather *et al.,* Phys. Rev. Lett. **112** 202503 (2014).

[6] C. Vaman, D. Fossan, T. Koike, K. Starosta, I. Lee, and A. Macchiavelli, Phys. Rev. Lett. **92**, 032501 (2004).

[7] J. Sethi, et al., Phys. Lett. B **725** 85(2013).

[8] P. Joshi et al., Phys. Lett. B **595**, 135 (2004); J. Timar et al., Phys. Lett. B **598**, 178 (2004); P. Joshi et al., Eur. Phys. J. A **24**, 23 (2005).

[9] C. M. Petrache, et al., Nucl. Phys. A **597** 106 (1996).

[10] K. Starosta, et al., Phys. Rev. Lett. **86** 971 (2001).

[11] C. Vaman, et al., Phys. Rev. Lett. **92** 032501 (2004).

[12] D. Tonev, et al., Phys. Rev. Lett. **96** 052501 (2006).

[13] S. Mukhopadhyay, et al., Phys. Rev. Lett **99** 172501 (2007).

[14] S. Mukhopadhyay, et al., Phy. Rev. C **78** 034311 (2008).

[15] E. Grodner, et al., Phys. Rev. Lett. **97** 172501 (2006).

[16] H. Ma, et al., Phy. Rev. C **88** 034322 (2013).

[17] S. H. Yao, et al., Proceedings of 13th National Conference on Nuclear Structure in China (NSC2010) (World Scientific, Singapore) 271 (2011).

[18] D. A. Volkov, A. I. Levon, A. A. Pasternak, Yad. Fiz. **50**, 1505, (1989).

[19] E. S. Macias, W. D. Ruhtur, D. C. Camp, and R. G. Lanier, Comput. Phys. Commun. **11**, 75 (1976).

[20] H. Ma, *et al*., Phy. Rev. C **88**, 034322 (2013).

[21] G. H. Bhat, J. A. Sheikh and R. Palit, Phys. Lett. B **707** 250 (2012).

[22] S. Roy, et al., Phys. Lett. B **710** 587 (2012).

[23] J. A. Sheikh and K. Hara, Phys. Rev. Lett. **82** 3968 (1999); J. A. Sheikh, G. H. Bhat, Y. Sun, G. B. Vakil and R. Palit, Phys. Rev. C **77** 034313 (2008); J. A. Sheikh, G. H. Bhat, Y. Sun and R. Palit, Phys. Lett. B **688** 305 (2010).

[24] V. I. Dimitrov, S. Frauendorf and F. Donau, Phys. Rev. Lett. **84** 5732 (2000).

[25] S. Roy, et. al., Phys. Lett. B **694** 322 (2011).

[26] Dan Jerrestam *et al.,* Nucl. Phys. A **577** 786 (1994).

[27] Santosh Roy *et al.,* Phy. Rev. C **81**, 054311 (2010).

[28] A. A. Pasternak *et al.,* Eur. Phys. J. A **23**, 191 (2005).

Chapter 7

Summary

The present thesis reports the angular momentum generation mechanisms in three nuclei of A $\sim$100 region, namely, ^{104,105}Pd and ^{106}Ag. The high spin states of ^{104}Pd and ^{105}Pd were populated in one experiment through the reactions ^{96}Zr(^{13}C, 5nγ)^{104}Pd and ^{96}Zr(^{13}C, 4nγ)^{105}Pd using the ^{13}C beam at 63 MeV from the 14-UD Pelletron at TIFR. In another experiment, also carried out at TIFR, the ^{106}Ag was populated through ^{96}Zr(^{14}N, 4nγ)^{106}Ag reaction using the ^{14}N beam at 68 MeV.

The de-exciting γ rays were detected using the Indian National Gamma Array (INGA) which comprised 20 Compton suppressed Clover detectors. The time stamped data from this array was sorted into various $\gamma - \gamma$ matrices and the $\gamma - \gamma - \gamma$ cube. The coincidence criteria was used to built the level schemes pertaining to these nuclei. The advantages of using Clover detector in addback mode and its use as a polarimeter have been discussed in detail in Chapter 3. The present INGA geometry also allowed the γ gated angular distribution measurements of the various relatively weak low lying γ transitions. The detectors at the forward and 90° rings were used for the DCO measurements of the γ photons de-exciting the various excited levels

that were populated during the fusion-evaporation reactions. These measurements were necessary for the spin assignment of each level. The parity assignments were performed by determining the electromagnetic character of the gamma transitions through PDCO measurements. These analysis techniques have been discussed in detail in Chapter 3. The procedure of the lifetime measurement using the DSAM technique and the corresponding error estimation is also discussed in this chapter.

The nuclei of this mass region exhibit single particle excitations and vibrations at low spins and collective rotation at high spins. Besides these well established angular momentum generation modes, they are also known to display a rich variety of exotic modes like the correlated single particle behavior, namely, the magnetic and the anti-magnetic rotation. These two phenomena are known to manifest in nuclei of low deformation, as no other favorable modes of excitations are present. However, the co-existence of the collective rotation and the anti-magnetic rotation was never observed. The co-existence of these two modes was observed in both these isotopes of Pd, namely, ^{104,105}Pd during the course of this work. Thus, these are the first instances when such a high spin behavior is reported. It may be noted that the only way that these two mechanisms can be distinguished is through the lifetime measurement.

The behavior of the AMR bands in ^{104,105}Pd have been well described by the numerical calculations based on the framework of SCPRM model. It may be interesting to note that in both the cases a prolate deformation of β $\sim$0.13 has been necessary to describe the transition rates. The co-existent collective bands also correspond to prolate shapes with β $\sim$0.19. Thus, the two Pd isotopes were found to have prolate deformation at higher spins.

In the neighboring odd-odd isotope of ^{106}Ag, a pair of doublet bands was already known and the moments of inertia (MOI) of these two bands were found to be different. During the course of the present work, the precise lifetime measurements

for the levels of the doublet bands have been performed. These measurements led to a unique observation regarding these doublet bands that though the MOI of the two bands are different, their transition rates are very similar. This novel observation has been reproduced by numerical calculations based on TPSM. This fact indicates that the doublet bands in ^{106}Ag originate due to the triaxial deformation. On the other hand, its other two bands originate due to an interplay between the shears mechanism and the collective rotation. Their high spin behavior can be understood within the framework of SPAC model which in turn assumes a prolate shape for the collective rotation. Thus, ^{106}Ag exhibits the co-existence of triaxial and axial shapes which is also supported by the TRS calculation.

Thus, the present experimental investigation and comparison with the various macroscopic models indicates a rich varity of angular momentum generation modes in these three nuclei which are:

(1) Interplay between AMR and collective rotation in one band of ^{104}Pd and two bands of ^{105}Pd.

(2) Collective rotation of a prolate shape for two bands of ^{104}Pd and one band in ^{105}Pd. These rotational bands are also associated with signature quantum numbers.

(3) Co-existence of AMR and collective rotation in ^{104,105}Pd.

(4) The doublet bands of ^{106}Ag arising due to the triaxially deformed core.

(5) The other two bands of ^{106}Ag arise due to an interplay between shears mechanism and collective rotation of a prolate core.

(6) co-existence of triaxial and axial deformation in ^{106}Ag.

The future direction of investigations which can be drawn from this thesis work

are as follows:

The present work has established the existence of anti-magnetic rotation outside Cd for the first time and further investigation in this mass region is necessary. The other mass regions of the nuclear chart must also be studied in this context to check whether AMR can be established as an alternative mechanism for the generation of high angular momentum across the periodic table. Besides, the various theoretical models should be explored to further understand this novel mechanism. The Projected Shell Model (PSM) may be particularly interesting for such a study.

The study of the doublet bands as a consequence of spontaneous chiral symmetry breaking is pursued very widely these days. However, the explanation of the experimental results for the doublet bands of ^{106}Ag in this work by the TPSM calculations indicates that invoking the complicated concept of spin chirality may not be necessary to understand the occurrence of doublet bands in nuclei. Further, the concept of chirality predicts that the transition rates of the doublet bands should be similar as a function of spin besides the moment of inertia (MOI) and routhians. Thus, the lifetime measurements of these bands whose MOI and routhians are similar are very critical and should be carried out. On the theoretical front, it should be studied whether the various doublet bands, which do not necessarily have all the properties (such as transition rates, MOI, routhian) similar, can be simply understood to be a manifestation of triaxiality. The TPSM may be the best choice for such a study.